warwick.ac.uk/lib-publications

Acoustic Metamaterials For Medical Ultrasound And Non-Destructive Evaluation

By

Stefano Laureti

Submitted for the degree of

Ph.D. in Engineering

to the

University of Warwick

describing research conducted in the

School of Engineering

Submitted December 2016

I

Table of Contents

List of Figures

List of Tables

List of Symbols

c	Speed of sound	λ	Wavelength
f	Frequency	T	Period
c_L	Longitudinal velocity	c_S	Shear velocity
σ	Poisson's ratio	ρ	Density
Y	Young's modulus	p	Pressure
T_{emp}	Temperature	k_G	Ratio of the specific heats
Z	Acoustic impedance	T_c	Transmission coefficient
R_c	Reflection coefficient	I	wave intensity
μ_c	Attenuation coefficient	D	Diameter
v	Sound velocity	SNR	Signal-to-noise ratio
P_{signal}	Signal power	P_{noise}	Noise Power
$h(t)$	Impulse response (time domain)	B	Bandwidth
$x(n)$	Input signal (discrete domain)	$y(n)$	Output signal (discrete domain)
$\Psi(n)$	Matched filter (discrete domain)	$\hat{h}(n)$	Impulse response estimation (discrete domain)
$\otimes$	Convolution operator	$e(n)$	Noise (discrete domain)
$\hat{\delta}(n)$	Dirac's delta function approximation	$\alpha_w(t)$	Windowing amplitude modulation
$s(t)$	Generic coded excitation signal	$\mathcal{R}$	Real part operator

T_{exc}	Excitation period	$\Phi(t)$	Accumulated signal phase
G_s^A G_s^B	GolayA and GolayB sequences	L	Sequence length
R_{gen}	Signal generation rate	f_c	Central frequency
APC	Acyclic pulse compression	CPC	Cyclic pulse compression
FFT	Fast Fourier Transform	$IFFT$	Inverse Fast Fourier Transform
p_{EX}	Energy delivered to the system	R_{ADC}	Rate of the Analog-to-Digital converter
MLW	Main lobe width parameter	$ML\text{-}SNR$	Main lobe SNR parameter
$MLW-SNR$	Mean lobe width SNR parameter	NSL	Near sidelobes level parameter
FSL	Far sidelobes level parameter	ε	Electric permittivity
μ	Magnetic permeability	n	Refractive index
k	Wave vector	ω	Angular frequency
E	Electric Field	K	Bulk modulus
Δ	Maximum achievable resolution	J_1	First order Bessel's function
Z_{nf}	Near field limit distance	θ	Sample temperature
q	Heat source magnitude	k_T	Thermal conductivity
σ	Complex wave number	α	Thermal diffusivity
μ_T	Thermal diffusion length	NDT	Non-Destructive Testing

UNDT	Ultrasonic NDT	LTI	Linear Time Invariant
L	Signal length (samples)	$s(t)$	Generic coded waveform
$y_{s,s}$	Output signal (steady-state)	PSD	Power Spectral Density
$\Psi_W(n)$	Matched Wiener filter	R_{ADC}	Analog-to-Digital Converter sampling rate
FIR	Finite Impulse Response	MChirp	Matching Chirp
LChirpAPC	Linear Chirp (Acyclic Pulse Compression)	GCS-APC	Golay Sequence (Acyclic Pulse Compression)
IRSGCS-APC	Inverse Repeated Golay Sequence (Acyclic Pulse Compression)	Env	Envelope
Abs	Absolute Value	$conj$	Conjugate (variable)
i	Imaginary unit	FPRs	Fabry-Peròt resonances
S_{np}	Overlap integral for the diffracted wave	G	Acoustic coupling between neighbouring holes
p_b	Background pressure	p_s	Scattered pressure
FEM	Finite Element Simulations	AM	Acoustic Metamaterial
Λ	Centre-to-centre distance	h	Metamaterial thickness
CZT	Chirp Z-Transform	FWMH	Full Width at Half Maximum
FE	Finite Element	MEMS	Micro Electro-Mechanical System

D_t	Transducer Diameter	PuC	Pulse Compression
DGS	Distance Gain Size	SAFT	Synthetic Aperture Focusing Technique
TV	Total Variation deconvolution	AT	Active Thermography
PuCT	Pulse Compression Thermography	PPT	Pulse-Phase Thermography
MF-LIT	Multi-Frequency Lock-in Thermography	μ_T	Thermal diffusion length
Θ	Temperature field	s_{SQ}	Square pulse signal
s_{TR}	True signal excitation	y_{TR}	True signal output
$\vartheta(t)$	Heaviside step function	AWG	Arbitrary Waveform Generator

Acknowledgements

I would like to express my sincere and gigantic gratitude to my thesis advisor Professor David Hutchins and to Dr. Marco Ricci for their huge help and perfect guidance during the research period. Their enthusiasm and optimism, as well as passion for research helped me tremendously in overcoming many difficulties. Thanks again for all you have both done for me.

My gratitude to Dr. Simon Leigh for his suggestions and recommendations on the realization of novel and complex devices.

Many thanks to Dr. Lee Davis for his help in the lab, his huge patience in demonstrating the equipment, and for many relaxing conversation sharing our passion for music.

My special thanks to my colleagues and friends Dr. Omololu Akanji, Dr. Ikhsan Mohamed, Dr. Riccardo Tomasello, Giuseppe Silipigni, for many good times shared together.

Special thanks also to all my friends, to my parents and sibling. Without your love, generosity and happiness this would not have been possible.

Declaration

This thesis is submitted to the University of Warwick in support of my application for the degree of Doctor of Philosophy. It has been composed by myself and has not been submitted in any previous application for any degree (apart from a part of the background material in Section 2.1, which was previously submitted for a Master's degree at Università degli Studi di Perugia, Italy, in 2013).

Both the experimental work and the post-processing were performed and evaluated by the present author, except where stated otherwise, and contributed to a collaboration between the University of Warwick and the University of Perugia, for which the present author was involved in a cotutelle Ph.D. program. All publications to date arising from this research are listed on the following pages.

Stefano Laureti

Publications

JOURNAL PAPERS

- <u>Laureti, S.</u>, Hutchins, D. A., Davis, L. A. J., Leigh, S. J., & Ricci, M. (2016). High-resolution acoustic imaging at low frequencies using 3D-printed metamaterials. *AIP Advances*, *6*(12), 121701.

- Mohamed, I., Hutchins, D., Davis, L., <u>Laureti, S.</u>, & Ricci, M. (2016). Ultrasonic NDE of thick polyurethane flexible riser stiffener material. *Nondestructive Testing and Evaluation*, 1-20.

- Hutchins, D., Burrascano, P., Davis, L., <u>Laureti, S.</u> and Ricci, M. (2014). Coded waveforms for optimised air-coupled ultrasonic nondestructive evaluation. *Ultrasonics*, 54(7), 1745-1759.

BOOK CHAPTERS

- Caporale, S., Callegari, S., Hutchins, D. A., <u>Laureti, S.</u>, Burrascano, P., & Ricci, M. (2015). Excitation and Deconvolution in Ultrasound Nondestructive Testing Systems. In *Ultrasonic Nondestructive Evaluation Systems* (pp. 85-140). Springer International Publishing.

- Senni, L., Battaglini, L., Burrascano, P., <u>Laureti, S.</u>, & Ricci, M. (2015). Industrial Applications: Ultrasonic Inspection of Large Forgings. In *Ultrasonic Nondestructive Evaluation Systems* (pp. 245-258). Springer International Publishing.

- Battaglini, L., Callegari, S., Caporale, S., Davis, L. A. J., <u>Laureti, S.</u>, Senni, L., & Hutchins, D. A. (2015). Industrial Applications of Noncontact Ultrasonics Techniques. In *Ultrasonic Nondestructive Evaluation Systems* (pp. 271-295). Springer International Publishing.

CONFERENCE PAPERS

- Mohamed, I., Hutchins, D., Davis, L., <u>Laureti, S.</u>, & Ricci, M. Pulse Compression Ultrasonic Non Destructive Evaluation of Thick Polymer Samples, ECNDT 2014, European Conference on Non-Destructive Testing, Prague.

- <u>Laureti, S.</u>, Davis, L. A. J., Ricci, M., & Hutchins, D. A. (2014, September). The study of broadband acoustic metamaterials in air. In Ultrasonics Symposium (IUS), 2014 IEEE International (pp. 1344-1347). IEEE.

- Battaglini, L., <u>Laureti, S.</u>, Ricci, M., Burrascano, P., Davis, L. A. J., & Hutchins, D. A. (2014, September). The use of Pulse Compression and Frequency Modulated Continuous Wave to improve Ultrasonic Non Destructive Evaluation of highly-

scattering materials. In Ultrasonics Symposium (IUS), 2014 IEEE International (pp. 1940-1943). IEEE.

- Hutchins, D. A., Laureti, S., Davis, L. A. J. and Ricci, M.,"The design of metamaterials for use at ultrasonic frequencies", Acoustofluidics 2014, Monash University, Prato

- Burrascano, P., Laureti, S., Hutchins, D. A., L.Senni and Ricci, M., "Efficient modelling of Nonlinear Ultrasonic NDT Systems", BiNDT 2015.

- Laureti, S., Akanji, O., Davis, L.A.J., Leigh, S.J., Ricci, M. and Hutchins, D.A., 'Design and characterization of 3D printed phononic crystals for sub-MHz ultrasound manipulation', IUS 2015, Taipei, Taiwan.

- Burrascano, P., Laureti, S., Hutchins, D.A., Ricci, M., Senni, L., "A pulse compression procedure for the measurement and characterization of non-linear systems based on exponential chirp signals.", IUS 2015, Taipei, Taiwan.

- Mohamed, I., Davis, L.A.J, Hutchins, D.A, Laureti, S., Ricci, M., "Low Frequency Coded Waveform for the Inspection of Concrete Structure", IUS 2015, Taipei, Taiwan.

- Silipigni, G., Burrascano, P., Hutchins, D.A., Laureti, S., Petrucci, R.,Senni, L., Torre, L., Ricci, M., (2015) "Application of pulse-compression to infrared thermography non-destructive testing of composites and thermo-plastic materials", Annual Meeting of AIVELA (Italian Association of Laser Velocimetry and non-invasive diagnostics), Perugia, Italy.

- Burrascano, P., Laureti, S., Ricci, M., Senni, L., (2015) "Accurate modelling of Hysteretic Systems for an efficient energetic conversion", ICRERA 2015.

INVITED TALK

- Laureti, S., Hutchins, D.A., Davis, L.A.J, Leigh, S.J. and Ricci, M., "High-resolution acoustic imaging at low frequencies using 3D-printed metamaterials", Phononics 2015, Paris, June 2015.

Abstract

This thesis shows both the use of acoustic metamaterials and coded waveforms for Non-Destructive Testing (NDT) applications.

The exotic features of the acoustic metamaterials have been exploited for imaging a sub-wavelength object at frequencies into the middle audible – low ultrasonic range, thus beating the so-called diffraction limit. This has been investigated by means of both Finite Element Modelling and a series of experiments. These demonstrate that acoustic metamaterials fabricated using additive manufacturing with a polymer substrate can be used successfully for imaging a subwavelength object within a frequency range that was not previously explored. The experimental setup made use of coded waveform excitation for characterising the performance of these metamaterials in the frequency domain. Such broadband excitations waveforms can be exploited together with advanced signal processing techniques such as Pulse Compression (PuC) to enhance the Signal-to-Noise Ratio (SNR). Hence, a first step toward the realization of an acoustic metamaterial device that can be used with coded waveforms and PuC has been investigated.

Parallel research on the optimal use of coded signals with PuC techniques has been carried out. The main characteristics of several widely-used coded waveforms and advanced algorithms have been reported. Their features have been investigated numerically so as to provide a benchmark for choosing an optimal coded waveform and pulse compression algorithm for a given NDT application. In addition, the improvement in inspection capabilities given by these advanced signal processing techniques has been tested using real industrial NDT applications in highly scattering and attenuating samples. This has been done by programming a tailored post-processing/imaging algorithm for each specific application.

Furthermore, a portable instrumentation system is described, which is capable of providing a performance comparable to standard bench-top PuC instruments.

Finally, an innovative strategy for using coded signals and PuC in active thermography inspection has been investigated. This results in an enhanced defect discrimination in challenging materials with respect to the standard PuC thermography procedure.

CHAPTER 1: Background

1.1   Acoustics and Ultrasound

Sound has always attracted the attention of human beings. Acoustics, as the science of sound, can be dated back to 530 BC when Pythagoras wrote the mathematical properties of stringed instruments [1]. Sound is a physical wave-phenomenon characterized by both a pressure variation and a coordinated vibration of molecules within a propagative medium, which can be a solid, liquid or gas. In common with other wave phenomena, sound can be described by its amplitude and its frequency. In particular, the latter parameter leads to the classification of sound shown in Fig.1.1, where signals having a frequency greater than 20 kHz are commonly referred to as being ultrasound:
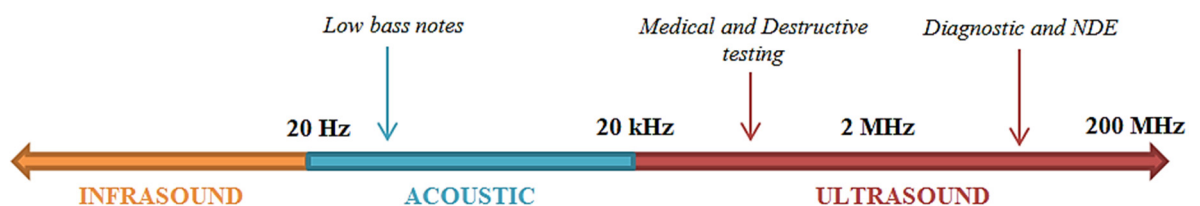
Figure 1.1: Acoustic field classification

Ultrasound is widely used in several different applications, ranging from metal materials cleaning[2], particle manipulation[3], medical applications [4], [5] and Non-Destructive Testing (NDT) [6], [7]. Medical ultrasound has developed significantly in recent years, and many people have experienced it as a diagnostic method in hospitals and clinics. Ultrasonic NDT (UNDT) is a non-invasive method used widely to investigate the integrity, the mechanical characteristics and/or the presence of flaws in a wide range of materials and industrial products, such as composites, plastics and metals materials, concrete, food and liquids. The first practical application of ultrasound can be found in 1917, when L. Paul and C. Constantin used it as method to detect submarines [8].

Both medical and NDT applications rely on the propagation of ultrasonic waves inside the sample under test, and researchers have tried to optimize the generation and the reception of ultrasonic signals, so as to improve imaging resolution and signal to noise ratio (SNR). This research will investigate one of the newest techniques that could potentially be used to enhance the resolution of ultrasonic imaging: the use of special "engineered" acoustic metamaterials characterized by unusual macro-properties. In addition, this thesis will describe studies into the use of coded waveforms and pulse compression techniques. These will be used to study both the performance of acoustic metamaterials and their use in improving the quality of NDT measurements in highly attenuating and scattering material.

In order to understand the research described later in this thesis, a mathematical and physical description of the phenomena involved in sound propagation will be given in this Chapter. This will describe mathematically the main modes in which sound travels through a medium. It will also highlight the limitation on image resolution imposed by the so-called "diffraction limit" in conventional ultrasonic imaging, illustrating why metamaterials that could break this limit are interesting. Finally, a brief description of the main properties of coded waveforms and acoustic metamaterials will be reported. The chapter ends with a thesis outline providing a brief introduction to the chapters that follow.

1.2   Properties of Ultrasound

In order to propagate, sound needs a medium which is able to change its local properties (such as density) when subject to a variable pressure field. In the absence of forces, particles of the medium lie in their equilibrium position. When a pressure field is applied to a medium, particles change their absolute position and transfer the energy to neighbouring particles. For longitudinal waves [9] in liquids and gases, the particle displacement is parallel to the perturbation direction. On the other hand, a displacement

orthogonal to the perturbation direction can exist in solid, *i.e.* transverse or orthogonal waves

[10]. Figures 1.2 and 1.3 depict the particles movement related to a longitudinal wave and

to a shear wave:
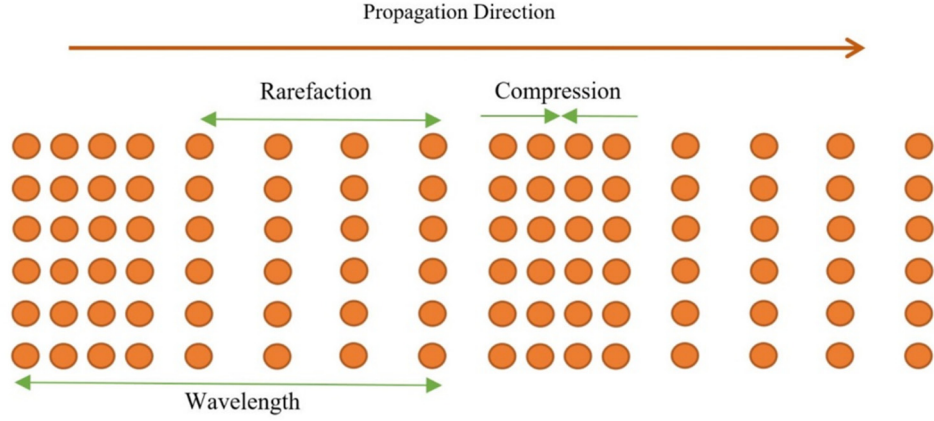
Figure 1.2: Longitudinal wave particle motion.
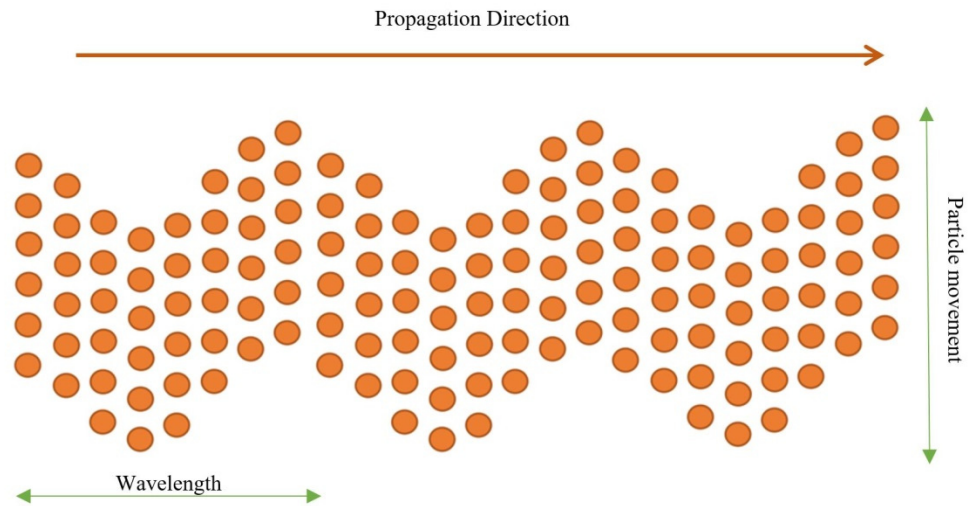
Figure 1.3: Shear wave particle motion

Every wavelike phenomenon can be described by its frequency f, its wavelength λ and the

period T, which is the time taken to complete one cycle. The wavelength λ is related to the

velocity of propagation of the medium c in which the wave travels, as for equation 1.1:

$$\lambda = \frac{c}{f}$$

$$T = \frac{1}{f}$$

(1.1)

The velocity of propagation c it is a quantity related to mechanical properties of the medium. The longitudinal (c_L) or shear (c_S) velocities of propagation are given by Equations 1.2 and 1.3:

$$c_L = \sqrt{\frac{Y(1-\sigma)}{\rho(1+\sigma)(1-2\sigma)}} \tag{1.2}$$

$$c_S = \sqrt{\frac{Y}{2\rho(1+\sigma)}} \tag{1.3}$$

where Y is the Young's modulus, σ the Poisson's ratio and ρ the volumetric density,

If the medium is an ideal gas, only one value of velocity exists as the medium allows only one propagation mode:

$$c = \sqrt{\frac{k_G p_0}{\rho_0}} \tag{1.4}$$

where p_0 and ρ_0 are the pressure at the standard environmental condition ($T_{emp} = 20\ °C$, and $p = 101.325$ kPa) and k_G the ratio of the specific heats at constant pressure and constant volume. For air, the velocity of propagation can be related to the temperature T_{emp} using Equation 1.5:

$$c = 331 + 0.6\ T_{emp} \tag{1.5}$$

with T_{emp} in Celsius and the resulting velocity of propagation c in ms^{-1}.

Table 1.1 shows the longitudinal velocity of propagation for several common propagation media [11]:

Material	Sound Velocity (m·s^{-1})
Rubber (polybutadiene)	1610
Air at 20 °C	343
Lead	1210
Gold	3240
Glass	4540
Copper	4600
Aluminium	6320

Table 1.1: velocity of propagation for several common media

1.2.1. Acoustic Impedance

As described above, different materials mechanical properties lead to different sound velocities. Acoustic impedance, *Z,* summarizes the acoustic properties of a medium in a way which is similar to the electrical impedance, and is defined as in equation (1.6):

$$Z = \rho\, c \qquad\qquad (1.6)$$

with ρ the medium density kgm^{-3}. Acoustic impedance Z is usually expressed in terms of Rayls (kgm^{-2}s^{-1}) [12]. It will be shown in the following section that acoustic impedance plays a key role in the propagation of ultrasound.

1.2.2. Reflection, Transmission and Refraction

Ultrasound waves reflection occurs at the interface between two media having different impedance values with an impedance mismatch. When an ultrasonic wave impinges perpendicularly onto the surface of a medium with different acoustic impedance, it can be either reflected and/or transmitted into the medium, as depicted in Figure 1.4:
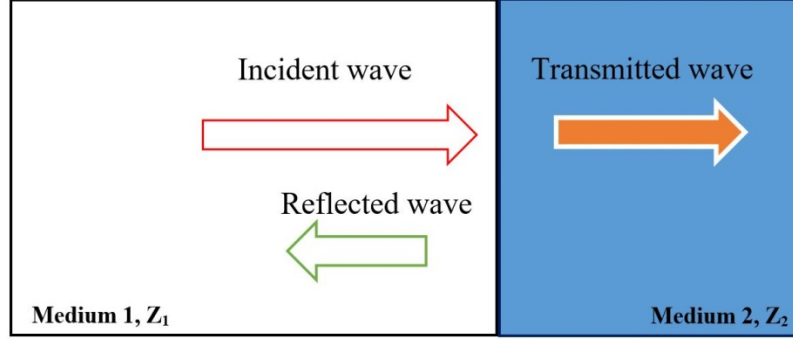
Figure 1.4: Reflection and transmission at the interface between two different mediums.

The amount of transmitted and/or reflected energy can be expressed in terms of the acoustic impedances of the first medium Z_1 and the one of the second medium Z_2, as for equation (1.7) and equation (1.8):

$$T_c = \frac{4Z_1 Z_2}{(Z_1 + Z_2)^2} \tag{1.7}$$

$$R_c = \left(\frac{Z_1 - Z_2}{Z_1 + Z_2}\right)^2 \tag{1.8}$$

where T_c and R_c are the transmission and the reflection coefficient respectively.

If Z_1 and Z_2 are the same, the incident wave is totally transmitted into the second medium. In most of real ultrasonic applications, the energy does not impinge perpendicularly onto the interface between the two media. In this case, the behaviour of the reflected and transmitted (refracted) energy is regulated by Snell's Law [13], as in equation (1.9):

$$\frac{\sin\alpha}{\sin\beta} = \frac{c_1}{c_2} \tag{1.9}$$

where α and β are the angles of incidence and refraction respectively, and c_1 and c_2 are the speed of sound in medium 1 and medium 2 respectively.
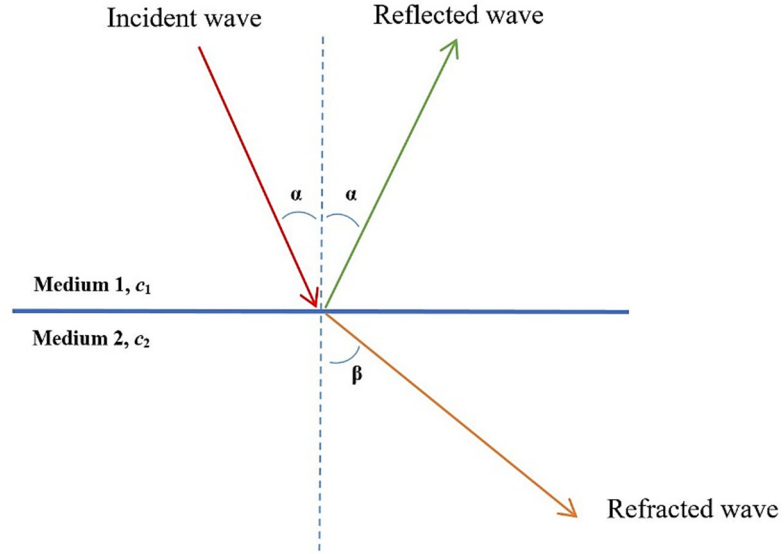
Figure 1.5: Illustration of Snell's law.

In some cases, longitudinal waves can be converted into shear waves and vice versa. As a consequence of the different values of shear and longitudinal sound velocity of each medium, the propagation modes are refracted and reflected at different angles. In particular, as the shear wave velocity is lower than the longitudinal wave velocity, the latter one is reflected and refracted at a bigger angle with respect to the normal surface direction [14].
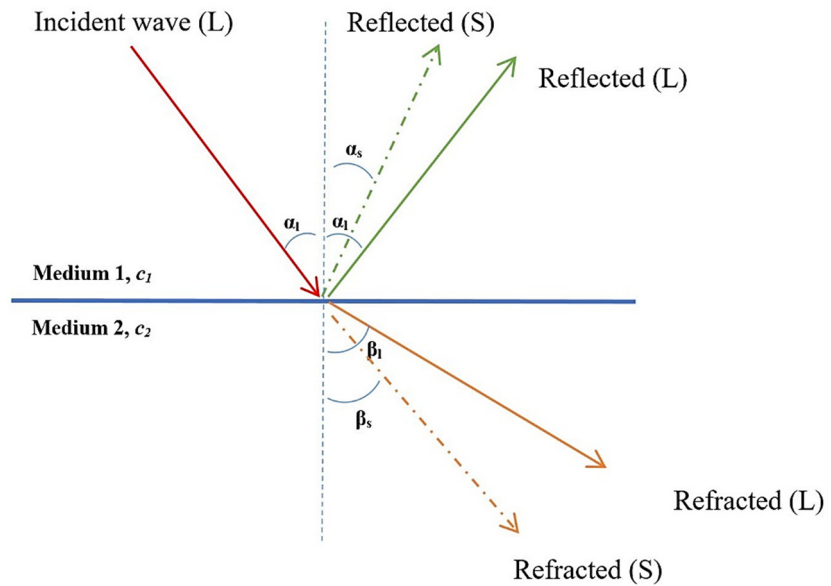
Figure 1.6: Snell's law for longitudinal to shear mode conversion.

The higher the impedance mismatch between the two media, the higher the amount of energy reflected from the interface, and hence a lower amount of energy is transmitted into the second medium. This is of utmost importance in NDT. In fact, the ultrasonic wave generated from a transducer has to travel into two different mediums at least before being recorded. Therefore, a matching layer placed at the outer surface of the ultrasound probe is needed to couple with the mechanical properties of the propagation medium. Thus, the choice of the right matching layer for a specific NDT application plays a key role for the quality of the test itself [15]–[18].

1.3   Limitations on the use of Ultrasonic Non-Destructive Testing

In order to understand the research described in this thesis, a more accurate description of the phenomena involved on the transmission and the reflection of an ultrasonic signal into a generic material is needed. As stated above, ultrasonic testing relies on the propagation of an ultrasonic wave into a sample to perform a wide range of test and structural quality assessment. This section shows what are the issues to take into account when an ultrasonic non-destructive testing is performed.

1.3.1. Attenuation

Commonly, a transducer (or some transducers) is used to generate an ultrasonic wave that travels towards the investigated sample. This acoustic energy is reflected from the back-wall surface of the sample and then collected from the transducer. A simplified scheme of a standard ultrasonic pulse-echo test is depicted in Figure 1.7:
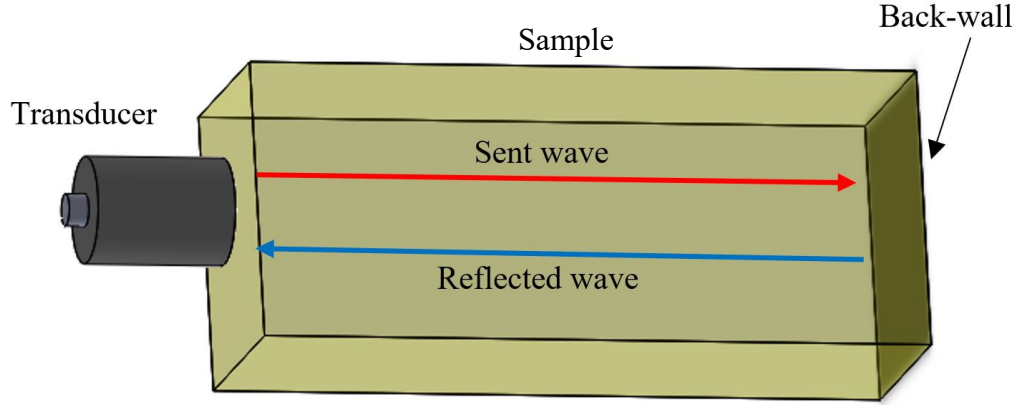
Figure 1.7: simplified ultrasonic NDT scheme.

However, the ultrasonic wave is attenuated during its path into the material. This means that only a portion of the originally sent ultrasonic energy can be collected by the probe afterwards. This phenomena is known as attenuation or absorption [19]. Attenuation occurs in any material and it is an exponential function of the propagation path in the medium. As a wave travels in a medium it causes the vibration of the particles around their equilibrium position. The vibrational energy is transferred from a particle to another, hence friction and thermal conductivity occur. Thus, the conversion from kinetic to thermal energy causes the weakening of the ultrasonic wave energy. Attenuation is usually expressed in terms of reduction of the intensity, as in equation (1.12):

$$I_x = I_0 \cdot e^{-\mu_c x} \qquad (1.12)$$

where I_x is the intensity of the ultrasonic wave measured at a distance into the material x, I_0 the intensity of the input signal and μ_c is a coefficient that takes into account all the effect of material attenuation. Note that μ_c is a function of the frequency of the input sound signal. In particular μ_c it is the sum of two terms: (i) $\mu_{c,a}$ which represents the loss due to molecular friction and (ii) $\mu_{c,s}$ for losses due from scattering. $\mu_{c,a}$ is a function of the viscosity, density,

temperature and speed of sound of the material, whilst $\mu_{c,s}$ is a function of the dimension of the inclusions into the material. Both are frequency-dependent.

In some examples of imaging using metamaterial devices that have been investigated in this thesis, sound has to travel through air before reaching the sample under investigation. As can be seen from Figure 1.10, where the attenuation coefficient μ_c (dB/m) is plot as a function of the frequency, attenuation increases with attenuation as expected. At 20 °C, the attenuation of air is about 160 dBm^{-1} at 1 MHz, and practically, it means that ultrasound can travel only for few centimetres in air at this frequency [20].
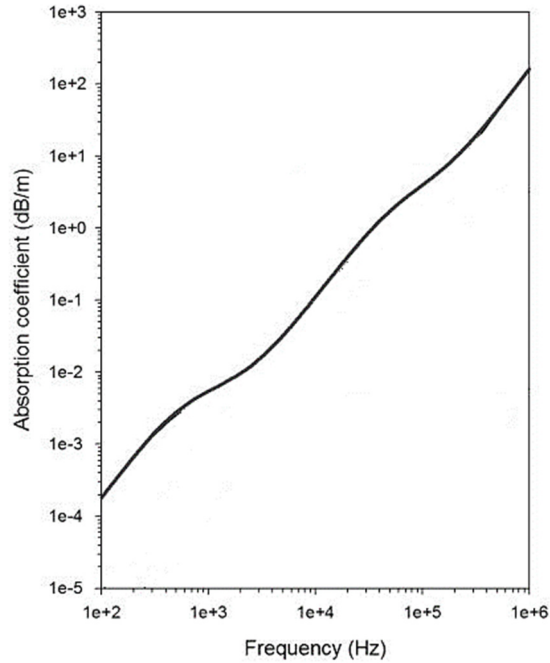
Figure 1.8: Absorption coefficient as a function of the frequency in air (taken from ref [21]).

1.3.2. Scattering and the Diffraction Limit

Flaws inside a material in which sound propagates could produce a reflection due to an acoustic impedance mismatch with the bulk material. This fact is of utmost importance when an ultrasonic test is used for detecting and imaging defects inside a sample. Therefore,

defects or objects that are a source of reflected waves, *i.e.* scatterers, can be detected and imaged, as in Figure 1.9:
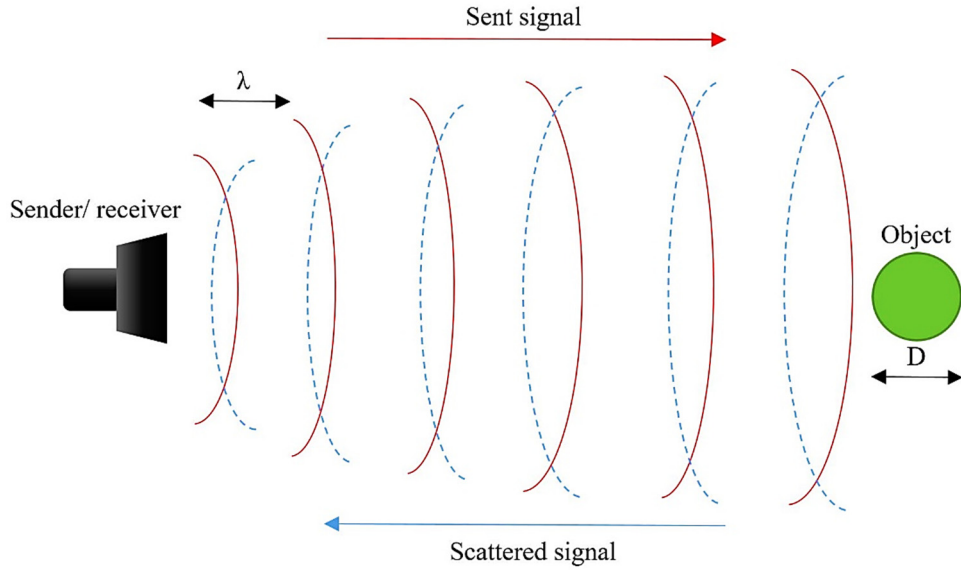
Figure 1.9: imaging of a scatter by an ultrasonic NDT.

However, nature sets a limit on the minimum dimension of the object that can be detected in this way. For simplicity, consider a perfectly sphere-shaped defect. For a fixed excitation wavelength λ, the minimum value of the object diameter D that can be imaged is [22]:

$$D = \lambda = \frac{v}{f} \qquad (1.13)$$

Equation (1.13) is a direct consequence of the Rayleigh's criterion for the diffraction of a wave from a finite dimension of a single slit [9]. This limitation is known as the diffraction limit. As a consequence, objects having dimensions smaller than the wavelength cannot be imaged using conventional instrumentation. However, it is known that an "Evanescent field" also exists, so that whenever an ultrasonic signal impinges on an object, two different kinds of waves are scattered: (i) *Propagation waves*, whose amplitude decays linearly by increasing the distance r from the object and (ii) *Evanescent waves*, which decay exponentially.
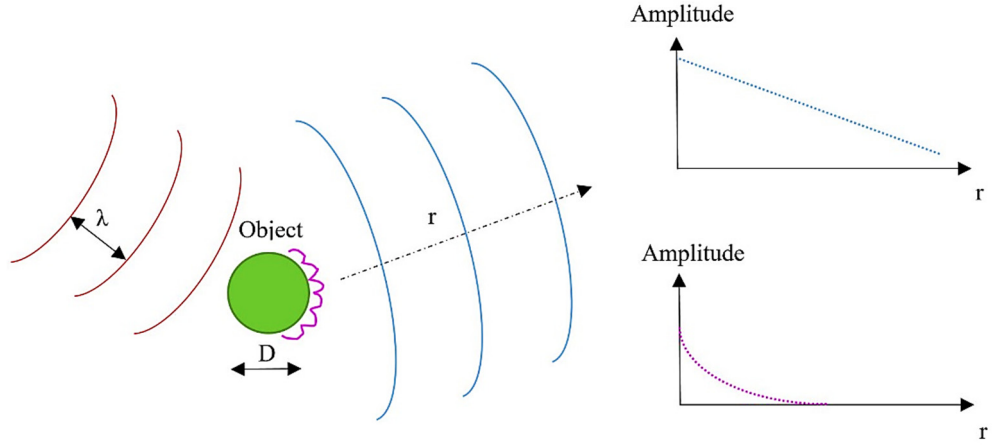
Figure 1.10: Propagation (blue) and evanescent (purple) waves scattered from an object.

Evanescent waves are tiny variations of the acoustic field just above the surface of the object. These waves carry sub-wavelength details of the object. However, they will not be detected by a conventional receiver as their amplitude decreases exponentially with distance from the sample surface. Therefore, only propagation waves can be imaged. This limits the maximum achievable resolution as in equation (1.13) [22]. It is the purpose of some metamaterials, to be described later in the thesis, to utilise these waves so as to increase resolutions beyond the limit imposed conventionally by equation (1.13).

1.4 Signal-to-Noise Ratio (SNR), Acoustic Metamaterials and Coded Excitations

To understand the research contained within this thesis, it is interesting to see how both coded waveforms and acoustic metamaterials can help in improving both SNR and imaging quality in ultrasonic measurements.

1.4.1. SNR and the proposed techniques

In a standard scheme, the transducer (or more than one) is typically connected by cables to a signal generator and to an oscilloscope, which digitalize the analogue signal coming

from the receiver transducer. The final aim of the said setup is to provide a readable signal (measurement) that can be post-processed and analysed by an operator. Measurements of any kind are always affected by noise. In general, noise found in an ultrasonic measurement is mainly due to either (i) *electromagnetic noise* transmitted by the cables or (ii) *quantization noise* that is related to the finite number of bits available in the Analog-to- Digital Converter (ADC) of the oscilloscope. The quality of the measurement is mathematically expressed by the SNR. Although many definitions of SNR exist, depending on the final aim of each measurement, they are always coherently related to the expression in equation (1.14):

$$SNR = \frac{P_{signal}}{P_{noise}} \hspace{4cm} (1.14)$$

where *P~signal~* and *P~noise~* are the respectively the power of the signal and the one of the noise. SNR is usually measured in *dB* [23]. For a fixed noise level, SNR can be enhanced only by increasing the received signal amplitude. It follows that sound attenuation, as in equation (1.12), dramatically reduces the achievable SNR.

A direct strategy to counterbalance the attenuation would consist of increasing the peak voltage amplitude of the sent signal. However, peak-to-peak voltage level operating on the transducer cannot be increased arbitrarily as it will damage the probe itself. Thus, for a particular testing frequency, *coded excitation* is a good way of enhancing the energy available in an ultrasonic test, and is discussed in greater detail in a later Chapter of this thesis. Note that lowering the testing frequency in general can decrease the attenuation and improve the SNR. However, as stated in the previous section, the lower the testing frequency, the lower the minimum object dimension that can be imaged.

To overcome this problem, a new class of engineered materials also known as Metamaterials can be used to maintain a low testing frequency , and thus counterbalancing the attenuation effect by increasing the imaging resolution that is available. This is achieved

by restoring the evanescent waves and recovering the sub-wavelength details, with a dramatic increasing of the maximum achievable resolution. In addition, Coded Signals can be used to counterbalance the signal attenuation, leading to a further improvement in SNR. The next sub-sections will describe briefly the features and the use of Coded Signals and Acoustic Metamaterials. The reader will find a more extensive mathematical analysis of the two techniques in Chapters 2 and 3.

1.4.2. Coded Waveforms and Pulse Compression

Ultrasonic NDT commonly excites the sample under test using an ultrasonic signal with a broad bandwidth, typically using a short voltage pulse to excite the transmitter. The response of the sample to this excitation, *i.e.* the impulse response, is therefore recorded by the receiver and analysed. Ideally, the short voltage impulse is a Dirac Delta function. Thus, its frequency spectrum is flat within the whole bandwidth. Figure 1.11 show the voltage impulse used as the excitation for the sender and its frequency spectrum, obtained after Fourier Transform:
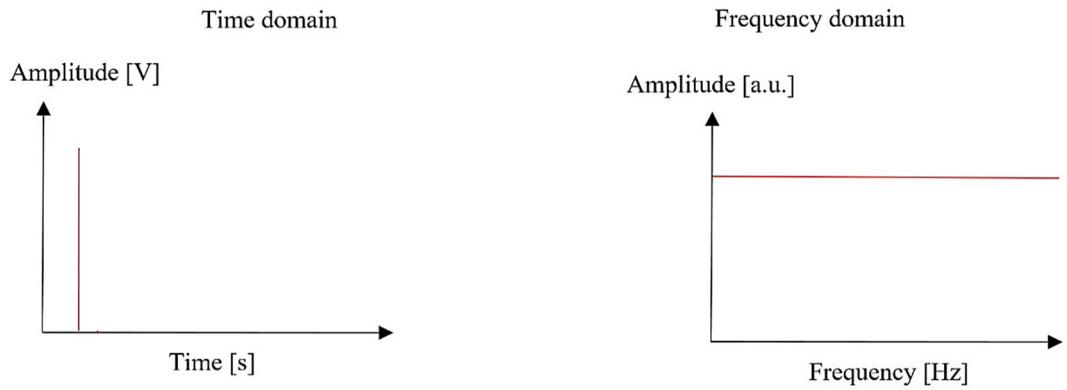
Figure 1.11: Impulse signal and its frequency spectrum.

As the attenuation increases at high frequencies, the signal amplitude must be sufficiently high to provide a good SNR in the measurement. This is done by simply increasing the signal voltage. However, transducers have electrical constraints on the

maximum applied voltage that they can handle. So, voltage cannot be increased arbitrarily. Furthermore, some industrial safety regulations limit the maximum voltage that can be applied to the transducer. A solution to this problem can be found in the use of Coded Waveforms and the so-called Pulse Compression algorithm. This class of signals, such as chirps or bipolar sequences, allow the use of low voltage excitations together with an improvement in SNR. This is because coded waveforms are made of a finite number of coded time-delayed impulses, which in turn assures a higher level of energy to be sent towards the sample under test. Their frequency spectrum can be considered relatively flat around a limited frequency range. An example of a coded waveform, a chirp signal in this case, is depicted in Figure 1.12:
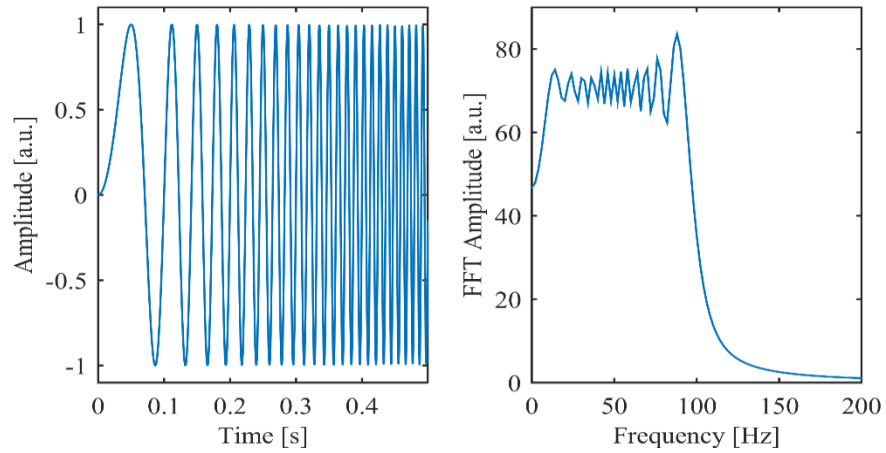
Figure 1.12: An example of a chirp signal and its frequency spectrum.

The impulse response of the object under test is obtained by cross-correlating the received signal and the input signal, leading to the Pulse Compression procedure. The gain in the impulse response SNR with respect to the standard use of the impulse is proportional to the time duration of the coded signal and the number of coded pulses [24]–[26]. Thus, the use of coded signal together with the pulse compression procedure it is a robust and powerful method exploited to counterbalance the acoustic attenuation by simply stretching the total time duration of the signal. In addition, this is done without missing any spectral information

in respect to the ideal single pulse excitation. The reader will find a deeper mathematical description on the use of coded signals and pulse compression in Chapter 2.

1.4.3. Acoustic Metamaterials

Although many slightly different definitions of "Metamaterial" can be found in the literature, the main features can be described as follows:

(i)   A metamaterial is a material that has properties that derive from its internal structure, and not just from those of the materials from which it is made.

(ii)   It contains structures within it that are much smaller than the wavelength of the incident energy.

(iii)   Its response to an acoustic or electromagnetic perturbation results from the sum of all these internal material parameters.

For the sake of simplicity, one can describe metamaterials (also known as Photonic Crystals in the electromagnetic case) as artificial materials that exhibit "exotic" properties which are not commonly observed in nature. In the particular case of the acoustic metamaterials, these structures provide the possibility to focus or collimate the sound using a flat lens, to build superlenses and to collect the evanescent waves from an object [27]–[29]. In this work the metamaterials will be used for imaging purposes. In particular, they are going to be designed and used to restore the evanescent field and giving sub-wavelength details of an object. It is important to point out that the ability to collect the evanescent waves is usually limited to specific discrete set of frequencies [29], [30], and this process will be described more fully in Chapter 3. Therefore, one of the main aims of this thesis is to produce and design an acoustic metamaterial that could be capable to work over a range of frequencies. This will be done by exploiting 3D printing, (or additive manufacturing), which allows a fast and relatively easy realization of acoustic metamaterials geometries.

Once this is achieved, metamaterials could be used in combination with coded signals and pulse compression.

1.5   Thesis Outline

This thesis concentrates on research into pulse compression and metamaterials. Each has the potential for improving the quality of measurements in various materials. Chapter 2 reports the mathematical background of several kind of coded excitations, as well as algorithms to perform pulse compression technique and filtering. Moreover, numerical simulations results are shown with the aim to give a guideline on the optimal choice of a coded excitation for a specific purpose. Chapter 3 is focused on the historical and theoretical background to acoustic metamaterial and phononic crystals. Chapter 4 shows the finite element simulation results for several exotic acoustic metamaterial structures. Numerical results on the use of acoustic metamaterial for sub-wavelength acoustic imaging are also shown. Experimental results on the use of acoustic metamaterials for sub-wavelength imaging purpose are given in Chapter 5, together with a path toward the realization of a broad-band acoustic metamaterial device. Chapter 6 reports the use of coded signals and advanced signal processing techniques for the non-destructive testing of several highly attenuating materials. Furthermore, it also shows the realization of a portable device for real time pulse compression, as well as its application on the investigation of concrete structure. An advanced application of the combined use of coded signals and pulse compression for thermography is shown in Chapter 7. Finally, Chapter 8 gives overall conclusions and ideas for further work.

References

[1]   R. W. Hall, "The Mathematics of Musical Instruments The willow flute," *Solutions*, pp. 1–11, 2000.

[2]   A. D. Farmer, A. F. Collings, and G. J. Jameson, "Effect of ultrasound on surface cleaning of silica particles," *Int. J. Miner. Process.*, vol. 60, no. 2, pp. 101–113, 2000.

[3]   C. Devendran, I. Gralinski, and A. Neild, "Separation of particles using acoustic streaming and radiation forces in an open microfluidic channel," *Microfluid. Nanofluidics*, vol. 17, no. 5, pp. 879–890, 2014.

[4]   W. D. O'Brien Jr, "Assessing the risks for modern diagnostic ultrasound imaging," *Japanese journal of applied physics*, vol. 37. pp. 2781–2788, 1998.

[5]   S. Mitragotri and B. A, "Healing sound: the use of ultrasound in drug delivery and other therapeutic applications.," *Nat. Rev. Drug Discov.*, vol. 4, no. March, pp. 255–60, 2005.

[6]   J. Blitz and G. Simpson, "Ultrasonic methods of non-destructive testing," *Springer Sci. Bus. Media*, vol. 2, 1995.

[7]   P. Pallav, T. H. Gan, and D. A. Hutchins, "Elliptical-Tukey Chirp Signal for Ultrasonic Imaging," *IEEE Trans. Ultrason. Ferroeletrics, Freq. Control*, vol. 54, no. 8, pp. 1530–1540.

[8]   C. Constantin and L. Paul, "Production of submarine signals and the location of suemarine orjects," *US Pat. 1,471,547*, 1923.

[9]   J. W. S. B. Rayleigh, *The Theory of Sound Vol.2*. Macmillan, 1896.

[10]   J. R. Frederick, "Ultrasonic engineering," 1965.

[11]   "The speed of sound in other materials." [Online]. Available: https://www.nde-ed.org/EducationResources/HighSchool/Sound/speedinmaterials.htm.

[12]   B. Lempriere, *Ultrasonic and Elastic Waves: Frequently Asked Questions*. 2002.

[13]   J. W. Shirley, "An Early Experimental Determination of Snell's Law," *Am. J. Phys.*, vol. 19, no. 9, p. 507, 1951.

[14]   T. L. Szabo, *Diagnostic Ultrasound Imaging: Inside Out*. Academic Pres, 2014.

[15] T. E. Gómez Alvarez-Arenas, "Acoustic impedance matching of piezoelectric transducers to the air.," *IEEE Trans. Ultrason. Ferroelectr. Freq. Control*, vol. 51, no. 5, pp. 624–633, 2004.

[16] S. P. Kelly, G. Hayward, and T. E. G. Alvarez-Arenas, "Characterisation and assessment of an integrated matching layer for air coupled ultrasonic applications," *IEEE transactions on ultrasonics, ferroelectrics, and frequency control*, vol. 51, no. 10, pp. 1314–1323, 2004.

[17] H. Tohmyoh, "Polymer acoustic matching layer for broadband ultrasonic applications," *J. Acoust. Soc. Am.*, vol. 120, no. 1, pp. 31–34, 2006.

[18] B. Hadimioglu and B. T. Khuri-Yakub, "Polymer films as acoustic matching layers," *IEEE Symp. Ultrason.*, pp. 1337–1340, 1990.

[19] S. Kocis and Z. Figura, *Ultrasonic Measurements and Technologies*. 1996.

[20] A. Vladišauskas and L. Jakevičius, "Absorption of ultrasonic waves in air," *Ultragarsas*, vol. 1, no. 1, pp. 46–49, 2004.

[21] D. A. Battaglini, L., Callegari, S., Caporale, S., Davis, L. A. J., Laureti, S., Senni, L., & Hutchins, "Industrial Applications of Noncontact Ultrasonics Techniques," in *Ultrasonic Nondestructive Evaluation Systems*, Springer International Publishing, 2015, pp. 271–295.

[22] J. B. Pendry, "Negative refraction makes a perfect lense," *Phys. Rev. Lett.*, vol. 85, no. 18, p. 3966, 2000.

[23] A. Carlson and P. Crilly, "Communication Systems, 5e," 2010.

[24] D. Hutchins, P. Burrascano, L. Davis, S. Laureti, and M. Ricci, "Coded waveforms for optimised air-coupled ultrasonic nondestructive evaluation," *Ultrasonics*, 2014.

[25] K. S. Ho, T. H. Gan, D. R. Billson, and D. a. Hutchins, "Application of pulse compression signal processing techniques to electromagnetic acoustic transducers for

noncontact thickness measurements and imaging," *Rev. Sci. Instrum.*, vol. 76, no. 5, p. 54902, 2005.

[26] T. H. Gan, D. A. Hutchins, D. R. Billson, and D. W. Schindel, "The use of broadband acoustic transducers and pulse-compression techniques for air-coupled ultrasonic imaging," *Ultrasonics*, vol. 39, no. 3, pp. 181–194, 2001.

[27] C. Wenshan and V. Shalaev, *Optical Metamaterials*, vol. 330, no. 6011. Springer New York, 2010.

[28] M. Ambati, N. Fang, C. Sun, and X. Zhang, "Surface resonant states and superlensing in acoustic metamaterials," *Phys. Rev. B*, vol. 75, no. 19, p. 195447, May 2007.

[29] J. Zhu, J. Christensen, J. Jung, and L. Martin-Moreno, "A holey-structured metamaterial for acoustic deep-subwavelength imaging," *Nat. Phys.*, vol. 7, no. 1, pp. 52–55, 2011.

[30] J. Christensen, L. Martin-Moreno, and F. J. Garcia-Vidal, "Theory of resonant acoustic transmission through subwavelength apertures," *Phys. Rev. Lett.*, vol. 101, no. 1, p. 14301, 2008.

CHAPTER 2: Coded Waveforms and Pulse Compression

2.1 Introduction: Pulse Compression

Commonly, ultrasonic NDT procedures rely on the use of a short time-duration voltage impulse to excite the ultrasonic probe and to retrieve information about the internal structure of the sample. A single transducer is often used to excite the sample under test, leading to a *Pulse Echo* inspection. A short pulse allows the sample to be excited across a broad frequency range. This is because a short time duration pulse is a good approximation to the Dirac Delta function, whose frequency spectrum can be considered ideally flat over the frequency range of interest [1]–[3]. Figure 2.1 shows an example of a pulsed signal and its corresponding frequency spectrum:
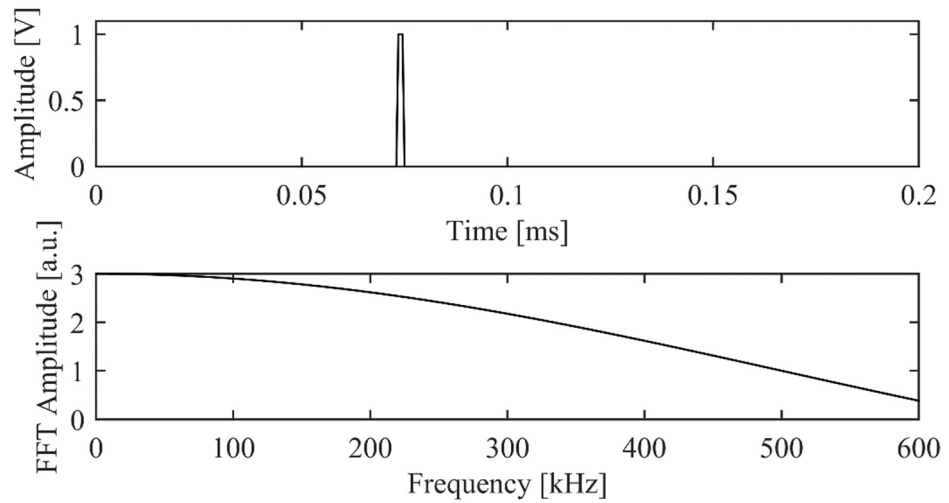
Figure 2.1: Pulsed signal and its frequency spectrum.

The signal recorded by using a single pulse input signal *x(t)* after its path into the sample it is called Impulse Response *h(t)* of the sample. If the excitation amplitude is not high enough to cause non-linear phenomena within the sample under test, then its behaviour can be considered Linear and Time Invariant (L.T.I.). Under these conditions, the Impulse Response represents ideally how the sample reacts across the frequency range of interest:
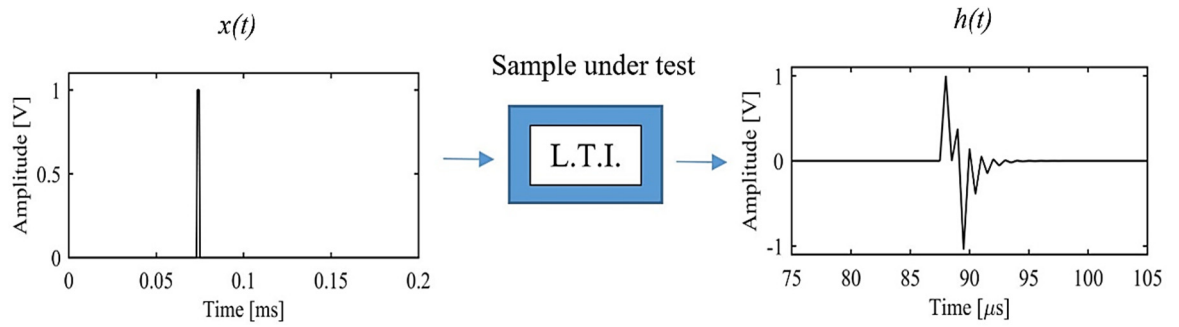
Figure 2.2: Illustration of the impulse response definition.

However, there are some limitations on the use of such pulsed techniques. When a test is performed either in highly attenuating environments (by using air-coupled ultrasound) or to inspect challenging materials such as composites, steel forgings and concrete, there is the need to enhance the amount of energy input into the sample, to maximize the SNR. In principle, this can be done by increasing the voltage excitation level. Industrial transducers can be excited by voltage levels of up to 1000 V peak-to-peak, but the resultant input energy is still not enough for many such applications. An alternative method to enhance the SNR consists of matching the signal to the resonant frequency of the sample under test, so as to maximize the transmitted acoustic energy. This can be done by means of a Tone Burst signal (Frequency Stopped Output) [4]–[6]. Figure 2.3 shows the time waveform and the frequency spectrum of a Tone Burst signal whose central frequency is 200 kHz:
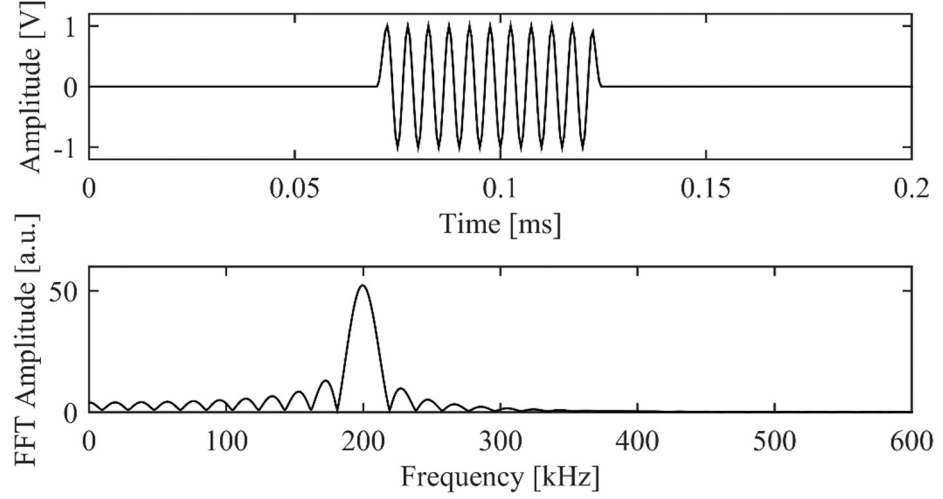
Figure 2.3: an example of a 200 kHz central frequency Tone Burst signal and its frequency spectrum.

However, when a test involves scanning a transducer over a given sample, a change in the local properties (such as density or thickness for example) leads to a change in the local resonance frequency. Therefore, it is difficult to use Tone Burst signals in real time applications. Moreover, the signal band is limited both from the transducer frequency properties and the time duration T of the signal used, *i.e.* the value $T*B$ (where B effective signal bandwidth) is about *unity* for Tone Burst signal.

To cope with these problems, the use of the Pulse Compression (PuC) technique has been proposed [7], [8]. PuC consists of the application of a matched filter to retrieve the impulse response of the systems, even in low SNR cases. In a standard PuC scheme, the sample under test is excited by a Coded Excitation signal *x(n)*, whose frequency spectrum can be considered flat across a broad range frequencies and which has an arbitrary time duration. The signal recorded after travelling within the sample (*y(n)*) is thus convolved with the matched filter *Ψ(n)*. In this way, an estimate of the impulse response of the system is retrieved. Note that both discrete-time, i.e. *(n),* and continuous-time domains, i.e. *(t)*, will be used here, to give the most general example of the use of the PuC technique.

A generic PuC scheme can be depicted as shown in Figure 2.4. Here, $\hat{h}(n)$ would be equivalent to the ideal impulse response *h(n)* if (i) the coded signal has an infinite time duration and (ii) its frequency spectrum is flat for all the frequency band considered. In other words, it happens when the time-frequency domain characteristics of the coded signal tends to match those of the ideal impulse.
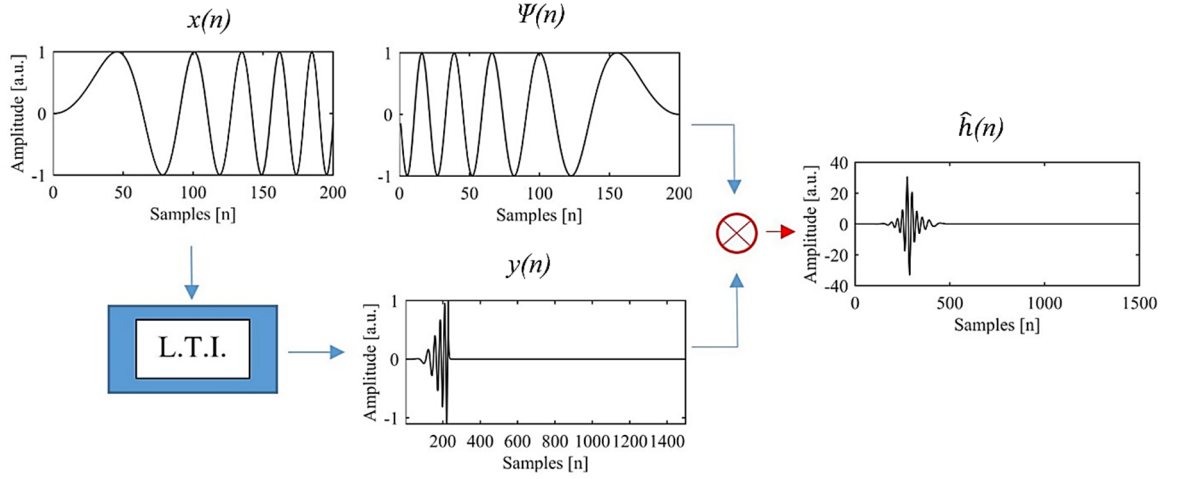
Figure 2.4: Pulse compression generic scheme. The red-crossed circle represents the convolution algorithm.

The key-point is that $\hat{h}(n)$ shows an amplitude gain proportional to the length of the coded signal used. This means that a low voltage level can be used and a high SNR can be reached simply by changing the signal length. The coded signals enhance the *T*B* value as the input signal duration is increased for a given available bandwidth. This means that the SNR can be increased, compared with $SNR_{Pulse\text{-}Echo}$, as follows:

$$GAIN = \frac{SNR_{pulse-compression}}{SNR_{pulse-echo}} = T * B \qquad (2.1)$$

Although a deeper analysis will be given in section 2.3, equation (2.2) summarizes the PuC procedure:

$$\hat{h}(n) = \Psi(n) \otimes y(n) = \Psi(n) \otimes (x(n) \otimes h(n) + e(n)) =$$
$$= \hat{\delta}(n) \otimes h(n) + \tilde{e}(n) \approx h(n) \qquad (2.2)$$

where *e(n)* represents noise of arbitrary type (environmental, quantization, instrumental, etc.) and $\hat{\delta}(n)$ is the approximation of Dirac's delta function.

The matched filter *Ψ(n)* is the one which has the impulse response:

$$h(n) = k \cdot x(\Delta - \bar{n}) \tag{2.3}$$

where k and Δ are arbitrary constants. This corresponds to perform a convolution between the output signal and the time-reversed input signal, shifted by a value $\bar{n}$. In other words, the optimal matched filter *Ψ(n)* is the time replica of the input signal, *i.e. Ψ(n)=x(-n)*. As will be explained in the following sections, matched filter optimization is one of the key-points that has to be taken into account with the use of coded signals. Moreover, it can be demonstrated that the matched filter is the one that maximizes the SNR enhancement at the output of the PuC procedure [9].

The next section describes the main types of coded waveforms, where particular attention is given to the ones that have been exploited in this research work. A detailed mathematical analysis of the two mains PuC procedures is reported in section 2.3.

2.2   Coded Waveforms

This section summarizes the main characteristics of the coded signals that have been used throughout this thesis. A classification of the different types of coded signals can be obtained by considering the different methods of encoding from which they are obtained:

- **Frequency Modulation**: modulating the frequency of the transmitted signal by the frequency of a modulated one. Chirp signals belong to this class.
- **Phase Modulation**: modulating the phase of the transmitted signal proportionally to the signal amplitude. Examples are Binary Sequences (MLS, Golay Sequences, Chaos Sequences, Barker Codes)

25

- **Amplitude modulation** where the signal is modulated in amplitude without any phase change.

In this work, Linear Chirp signals, Golay Sequences and their Inverse Repeated version have been exploited. These are described further in the following sub-sections.

2.2.1. Linear Chirps

In nature, a chirp describes the sound that birds produce. In NDT, a chirp is a signal whose frequency increases linearly with time. An example of a chirp is given in Figure 2.5, together with is frequency spectrum. Please note that the time waveform in Figure 2.5(a) is an expanded version of the real waveform to illustrate the changing frequency with time.
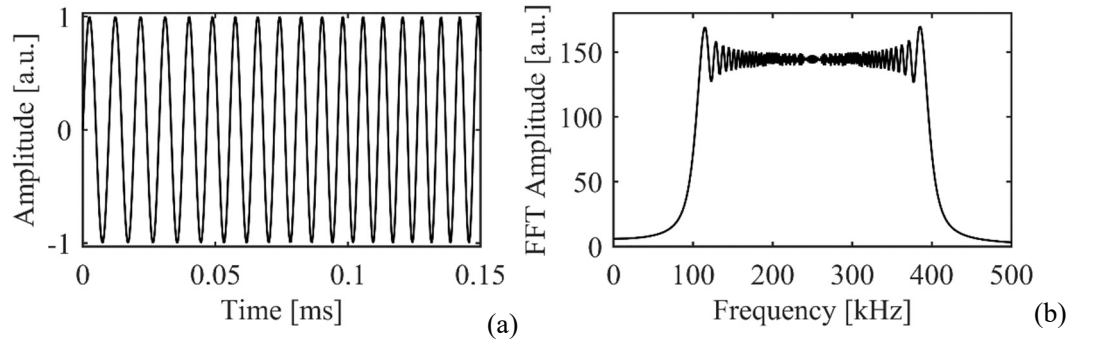
Figure 2.5: (a) Linear Chirp signal and (b) its frequency spectrum

A general mathematical form of a chirp signal in the continuous time domain $s(t)$ is given:

$$s(t) = \alpha_w(t)\sin\left(2\pi f_0 t + \Phi(t)\right) = \alpha_w(t)\mathcal{R}\left(e^{2\pi i\left(f_0 t + \frac{B}{2}\int_0^t x(\tau)d\tau\right)}\right) =$$

$$= \alpha_w(t)\mathcal{R}(e^{2\pi i\phi(t)})$$

(2.4)

where $\alpha_w(t)$ is the windowing amplitude modulation of $s(t)$ that voids the signal out of the range $t \in [0, T_{exc}]$, *i.e.* for the chirp duration of interest; $x(\tau)$ is a monotonically increasing, smooth modulating signal whose valid values are limited in the interval $[-1,1]$; $\Phi(t)$ refers to the accumulated signal phase and B is the signal bandwidth, i.e. the difference between the

higher chirp frequency and lower one. The instantaneous frequency can be derived by differentiating the accumulated phase, i.e. $f(t) = \frac{d\Phi(t)}{dt}$. For a linear chirp signal, the phase is quadratic $\Phi(t) = f_0 t + \frac{B}{2T} t^2 - \frac{B}{2} t$ and the respective instantaneous frequency is linear: $f(t) = \left(f_0 - \frac{B}{2} \right) + \frac{B}{T} t$. This modulation works like a frequency band pass filter.

Equation (2.2) illustrates that in to perform the PuC algorithm, a convolution of the received signal *y(n)* (or *y(t)*) with the matched filter is needed. The equation is here reported again for the sake of clarity in the continuous time domain:

$$\hat{h}(t) = \Psi(t) \otimes y(t) = \Psi(t) \otimes x(t) \otimes h(t) = \hat{\delta}(t) \otimes h(t) \sim \hat{h}(t) \tag{2.4}$$

However, as stated in the introduction, $\Psi(t) = x(-t)$. Therefore, pulse compression effectiveness depends on the quality of the convolution between the signal and its time replica, which corresponds to performing the autocorrelation of the transmitted signal. Figure 2.6 shows an expanded view of the normalized envelope of the autocorrelation values for both a single pulse and a linear chirp:
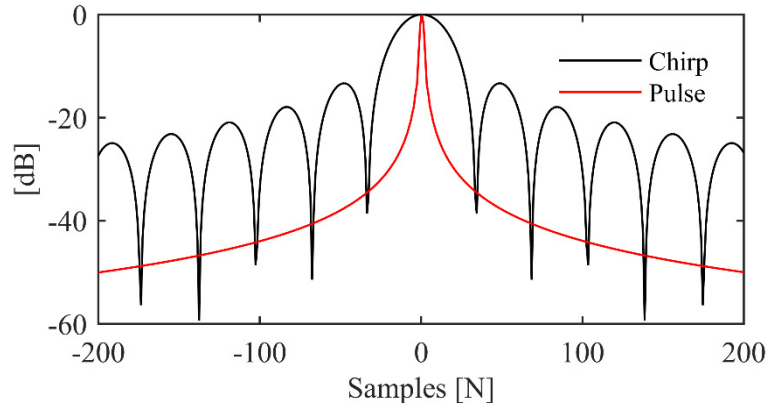
Figure 2.6: Linear chirp (black) and single pulse (red) autocorrelation example.

As can be seen in Figure 2.6, the use of a chirp signal leads to a lower spatial resolution with respect to the pulsed excitation - *i.e.* there is a wider main peak. Again, these differences can be reduced by enhancing both the time duration of the chirp and by broadening its frequency spectrum. Although any chirp signal could be designed to have a very high value

of the *T*B* product, i.e. *T*B*→∞ theoretically, the actual band-pass frequency characteristic of any real transduction system limits the useful bandwidth of the signal itself when the chirp is exploited in ultrasonic NDT. Therefore, a narrow-band transduction system would limit the maximum achievable value of the *T*B* product for a given signal time duration *T*. Finally, it can be seen that the chirp autocorrelation function is affected by the presence of side-lobes, which will affect the estimation of the impulse response. These phenomena can be reduced by carefully choosing a proper windowing function to be applied to both the transmitted signal and to its corresponding matched filter. Windowing minimizes noise effects, reducing noise out of the input signal bandwidth at the cost of a lower amount of energy for a given maximum signal amplitude available [10]–[12]. The reader will find a deeper analysis of the windowing function and different matching filter strategies in Section 2.4.

2.2.2. Golay Sequences and Inverse Repeated Golay Sequences

Among the existing type of binary sequences, Golay sequences and Maximum Length Sequences (MLS) are those exhibiting δ-like properties. Throughout this work, only Golay codes and an existing particular version of them called Inverse Repeated Golay Sequences have been utilised. Golay sequences were first introduced by Marcel J.E. Golay in 1949 for infrared spectroscopy [13]. Golay sequences consist of two binary sequences, G_s^A and G_s^B, both defined by recursion from two seed sequences. An example of a Golay sequence, together with the autocorrelation functions, is depicted in Figure 2.7.
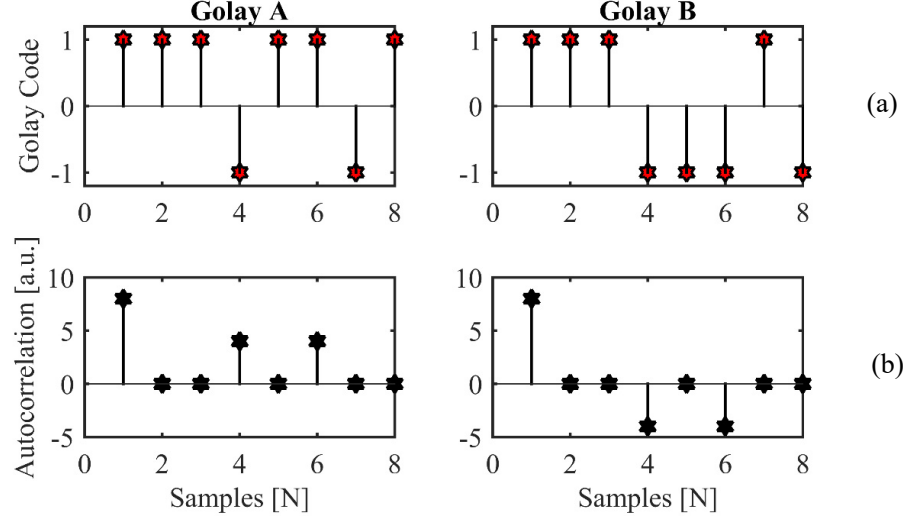
Figure 2.7: Example of (a) a Golay sequence (Golay A and B) and (b) the result of their respective autocorrelation.

The peculiar property is that their autocorrelation coefficients $\hat{\delta}$ sum to zero, as described in equation (2.5):

$$\hat{\delta}_G^A(n) = -\hat{\delta}_G^B(n) \;\forall\, n \neq 0, \qquad \hat{\delta}_G^A(n) + \hat{\delta}_G^B(n) = 2L \times \delta(n) \tag{2.5}$$

where L is the sequence length. Figure 2.8 shows the above-mentioned property:
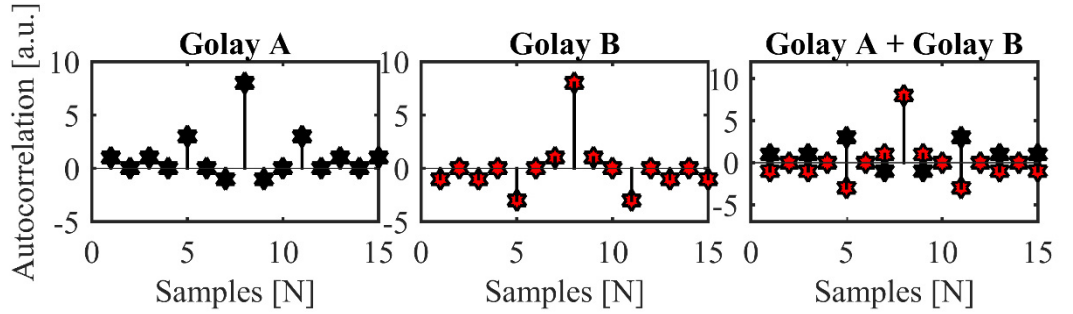
Figure 2.8: Complementary autocorrelation property for the Golay sequence.

As is the case for chirp signals, the energy reached by using Golay codes is proportional to the length of the sequence itself. The complementary property of the auto-correlation can be usefully exploited in pulse compression by modifying the procedure described in equation (2.2) in this way:

(i)   The two complementary sequences are both used as input of the system under test;

(ii)   The matched filter is applied separately to each input (A and B) to obtain the two estimates of the respective impulse response, as for equation (2.6):

$$\hat{h}_G^A(n) = \hat{\delta}_G^A(n) \otimes h(n)$$
$$\hat{h}_G^B(n) = \hat{\delta}_G^B(n) \otimes h(n)$$

(2.6)

(iii) The impulse response is reconstructed without any approximation (ideally) by summing both the contributions of equation (2.6) to obtain:

$$2L \times h(n) = \left(\hat{h}_G^A(n) + \hat{h}_G^B(n)\right)$$

(2.7)

Golay sequences are the only ones that theoretically exhibit a perfect pulse compression output at the end of the overall procedure. As a consequence, the frequency spectrum of a Golay sequence is almost the same as that of the perfect pulsed excitation. For this reason, they are often exploited in NDT, especially when used together with a broadband transduction system.

However, when a Golay sequence is used in a real ultrasonic application, it should be noted that any "1" or "-1" of the sequence results in a voltage level of finite duration dT, which is related to the update rate of generation R_{gen} of the sequences by $dT = \frac{1}{R_{gen}}$. The value of R_{gen} can be chosen to concentrate the energy on the actual bandpass of the system (transducers, amplifiers, sample). It can be demonstrated that a good criterion is to choose $2f_c < R_{gen} < 4f_c$, where f_c is the central frequency of the transducers.

Normally, transducers exhibit a band-pass behaviour over a range of frequencies B, which is a fraction of f_c. As a consequence, standard Golay sequences would excite the transduction system in frequencies outside their useful bandwidth, resulting in wasting energy. A method to cope with this problem has been proposed in the literature. It consists of modulating the standard Golay sequences by replacing their "1" or "-1" with short

sequences of binary values, so performing some spectral shaping. As an example, it can be achived by substituting each "1" value within the combination "1, -1" and each "-1" with the opposite combination "-1, 1". This strategy leads to the so called Inverse Repeated Golay Sequences. Figure 2.9 shows an example of Golay sequences and their Inverse Repeated Version, for a fixed R_{gen}:
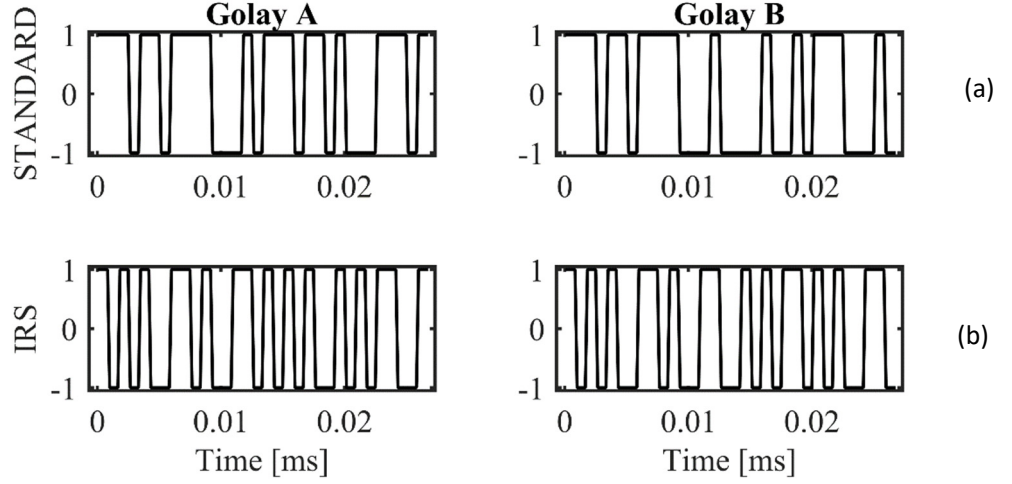
Figure 2.9: an example of (a) standard Golay sequences and (b) their Inverse Repeated replica.

Figure 2.9 shows the respective Power Spectral Density (PSD) of the sequences considered above. It can be clearly seen that the Inverse Repeated version of Golay sequences would better suit a narrow-band transduction system [14], [15]:
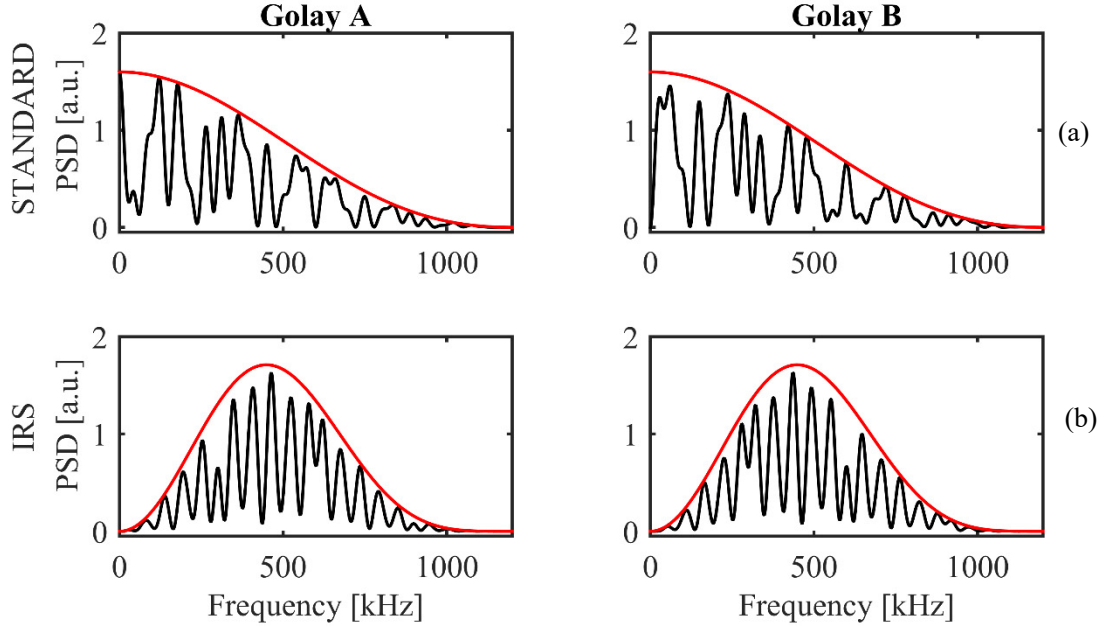
Figure 2.10: (a) Golay and (b) Inverse Repeated Golay frequency spectra (black lines). The red line shows the resulting envelope for both cases.

2.3   Pulse Compression Strategies

A pulse compression scheme can exploit either single-shot or continuous (periodic) excitations. It follows that the impulse response of a system can be obtained by using either an Acyclic Pulse Compression (APC) or a Cyclic Pulse Compression (CPC) method. In this section, the main differences between the two methods are described, and the pros and cons of both procedures are analysed. Suppose that for the APC and the CPC methods, pairs of signals exist that satisfies the equation (2.8):

$$s_1(t) \otimes s_1(-t) = \delta(t); \qquad \bar{s}_2(t) \otimes \bar{s}_2(-t) = \bar{\delta}(t) , \qquad (2.8)$$

where $s_1(t)$ is a generic coded waveform defined in the time interval $t \in [0, T_{s1}]$, $\bar{s}_2(t)$ is a generic periodic coded waveform having period T_{s2}, and $\bar{\delta}(t)$ consists of a periodic train of $\delta(t)'s$ spaced by T_{s2}, as illustrated in Figure 2.11:
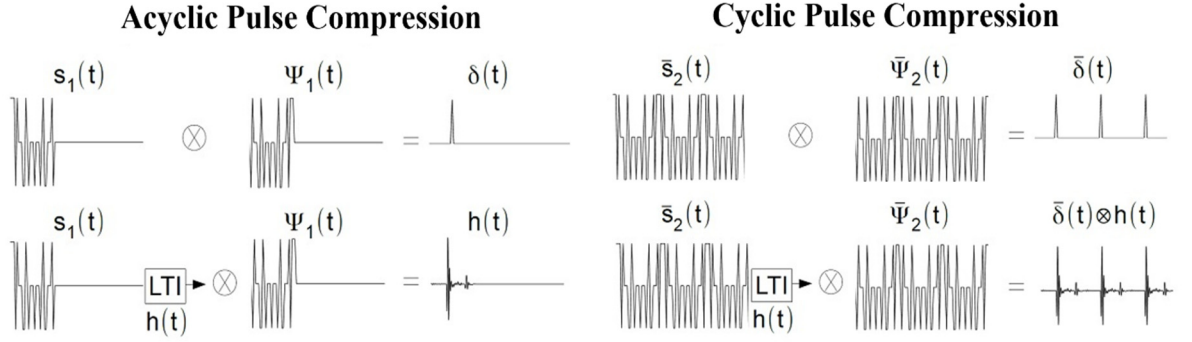
Figure 2.11: Sketches of the Acyclic (left) and the Cyclic (right) Pulse Compression procedures.

For the APC case, the signal $s_1(t)$ is convolved with the matched filter $\Psi_1(t)$ to obtain the impulse response *h(t)*. For the CPC case, the same procedure leads to *h(t)* convolved with the periodic delta function $\bar{\delta}(t)$. This represents the main difference between APC and CPC schemes.

If the time duration of the impulse response (*h(t)*) of the system under test is shorter than the input signal period, the convolution between *h(t)* and $\bar{\delta}(t)$ results in a periodic train of non-overlapping $\delta(t)'s$, whilst if *h(t)* has time duration longer than the input signal period, an overlapping is present in the retrieved $\delta(t)'s$. It follows that the CPC algorithm can only be implemented if the impulse response time duration is known *a priori*. On the other hand, the APC approach is not limited by the time duration of *h(t)*. However, in real applications the duration of the excitation signal is normally longer than *h(t)*. This is because the SNR gain achievable by using coded signals is again proportional to their time duration.

There are several differences on how to perform the APC and CPC algorithm in real experimental applications. In the APC scheme, the coded signal $s_1(t)$ of length T_{s1} excites the system and produces an output signal $y_1 = h(t) \otimes s_1(t)$ having time duration of $T_{y1} = T_{s1} + T_h$. As a consequence, if *h(t)* has to be completely reconstructed, the output signal has to be recorded for a time length $T_{rec} \geq T_{y1}$. The pulse compression is then implemented by convolving the output signal with the matched filter.

In the CPC scheme, a periodic signal $\bar{s}_2(t)$ having a period of $T_{s2} \geq T_h$ is switched on at $t=0$, thus producing an output signal given by $y_2 = h(t) \otimes \bar{s}_2(t)$. For a transient of duration T_{s2}, the output will be periodic with the same period T_{s2}, and the impulse response is retrieved by performing the cyclic convolution between a single period of the $y_{s,s}$ of the steady-state of y_2 and a single period of the excitation signal $\bar{s}_2(t)$. In practice, to successfully perform CPC it is common to transmit only two periods of the excitation signal and to record the output corresponding to the second excitation period only. By exploiting the Convolution Theorem for Discrete Signals, the cyclic convolution can be successfully performed as shown in equation (2.9):

$$y_{s,s}(n) \otimes \bar{s}_2(n) = IFFT\left\{FFT\{y_{s,s}(n)\} \cdot FFT\{s_2(n)\}\right\}, \qquad (2.9)$$

where *FFT* is the Fast Fourier Transform algorithm and *IFFT* is the Inverse Fast Fourier Transform. It is worth noting that the Convolution Theorem can also being applied in the APC scheme. Assuming that assumed $T_h < T_{s1}$, the convolution theorem can be applied correctly if the input and output signal are both padded with zeroes up to double the number of samples of the input signal.

From the SNR point of view, if the APC scheme is assumed to be implemented so as to have the output signal recoded for the minimum time needed to recover the whole *h(t)*, it can be assumed that the fraction of the measurement time at which the energy is delivered to the system is $p_{EX} = (T_{s1}/(T_{s1} + T_h))$. Therefore, the final SNR is given by $SNR(p_{EX}) = p_{EX} \times SNR_{max}$, where SNR_{max} is defined as the maximum SNR value achievable for $T_{s1} \gg T_h$.

For the CPC scheme, the excitation is shifted on for the whole acquisition time. This results in saturating the SNR for a given excitation power. A strategy to increase the SNR in APC scheme is to perform averages by sending a train of single-shot excitations, but the

minimum averaging repetition time must be $T_{s1} + T_h$. Conversely, averages in CPC can be easily performed by considering several consecutive periods.

From computational point of view, the input and the output signal that have to be processed for the CPC scheme are always equal or shorter than the APC one. As a consequence, less computational efforts are required for the CPC scheme with respect to the APC one. Furthermore, it can be shown that the cyclic convolution exploits better the *FFT* than the standard convolution. In conclusion, when information about the time duration of the impulse response are available, the Cyclic Pulse Compression scheme offers the best approximation of the *h(t)* [15].

2.4   **Numerical Results**

It has been assumed in the previous section that coded signals give a perfect output of the pulse compression, *i.e.* a perfect value of the *h(t)*. In practice, none of the time/bandwidth limited signals can give a perfect handling of the impulse response. As has been described in the introduction, a limited bandwidth provided by a finite length chirp signal leads to the creation of "side-lobes". In addition, the impulse response retrieved after the pulse compression algorithm is broader than the one obtained by using the pulsed excitation. In this section, some strategies to reduce the presence of both side-lobes and the width of the impulse response are discussed. Moreover, an analysis of the coded signals robustness against the unavoidable presence of noise is given.

2.4.1. **Sidelobe Reduction: Windowing and Wiener Filtering**

In order to reduce the side-lobe levels, it is common to amplitude-modulate a linear chirp by applying a windowing function. To reach this aim, spectral windowing is obtained by applying a time domain amplitude modulation. Under the assumption the that the matched

filter $\Psi(t)$ is $\Psi(t) = s(-t)$, the resulting impulse response estimation $\bar{\delta}(t)$ is proportional to the Inverse Fourier Transform of the Power Spectral Density (PSD) of the signal $s(t)$ itself, according to Wiener-Khinchin theorem [16]–[18]. Side-lobes are mainly due to abrupt variations of the PSD, in the proximity of the starting and ending frequency values of the signal itself. It is therefore possible to reduce this unwanted effected by applying a windowing function, which smooths the signal PSD variation, at the cost of reducing the signal energy. As a drawback, losing the constant signal envelope and its effective bandwidth causes a broadening on the main peak of the retrieved cross-correlation. There are many different types of windows that the can be applied to the signal, such as Gaussian, Blackman, and Tukey, plus other arbitrary types resulting from the mixing of the above-mentioned ones. An example of the advantage of the windowing procedure on a chirp is considered using the chirp signal time-frequency characteristics shown in Figure 2.12. Here, an Elliptical Tukey window is applied to a linear chirp. The resulting spectrum is smoother when compared to a non-windowed standard linear chirp.

(a)

(b)
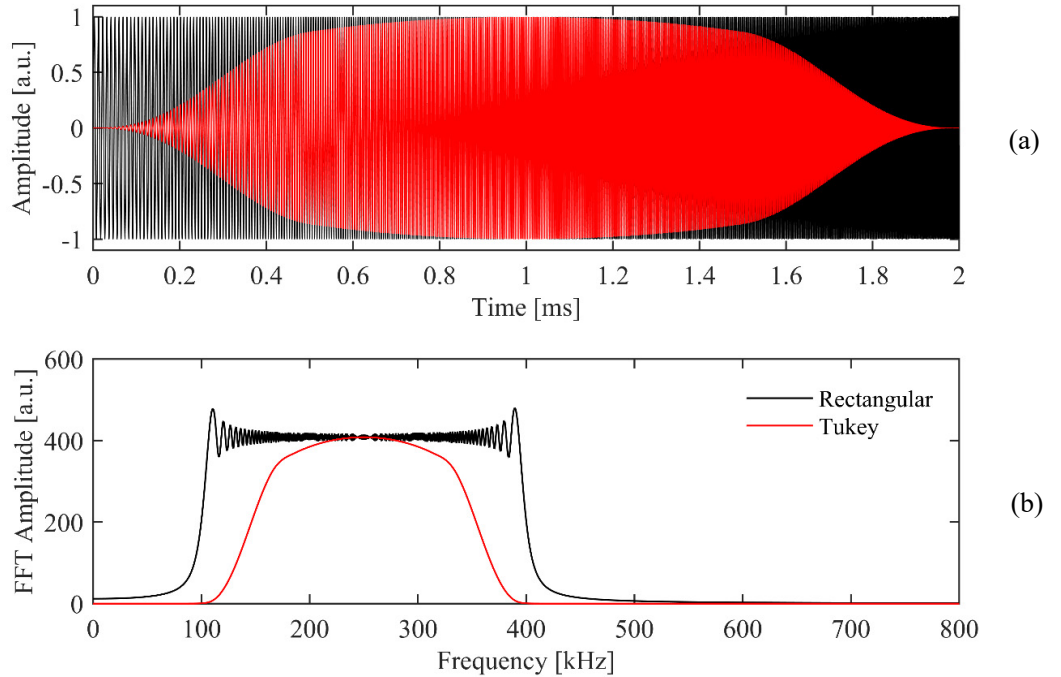
Figure 2.12: (a) Comparison of an un-windowed linear chirp (black) and Tukey-Elliptical windowed linear chirp (red) time signal; (b) corresponding frequency spectra.

A smoother frequency spectrum with respect to an un-windowed linear chirp results in decreased side-lobes levels. This can be appreciated if the autocorrelation function of both the signals is plotted, as shown in Figure 2.13:
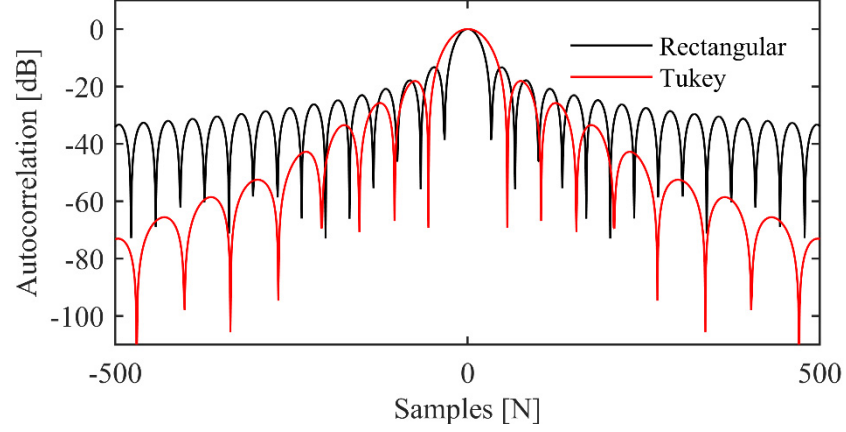
Figure 2.13: linear un-windowed chirp (black) and Tukey-Elliptical windowed linear chirp normalized autocorrelation.

As stated above, the side-lobe level is reduced by windowing the signal amplitude [14], [15], [19], [20]. On the other hand, it can be noted that the main peak width is larger when windowing is performed. For this reason, it can be shown that the Wiener filter technique applied to the matched filter leads to a narrower impulse response estimation of the main peak width. Mathematically, the use of a Wiener filter simply consists of replacing the matched filter $\Psi(t)$ with a new one, $\Psi_W(t)$, having the same phase profile in the frequency domain but showing a different spectrum amplitude. For the results reported in Figure 2.14, where a Wiener-filtered linear chirp autocorrelation function has been compared to the standard linear case (rectangular window), a Wiener filter $\Psi_W(t)$ defined in the frequency domain as follows has been used:

$$\Psi_W(f) = \frac{\Psi(f)}{|\Psi(f)|^2 + a + b \cdot f} \tag{2.10}$$

where a and b are two regularization parameters that damp the oscillations in the autocorrelation function, *i.e.* in the recovered impulse response obtained by the use of such signals. Note that b damps high-frequency oscillations in particular.
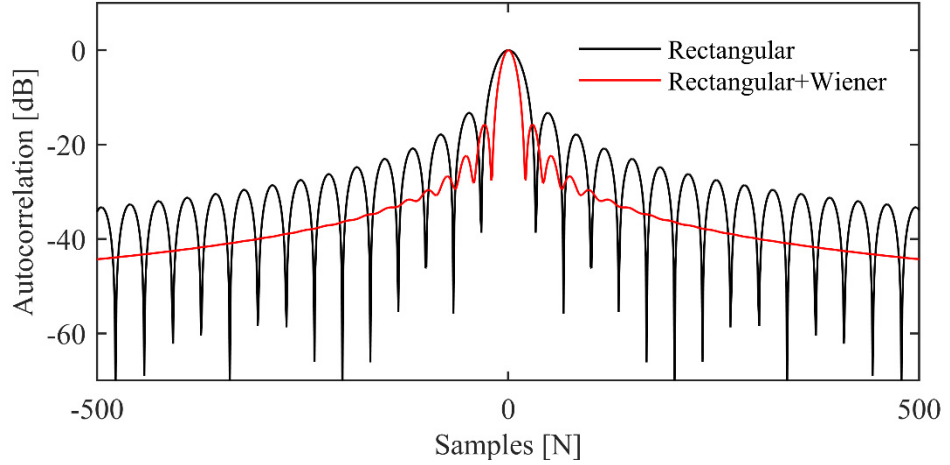
Figure 2.14: Autocorrelation normalized amplitude for un-windowed linear chirp and for Wiener matched filter approach.

In conclusion, when the aim is to identify features in noisy environments, the best solution is to use a windowing function to reduce mathematical noise due to the presence of side-lobes on the estimated impulse response. However, the use of such amplitude-phase modulation would broaden the main peak width. As a consequence, searching for very close defect or scatters into a sample under test can be challenging. To cope with this, one strategy is the use of Wiener Matched Filter approach [21]. The above strategy has been widely used in the experiments reported in later Chapters of this thesis.

2.4.2. SNR of Coded Signals – example using air-coupled transducers

The choice of the coded waveforms for air-coupled ultrasonic NDT strongly depends on the frequency characteristics of the system. As stated above, one can expect that it should be better to use a chirp instead of using a broadband excitation, such as binary sequences, for transducers with a restricted bandwidth for pulse compression (PuC) testing in air, but in

some cases the choice is perhaps not so obvious. The author contributed to a published journal paper, which analysed this problem for air-coupled ultrasound [14]. Although this type of testing is not considered experimentally in this thesis, numerical simulations results are reported in this section for air-coupled ultrasound as a guide to the selection of particular coded signals for different experimental setups. In particular, the maximum ideally SNR attainable for a fixed excitation duration and peak power is investigated by varying the transducer bandwidth and the noise level. The results proved very useful for the experimental designs of later pulse compression experiments in different applications, which are discussed in later Chapters.

The simulations were performed by assuming normalized frequencies values, so the results were valid for the most general real cases. To allow this, the bandwidth B represents a percentage of the central frequency f_c of the system itself (including transmitter, receiver and amplifier) which varied from 10% to 200%. This is taken as the limiting case of an almost-ideal broadband system in the range [0,B]. The signals were sampled from the continuous-time domain at a rate of $R_{ADC}=20f_c$. Several bandpass FIR (Finite Impulse Response) filters have been utilized and convolved with the transmitted signals with the aim of simulating the system impulse response. Figure 2.15 shows examples of the FIR utilized for the numerical model. In particular the top subplots in Figure 2.15 show the impulse responses of the filters, whilst their respective transfer function magnitudes are shown below.
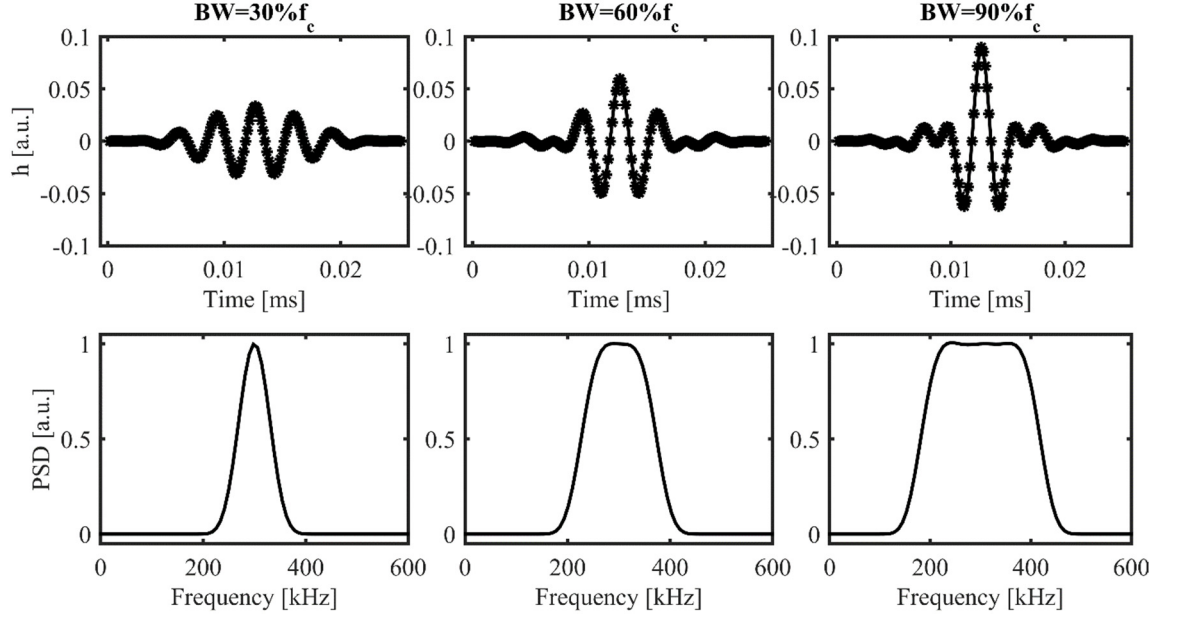
Figure 2.15: Examples of Impulse Responses (top) and Power Spectral Densities (bottom) of FIR filters used to simulate the effect of a measurement set-up (transducers + amplifier) for different BW values of the filters.

The simulations have been carried out by examining the following combinations of waveforms and PuC schemes:

1. Acyclic Pulse Compression & Tukey-windowed Linear Chirp (LChirpAPC);

2. Acyclic Pulse Compression & Golay (GCS-APC);

3. Acyclic Pulse Compression & IRS-Golay (IRSGCS-APC);

To compare the waveforms, both Golay codes and chirps were designed to have the same time duration and amplitude. In particular, the length of both signals was chosen to be $k2^9$ samples long, with $k=5$. It should be noted again, that the binary sequences have a doubled power and an additional 6dB of SNR with respect to chirp signals, *i.e.* squared wavelet and two sequences used for Golay [22].

The binary sequences were designed to suit the frequency range over the interval [0-$2f_c$]. The IRS-binary Golay sequence was chosen so as to have the maximum of the PSD at f_c, whereas the Chirp signal instead has been defined with either a fixed bandwidth $B= 2f_c$ or

with various *B* values. This was to match the overall simulated experimental system frequency characteristics. This latter case was called a "Matching Chirp" (MChirp).

The simulations results rely on the evaluation of the magnitude of four different parameters calculated in presence of noise, which was added in order to consider different aspects related to detection, resolution, etc. In particular, the parameters are (a) the width of the main lobe ("MLW"), (b) the SNR in the main lobe ("ML-SNR"), (c) the near side-lobe level ("NSL") and (d) the far side-lobe level ("FSL"). Each parameter was calculated within a different region of the measured signal, as shown in Figure 2.16:
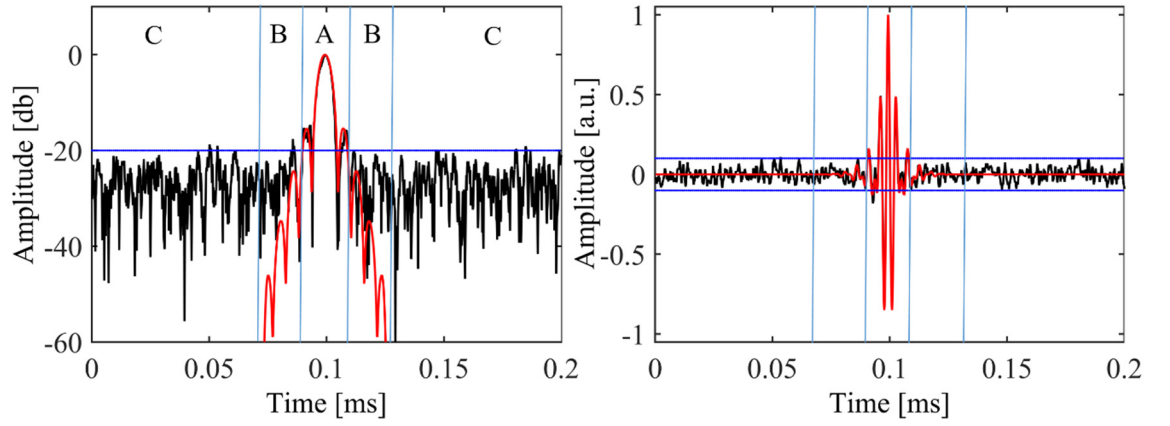
Figure 2.16: Definition of main-lobe (A), near side-lobes (B) and far side-lobes regions (C).

In Figure 2.16, the letters A, B and C indicate:

A. The main lobe, that is the region outside of which the envelope of the expected signal is 20 dB below the maximum;

B. Near side-lobes, *i.e.* two regions at the sides of the main lobe, each with the same width as the main lobe;

C. Far side-lobes, that is the outer regions beyond near side-lobes.

The *MLW* parameter gives an estimation of the resolution of the pulse compression procedure, using the following expression:

$$MLW = min\{\Delta \ s. \ \backslash t. h^{ex} \ [n < n_1, n > n_1 + \Delta] < 0.1 \ Max \ (h^{ex}), \forall n \ \} \qquad (2.11)$$

MLW values are important in Time-of-Flight (ToF) measurements or in range detection. In fact, small *MLW* values means a better temporal-spatial resolution of the measurement. In addition, the parameter *ML-SNR* gives a numerical estimation of the capacity of detecting a signal buried in noise. *ML-SNR* is defined as in equation (2.12):

$$MLW - SNR = \frac{\sum_{n \subset MainLobe}(h^{ex}(n))^2}{\sum_{n \subset MainLobe}(h^{ex}(n) - h^m(n))^2} \qquad (2.12)$$

It is thus defined as the ratio between the energy of the expected impulse response after PuC without the presence of noise $h^{ex}(n) = h^{FIR}(n) \otimes s(n) \otimes \Psi(n)$, to the energy of the noise inside the main lobe, where $h^{FIR}(n)$ is the FIR impulse response used to simulate the system, and $h^m(n) = (h^{FIR}(n) \otimes s(n) + e(n)) \otimes \Psi(n)$ is the measured impulse response in presence of the simulated additive Gaussian white noise level $e(n)$.

NSL is defined as the ratio between the maximum absolute amplitude of $h^{ex}(n)$ and the mean value of the envelope of $h^m(n)$ in the near side-lobes region (in dB):

$$NSL = \frac{Max(h^{ex}(n))}{Mean(Env(h^m(n)))_{n \subset NearSideLobe}} \qquad (2.13)$$

FSL parameter is defined as the ratio between the maxim absolute amplitude of h^{ex} and the maximum value of the envelope of $h^m(n)$ in the far side-lobes region:

$$FSL = \frac{Max(h^{ex}(n))}{Max(Env(h^m(n)))_{n \subset FarSideLobe}} \qquad (2.14)$$

NSL and *FSL* quantify the noise level. Furthermore, they both express the limit value that a secondary signal would not be detected. Therefore, the values reached by these parameters have to be taken into account when complex impulse responses have to be measured, such as in the case of multi–path reflection, multi-layered structures, etc. Figure 2.17 shows surface plots of the *ML-SNR* versus the noise power and the different analysed bandwidth *BW* values of the simulated system:
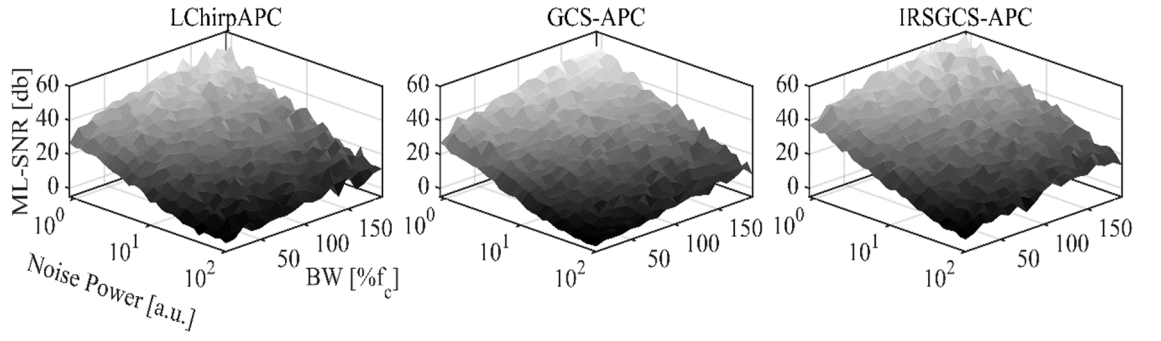
Figure 2.17: ML-SNR results for the Linear chirp, Golay standard code and Golay IRS version.

It can be seen that higher SNR values are attained with broadband systems, as expected for the chosen excitations. Some improvements are attained by using the IRS approach with respect to standard linear chirp and Golay. In fact, the IRS Golay sequences shows the highest value of ML-SNR.

If the MChirp is considered, a high value of chirp SNR is achieved, as the bandwidth of the chirp suits perfectly that of the experimentally-simulated system. Figure 2.18 shows the surface plot of the *ML-SNR* for the MChirp compared to that of the IRSGCS-APC. Of particular interest is the plot to the right, where the Noise Power – System *BW* region for which IRSGCS-APC exhibits a SNR higher than MChirp is highlighted in white:
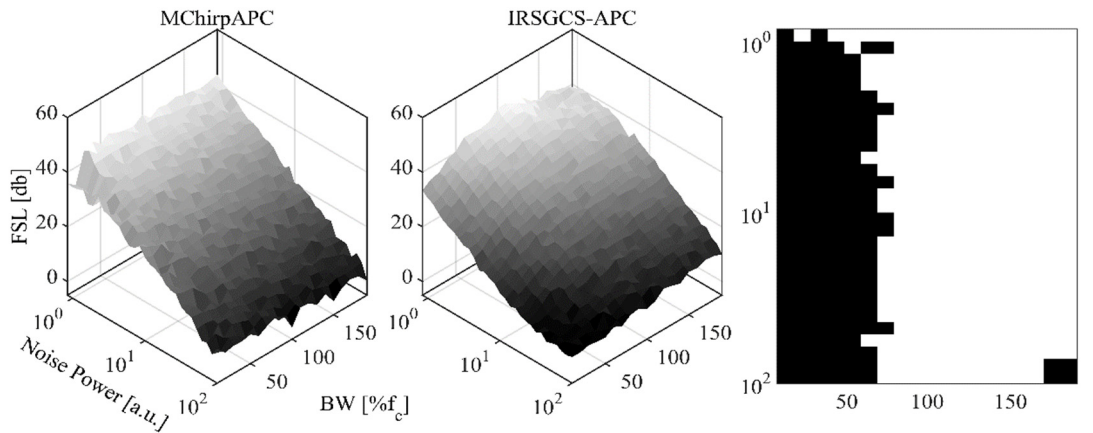
Figure 2.18: Comparison of the ML-SNR achievable for IRSGCS-ACP and MChirp schemes. The plot to the right (in white) shows the Noise-BW region in which the IRS Golay has a higher SNR than the matched chirp.

It can be noted that when $BW \geq 90f_c$ (approximately), the IRSGCS performs better than MChirp; On the other hand, for $BW < 90f_c$ a higher SNR is attained by using MChirp, designed in fact to optimally suits the system frequency characteristics. This was an expected result, as about half of the input energy is filtered out by the transduction system for $BW=f_c$, thus lowering the theoretical advantage of using binary sequences. On the other hand, MChirp gave the lowest spatial resolution amongst the various excitation schemes, corresponding to a high value of the *MLW* parameter. This can be seen in Figure 2.19, which reports the trends of the *MLW* for all the simulated excitations. In fact, the matched higher SNR values are counterbalanced with a significant decrease of the resolution, accentuated for *BW<90%f_c*.
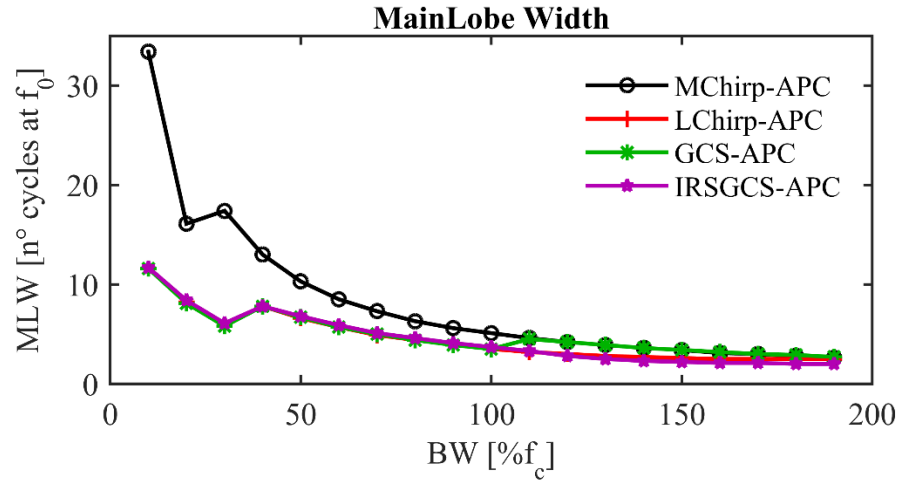
Figure 2.19 Main lobe width (MLW) versus various BW values for the various pulse compression schemes.

Figures 2.20 and 2.21 show the same comparison as that of Figure 2.18, but this time representing the *NSL* and the *FSL* values respectively:
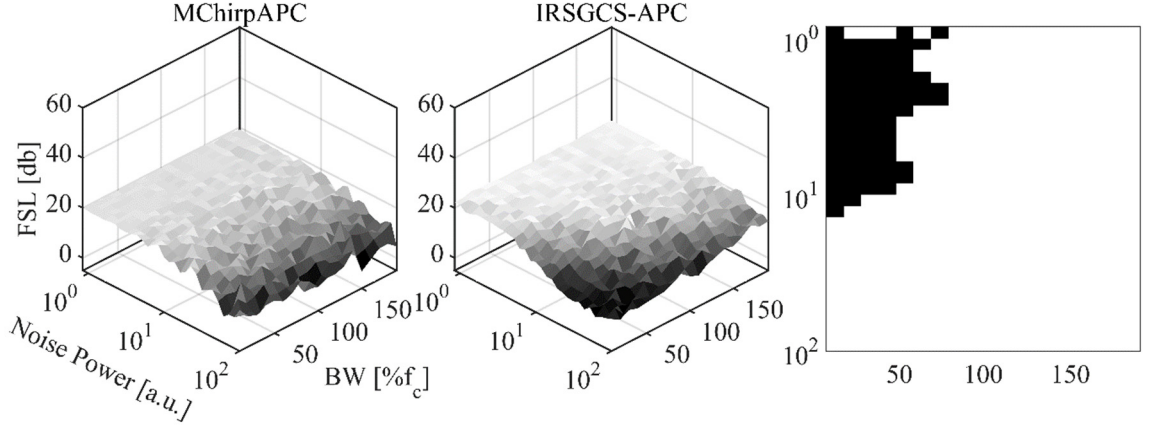
Figure 2.20: Comparison of the NSL values obtained for IRSGCS-ACP and MChirp schemes. The subplot on the right (in white) shows the Noise-BW region in which the IRS Golay performs better than the MChirp, for the given parameter.
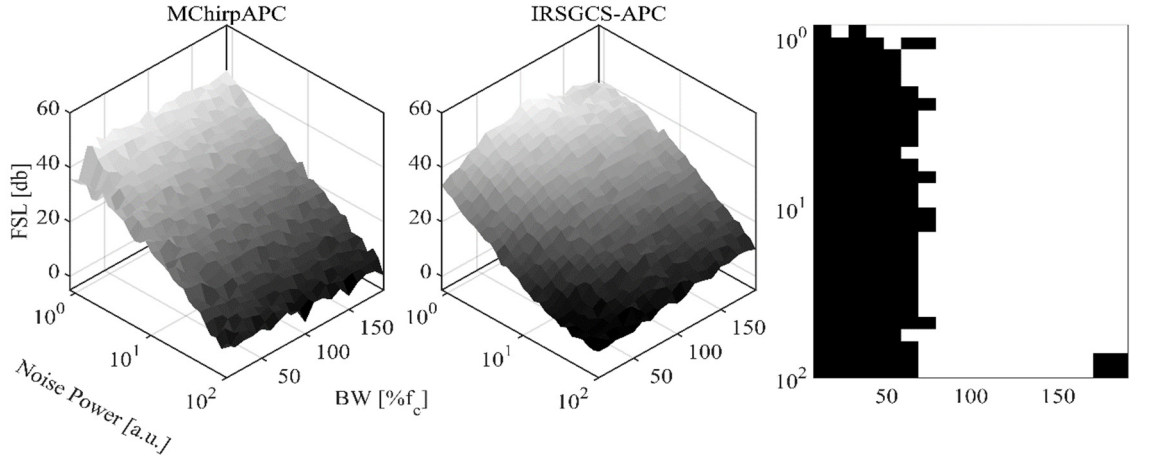
Figure 2.21: As Figure 2.20, but for the FSL values.

It can be concluded that the numerical simulations indicate binary sequences as the best signal to be used in combination with sufficiently-broadband systems, both in terms of resolution, SNR and side-lobe levels. On the other hand, a chirp signal designed to optimally match the bandwidth of the experimental system overcomes the binary sequences in terms of maximum achievable SNR of the main lobe detection when the bandwidth of the measuring system is lower than the central frequency value, *i.e.* when $BW<f_c$. However, this performance is achieved at the cost of a deteriorating resolution.

Thus, the band-pass behaviour of chirp signals counterbalances the higher energy given by the use of binary sequences. This is because the chirp fits the overall transfer function of the system better. This effect becomes more and more significant if narrow-bandwidth systems are used. In fact, by using a standard binary sequence, only a relatively small portion of the input energy can be transferred to the measuring system. Conversely, the frequency spectrum of a chirp signal can be tailored to better fit the transducer bandwidth. Therefore, chirp signals are a good choice for narrowband transduction systems

It is worth stressing that the IRS Golay achieves the best results among the investigated binary sequences. By using such approach (IRS), the binary sequences could potentially out-perform chirps, even with narrow-band transducers [14]. Please note that "narrow-band" and "broad-band" simulated transduction systems have been designed by considering a 3 dB attenuation bandwidth from the central frequency peak of each retrieved PSD for all the three simulated FIR filters, as described in [23]. It follows that the simulated FIR filters (see Figure 2.15) having either $BW= 0.3 \cdot f_c$ or $BW= 0.6 \cdot f_c$ have been considered to be narrow-band. Conversely, the simulated FIR filter having $BW= 0.9 \cdot f_c$ has been considered to be broad-band.

2.5   Conclusions

In this chapter, a mathematical formulation of the features related to the signals used in this thesis work have been given. Furthermore, guidelines on the use of different pulse compression schemes, as well as their pros and cons, have been reported. In addition, an overview of windowing and side-lobe noise reduction has been presented. Numerical simulations demonstrated that coded signals have to be chosen carefully depending on frequency characteristics of the measurement system. It also showed that they can be used

to retrieve information even in noisy environments. These simulations will help to understand some practical issues described later experimental Chapters.

References

[1]   M. E. Anderson and G. E. Trahey, "The direct estimation of sound speed using pulse-echo ultrasound.," *J. Acoust. Soc. Am.*, vol. 104, no. 5, pp. 3099–3106, 1998.

[2]   H. G. Tattersall, "The ultrasonic pulse-echo technique as applied to adhesion testing," *J. Phys. D. Appl. Phys.*, vol. 6, no. 7, pp. 819–832, 2002.

[3]   W. Wright and D. Hutchins, "Air-coupled ultrasonic testing of metals using broadband pulses in through-transmission," *Ultrasonics*, 1999.

[4]   J. J. Pacella, J. Brands, F. G. Schnatz, J. J. Black, X. Chen, and F. S. Villanueva, "Treatment of microvascular micro-embolization using microbubbles and long-tone-burst ultrasound: An invivo study," *Ultrasound Med. Biol.*, vol. 41, no. 2, pp. 456–464, 2015.

[5]   R. Strelitzki, A. J. Clarke, and J. A. Evans, "The measurement of the velocity of ultrasound in fixed trabecular bone using broadband pulses and single-frequency tone bursts," *Phys. Med. Biol.*, vol. 41, no. 4, pp. 743–753, 1996.

[6]   J. Wu and G. Du, "Temperature Elevation in Tissues Generated by Finite-Amplitude Tone Bursts of Ultrasound," *Ultrasound Med. Biol.*, vol. 88, pp. 1562–1577, 1990.

[7]   M. Ricci, L. Senni, and P. Burrascano, "Exploiting pseudorandom sequences to enhance noise immunity for air-coupled ultrasonic nondestructive testing," *IEEE Trans. Instrum. Meas.*, vol. 61, no. 11, pp. 2905–2915, 2012.

[8]   T. H. Gan, D. A. Hutchins, D. R. Billson, and D. W. Schindel, "The use of broadband acoustic transducers and pulse-compression techniques for air-coupled ultrasonic imaging," *Ultrasonics*, vol. 39, no. 3, pp. 181–194, 2001.

[9]   P. Burrascano, A. Pirani, and M. Ricci, "Exploiting Pseudo Orthogonal PN-Sequences for Ultrasonic Imaging System.," *CSIE*, 2009.

[10]   S. Callegari *et al.*, "From chirps to random-FM excitations in pulse compression ultrasound systems," in *IEEE International Ultrasonics Symposium, IUS*, 2012, pp. 471–474.

[11]   G. Betta, P. Burrascano, L. Ferrigno, M. Laracca, M. Ricci, and G. Silipigni, "An experimental comparison of complex excitation sequences for eddy current testing," *Measurement*, vol. 4, no. 1, pp. 128–134, 2015.

[12]   T. H. Gan, D. A. Hutchins, R. J. Green, M. K. Andrews, and P. D. Harris, "Noncontact, high-resolution ultrasonic imaging of wood samples using coded chirp waveforms," *IEEE Trans. Ultrason. Ferroelectr. Freq. Control*, vol. 52, no. 2, pp. 280–287, 2005.

[13]   M. Golay, "Multi-slit spectrometry," *JOSA*, 1949.

[14]   D. Hutchins, P. Burrascano, L. Davis, S. Laureti, and M. Ricci, "Coded waveforms for optimised air-coupled ultrasonic nondestructive evaluation," *Ultrasonics*, 2014.

[15]   M. Caporale, S., Callegari, S., Hutchins, D. A., Laureti, S., Burrascano, P., & Ricci, "Excitation and Deconvolution in Ultrasound Nondestructive Testing Systems," in *Ultrasonic Nondestructive Evaluation Systems*, 2015, pp. 85–140.

[16]   W. Lu and N. Vaswani, "The Wiener-Khinchin Theorem for Non-wide Sense stationary Random Processes," *arXiv Prepr. arXiv0904.0602*, p. 4, 2009.

[17]   B. Klein, S. D. Philipp, I. Krämer, C. Kasemann, R. Güsten, and K. M. Menten, "The APEX digital Fast Fourier Transform Spectrometer," *Astron. Astrophys.*, vol. 454, pp. L29–L32, 2006.

[18]   L. Cohen, "Generalization of the Wiener-Khinchin Theorem," *IEEE Signal Process. Lett.*, vol. 5, no. 11, pp. 292–294, 1998.

[19] P. Pallav, T. H. Gan, and D. A. Hutchins, "Elliptical-Tukey Chirp Signal for Ultrasonic Imaging," *IEEE Trans. Ultrason. Ferroelectr. Freq. Control*, vol. 54, no. 8, pp. 1530–1540, 2007.

[20] P. Pallav, T. H. Gan, and D. A. Hutchins, "Elliptical-Tukey Chirp Signal for Ultrasonic Imaging," *IEEE Trans. Ultrason. Ferroeletrics, Freq. Control*, vol. 54, no. 8, pp. 1530–1540.

[21] G. Silipigni, P. Burrascano, D.A. Hutchins, S. Laureti, R. Petrucci, L. Senni, L. Torre, M. Ricci, "Optimization of the pulse compression technique applied to the infrared thermography nondestructive evaluation," *NDT&E, (SUBMITTED).*

[22] M. Ricci, S. Laureti, D. Hutchins, and L. Davis, "A comparison of coded waveforms for air-coupled ultrasonic inspection," in *2013 18th International Conference on Digital Signal Processing, DSP 2013*, 2013.

[23] Shull, Peter J., "Nondestructive evaluation: theory, techniques, and applications*". CRC press*, 2016, pp. 140.

CHAPTER 3: An Introduction to Acoustic Metamaterials and Phononic Crystals

3.1   Introduction

Work described later in this thesis considers the use of pulse compression, described in Chapter 2, to acoustic metamaterials. This Chapter thus discusses these materials in some detail, describing the main classes of these materials, and giving some insight into how they operate.

In the last fifteen years, the extraordinary effects promised by the use of metamaterials have caught the attention of researchers and scientists. The possibility of manipulating the sound (and mechanical waves in general) in a new way leads to many new possibilities in many different fields of research. Many slightly different definitions of "Metamaterials" can be found in literature [1], but the main features can be described as follows:

(i)   A metamaterial is one that has properties which derive from its internal structure, and not just from those of the materials from which it is made.

(ii)   It contains structures within it that are much smaller than the wavelength of the incident energy.

(iii)   The resulting response arises from the sum of all these internal material parameters.

Figure 3.1 shows the difference between common materials and metamaterials. In particular, the properties of conventional materials depend on their atomic structures, whilst the properties of metamaterials arise from the type of engineered structures that they contain:
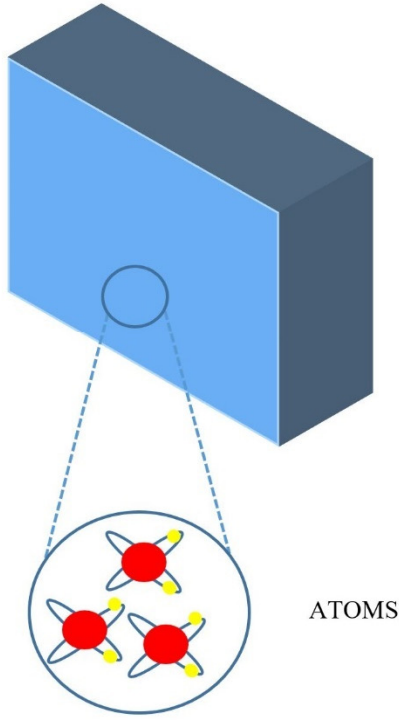
Figure 3.1: Conventional materials and Metamaterials structures.

For the sake of simplicity, one can also describe metamaterials (also known as Photonic Crystals in the electromagnetic case) as artificial materials that exhibit exotic properties which are not observed easily in nature.

Although this research project focuses on the study of acoustic metamaterials, their electromagnetic counterpart cannot be neglected for two main reasons: the study of electromagnetic metamaterials occurred before the acoustic equivalents were studied, and many useful mathematical tools and ideas cannot be understood without exploring the electromagnetic case. In this chapter a detailed description of the main properties of electromagnetic metamaterials, acoustic metamaterials and phononic crystals will be given. As this thesis work is focused on a specific class of acoustic metamaterials, *i.e.* a holey-structured acoustic metamaterial, a mathematical description about the phenomena involved in the sound propagation through them will be also reported.

3.2   Electromagnetic metamaterials

In his pioneering work of 1968, Veselago [2] hypothesized the existence of unexplored phenomena in the electromagnetic field, such as negative refraction, as long as both electric permittivity ε and magnetic permeability μ are negative. The refraction index n for the electromagnetic wave propagation is defined as:

$$n = \sqrt{\varepsilon\mu} \qquad (3.1)$$

The way in which a wave travels, *i.e.* its magnitude, direction and orientation, can be described by considering the wave vector k:

$$k = n\omega c_0 \qquad (3.2)$$

where $\omega = 2\pi f$ and c_0 is the speed of light in vacuum. Whenever ε and μ have both negative values, one is forced to choose the negative root of equation (3.1). A negative value of n then occurs, causing the wave to propagate in peculiar ways. This behaviour is shown in Figure 3.2, where θ_1 and θ_2 are the angle of incidence and angle of refraction respectively and n_1 and n_2 are the refraction index of the first and of the second medium respectively:
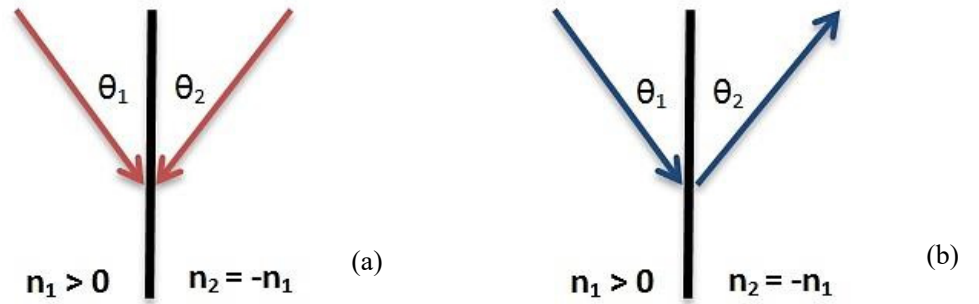
Figure 3.2: Snell's Law for a negative refraction index (n) material. (a) Wave vectors and (b) Energy flow.

What then are the consequences of double negativity? In general, a typical lens cannot focus light into an area smaller than a wavelength in diameter. As stated in Chapter 1, this limits the maximum achievable resolution of any type of conventional imaging to the

wavelength used for the said test. In 2006, Pendry [3] proved theoretically that a flat slab of double negative material (or here also called metamaterial) can act as a perfect lens. By recovering and amplifying the so called "Near Field" evanescent waves, this metamaterial lens can, in principle, exceed the diffraction limit for conventional optics, a phenomenon known as "superlensing".

The working principle of this perfect lens is described here mathematically. Consider an infinitesimal dipole of frequency ω placed in front of an optical lens. By exploiting 2D Fourier expansion and choosing the axis of the lens to be the z axis, the electric field $E(r,t)$ can be expressed as:

$$E(r,t) = \sum_{\sigma,k_x,k_y} E_\sigma(k_x,k_y) \times e^{(ik_z z + ik_x x + ik_y y - i\omega t)} \tag{3.3}$$

where k_x, k_y, k_z are the transverse wave vectors in the direction x,y,z respectively. Maxwell's equations state that:

$$k_z = +\sqrt{\omega^2 c^{-2} - k_x^2 - k_y^2}, \quad \omega^2 c^{-2} > k_x^2 + k_y^2 \ . \tag{3.4}$$

The main function of each lens is to apply a phase correction to each of the Fourier components. This allows the fields to focus at a certain distance and hence an image of the source (a dipole source in this case) can be reconstructed. However, the original image is not completely restored. The missing information, *i.e.* very tiny variations of the electromagnetic field called "evanescent waves", are located near the object (in the near field) and they cannot be restored and focused successfully with a conventional lens. The reasons for this limitation are explained mathematically below.

For larger values of the transverse wave vector, k_z can be written in the form:

$$k_z = +i\sqrt{k_x^2 + k_y^2 - \omega^2 c^{-2}}, \quad \omega^2 c^{-2} < k_x^2 + k_y^2 \tag{3.5}$$

These evanescent waves decay exponentially with z. Therefore, no phase correction can restore them to the original amplitude. It follows that they are removed from the reconstructed image, which generally comprises only the propagating waves, as described by equation (3.4). Since the propagating waves are limited to the region where

$$k_x^2 + k_y^2 < \omega^2 c^{-2},$$
(3.6)

the maximum resolution achievable in the image Δ can never be greater than

$$\Delta \approx \frac{2\pi}{k_{max}} = \frac{2\pi c}{\omega} = \lambda.$$
(3.7)

This is valid for every kind of lens and is known as the Diffraction Limit.

Consider now the use of a medium with $n = -1$ to produce a lens. A sketch of the working principle of this exotic lens is depicted in Figure 3.3 [3]. It can be observed that the light is refracted by a negative angle with respect to the normal direction. Furthermore, the other observed characteristic is the double focusing effect, the first into the lens itself, the second one at a distance z equal to:

$$z = d_2 - d_1$$
(3.8)

where d_1 is the distance of the source in respect to the lens and d_2 is the lens thickness.
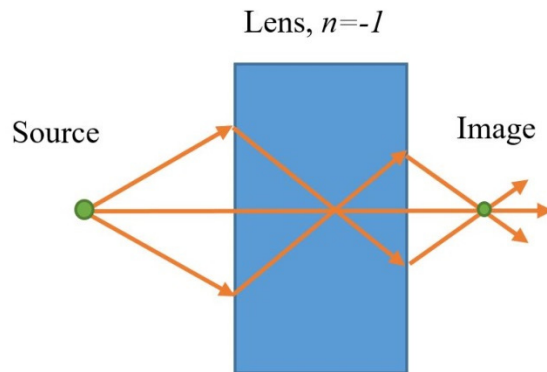
Figure 3.3: Double focusing effect and negative refraction in an ideal lens with n=-1.

To obtain $n = -1$, electric permittivity ε and magnetic permeability μ are chosen to be both negative and equal to -1. It then follows that the refractive index becomes that of the vacuum:

$$n = \sqrt{\varepsilon\mu} \qquad (3.9)$$

When both ε and μ are negative, the negative root of equation (3.9) must be chosen. However, the impedance of the medium (Z) has still a positive value, which is given by equation (3.10). This means that when $\varepsilon = -1$ and $\mu = -1$ the lens is a perfect match to free space and it shows no reflection to the impinging energy.

$$Z = \sqrt{\frac{\mu\mu_0}{\varepsilon\varepsilon_0}} \qquad (3.10)$$

However, the energy transmission occurs in a strange way. In particular, the transport of energy within the lens in the $+z$ direction requires that:

$$k_z' = -\sqrt{\omega^2 c^{-2} - k_x^2 - k_y^2} \qquad (3.11)$$

Please note that the superscript in k_z' indicates that the quantity exists within the lens. Overall the transmission coefficient T_c of the medium then becomes:

$$T_c = tt' = e^{(ik_z'd)} = e^{\left(-i\sqrt{\omega^2 c^{-2} - k_x^2 - k_y^2}\,d\right)} \qquad (3.12)$$

with d being the lens thickness. Negative phase results from the choice of the wave vector forced by a causality restriction. It is of utmost importance to point out that it is this phase reversal that allows the lens to refocus light by canceling the phase acquired by the wave as it travels away from the source [2]. In addition, this exotic lens can also cancel the decay in amplitude of the evanescent waves. In this way, the diffraction limit can be overcome successfully. To demonstrate this, it needs to be shown that the lens enhances the evanescent waves during their path into the lens itself. Note that this does not violate energy conservation rules because evanescent waves transport no energy.

Assuming an *S*-polarized light in vacuum, the electric field $\boldsymbol{E}_{0S+}$ is given by:

$$\boldsymbol{E}_{0S+} = [0, \quad 1, \quad 0] \times e^{(ik_z z + ik_x x - i\omega t)} \tag{3.13}$$

where the wave vector k_z, given by

$$k_z = +i\sqrt{k_x^2 + k_y^2 - \omega^2 c^{-2}}, \quad \omega^2 c^{-2} < k_x^2 + k_y^2, \tag{3.14}$$

implies exponential decay. Some light $\boldsymbol{E}_{0S-}$ is reflected at the interface with the lens:

$$\boldsymbol{E}_{0S-} = r[0, \quad 1, \quad 0] \times e^{(-ik_z z + ik_x x - i\omega t)} \tag{3.15}$$

and a part of $\boldsymbol{E}_{1S+}$ it is transmitted into the medium:

$$\boldsymbol{E}_{1S+} = t[0, \quad 1, \quad 0] \times e^{(-ik_z' z + ik_x x - i\omega t)} \tag{3.16}$$

where

$$k_z' = +i\sqrt{k_x^2 + k_y^2 - \varepsilon\mu\omega^2 c^{-2}},$$

$$\varepsilon\mu\omega^2 c^{-2} < k_x^2 + k_y^2 \tag{3.17}$$

The causality condition requires the choosing of a wave which decays exponentially with distance from the medium. The amount of energy transmission (*t*) and reflection (*r*) for a wave that travels into the vacuum and impinges the lens can be calculated by matching the wave fields at the interfaces:

$$t = \frac{2\mu k_z}{\mu k_z + k_z'}, \qquad r = \frac{\mu k_z - k_z'}{\mu k_z + k_z'}. \tag{3.18}$$

On the other hand, transmission (*t'*) and reflection (*r'*) values can be calculated for a wave traveling through the medium and impinging on the interface with the vacuum:

$$t' = \frac{2k_z'}{k_z' + \mu k_z}, \qquad r' = \frac{k_z' - \mu k_z}{k_z' + \mu k_z} \tag{3.19}$$

To calculate the overall transmission through both sides of the lens, a sum of all the multiple scattering events is needed:

$$T_{c,s} = tt'e^{(ik_z' d)} + tt'r'^2 e^{(3ik_z' d)} + tt'r'^4 e^{(5ik_z' d)} + \cdots = \frac{tt'e^{(ik_z' d)}}{1 - r'^2 e^{(2ik_z' d)}} \tag{3.20}$$

By combining equation (3.19) and equation (3.20) and taking the limit:

$$\lim_{\substack{\mu \to -1 \\ \varepsilon \to -1}} T_{c,s} = \lim_{\substack{\mu \to -1 \\ \varepsilon \to -1}} \frac{tt' e^{(ik_z'd)}}{1 - r'^2 e^{(2ik_z'd)}} =$$

$$= \lim_{\substack{\mu \to -1 \\ \varepsilon \to -1}} \frac{2\mu k_z}{\mu k_z + k_z'} \frac{2k_z'}{k_z' + \mu k_z} \frac{e^{(ik_z'd)}}{1 - \left(\frac{k_z' - \mu k_z}{k_z' + \mu k_z}\right)^2 e^{(2ik_z'd)}} \tag{3.21}$$

$$= e^{(-ik_z'd)} = e^{(-ik_zd)}$$

The reflection coefficient $R_{c,s}$ can be calculated by:

$$\lim_{\substack{\mu \to -1 \\ \varepsilon \to -1}} R_{c,s} = \lim_{\substack{\mu \to -1 \\ \varepsilon \to -1}} r + \frac{tt'r' e^{(2ik_z'd)}}{1 - r'^2 e^{(2ik_z'd)}} = 0 \tag{3.22}$$

A similar result can be obtained for a *P*-polarized evanescent waves:

$$\lim_{\substack{\mu \to -1 \\ \varepsilon \to -1}} T_{c,P} = \lim_{\substack{\mu \to -1 \\ \varepsilon \to -1}} \frac{2\epsilon k_z}{\epsilon k_z + k_z'} \frac{2k_z'}{k_z' + \epsilon k_z} \frac{e^{(ik_z'd)}}{1 - \left(\frac{k_z' - \epsilon k_z}{k_z' + \epsilon k_z}\right)^2 e^{(2ik_z'd)}} = e^{(-ik_zd)} \tag{3.23}$$

The final result is that the medium having the above described properties, here in the form of a lens, does amplify the evanescent waves. As a consequence, a perfect reconstruction of the image can be obtained [4].

The first double-negative material was made in 2000 by Smith *et al.* [5]. They built a composite medium made of an array of nonmagnetic split ring resonators. It acted as a left-handed material (double negativity), where the phase velocity and the wave vector are opposite to the energy flow, for only a well-defined frequency. Moreover, due to the space invariance of Maxwell's Equation when stretched via a spatial transformation, the possibility that the electromagnetic signals could travel in a different way to conventional optics was suggested. In particular, the only parameters affected by coordinate transformation were the permeability and permittivity tensor components. This opened the path towards the electromagnetic invisibility cloaking of objects, and in the same year, Pendry *et al.*[6] gave a mathematical and physical analysis of the electromagnetic cloaking phenomena based on spatial transformation of Maxwell's Equations.

Many subsequent studies have attempted to make this phenomenon happen over a range of different frequencies. For example, in [7], the authors suggested the use of strongly anisotropic material as a condition to reach a broad-bandwidth negative index of refraction. For this purpose, they used metal-dielectric composites rather than bulk materials. The first experimental 2-D electromagnetic cloaking was realized by Schuring *et al.* [8]. At microwave frequencies, they demonstrated that a cloak of structured metamaterial can hide an object successfully, while also reducing the scattering, thus reducing the capability of being detected by radar.

As might be expected, the interest of researchers in electromagnetic cloaking moved from microwave frequencies to optical frequencies. A metal wire composite cloak based on linear coordinate transformation provided a good reduction in scattering and high invisibility at a wavelength of 632.8 nm [9]. Furthermore, the same group of researchers provided a more accurate method based on quadratic transformation to ensure less scattering at the same frequencies[10], [11]. By exploiting the metamaterial properties, it appeared also possible to reach second harmonic generation if a certain type of polarization inside the device was achieved [12], [13]. Third harmonic generation has also been demonstrated by using a structured gold split ring resonator in which a circulating current is induced by the impinging light [14].

Much literature can also be found concerning the superlensing topic. Several standard methods to exceed the diffraction limit have been reported. An example is in Near-Field Scanning Optical Microscopy, in which the near field evanescent wave is recovered by a careful point-by-point scan. Although this technique is widely used within the research community, it is easy to understand that it cannot provide a real-time scan of the near field [15], [16], as would be needed in many practical applications. A possibility to overcome this constraint is provided by the use of metamaterials. As stated both in [17], [18] a metamaterial

slab helps in recovering the exponentially decaying of the evanescent field scattered by an object. This has been proved by exciting the surface Plasmon on thin layer of silver that acts as a metamaterial [17]. The evanescent waves are characterized by very large wave vector and therefore they carry sub-wavelength information. The resolution capability of a metamaterial super lens can be described as the number of sub-wavelength mode of propagation that one can retrieve both in amplitude and phase after the metamaterial layer. One limitation is that the superlensing effect works only for a well-defined and narrow frequency range. One attempt at going beyond this restriction was shown in [19], where the use of a composite metal-dielectric film stretches the capability of the super lens to a wider portion of the electromagnetic spectrum.

Due to its strong relationship with the work contained within this thesis, it is important to mention the work of Jung *et al.* [20]. With the help of numerical analyses, they showed that a holey-structured layer of electromagnetic material can provide superlensing by exploiting Fabry-Pèrot resonances in the holes. A sub-wavelength resolution was reached using interference effects close to the far surface. The mathematical background and working principles of this class of metamaterial were also described.

3.3   Phononic crystals and acoustic metamaterials

As a natural consequence of the growth of interest in electromagnetic metamaterials, scientists started to look into their acoustic counterpart [need a reference]. Although the phenomena involved in electromagnetic and acoustic wave propagation are very different, it is possible to describe both of them with the same equation set by carefully choosing the physical quantities involved. In particular, μ and ε of the electromagnetic case should be replaced by ρ and K, which are the density and the bulk modulus respectively and E should be replaced with the acoustic pressure field P. In this way, the same results obtained in

equation (3.22), equation (3.23) and equation (3.24) can be obtained for the acoustic case. It should be mentioned that there are two different ways in which a material can exhibit negative bulk modulus and negative density. Materials that reach negative index of refraction due to Bragg's Scattering effect are called "Phononic Crystals" and they were the first chronologically to be explored. On the other hand, materials that achieve the same goal by local resonances are the so-called "Acoustic Metamaterials"[21].

3.3.1. Phononic crystals

Phononic crystals involve a spatial arrangement of two different materials with a very high acoustic impedance mismatch. In order to exhibit their special features, the scale of the geometric arrangement must be comparable to the incident wavelength. A good example of the work that led to the studies on phononic crystals can be found in the pioneer works of John Page. In [22] and [23], the exotic properties of 3-D hexagonal geometric arrangement of steel spheres embedded in water were explored:
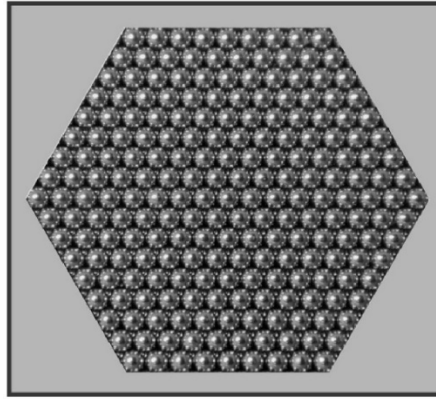
Figure 3.4: 3D hexagonal geometric arrangement of steel spheres embedded in water (taken from ref [24]).

By exciting the structure with a relatively narrow bandwidth signal, a band-fold effect appeared at some frequencies. Furthermore, due to the so called "tunneling effect", the measured group velocity inside the band-gap changed with the sample thickness. Since the equivalent effect appears also in the electromagnetic field case, via a structured material

called a "Photonic Crystal", their acoustic counterparts were automatically named Phononic Crystals. Moreover, this peculiar anisotropic structure showed a negative index of refraction at frequencies outside the band-fold gap. This implies that the phononic crystal can focus the acoustic field [24], [25]. Figure 3.5 shows the first observed negative refraction phenomenon in a 2D photonic crystal made by a regular triangular arrangement of steel rods in water:
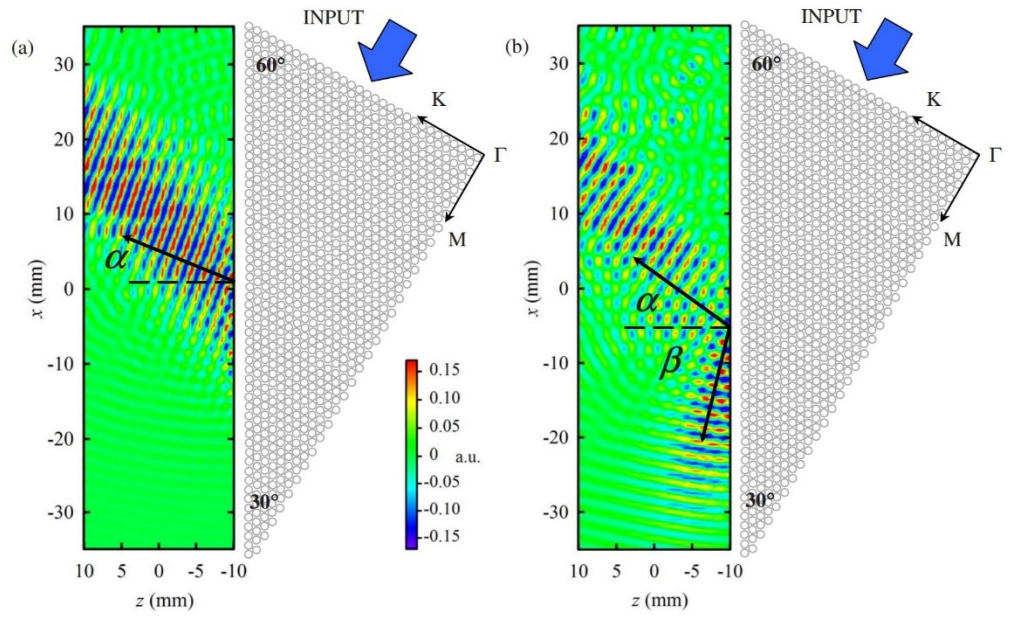
Figure 3.5: Negative refraction experiment, at an excitation frequency of (a) 0.85 MHz and (b) 0.75 MHz. α and β are the angles of refraction and transmission respectively (taken from ref [26]).

The same research work shows that the maximum achievable focus spot achieved by the use of photonic crystal is almost comparable with the diffraction limit at a specific excitation frequency:
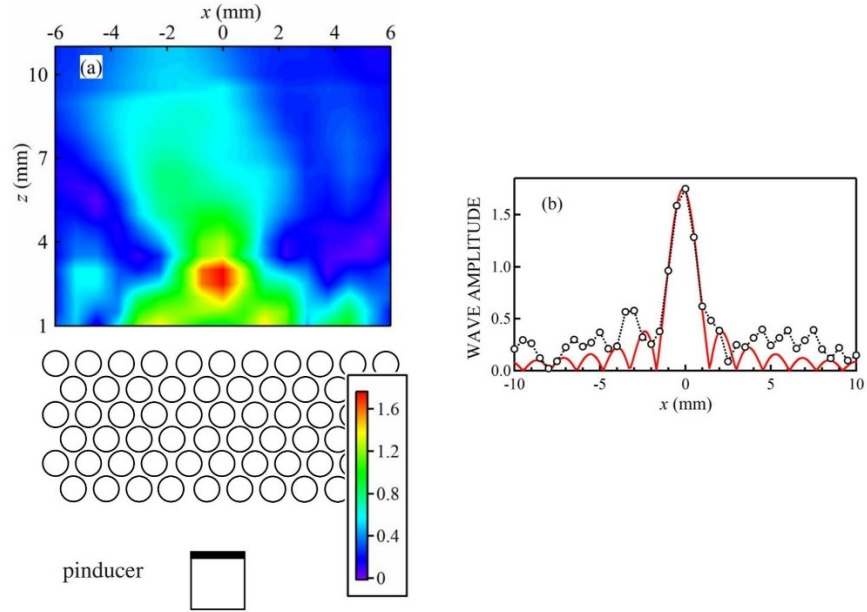
Figure 3.6: Experimental data of imaging the field of a small transducer at 0.55 MHz with a flat phononic crystal filled with methanol. (a) 2D image plot of the wave field amplitude. (b) Field profile obtained from the image plot by plotting along the x direction at z= 2.9 mm; open circles connected with a dashed line and fit of the absolute value of the sinc function, red solid line (taken from ref [26]).

As the crystallographic geometric arrangement on the phononic crystals is forced to be equal to the wavelength, one should note that they provide a maximal resolution of a wavelength and thus they cannot help much to overcome the diffraction limit [27]–[29] . In addition, it is worth noting also that the sound focusing efficiency strongly depends on the regularity of the geometric disposition inside the crystal. As an example, by replacing a tungsten carbide sphere with any other of a different material, a peak of transmission appears within the band-gap. In addition, the position of the peak can be easily tuned by changing the density of the defect or filling it with a liquid [30].

The extraordinary properties of phononic crystals are mainly due to the Bragg's scattering effect. The theory and mathematical models that describe their operation have been widely studied in literature. The reader is referred to the cited work for an exhaustive mathematical explanation of all the phenomena involved [31]. Simply, it can be stated that

inclusions trapped within a matrix of material (such as steel spheres in water) act as scattering sources. A schematic description of this phenomenon is depicted in Figure 3.7:
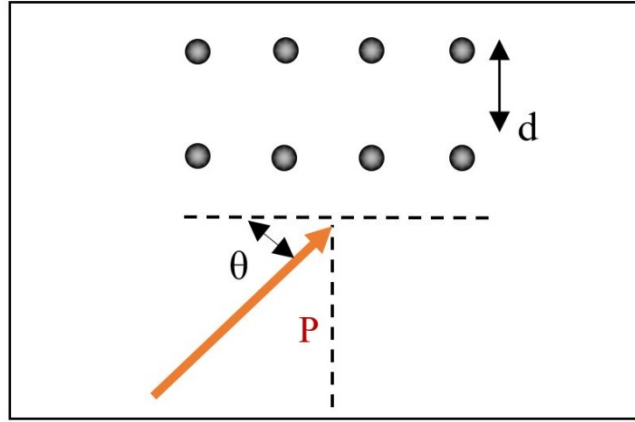
Figure 3.7: Bragg's scattering phenomena: the pressure field P is incident upon the array of spheres at an angle θ with respect to the surface of the arrays.

A pressure field P impinges on a series of scatters at an incidence angle θ. The scattering spheres are in rows with a vertical separation of d. Let λ be the wavelength of the impinging pressure field P and assume that each sphere scatters the field as a source of spherical waves, with the amplitude of the spherical waves depending on the acoustic impedance mismatch between the scatterers and the surrounding medium. The Bragg's scattering effect, that is an extraordinary intensity of reflection, appears when the following condition is satisfied:

$$2d \sin \theta = k\lambda \tag{3.24}$$

with $k=1,2,3…n, \ n \in N$.

When there are many planes of scatterers, and the incident field is well approximated by a plane wave, the reflection maxima are of high amplitude, and are at particular angles and frequencies [32]. As a consequence of this extraordinary reflection (band-fold effect), the effective parameters that describe the properties of the phononic crystals, *i.e.* effective bulk modulus B_{eff} and effective density ρ_{eff}, can have both negative values. This can lead to superlensing phenomenon, for the same reasons described mathematically in Section 3.2.

3.3.2. Acoustic Metamaterials using local resonances

These acoustic metamaterials achieve a negative refractive index by exploiting local resonances rather than scattering and interference effects. Furthermore, the lateral dimensions of each unit cell have to be much smaller than the incident wavelength. This fact makes the metamaterials more suitable than phononic crystals for producing a negative refractive index, involving a negative effective bulk modulus K_{eff} and a negative effective density ρ_{eff}. Since the cell dimensions are smaller than the wavelength, the spatial periodic modulation of the impedance occurs at the same resolution; hence, all the metamaterials properties can be related to an effective homogenous description of the Lorentz form. An accepted method to measure their physical properties is to evaluate the transmission and reflection coefficient when the metamaterial is excited by an acoustic wave. The measured coefficients are then mathematically inverted to recover the bulk modulus and the density [33].

One of the first examples of such acoustic metamaterials can be found in [34]. An array of sub-wavelength Helmotz resonators drilled inside an aluminum samples showed a left-handed behavior in the frequency range of 30-35 kHz. The design exploited in the latter work is depicted in Figure 3.8:
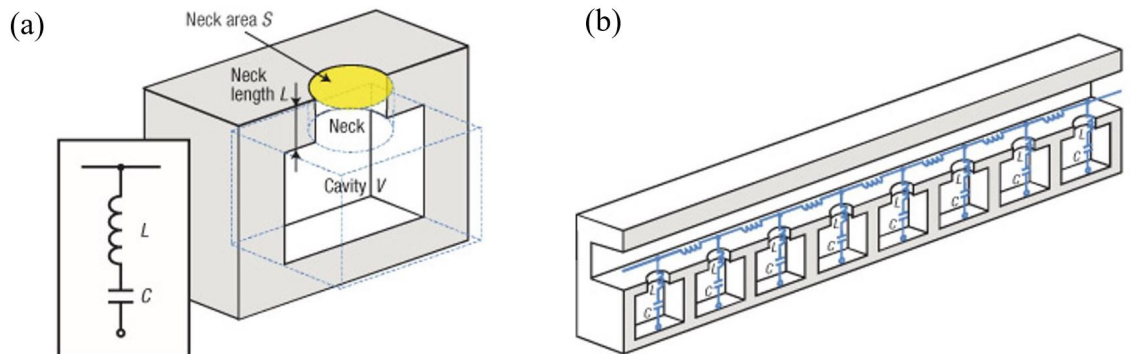
Figure 3.8: (a) an example of acoustic metamaterial fundamental structure geometry and its respective electric model. (b) 1D-array arrangement of the said structure (Taken from ref [34]).

Moreover, it was shown that a negative refraction index introduces surface oscillations characterized by a very large wave vector k. As for their electromagnetic counterpart, these surface oscillations allow the evanescent field scattering by an object to be recovered, *i.e.* superlensing is possible.

It should be noted that the first work related to the study of such metamaterials has been done by simply testing new designs without the aid of a well-developed mathematical model. A first attempt to provide a coherent mathematical analysis on this field was given in [35]. The authors related the changing on the radius of locally resonant cylindrical structures to the values of the sound velocity and density inside the metamaterial. A two-dimensional numerical simulation has also been provided by Ambati *et al.* [36]. They related the evanescent field recovering ability of a metamaterial with its thickness, as well as the resulting resolution limit, which is related to the sub-wavelength dimensions. Later work on the Helmotz-resonator metamaterial explained that the arrangement in series or parallel leads to very different intervals in which the negative index of refraction can be achieved. These frequency gaps can be easily calculated by describing the sound propagation inside the metamaterials with an analogous electric model. It is worth mentioning that multi band-fold gap acoustic metamaterials have been explored. In particular, the behavior of a multiple band-gap can be predicted if a multiresonator mass-in-mass lattice system is taken into account as a mathematical model [37].

Of relevance to this thesis are the metamaterials that achieve super-resolution via Fabry-Pèrot resonances inside drilled sub-wavelength holes. The first theoretical approach was described in [38]. By exploiting numerical simulation on a single hole embedded in water or air, the researchers found that the frequency of resonance is related to thickness of the hole. Furthermore, the resonances appear at higher harmonics, showing that the behavior is related to the Fabry-Pèrot theory. Moreover, the authors pointed out the importance of (i)

considering the material surrounding the holes as being rigid, (ii) having a high acoustic impedance mismatch between the two media and (iii) using a planar incident acoustic wave. Using such designs, a simple block of brass material with sub-wavelength drilled holes provided a super-resolution that can be easily tuned by changing the distance between each hole [27]. Furthermore, a brass acoustic magnifying lenses which operates in the audible range show a resolution up to a fifth of the wavelength [39].

Other studies demonstrate possibilities for reaching a wider bandwidth behaviour in metamaterials. By exploiting solid inclusions in air, it is possible to reach a broad-band left-handed metamaterials [40]. Moreover, the band-gap can be controlled by scaling the geometry to suit another frequency range [41]. Metamaterials made by piezoelectric inclusions can also provide novel application. By varying the applied voltage level, a membrane of piezoelectric material embedded in a solid matrix changes its corresponding acoustic impedance [42]. Alternative studies on how to focus the sound with a metamaterial also exist. By changing the dimension along and the filling ratio of solid inclusions in air it is possible to fabricate a gradient index lenses. By changing the latter parameters, the focusing focal length can be tailored to particular applications [43]. Moreover, the geometry of the inclusions can be engineered with a genetic stochastic algorithm [44].

Highly anisotropic metamaterials can also be exploited to hide an object from an acoustic radar. Perforated plastic plates, which are well-suited to air coupled applications, or circuits of acoustic capacitors and inductors elements are capable of hiding a metal object – an example of acoustic cloaking [45]–[47] :
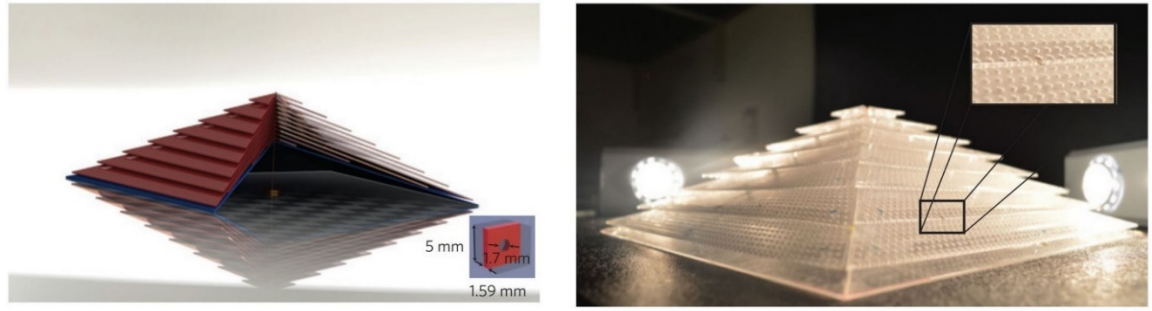
Figure 3.9: An example of 3D broadband acoustic cloaking (taken from ref [47]).

Since the resolution of measurements made in either medical ultrasound or NDT is limited to the wavelength of the ultrasonic wave by the natural diffraction limit, it is easy to understand that the use of high frequency ultrasonic signals increase the resolution of the ultrasonic inspection. In standard ultrasonic testing, broad-band coded signals such as Golay or Chirps can be used to enhance the resolution [48], as was described in Chapters 1 and 2. However, due to attenuation phenomena that affect the SNR, the frequency of the input signal cannot be increased arbitrarily. A trade-off exists between resolution and signal attenuation, and this must be taken into account for each measurement. Thus, the use of acoustic metamaterials could provide a possible way to avoid the frequency/attenuation constraint by creating focusing effects that could normally only be produced using higher frequencies.

Note that most applications of ultrasound occur at frequencies higher than those examined to date using such metamaterials, and there is still a need to build a metamaterial device that can be exploited at frequencies of up to 1 MHz or higher. So far, the limitations on the achievable metamaterial cell dimensions have forced researchers to produce metamaterial devices only in the low frequency acoustic range (100Hz to 20 kHz), and most often in air. As an example, to produce a Fabry-Pèrot metamaterial useful at 2 kHz, one has to be able to drill squared holes of 0.79 mm x 0.79 mm [27]. By rescaling the dimension to

suit higher frequency uses, it is evident that alternative ways to fabricate metamaterials have to be explored. This is a subject of a later chapter in this thesis.

3.4   Holey-structured acoustic metamaterials: theoretical background

A study by Christensen *et a*l. [38] demonstrated the action of a 2D array of square-shaped holes within a bulk material. The results showed that Fabry-Peròt resonances (FPRs) existed within these holes, the peak frequency values of which were related to the thickness *h* of the metamaterial. Furthermore, FPRs could be excited by very large wave vectors *k* which carry sub-wavelength information. This is the key-point that needs to be understood in order to gain insight into the operation of holey structured acoustic metamaterials.

In order to understand better how holey metamaterials help in coupling the evanescent field scattered from an object of sub-wavelength dimensions, the same formalism utilized by Zhu *et al.* [27] is used here. The effective medium limit approximation is here considered, that is when the wavelength of the impinging plane wave λ is much larger than the channel's lattice constants *a* and *Λ*, *a* being the lateral dimension of the square-shaped hole and *Λ* the lattice parameter or center-to-center distance, see Figure 3.10:
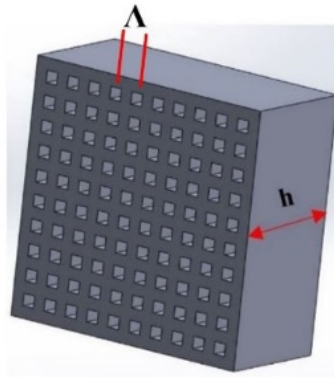
Figure 3.10: Acoustic metamaterial with h = 14.8mm, containing a=1.48mm wide square-sided holes, with their centres separated by 2.96mm

Under these conditions, propagation within the holes via FPRs dominates the acoustic energy transmission process. The probability of the plane wave of parallel

momentum $\vec{k}_{\parallel} = (k_x, k_y)$ to be transmitted to the other side of the metamaterial in a diffracted plane wave with $\vec{k}_{\parallel}^{(n,p)} = \left(\frac{k_x + n2\pi}{\Lambda}, \frac{k_y + p2\pi}{\Lambda}\right)$, it is expressed by the transmission coefficient T_c^{np}:

$$T_c^{np}(\lambda, \vec{k}_{\parallel}) = -S_{np}v', \tag{3.25}$$

where S_{np} is the overlap integral between the diffracted wave of order (n,p), $v' = \frac{I_0 G_v}{(G - \Sigma)^2 - G_v^2}$.

The term I_0 is proportional to the overlap integral between the incident wave and the fundamental mode, S_{00}, where $I_0 = 2iS_{00}$. G_v and Σ depend on the propagation constant of the fundamental mode k_0, and on the thickness h of the acoustic metamaterial:

$$\Sigma = \frac{\cos k_0 h}{\sin k_0 h}$$

$$G_v = \frac{1}{\sin k_0 h} \tag{3.26}$$

The G terms that takes the coupling between adjacents holes into account are expressed as a sum of diffracted modes:

$$G = i \sum_{lm} \frac{k_0}{k_z^{(l,m)}} |S_{lm}|^2 \tag{3.27}$$

where $k_z^{(l,m)} = \sqrt{k_0^2 - \left[\vec{k}_{\parallel}^{(l,m)}\right]^2}$.

It can be seen that the first term of the above sum, $(l=m=0)$, is dominant and thus $G = iY|S_{00}|^2$, where $Y = \frac{k_0}{\sqrt{k_0^2 - k_{\parallel}^2}}$. By substituting all these quantities into equation (3.25), it follows that:

$$T_c^{00}(\lambda, \vec{k}_{\parallel}) = \frac{4|S_{00}|^2 Y e^{iq_z h}}{(1 + Y|S_{00}|^2)^2 - (1 - Y|S_{00}|^2)^2 e^{2iq_z h}} \tag{3.28}$$

For wavelengths corresponding to a FPR, $\lambda_R = \frac{2h}{m}$, reduces to:

$$T_c^{00}\left(\lambda_R, \vec{k}_{\parallel}\right) = (-1)^m \tag{3.29}$$

This is valid for all values of $\vec{k}_{\parallel}$. Figure 3.11 shows numerical simulations performed to retrieve the amplitude of the transmission coefficient for various k_x values:
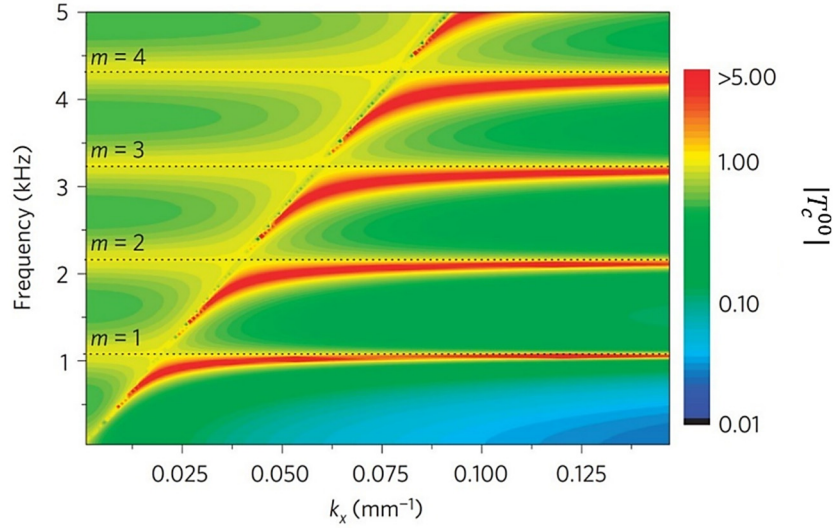
Figure 3.11: Simulated amplitude of the zero-order transmission coefficient for different parallel momentum and frequencies values (log-scale). The amplitude of the transmission coefficient is one when FPR conditions are matched (taken from ref [27]).

This shows that, at the resonance condition, even those values associated with evanescent waves (which carry sub-wavelength details) are successfully transferred to the outer side of the metamaterial, and can contribute to imaging.

This is the key point in understanding the working principle of holey-structured acoustic metamaterials: they allow the near field region of the acoustic field to be transferred over distances at which it would not normally be possible to be observed.

In addition, the holey structure behaves as a homogeneous medium with an effective bulk modulus K_{eff} and an effective mass density ρ_{eff} that can be expressed as:

$$\rho_{eff}^x = \rho_{eff}^y = \rho_{eff} = \frac{\Lambda^2}{a^2}\rho_{air} \tag{3.30}$$

$$K_{eff}^x = K_{eff}^y = K_{eff} = \frac{\Lambda^2}{a^2} K_{air} \qquad (3.31)$$

In the z-direction $\rho_{eff}^z = \frac{1}{K_{eff}^z} = \infty$.

It is worth stressing that, for equations (3.30) and (3.31) to be valid, a high impedance mismatch between the bulk material and the air into the holes needs to be present [49].

3.5 Using pulse compression with acoustic metamaterials and phononic crystals: advantages

It has been stressed throughout the previous sections that metamaterials usually work for a certain specific single frequency (or a very narrowband frequency range) or for specific discrete set of frequencies. This is mainly due to their geometrical arrangement from which their extraordinary properties arise. Being able to realize them in such a way that they can be exploited along a broad-frequency range would allow them to be used on real applications, especially in the ultrasonic region for ultrasonic non-destructive testing applications and medical imaging. Moreover, since chirps and coded signals provide the well-described properties and gains described deeply in Chapter 2, they would be successfully used in combination with such broadband devices. As a consequence, metamaterials energy losses can be counterbalanced by using such coded excitation. Moreover, phase-time information can be restored after acoustic wave travel into the metamaterial by using such coded excitations.

3.6 Conclusions

In this chapter, a literature review which considers electromagnetic metamaterials, phononic crystals and acoustic metamaterials has been given. Moreover, a deep mathematical description of metamaterials working principles, as well as the way to overcome the diffraction limit has been given. In particular, since this thesis research focuses

its effort on a specific class of acoustic metamaterials, i.e. holey-structured acoustic metamaterial, their peculiar working principles and main properties have been described in detail. The next chapter will describe a Finite Element Analysis that has been carried out to validate the exotic features promised by the use of such acoustic metamaterials for sub-wavelength imaging purposes.

References

[1]   C. Wenshan and V. Shalaev, *Optical Metamaterials*, vol. 330, no. 6011. Springer New York, 2010.

[2]   V. G. Veselago, "The electrodynamics of substances with simultaneously negative values of ε and μ," *Physics-Uspekhi*, vol. 10, no. 4, pp. 509–514, 1968.

[3]   J. B. Pendry, "Negative Refraction & the Perfect Lens Refraction of Light – Snell / Descartes," vol. 7, 2006.

[4]   J. B. Pendry, "Negative refraction makes a perfect lense," *Phys. Rev. Lett.*, vol. 85, no. 18, p. 3966, 2000.

[5]   D. Smith, W. Padilla, D. Vier, S. Nemat-Nasser, and S. Schultz, "Composite medium with simultaneously negative permeability and permittivity," *Phys. Rev. Lett.*, vol. 84, no. 18, p. 4184, May 2000.

[6]   J. B. Pendry, D. Schurig, and D. R. Smith, "Controlling electromagnetic fields," *Science (80-.).*, vol. 312, no. 5781, pp. 1780–1782, Jun. 2006.

[7]   V. M. Shalaev and V. M. Shalaev, "Optical negative-index metamaterials," *Nat. Photonics*, vol. 1, no. 1, pp. 41–48, 2007.

[8]   D. Schurig *et al.*, "Metamaterial electromagnetic cloak at microwave frequencies," *Science (80-.).*, vol. 314, no. 5801, pp. 977–980, Nov. 2006.

[9]   W. Cai, U. K. Chettiar, A. V. Kildishev, and V. M. Shalaev, "Optical cloaking with metamaterials," *Nat. Photonics*, vol. 1, no. 4, pp. 224–227, Apr. 2007.

[10]   W. Cai, U. K. Chettiar, A. V. Kildishev, V. M. Shalaev, and G. W. Milton, "Nonmagnetic cloak with minimized scattering," *Appl. Phys. Lett.*, vol. 91, no. 11, p. 111105, 2007.

[11]   W. Cai, A. V Kildishev, U. K. Chettiar, and V. M. Shalaev, "Designs for optical cloaking with high-order transformations transformations," *Opt. Express*, vol. 16, no. 8, pp. 5444–5452, 2008.

[12]   M. W. Klein, C. Enkrich, M. Wegener, and S. Linden, "Second-harmonic generation from magnetic metamaterials.," *Science*, vol. 313, no. 5786, pp. 502–504, Jul. 2006.

[13]   A. Popov and V. Shalaev, "Negative-index metamaterials: second-harmonic generation, Manley–Rowe relations and parametric amplification," *Appl. Phys. B*, vol. 84, no. 1–2, pp. 131–137, 2006.

[14]   M. Klein, M. Wegener, N. Feth, and S. Linden, "Experiments on second-and third-harmonic generation from magnetic metamaterials," *Opt. Express*, vol. 15, no. 8, pp. 5238–5247, 2007.

[15]   Z. Liu *et al.*, "Far-field optical superlens," *Nano Lett.*, vol. 7, no. 2, pp. 403–408, Feb. 2007.

[16]   T. Taubner, D. Korobkin, and Y. Urzhumov, "Near-field microscopy through a SiC superlens," *Science (80-.).*, vol. 313, no. 5793, pp. 1595–1595, 2006.

[17]   N. Fang, H. Lee, C. Sun, and X. Zhang, "Sub–Diffraction-Limited Optical Imaging with a Silver Superlens," *Science (80-.).*, vol. 308, no. 5721, pp. 534–537, 2005.

[18]   Z. Jacob, L. V Alekseyev, and E. Narimanov, "Optical Hyperlens : Far-field imaging beyond the diffraction limit," *Opt. Express*, vol. 14, no. 18, pp. 8247–8256, 2006.

[19]   W. Cai, D. Genov, and V. Shalaev, "Superlens based on metal-dielectric composites," *Phys. Rev. B*, vol. 72, no. 19, p. 193101, Nov. 2005.

[20]   J. Jung, F. García-Vidal, L. Martín-Moreno, and J. Pendry, "Holey metal films make perfect endoscopes," *Phys. Rev. B*, vol. 79, no. 15, p. 153407, Apr. 2009.

[21]   P. A. Deymier, *Acoustic Metamaterials and Phononic Crystals*, vol. 173. Springer, 2013.

[22]   J. H. Page, A. L. Goertzen, S. Yang, Z. Liu, C. T. Chan, and P. Sheng, "Acoustic Band Gap Materials," in *Photonic Crystals and Light Localization in the 21st Century*, 2001, pp. 59–68.

[23]   S. Yang, J. H. Page, M. L. Cowan, C. T. Chan, and P. Sheng, "Phononic Crystals," *La Phys. au Canada*, pp. 187–189, 2001.

[24]   C. Chan and P. Sheng, "3D Phononic Crystals," in *Wave Scattering in Complex Media: From Theory to Applications*, 2003, pp. 282–307.

[25]   S. Yang, J. Page, Z. Liu, M. Cowan, C. Chan, and P. Sheng, "Ultrasound Tunneling through 3D Phononic Crystals," *Phys. Rev. Lett.*, vol. 88, no. 10, p. 104301, Feb. 2002.

[26]   A. Sukhovich, L. Jing, and J. H. Page, "Negative refraction and focusing of ultrasound in two-dimensional phononic crystals," *Phys. Rev. B - Condens. Matter Mater. Phys.*, vol. 77, no. 1, 2008.

[27]   J. Zhu, J. Christensen, J. Jung, and L. Martin-Moreno, "A holey-structured metamaterial for acoustic deep-subwavelength imaging," *Nat. Phys.*, vol. 7, no. 1, pp. 52–55, 2011.

[28]   A. Sukhovich, L. Jing, and J. H. Page, "Negative refraction and focusing of ultrasound in two-dimensional phononic crystals," *Phys. Rev. B - Condens. Matter Mater. Phys.*, vol. 77, no. 1, 2008.

[29]   J. F. Robillard *et al.*, "Resolution limit of a phononic crystal superlens," *Phys. Rev. B - Condens. Matter Mater. Phys.*, vol. 83, no. 22, 2011.

[30]   J. H. Page and A. Sukhovic, *McGraw-Hill Yearbook of Science & Technology*. 2006.

[31]   Z. Liu, C. Chan, P. Sheng, a. Goertzen, and J. Page, "Elastic wave scattering by periodic structures of spherical objects: Theory and experiment," *Phys. Rev. B*, vol. 62, no. 4, pp. 2446–2457, 2000.

[32]   S. Laureti, O. Akanji, L. Davis, and S. Leigh, "Design and characterization of 3D-printed phononic crystals for sub-MHz ultrasound manipulation," *Ultrasonics Symposium (IUS), 2015 IEEE International. IEEE,* 2015.

[33]   V. Fokin, M. Ambati, C. Sun, and X. Zhang, "Method for retrieving effective properties of locally resonant acoustic metamaterials," *Phys. Rev. B*, vol. 76, no. 14, p. 144302, 2007.

[34]   N. Fang *et al.*, "Ultrasonic metamaterials with negative modulus.," *Nat. Mater.*, vol. 5, no. 6, pp. 452–456, Jun. 2006.

[35]   D. Torrent and J. Sánchez-Dehesa, "Acoustic metamaterials for new two-dimensional sonic devices," *New J. Phys.*, vol. 9, no. 9, p. 323, Sep. 2007.

[36]   M. Ambati, N. Fang, C. Sun, and X. Zhang, "Surface resonant states and superlensing in acoustic metamaterials," *Phys. Rev. B*, vol. 75, no. 19, p. 195447, May 2007.

[37]   G. L. Huang and C. T. Sun, "Band Gaps in a Multiresonator," *J. Vib. Acoust.*, vol. 132, no. 3, p. 31003, 2010.

[38]   J. Christensen, L. Martin-Moreno, and F. J. Garcia-Vidal, "Theory of resonant acoustic transmission through subwavelength apertures," *Phys. Rev. Lett.*, vol. 101, no. 1, p. 14301, 2008.

[39]   J. Li, L. Fok, X. Yin, G. Bartal, and X. Zhang, "Experimental demonstration of an acoustic magnifying hyperlens," *Nat. Mater.*, vol. 8, no. 12, pp. 931–934, 2009.

[40]   L. Zigoneanu and B. Popa, "Design and measurements of a broadband two-dimensional acoustic metamaterial with anisotropic effective mass density," *J. Appl. Phys.*, vol. 109, no. 5, p. 54906, 2011.

[41]   B. Popa and S. A. Cummer, "Design and characterization of broadband acoustic composite metamaterials," *Phys. Rev. B*, vol. 80, no. 17, p. 174303, 2009.

[42]   B. Popa, L. Zigoneanu, and S. A. Cummer, "Tunable active acoustic metamaterials," *Phys. Rev. B*, vol. 88, no. 2, p. 24303, 2013.

[43]   A. Climente and D. Torrent, "Sound focusing by gradient index sonic lenses," *Appl. Phys. Lett.*, vol. 97, no. 10, pp. 104103-104103–3, 2010.

[44]   D. Li, L. Zigoneanu, B. Popa, and S. A. Cummer, "Design of an acoustic metamaterial lens using genetic algorithms," *J. Acoust. Soc. Am.*, vol. 132, no. 4, pp. 2823–2833, 2012.

[45]   S. Zhang, C. Xia, and N. Fang, "Broadband Acoustic Cloak for Ultrasound Waves," *Phys. Rev. Lett.*, vol. 106, no. 2, p. 24301, 2011.

[46]   B. Popa, L. Zigoneanu, and S. A. Cummer, "Experimental Acoustic Ground Cloak in Air," *Phys. Rev. Lett.*, vol. 106, no. 253901, pp. 1–4, 2011.

[47]   L. Zigoneanu, B. Popa, and S. a Cummer, "Three-dimensional broadband omnidirectional acoustic ground cloak," *Nat. Mater.*, vol. 13, no. March, pp. 1–4, 2014.

[48]   P. Pallav, T. H. Gan, and D. A. Hutchins, "Elliptical-Tukey Chirp Signal for Ultrasonic Imaging," *IEEE Trans. Ultrason. Ferroeletrics, Freq. Control*, vol. 54, no. 8, pp. 1530–1540.

[49]   S. Laureti, D. Hutchins, L. Davis, S. Leigh, and M. Ricci, "High-resolution acoustic imaging at low frequencies using 3D-printed metamaterials," *AIP-Advances*, vol. 6, no. 12, 2016.

CHAPTER 4: Finite Element Simulations of Acoustic Metamaterials

4.1   Introduction

Numerical simulations allow the user to both understand and verify the working principles of novel designs and complex structures before realizing expensive experimental measurements. They can be a powerful method to either predict or to allow interpretation of the experimental results.

Designing acoustic metamaterials can be complicated, and for this reason numerical simulations open the way to understanding whether a new design can provide the expected effects. In addition, geometrical features and physical properties can be varied almost arbitrarily during the simulation process, leading to an easy understanding of what ideas are worth following and which ones should be abandoned.

In this research, a Finite Element Method (FEM) have been exploited to perform simulations on complex designs, *i.e* 1D, 2D or 3D geometrical problems. FEM is a reliable tool used to search for approximates solutions of partial differential equation problems. In particular, this method divides the required geometry into a finite number of elements, to form a mesh. COMSOL® FE software has been used throughout this thesis research to investigate metamaterial structures.

As described in Chapter 3, the aim is to realize an acoustic metamaterial device that (i) can be manufactured, (ii) is exploitable within the ultrasonic frequency range and (iii) is capable of showing extraordinary effects across a range of frequencies. Thus, there is the need to show that an acoustic metamaterial can by successfully realized by additive manufacturing (AM) methods. In addition, increasing the working frequency of a Holey-structured Acoustic Metamaterial requires an increase in the resolution of the model. This in

turn affects the complexity of the FE modelling, leading to very long simulation time even though very powerful workstations are exploited. The following sections report the simulations results over different acoustic metamaterial designs, and describes the approach used to reduce the time duration of FE simulations.

4.2 Frequency Domain FEM acoustic simulations

Two main approaches can be followed to solve partial differential equations for acoustic problem in COMSOL: (i) time domain or (ii) frequency domain analysis. In general, time domain analysis applied to 3D FEM problems requires very high computational resources, as well as very long simulation time. On the other hand, if carefully implemented, frequency domain analysis can be successfully applied to the current case of study. In particular, the *Pressure Acoustic Frequency Domain Analysis* in COMSOL has been used throughout the simulations described below.

This method works by simulating an amplitude-limited background pressure field p_b at various frequencies imping over a selected surface of the acoustic metamaterial design under test. The resulting scattered pressure p_s, which contains the information about the effect of the metamaterial on the impinging pressure field, can be calculated as in equation (4.1):

$$p_s = p_t - p_b \tag{4.1}$$

where p_t is the total pressure field and is calculated by the software. The Finite Element (FE) modelling implemented is shown in Figure 4.1. A single hole acoustic metamaterial (1) is simulated to be situated within a control volume (3) surrounded by a perfectly-matched layer, which locally dumps the pressure field avoiding any unwanted reflections. Two outer control volumes are placed at the inner side and at the outer side of the material respectively. In this way, mesh elements side dimensions can be locally increased leading to an enhanced

precision of the retrieved pressure field, without compromising the computational time duration.
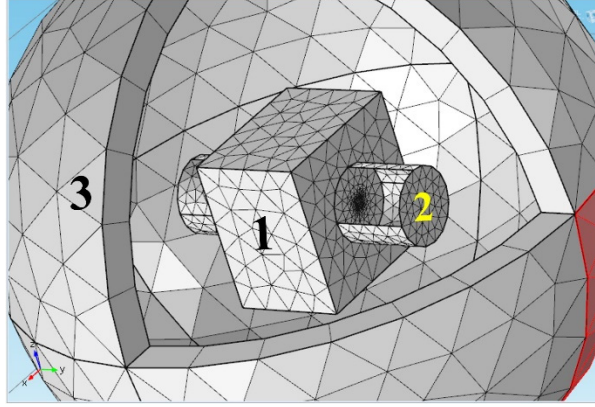
Figure 4.1: FE modelling sketch.

The working principle of this method for a single hole metamaterial can be understood by looking at Figure 4.2, where the difference between the impinging plane wave pressure field p_b and the resulting scattered pressure field p_s is highlighted in a simplified way after having travelled through the hole. Note that the metamaterial is assumed to have an acoustic impedance much different to the surrounding medium. This general approach has been followed for all the below described simulations.
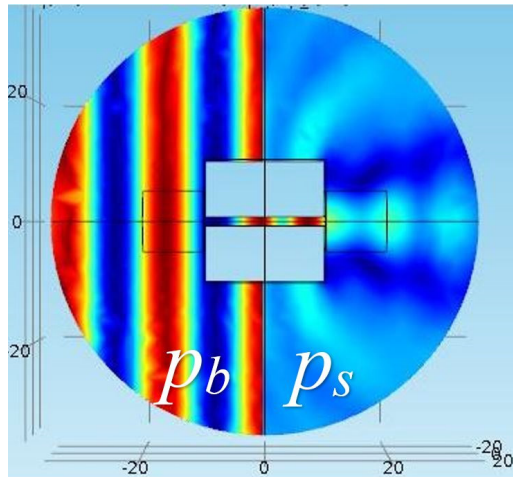
Figure 4.2: Background pressure field p_b and scattered pressure field p_s highlighted on both side of a single hole acoustic metamaterial.

Please note that an alternative and robust modelling strategy relies on the use of an amplitude-limited planar pressure field simulated at one of the control volume surface outer

surface (e.g. see Figure 4.1 – control volume "2"). This can be done easily in COMSOL by adding a "Plane Wave Radiation Condition" where needed.

As described in Chapter 3, extra-ordinary properties arise when Fabry-Pèrot resonant conditions are matched into an array of such air channels. Therefore, FEM has been utilised to verify the appearance of those effects, starting from a simple polymer metamaterial design operating in air. The next subsection describes the preliminary steps that had to be carried out in order to validate the FEM results. This ensures that the validity and robustness of FEM results predicted for more complex geometries can be relied upon.

4.2.1. Optimal mesh dimension and solution convergence on a single hole AM

Performing FEM simulations implies the careful choice of mesh element dimensions. This is because the retrieved solutions, here in the form of the modulus and phase of the acoustic pressure amplitude at each element of the mesh, is highly influenced by the dimension of the mesh itself. Furthermore, mesh element geometry must be chosen carefully in order to obtain reliable FEM results. As an example, meshing a spherical object is very challenging. This is because an infinite number of elements is theoretically needed to avoid surface edges discontinuities. However, there is a minimum dimension of the mesh elements that can be implemented to assure the consistency of the retrieved pressure values, *i.e.* convergence of the solutions. In particular, the use of six elements at least per wavelength is suggested in literature [1].

In order to investigate both the appearance of Fabry-Pèrot resonance effects and to verify the minimum mesh elements dimensions that assure convergence of the solutions, a single hole material has been studied by FEM. Figure 4.3 shows the investigated design:
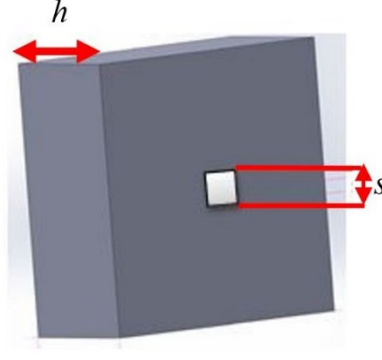
Figure 4.3: single hole acoustic metamaterial. Thickness h was chosen to be 14.8 mm. The side dimension of the squared-shaped hole s is 1.48 mm.

The theory of the wave propagation inside a single sub-wavelength hole has been presented in [2], [3]. Here some considerations about the expected results are given. Consider a plane wave impinging perpendicularly onto the metamaterial surface. Let λ be the wavelength of the acoustic wave in air and h the metamaterial thickness. Fabry-Pèrot resonances into the hole are expected for certain values of λ. In particular, the first resonance emerges when the wavelength is twice the AM thickness, so when:

$$\frac{\lambda}{2} = h \qquad (4.2)$$

This corresponds to a resonance frequency f_1 equal to:

$$f_1 = \frac{v}{2h} \qquad (4.3)$$

In general, resonances are expected for frequency values f_k such that:

$$f_k = kf_1 \qquad (4.4)$$

with $1 \le k \le k_{max}$, where k_{max} is the maximum resonance order admitted by the structure. Although Fabry-Pèrot conditions hold for any k, resonance effects are expected to disappear when the sub-wavelength model is no more valid, hence when wavelengths are consistent

with the hole dimension. Considering s being the side dimension of a squared-side hole and v the sound velocity in air, then the maximum frequency of resonance f_{max} is:

$$f_{max} = \frac{v}{\lambda_{min}} = \frac{v}{s}$$ (4.5)

By combining equation (4.3) and equation (4.5), the number n of resonances frequencies visible for a specific metamaterial design is:

$$k_{max} = \frac{f_{max}}{f_1} = \frac{2h}{s}$$ (4.6)

Here only the round-trip condition of Fabry-Pèrot resonances has been considered. In practice, other aspects arise that modify the values of the resonant frequencies as well modulate their amplitudes [4]. For the present design, the thickness h was chosen to be 14.8 mm, whilst the side dimension of the squared-shaped hole s was 1.48 mm (see Figure 4.3). This in turns corresponds to expected Fabry-Pèrot resonances at every integer multiple of the fundamental frequency f_1, which can be calculated via equation (4.4) to be f_1=11,588 Hz.

In order to compute the solution, the method needs the numerical values of the mass densities and sound velocities of both the bulk material with air as the background medium. The values chosen for air were ρ_{air} = 1.225 kg*m^{-3} and v_{air} = 343 m*s^{-1}, whilst for the polymer material they were $\rho_{polymer}$ = 1,190 kg*m^{-3} and $v_{polymer}$ = 2,200 m*s^{-1}. (Note, that the values chosen for the polymer are similar to those of an actual material used in experiments later in the thesis). The FEM results are shown in Figure 4.4, where the absolute pressure values retrieved at the outer side of the single hole for different values of the mesh size have been plotted for the frequency range 1-100 kHz. It can be seen that resonances due to Fabry-Pèrot effects appear clearly as expected theoretically. Moreover, a minimum mesh element side dimension of 0.5 mm can be chosen as this assures the resulting accuracy to be

comparable to lower mesh element dimensions. This guarantees the computational time to be as low as possible without compromising the quality of the results.
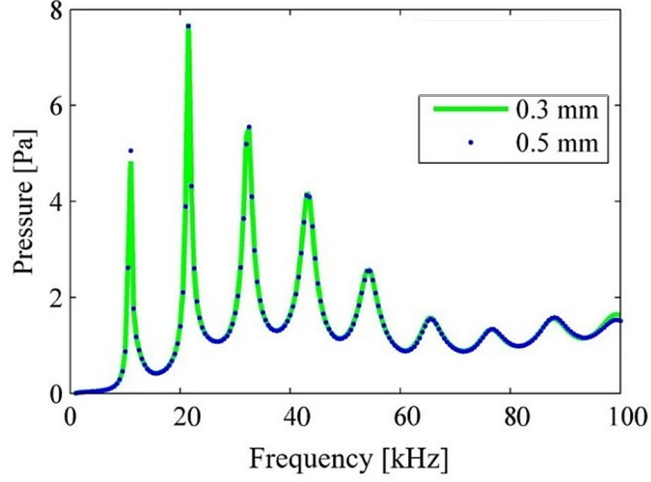
Figure 4.4: single hole acoustic metamaterial FEM results for different mesh elements side dimensions.

It is interesting to see what happens within the hole when Fabry-Peròt conditions are met. Figure 4.5 shows the appearance of stationary waves within the hole channel for the fundamental resonance frequency f_1 (around 11.5 kHz) and f_2, f_3, f_5. Small numerical differences from values expected from equation (4.4) are mainly due to the limited frequency resolution used in the FE model, as the incident plane wave pressure excitation has incremental frequency values of 500 Hz.

$f_1 = 11.5$ kHz $f_2 = 23$ kHz

$f_3 = 34.5$ kHz $f_5 = 57.5$ kHz
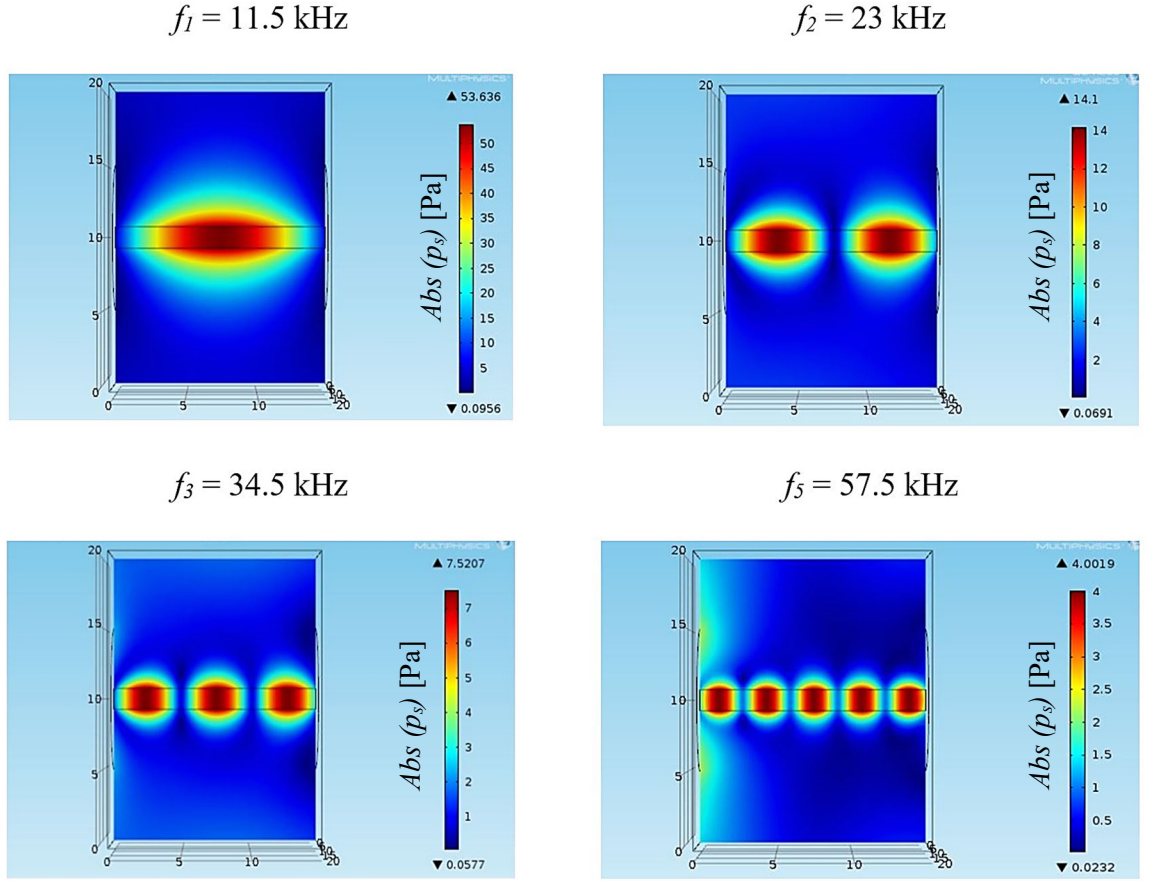
Figure 4.5: Stationary wave condition into a single hole acoustic metamaterial for different resonance frequencies.

To further validate the results obtained by the chosen FE approach, simulations of the expected frequency domain outputs have been performed on single hole materials having different thicknesses h. Equation (4.3) shows that a shift to lower resonant frequencies can be observed if greater thickness h are used, as might be expected. Figure 4.6 shows the result for $h = 14.8$ mm, 17.8 mm and 24.8 mm. This is obtained by plotting the normalized absolute value of the pressure field at the outer exit of the single hole across the frequency range 6-12.5 kHz. It can be noted that FEM predictions show the expected shift to lower frequencies for greater values of h.
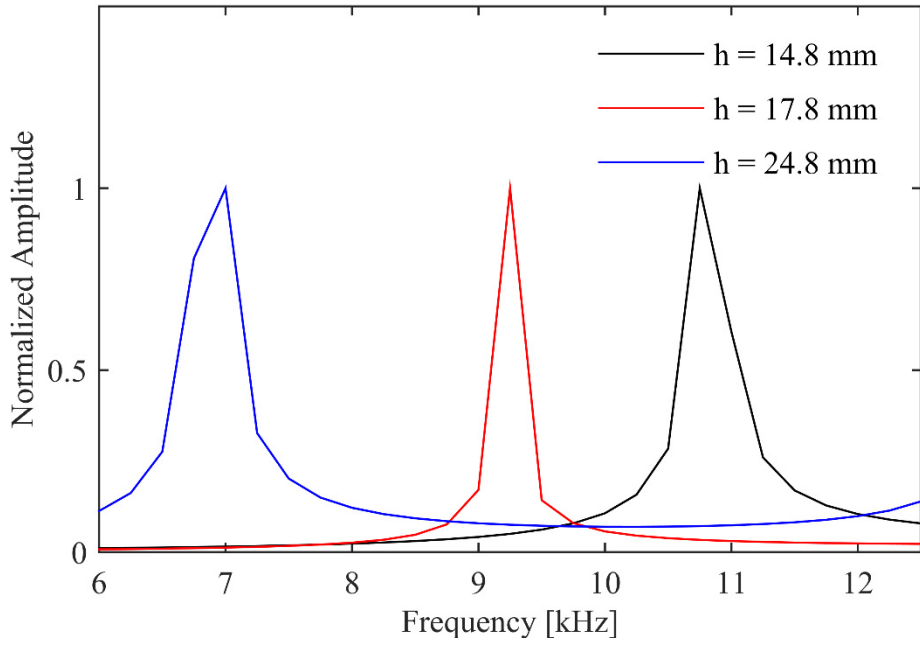
Figure 4.6: FEM simulations among AM with different thicknesses.

4.2.2. Focusing effect on a nine holes Holey-structured Acoustic Metamaterial

Interesting effects can be observed if more complex structures are investigated, rather than a simple single hole. A good example is represented by the investigation of nine holes (3 by 3) structure, shown in Figure 4.7. The thickness h was chosen to be h=14.8 mm and s=1.48 mm and the center-to-center distance between holes was $\Lambda = 2.22$ mm.
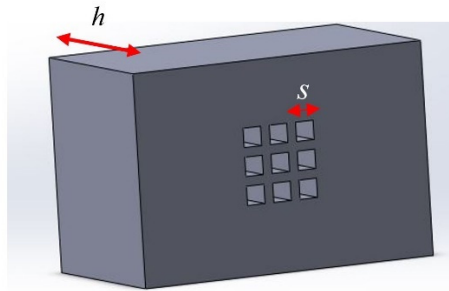
Figure 4.7: nine holes AM investigated design. Thickness h=14.8 mm; squared-holes side dimension s=1.48 mm.

Since t and h have the same numerical values as for the single hole metamaterial previously investigated, the pattern of resonant frequencies is expected to be the same. Figure 4.8 shows the comparison of the pressure amplitude between the single hole AM and

nine holes one, again having same thickness *h*=14.8 mm and squared-holes side dimension *s*=1.48 mm. Note that the pressure amplitude for the nine holes AM design refers to a point at the outer exit of the central hole:
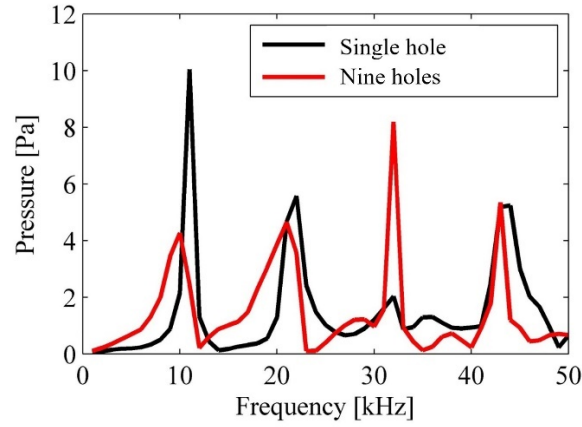
Figure 4.8: Comparison between the pressure amplitude retrieved after FEM for the single hole (red) and the nine holes one (red).

It can be noted that the fundamental resonance value of the nine holes AM (about 10 kHz) appears to be slightly lower than the expected one (*i.e.* the fundamental frequency calculated by equation (4.3) for the single hole). This effect can be explained by observing what happens into both the air channels and the surrounding plastic bulk material, when in-resonance condition is matched, i.e. *f*= 10 kHz:
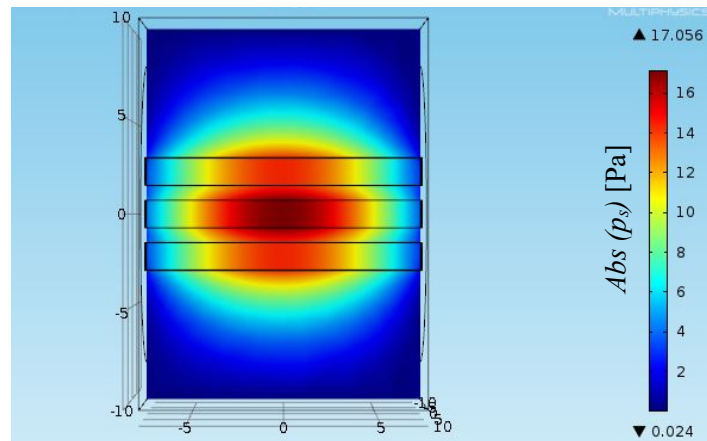
Figure 4.9: 2D view of the pressure amplitude into the nine holes AM for a frequency f=10 kHz.

Due to the presence of a stationary wave into the air channels, an exchange of acoustic energy between the holes seems to appear. This in turns causes the fundamental frequency f_1 to change slightly from what expected for the ideal single hole case.

It is also worth investigating the spatial behaviour of the pressure field once it has left the metamaterial surface. Figure 4.10 shows 2D slices of the pressure field amplitude at the outer side of the metamaterial for two fixed frequencies, corresponding to an in-resonance condition (Figure 4.10(a)) and to an off-resonance condition (Figure 4.10(b)). It can be seen that the energy is much more localised for the in-resonance condition, and this is an example of the so-called "focusing" effect that is one of the exciting features of such structures.
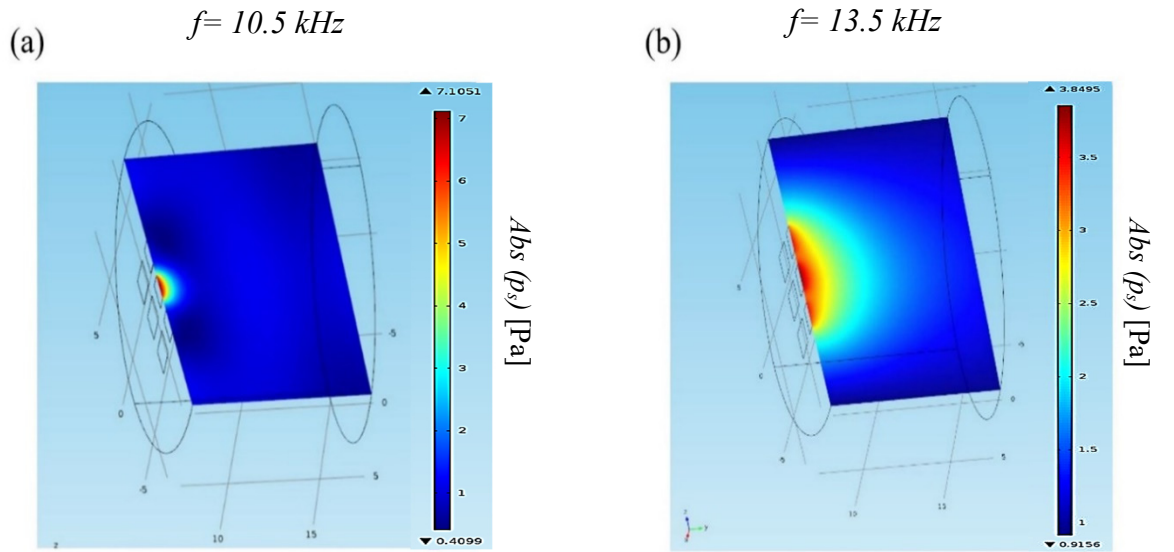
Figure 4.10: Retrieved acoustic field for a metamaterial with 9 holes when it is (a) in resonance and (b) off-resonance

The simple structures investigated give indications about the robustness and validity of the chosen FEM approach. This is because a good match between the expected resonance frequency pattern and their counterpart obtained by FEM has been observed. Focusing effects and shifts in the resonance frequency pattern have also be observed as a consequence of the metamaterial geometry.

4.3   Holey-structured acoustic metamaterial for subwavelength imaging

It was mentioned in Chapter 3 that the diffraction limit can be beaten by using metamaterial devices when the conditions for Fabry-Pèrot resonances occur. Section 4.2 demonstrates that Fabry-Pèrot conditions can be obtained by using a polymer as the bulk material from which the metamaterial structures are made. Thus, it should then be possible to realize an acoustic metamaterial device for sub-wavelength imaging purpose by 3D printing. The next section is focused on the preliminary FEM investigation of such an exotic device, designed as an array of 10 by 10 holes into a bulk of plastic material.

4.3.1. 10 x 10 holey acoustic metamaterials: preliminary analysis

An acoustic metamaterial device containing a 2D array of 10x10 squared-side holes has been engineered with the aim to be exploited for acoustic sub-wavelength imaging purposes. Figure 4.11 shows the device dimensions, with the thickness h chosen to be h=14.8 mm, whilst the squared-hole depth is s = 1.48 mm. The centre of each hole is separated from the other by a 2.96 mm gap, resulting in an overall AM width and length of 31.08 mm:
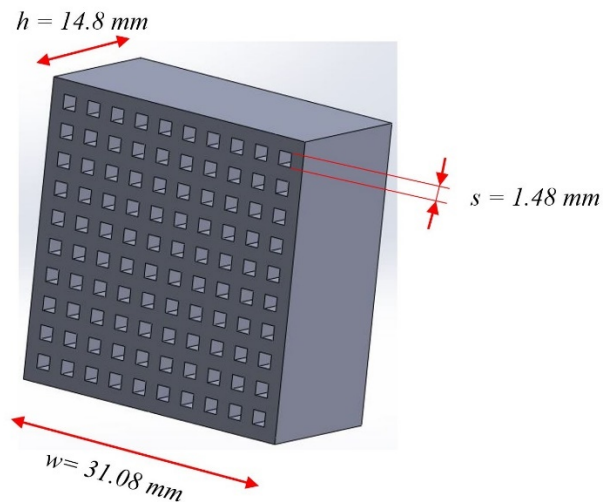
Figure 4.11: 10x10 holes AM design and dimensions. Thickness h = 14.8 mm; squared-hole side dimension s=14.8 mm; width w= 31.08.

As reported in section 4.2, Fabry-Pèrot resonances are expected for every integer multiple of the fundamental frequency f_1, which for a single hole would be 11.6 kHz for the chosen thickness. Interesting phenomena can be observed by looking at the two-dimensional spatial changes in acoustic pressure field at a fixed distance close to the outer metamaterial surface, for several different frequency values. It can be seen that resonant frequency, identified by the expected focussing effect, seems to be shifted toward lower frequency values (around 9-10 kHz) with respect to the theoretical prediction made for the single hole design. This fact suggests that a stronger acoustic energy exchange than the one observed for the material containing 9 holes has taken place. More complex spatial variations seemed to occur at other frequencies away from 9 kHz, with the energy spread across a wider spatial region.
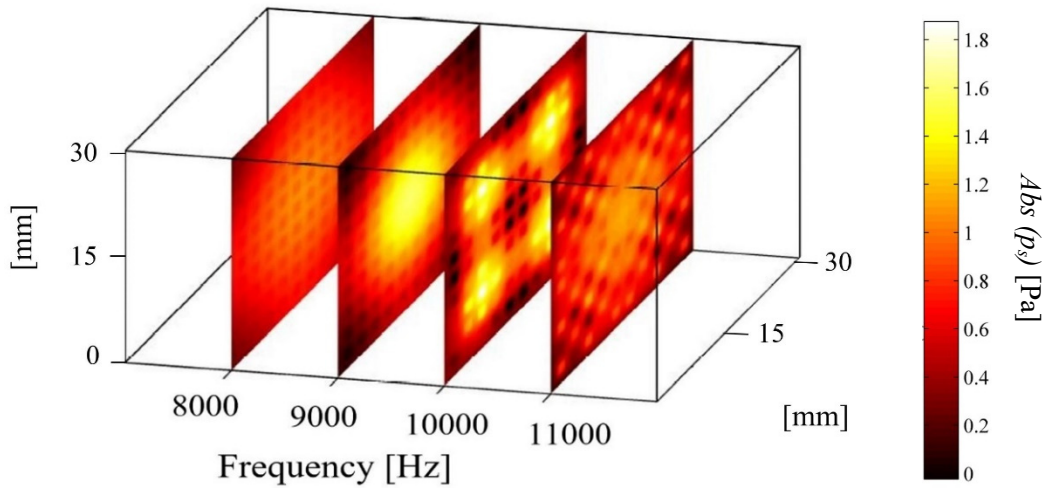
Figure 4.12: Retrieved pressure field absolute value at the outer metamaterial surface for several different frequency values.

When operated at 9 kHz, the predictions show that a collimation effect occurs, with the diameter of the highly localised energy region being maintained as the distance from the metamaterial outer surface increases. Figure 4.13 illustrates this collimation effect at 9 kHz for several different distances from the outer metamaterial surface:
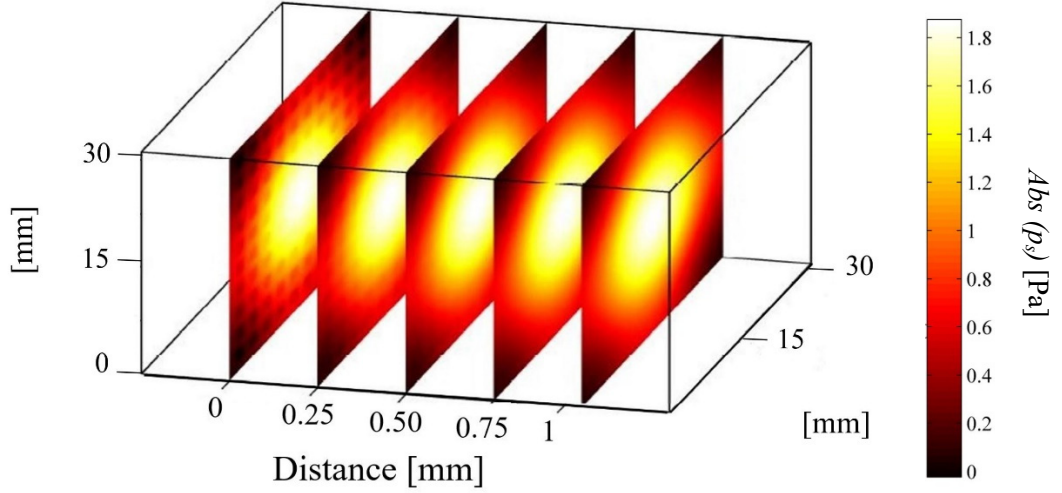
Figure 4.13: Collimation effect illustrated by plotting the spatial distribution of the resulting acoustic field at different distances from the outer metamaterial surface at the resonant frequency of 9 kHz.

The next subsection is focused on the use of this device for subwavelength imaging.

4.3.2. Sub-wavelength imaging FEM results

Chapter 3 described the importance of matching the Fabry-Pèrot condition for the extraordinary transmission properties of such holey metamaterials to arise. This is because the transmission coefficient T_c reaches unitary values when Fabry-Pèrot resonances appear. Mathematically, it means that for every f_k derived from equation (4.4) to which corresponds a specific resonance wavelength λ_R, the probability of the plane wave of parallel momentum $\vec{k}_\parallel = (k_x, k_y)$ to be transmitted to the outer surface of the metamaterial is expressed by the transmission coefficient t:

$$T_c(\lambda_R, \vec{k}_\parallel) = (-1)^k \tag{4.7}$$

From the considerations described in Chapter 3, super resolution effects should be expected whenever t reaches its maximum value of unity. Figure 4.14 shows the frequency behaviour

of the transmission coefficient T_c retrieved at the outer side of the 10x10 hole metamaterial when excited by a planar pressure field at various frequencies:
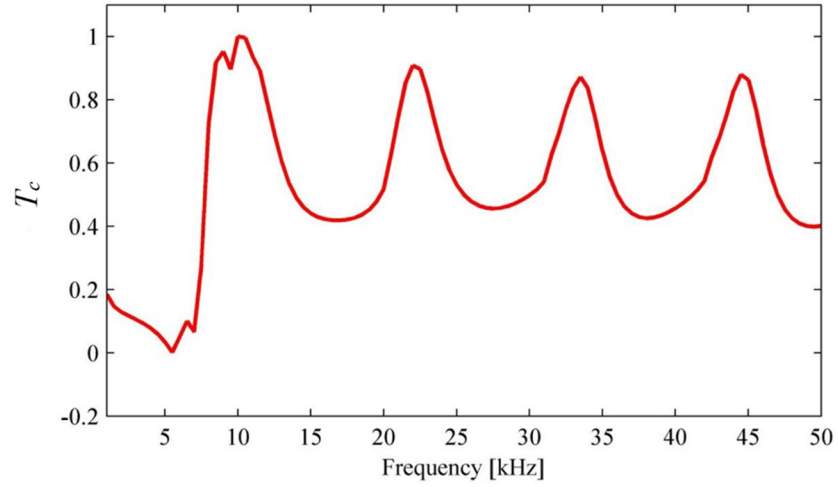
Figure 4.14: Transmission coefficient retrieved values for several different frequencies.

It can be seen that this device can successfully transfer all the wave vectors $\vec{k}_\parallel$ from the input to the output side for specific discrete set of frequencies. These frequencies are the ones related to the appearance of Fabry-Pèrot effects. Of utmost importance is to point out again that the above simulations indicate that a polymer material could be successfully used to produce a working device for sub-wavelength imaging purposes, theoretically up to the ultrasonic range if the structures were sufficiently small. Therefore, there is the need to demonstrate both numerically and experimentally that this kind of device can be successfully exploited for the imaging of a sub-wavelength dimension object.

The 10 x 10 holes design depicted earlier in Figure 4.11 has been used within an FEM simulation, aimed at illustrating the ability to image an object with sub-wavelength dimensions. The simulated sub-wavelength dimension object was an L-shaped aperture made in a thin aluminium slab. The L-shaped aperture (Figure 4.15) had both a width w and a length l of 20 mm, whilst its thickness d was chosen to be 3 mm. This object is assumed to be positioned at a distance of 2 mm from the input metamaterial surface (to the left), and excited with a planar pressure field at various frequencies. Note that for the expected first

value f_1 of the resonance frequency, i.e. about 9-11 kHz (see Figure 4.14), the dimensions of the L-shaped object are sub-wavelength. In particular, its thickness $d = 3$ mm is deeply sub-wavelength when compared to the wavelength λ in air at f_1, (31.18 mm). Moreover, the thickness dimension d almost coincides with hole centre-to-centre distance Λ, resulting in stretching the maximum achievable space resolution of an acoustic metamaterial to its limit [2].
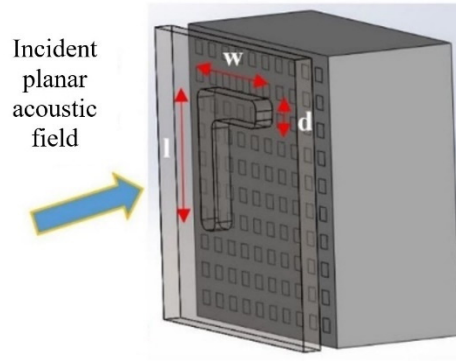
Figure 4.15: L-shaped aperture with dimension l = 20 mm; w = 20 mm; d = 3 mm, positioned with a 2 mm gap from the metamaterial surface.

Simulation results are shown in Figure 4.16, where the retrieved pressure field amplitude at the outer metamaterial side has been plotted for several different distances from the outer surface of the metamaterial, for a frequency of 10 kHz:
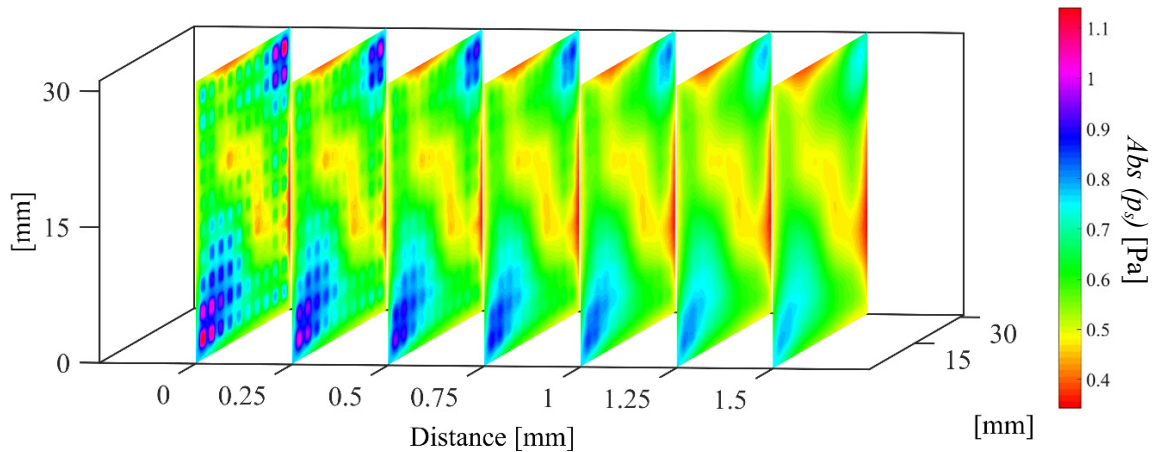
Figure 4.16: FEM results at several distances from the metamaterial surface, frequency 10 kHz.

The results show clearly that the L-shaped sub-wavelength object can be successfully imaged by exploiting such a metamaterial. In particular, the dimensions of the imaged object were about a tenth of the corresponding wavelength in air at the analysed frequency.

4.4   Space-channelled structures

As said, FEM simulations are a powerful method to simulate the behaviour of unexplored designs under controlled circumstances. Once proven that the chosen FEM method, here in the form of Acoustic Pressure Frequency Domain analysis, gives both expected and consistent results, very exotic and innovative structures can be tested. A class of such exotic materials is represented by the so called "Space coiling acoustic material", in which spiral paths within a bulk material lead to focusing effects and the possibility of negative refraction properties ($\eta_{EFF} < 0$) [5]–[7]. Starting from this assumption, a channelled structure named for simplicity "spiral" has been designed. Figure 4.17 shows the spiral design and dimension, as well as the geometry followed by the channels into the bulk of the simulated plastic material:
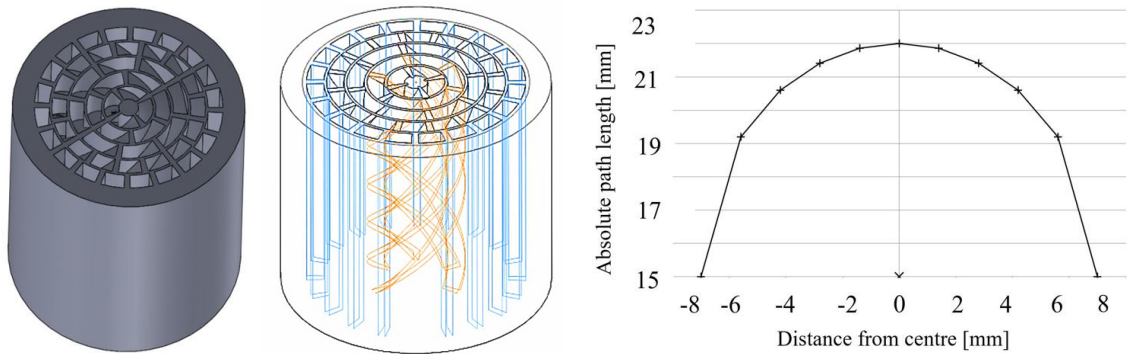
Figure 4.17: "Spiral" metamaterial design and geometry followed by channels at two different path lengths with radius. The absolute path length of each channel in [mm] is also reported.

It can be seen that total length of each channel increases as one moves from the outer circumference of the spiral toward the inner one. The idea is that the difference in the path length of the channels could lead to a focusing of the flat acoustic pressure field at the outer

side of the spiral. This in principle can be valid if the sample is excited with wavelength comparable to squared-hole side dimension. Conversely, acoustic metamaterials exhibit their extraordinary properties when excited with a wavelength much larger than the side dimensions of their artificial structure. Moreover, two other expected effects can lead to an exotic manipulation of the acoustic pressure field impinging on the sample. The first one is that different path length lead to different Fabry-Pèrot resonance frequencies, which can be calculated again by solving equation (4.3) and equation (4.4). In addition, as explored for the planar holey metamaterials above, the exchange of acoustic energy between adjacent holes can lead to novel and unexplored global phenomena.

The sample has been studied by excitation with a plane wave whose frequency varies across the range 1-35 kHz. The transmission coefficient T_c for the design is shown in Figure 4.18:
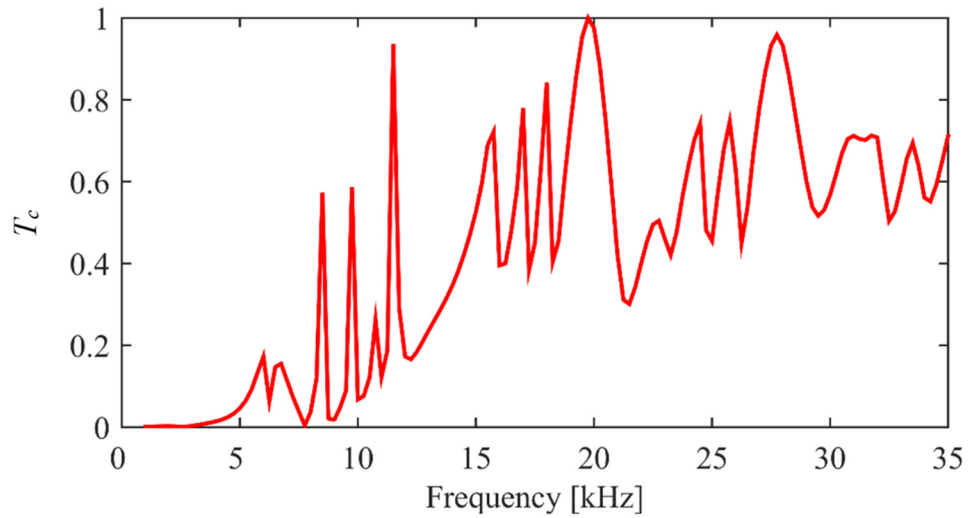
Figure 4.18: Transmission coefficient T_c for the spiral design at various frequencies.

This result suggests that there are complex phenomena occurring which could lead to the formation of several spectral peaks in the observed transmission coefficient. Thus, this spiral design behaviour cannot be modelled by means of the fundamental set of equations that forecast the frequency peak position of the Fabry-Pèrot effect. However, interesting phenomena can be observed by analysing the 2D data of the retrieved pressure field just

above the outer (exit) surface of this design. Figure 4.19 shows a 2D image of the retrieved pressure plane for a frequency of 9.25 kHz, which corresponds to one of the peaks of the retrieved transmission coefficient T_c (see Figure 4.18):
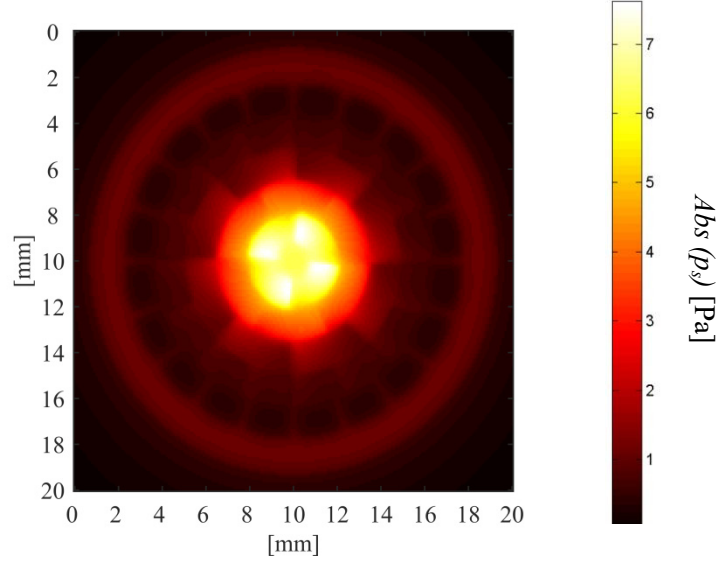
Figure 4.19: 2D pressure field retrieved at the outer side of the spiral at f= 9250 Hz.

It seems that a focusing of the pressure field occurs. In standard optics or acoustics, the focal distance (*i.e.* the distance from the outer surface of a lens at which the focusing effect occurs) can be calculated by means of ray geometry or other common trigonometric approaches. However, this design shows dimensions of the channels that are much smaller than the wavelength. This, as mentioned earlier, causes exotic effects to occur. Thus, the focal point cannot be forecast by means of standard approaches.

Figure 4.20 shows the spatial behaviour of the acoustic beam by exploiting a series of 2D images of the retrieved pressure plotted for several distances from the outer surface:
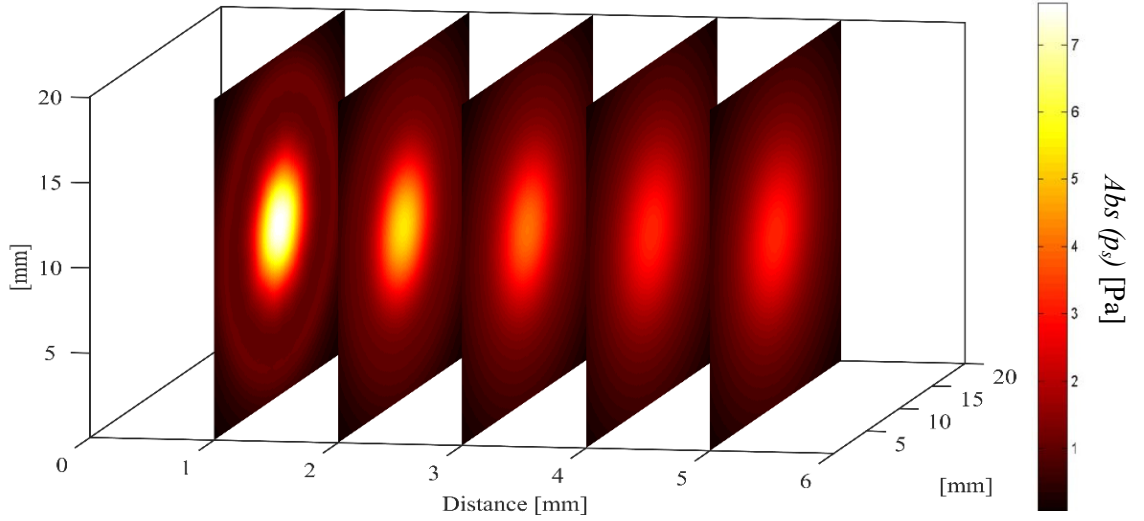
Figure 4.20: Acoustic pressure field behaviour at several distances from the spiral outer surface.

This suggests that the focal point can be estimated to occur at distance of about 1 mm from the outer surface of the metamaterial. It can be seen from the literature that a plane wave impinging on a circular aperture results in a diffracted pressure field that can be described by Airy model [7]. In particular, the acoustic pressure field amplitude at different angles $I(\theta)$ from the axis of the aperture parallel to the impinging k wave-vector of the plane wave it is analytically represent by a Bessel's function of the first order J_1 [9]:

$$I(\theta) = I_0 * \left(\frac{2J_1(k_n a \, sin\theta)}{k_n a \, sin\theta} \right)^2 \qquad (4.8)$$

where I_0 is the intensity of the acoustic pressure at $\theta = 0°$, $k_n = \frac{2\pi}{\lambda}$ is the wavenumber, a is the radius of the aperture. By following this approach, a fit of the retrieved 1D pressure along the central point of the spiral with the analytic function of equation (4.8) has been performed. Figure 4.21 shows the obtained FEM pressure amplitude and the corresponding data fit obtained by exploiting non-linear curve fitting in least-square sense:
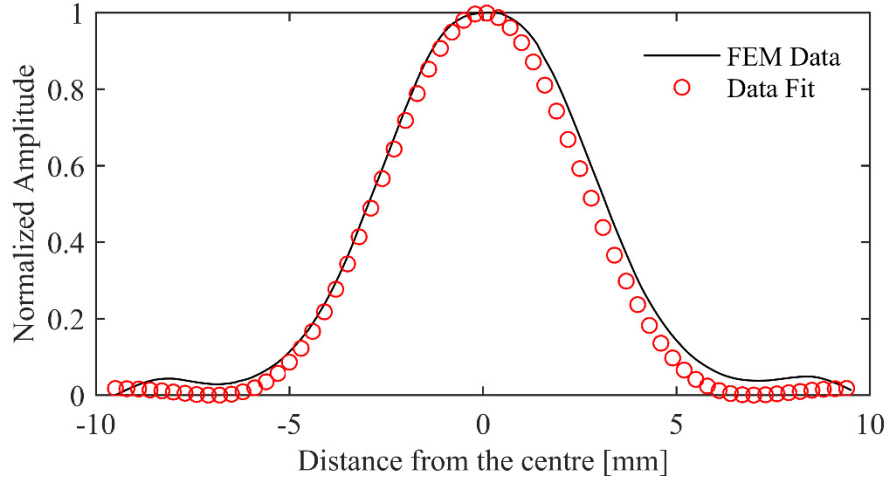
Figure 4.21: 1D pressure field along the centre of the spiral FEM data (black) and data fit (red) by Airy model.

The results show that FEM method data fits very well with the adopted model. Thus, an estimation of the focal spot diameter can be obtained by taking into account the full-width at half of the maximum value *FWHM* for the data fit curve [10]. The obtained *FWMH* is equal to 5.6 mm. At the chosen frequency *f=9250* Hz corresponds a wavelength λ of 37.08 mm in air. Therefore, the ratio between them is:

$$\frac{\lambda}{FWMH} \approx 6.62 \tag{4.9}$$

and this is approximately maintained for all the inspected distances.

4.5   Additional FEM results for wider bandwidth devices

It has been shown in the previous sections by FEM that polymer holey metamaterials containing a regular array of square holes can theoretically being exploited to successfully imaging an object having sub-wavelength dimensions. In addition, it has been observed that an exotic and unexplored design as the "spiral" leads to a focusing effect. However, those extraordinary effects appear for a specific set of frequencies or for a very narrow band around these. In particular, the planar materials described above, used for sub-wavelength imaging

purposes, shows these effects for the frequency pattern related to the appearance of Fabry-Pèrot resonance, *i.e.* when transmission coefficient *t* reaches unitary value. In order to exploit such materials in real applications, there is the need to broaden the frequency range into which the transmission coefficient of a given metamaterial is unitary. In this way, chirp and coded waveforms properties could be exploited together with the metamaterial to give a much wider range of applications. However, this is not an easy task to be faced. In fact, it should be clear now to the reader that the extraordinary transmission properties are strictly related to the thickness *t* of the material in such designs.

A first attempt to broaden the working frequency range can be done by realizing a device in such a way that it contains holes with different path length. By referring again to Figure 4.6, a device designed in such a way should shows different pattern of resonances. In principle, this effects should have been observed for the "spiral" design, but the transmission coefficient value is not only influenced by the resonance of each channel but also from extraordinary phenomena of acoustic energy exchange among the holes. One possible approach is to change the shape of the holes. Figure 4.22 shows the pressure amplitude results obtained for a single hole metamaterial having the same dimensions of the device described in Figure 4.3, for both a squared-sided hole and a circular-shaped hole of comparable side and radial dimensions respectively. It can be seen that the hole shape does not give a broadening on the expected resonance peak.
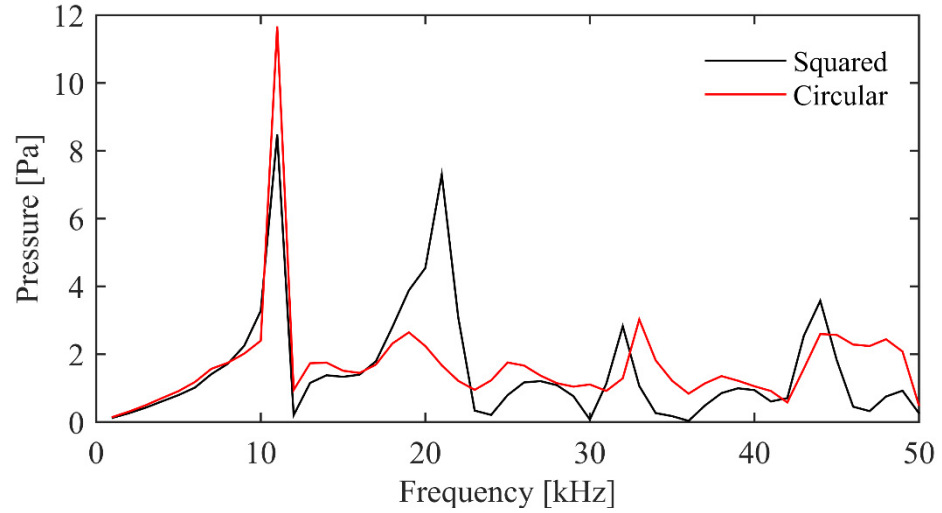
Figure 4.22: Pressure amplitude at the outer surface of a single hole metamaterial for both a squared-sided (black) and a circular (red) hole.

A more complicated approach has thus been investigated. As described in Chapter 3, coded signals show a broad-band frequency spectrum. These signals, such as Golay sequences, Maximum Length Sequences and Legendre sequences, are obtained from a seed (or a pair of two seeds sequences) made of a codified succession of "1" and "-1". This coded numerical series provides the broad-band frequency characteristics to those signals. By referring to the invariance of the mathematical properties described in [11]–[14], a 100 samples Legendre sequence has been produced and transformed into a 10 row by 10 row matrix. Therefore, a metamaterial having thickness h and squared-hole side dimension s equal to the one utilised for imaging purpose (see Figure 4.11) and hole centre-to-centre distance $\Lambda = 2.22$ mm has been designed, by placing a hole only where Legendre sequence matrix show value "1" . This complicated design can be more easily understood by looking at Figure 4.23:
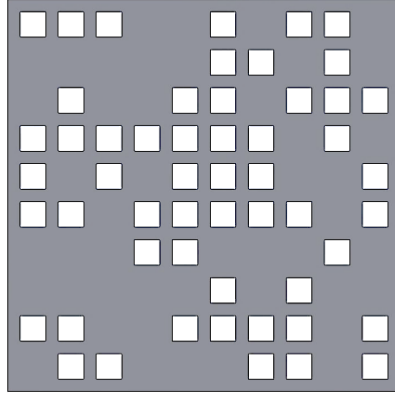
Figure 4.23: Acoustic metamaterial obtained by means of a Legendre sequence 2D array.

The transmission coefficient T_c can be obtained for the frequency range under interest, as shown in Figure 4.24:
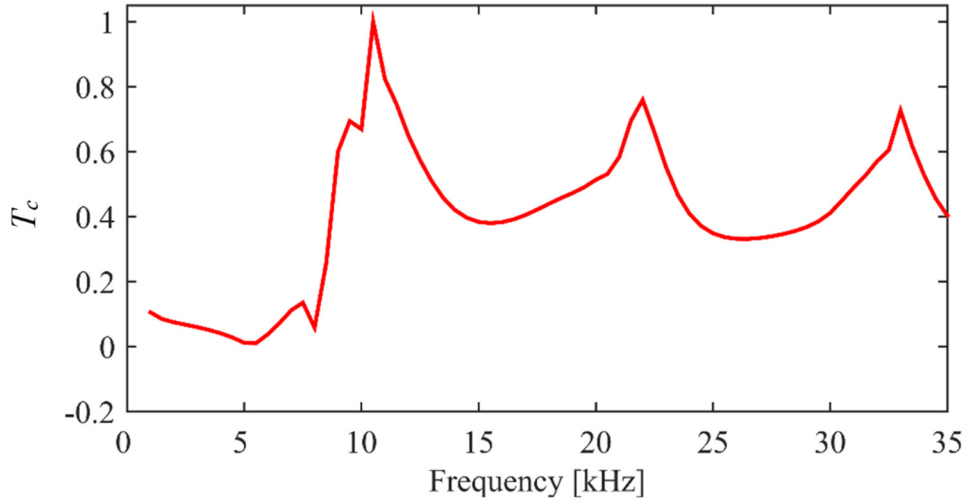
Figure 4.23: transmission coefficient for the Legendre 10x10 holes AM design.

It can be seen that the frequency values at which the transmission coefficient T_c shows unitary values is that expected for this thickness of metamaterial. However, the peaks are not as sharp as those from a regular array of square holes, indicating that some extension of available bandwidth has occurred.

4.6   Conclusions

FEM simulation has been used to predict the exotic effects provided by acoustic metamaterial designs. In particular, Acoustic Frequency Domain Analysis in COMSOL has

been selected as FE inspection method. The FEM results of simple AM structures matched the analytical predicted ones. Thus, it has been demonstrated that FE chosen method can be successfully exploited to predict the behaviour of complex acoustic metamaterial structures.

FEM results shows that a 10 by 10 holes AM design realized by means of a polymer material can be used for imaging an object having sub-wavelength dimensions into the high audible frequency and the ultrasonic range. An exotic design made of plastic cylinder containing different path lengths of the channels produced a focusing spot dimension of the acoustic field which was much smaller than the wavelength. Finally, a very innovative design of acoustic metamaterial in which the hole positions are codified by a Legendre matrix has been proposed, and has been shown to modify the response further.

References

[1]   S. Marburg, "Six boundary elements per wavelength: is that enough?." *Journal of Computational Acoustics*, pp- 25-51, 2002.

[2]   J. Zhu, J. Christensen, J. Jung, and L. Martin-Moreno, "A holey-structured metamaterial for acoustic deep-subwavelength imaging," *Nat. Phys.*, vol. 7, no. 1, pp. 52–55, 2011.

[3]   J. Christensen, "Theory of Resonant Acoustic Transmission through Subwavelength Apertures," *Phys. Rev. Lett.*, vol. 101, no. 1, p. 14301, 2008.

[4]   S. Laureti, L. A. J. Davis, M. Ricci, and D. A. Hutchins, "The study of broadband acoustic metamaterials in air," in *Ultrasonics Symposium (IUS), 2014 IEEE International*, 2014, pp. 1344–1347.

[5]   Z. Liang and J. Li, "Extreme acoustic metamaterial by coiling up space," *Phys. Rev. Lett.*, vol. 108, no. 11, 2012.

[6]   Z. Liang, T. Feng, S. Lok, F. Liu, K. B. Ng, C. H. Chan, J. Wang, S. Han, S. Lee, and J. Li, "Space-coiling metamaterials with double negativity and conical dispersion.,"

Sci. Rep., vol. 3, p. 1614, 2013.

[7]   Y. Xie, A. Konneker, B. I. Popa, and S. A. Cummer, "Tapered labyrinthine acoustic metamaterials for broadband impedance matching," *Appl. Phys. Lett.*, vol. 103, no. 20, 2013.

[8]   G. B. Airy, "On the Diffraction of an Object-glass with a Circular Aperture," *Trans. Cambridge Philos. Soc.*, vol. 5, pp. 283–291, 1834.

[9]   J. C. Wyant and K. Creath, *Basic wavefront aberration theory for optical metrology*, vol. Xl. 1992.

[10] M. Molerón, M. Serra-Garcia, and C. Daraio, "Acoustic Fresnel lenses with extraordinary transmission," *Appl. Phys. Lett.*, 2014.

[11] S. K. Barber, E. D. Anderson, R. Cambie, W. R. McKinney, P. Z. Takacs, J. C. Stover, D. L. Voronov, and V. V. Yashchuk, "Binary pseudo-random gratings and arrays for calibration of modulation transfer functions of surface profilometers," *Nucl. Instruments Methods Phys. Res. Sect. A Accel. Spectrometers, Detect. Assoc. Equip.*, vol. 616, no. 2–3, pp. 172–182, 2010.

[12] F. J. MacWilliams and N. J. A. Sloane, "Pseudo-random sequences and arrays," *Proc. IEEE*, vol. 64, no. 12, pp. 1715–1729, 1976.

[13] D. Calabro and J. K. Wolf, "On the synthesis of two-dimensional arrays with desirable correlation properties," *Inf. Control*, vol. 11, no. 5–6, pp. 537–560, 1967.

[14] P. D'Antonio and H. Konnert, John, "The reflection phase grating diffusor: Design theory and application," *J. Audio Eng. Soc.*, vol. 32, no. 4, pp. 228–238, 1984.

CHAPTER 5: Experimental measurement of acoustic metamaterials using pulse compression

5.1   Introduction

It was observed in Chapter 4 that holey-structured acoustic metamaterials realized using a polymer substrate can lead to exotic effects. This has been demonstrated by means of a series of Finite Element (FE) simulations. In particular, starting from a simple acoustic metamaterial design where a single hole was realized in a bulk of plastic material. It has been shown that Fabry-Pèrot resonances result with frequency characteristics that are related to the acoustic metamaterial thickness. This demonstrated that the FE method used was a reliable tool, and that it could thus be used to investigate more complicated acoustic metamaterial designs. Further simulations showed that acoustic metamaterials could potentially be used to focus the acoustic beam and image an object with sub-wavelength dimensions.

Using these simulation results, several different acoustic metamaterials devices, each having specific hole dimensions and thickness, have been realized by means of additive manufacturing. Examples of the devices manufactured in this way are shown in Figure 5.1:
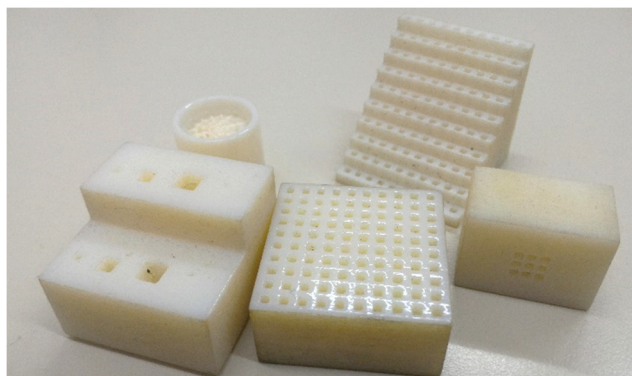
Figure 5.1: Examples of acoustic metamaterial devices realized by additive manufacturing.

The composition of the polymeric material used for 3D printing the metamaterials is a form of polymethyl methacrylate (PMMA) plastic material. The important parameter is the acoustic impedance. The density and sound velocity for this material have been measured to be $\rho_{polymer} = 1{,}190$ kg.m^{-3} and $v_{polymer} = 2{,}200$ ms^{-1} respectively. This leads to an Acoustic Impedance $Z_{polymer}$ that is much greater than that of air, thus meaning that the sound field will be localised within the holes, with little energy entering the solid material (an assumption made in the FE simulations). There is now a need to demonstrate experimentally that these devices match the numerically predicted results. Thus, this chapter is focused on the experimentally activities carried out to demonstrate that acoustic metamaterial can be exploited in real applications. The acoustic metamaterial design geometry is specified for each set of results reported in the sections to follow.

5.2   Limitations and issues

It was shown in Chapter 4 that FE simulation results rely on the correct choice of the modelling conditions, *e.g.* a perfectly-matched domain surrounding the material (so as to avoid acoustic energy unwanted reflections), plane wave excitation, and mesh element dimensions that are sufficiently small. Whenever these parameters are selected and fixed, the ability to solve complex 2D or 3D problems is then limited by the available computational power. In particular, two main hardware specifications limit the capabilities of FE: (i) CPU clock frequency and (ii) available RAM. While the CPU clock frequency only influences the computational simulation time, the available RAM bounds the maximum complexity of the geometrical model that can be simulated and solved. Therefore, there is no theoretical limit on the complexity of a FE model that can be solved since the computational power can be increased by literally just adding RAM gigabytes.

Conversely, experimental activities face issues that sometime cannot be overcome by only buying new equipment. The reason why is simple: tools and equipment with the necessary features, precision and characteristics may not exist.

It can be found in literature [1]–[3] that the experimental study of acoustic metamaterials have been carried out mainly within the low audible frequency range. In particular, this range has been chosen historically for the experimental realization of holey structured acoustic metamaterials and flat acoustic lenses, and the subsequent 3D characterization of their exotic effects. This is because the lateral dimensions of the holes or any other artificial structures within a metamaterial design will be a minimum of 10 mm at frequencies in the low audible range, and sometimes much larger. Therefore, a woofer and a small microphone can be successfully exploited to both excite and to characterize the exotic effects of the investigated metamaterials. However, the objectives of the present research was to

(i)   Realize a polymeric acoustic metamaterial device;

(ii)   Demonstrate that it can be successfully exploited for sub-wavelength imaging at as high a frequency as possible;

(iii)   Use this device in combination with chirp signals. If frequencies are to be used that are much greater than those studied in [1-3] then the hole sizes have to reduce accordingly.

The FE simulations carried out in Chapter 4 have shown that for operation in the middle audible – low ultrasonic frequency range, the dimensions of the artificial structures (hole dimensions and centre-to-centre distance) have to be in the order of millimetres. In addition, a "spiral" acoustic metamaterial design was shown numerically to produce a focusing effect, where again the dimensions of the "spiral" channel would have to be in the order of millimetres. The work presented below is intended to characterize the resonance

spectra of such polymeric acoustic metamaterial designs, to retrieve the 3D characteristic of the acoustic beam at the outer side of the acoustic metamaterial and to provide an experimental demonstration of sub-wavelength imaging.

In order to investigate these aims, two different experimental setups have been exploited. Their features, characteristics and details are shown in the next section.

5.3   Experimental Setups

It was essential that a broadband acoustic source and a broadband receiver were used for characterization of the acoustic metamaterials. Moreover, their frequency response should be as flat as possible into the exploited frequency range, namely the middle audible to low ultrasound frequency range. Two different experimental setups have been exploited, so as to characterize the acoustic response of the metamaterial designs and to understand the effect of the acoustic metamaterial on an incident pressure field. One used a laser vibrometer to measure vibrations at the metamaterial surface, whereas a Micro Electro-Mechanical Systems (MEMS) microphone was used to plot the emitted 3D pressure field. Both setups relied on the use of a ribbon acoustic tweeter as source for the acoustic pressure field. This acoustic source was able to provide a very flat spectrum acoustic excitation over a 10-60 kHz frequency range. The signal used to drive the source in both experiments was a linear chirp, having different time-frequency characteristics for each investigated acoustic metamaterial. The characteristics of both setups are specified in the next subsections.

5.3.1. Laser vibrometer and reflective membrane measurement at the metamaterial surface

The idea behind this arrangement was that resonances within the air-filled channels of the acoustic metamaterial could be observed by looking at the vibration of a thin reflective membrane glued onto the metamaterial surface. The reflective membrane used was a 5 μm

thick Mylar membrane, with a nm thick metal coating on one side, which was glued onto the surface of the acoustic metamaterial from which the field was to be emitted. The acoustic field emanating from individual holes within the metamaterial were retrieved by monitoring the vibrations of this membrane using a Polytec OFV-505 laser vibrometer. The laser beam was focused on the holes and the vibrations were recorded using a Tektronic DPO 3012 oscilloscope. A Fountek Neocd2.0 Ribbon acoustic transducer was used as acoustic/ultrasonic source in order to generate a flat pressure field impinging on the metamaterial samples (see Appendix for further details). The input signal, i.e. chirp signal, was loaded into an Agilent 33120A arbitrary waveform Generator and it has been amplified by a Yamaha XP1000 amplifier. A sketch of the experimental setup is depicted in Figure 5.2:
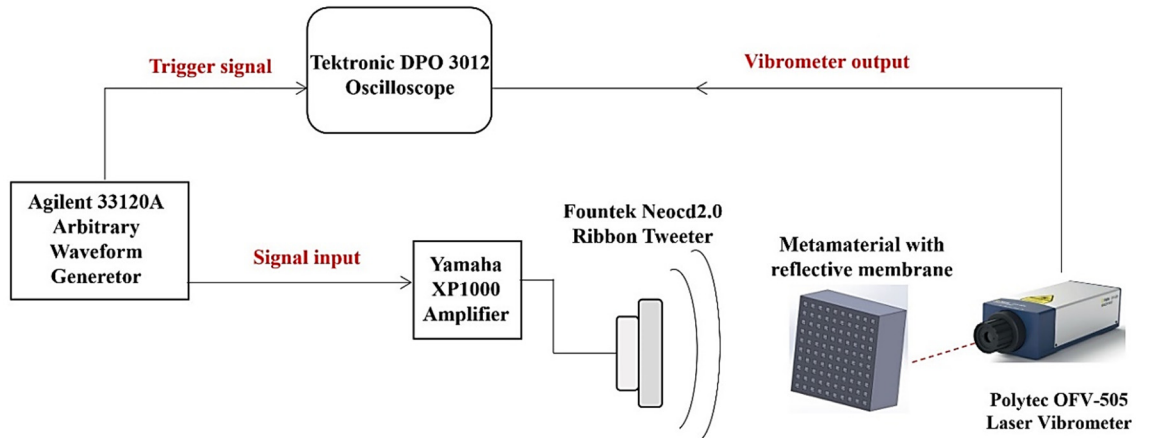
Figure 5.2: Laser vibrometer experimental setup sketch.

For the sake of clarity, Figure 5.3 shows a picture of the laser vibrometer experimental setup, where the Mylar membrane glued onto the metamaterial surface it is clearly visible, as well as the laser spot and the ribbon tweeter. The laser vibrometer had a frequency range that extended up to 24 MHz, well beyond that needed for the measurement. The signal was recorded at 8 bits, and at sampling rates of up to 10 Msamples/sec, resulting in a good frequency characterization of the acoustic metamaterial.
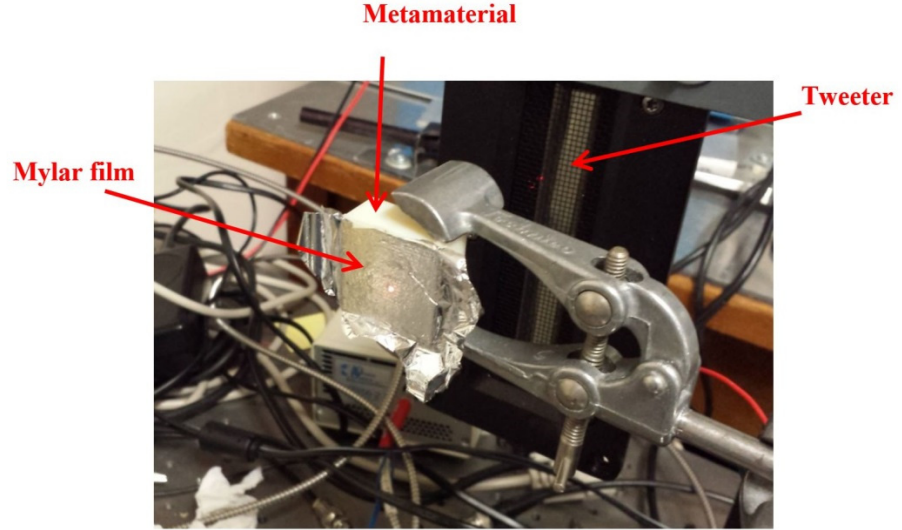
Figure 5.3: a picture of the laser vibrometer experimental setup.

It should be noted that the measured resonances are related to the movement of the thin membrane glued onto the metamaterial surface. As this membrane is restricted by being glued to the surface, its motion over a particular hole will depend on both this and its own stiffness. This in turn could affect the measurement of the resonant frequency of the hole. Nevertheless, this setup still represents a robust method to corroborate the numerical prediction over simple metamaterial structures by measuring the resonant frequency of individual holes.

5.3.2. MEMS setup for scanning the radiated acoustic field

In order to scan the acoustic field variations emitted by the acoustic metamaterial, there was a need to find a small-enough microphone, sensitive over the frequency range of interest, which could be scanned in a 3D volume. This choice was challenging for several reasons. In particular, the frequency sensitivity required ranged from the audible to ultrasonic frequencies, resulting in an overlap between the usual commercial receiver spectral characteristics. Furthermore, the dimensions of the desired device should be ideally comparable or smaller than the lateral dimension of the holes within the metamaterial, thus

avoiding spatial averaging of the acquired pressure field. It followed that a good choice was a Micro Electro-Mechanical Systems (MEMS) microphone.

The chosen model was a Knowles SPM0404HE5H-T MEMS acoustic microphone having a sensitive circular area diameter of 0.25 mm and working nominal frequency band 1-10 kHz (see Appendix for further details). However, the device showed sensitivity up to 25-30 kHz. The drawback of using such a small device MEMS is that its sensitivity is not very high, leading to noisy measurements, and moreover its spectrum is not flat in the frequency region of interest. A photograph of the MEMS microphone is shown in Figure 5.4:
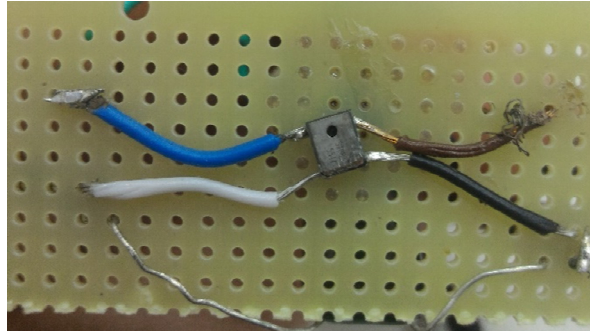
Figure 5.4: a photograph of the MEMS device used.

Figure 5.5 (b) shows the frequency response of this device to a linear chirp excitation from 3 kHz to 25 kHz (Figure 5.5 (a)). A resonance frequency around 15 kHz is evident. Therefore, it was necessary to normalise all the results acquired by the MEMS microphone using its known frequency response.
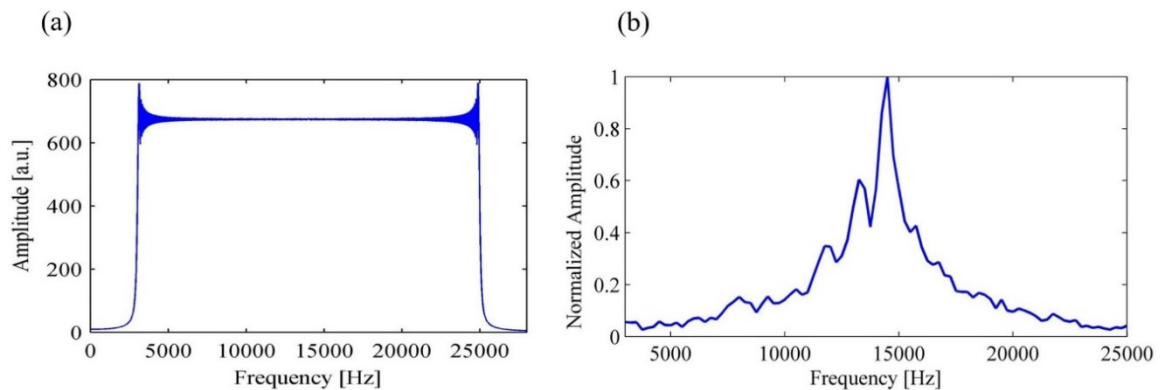
Figure 5.5: Sent chirp frequency spectrum (a) and MEMS normalized frequency response (b).

A 3D -motorized scanning stage moved the microphone to measure the pressure field across 2D planes perpendicular to the acoustic propagation axis at the far side of each investigated metamaterial device. A schematic diagram of the experimental setup is depicted in Figure 5.6. The signal acquisition/generation was managed by a National Instrument 6259 board. The ribbon tweeter used for the acoustic generation was a Monacor RBT 20 (see Appendix for further details), together with a STA-225 broadband amplifierA waveguide, whose inner surfaces were covered with an absorbing acoustic foam layer, was used in order to make the acoustic pressure field as flat as possible.
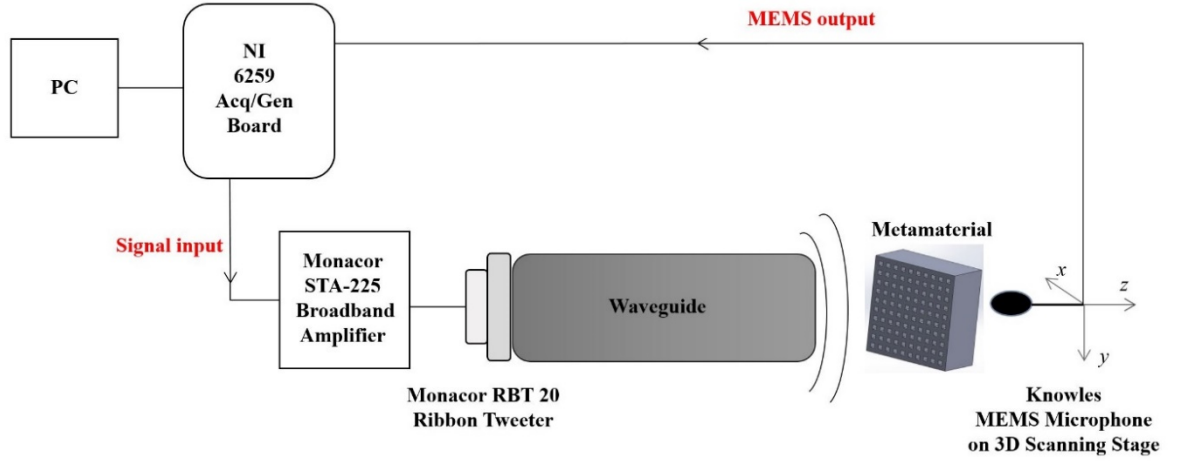
Figure 5.6: MEMS microphone experimental setup sketch.

The next sections report the experimental results achieved by using both the above described experimental setups. For each investigated acoustic metamaterial, the experimental setup used will be mentioned, e.g. laser vibrometer or MEMS microphone setup.

5.4   Preliminary experimental results

5.4.1. Acoustic metamaterials with various hole sizes and thicknesses

In order to further corroborate the FEM predictions made on several simple metamaterials designs, devices having four different square-side hole sizes and two different

thicknesses have been realized by means of 3D printing. In particular, the hole side dimension s were 4.44 mm, 2.96 mm, 1.48 mm and 0.74 mm (referred to the following as hole numbers 1, 2, 3 and 4 respectively) within two different device thicknesses of $h_1 = 19.8$ mm and $h_2 = 14.8$ mm. Figure 5.7 shows a photograph of the metamaterial sample.
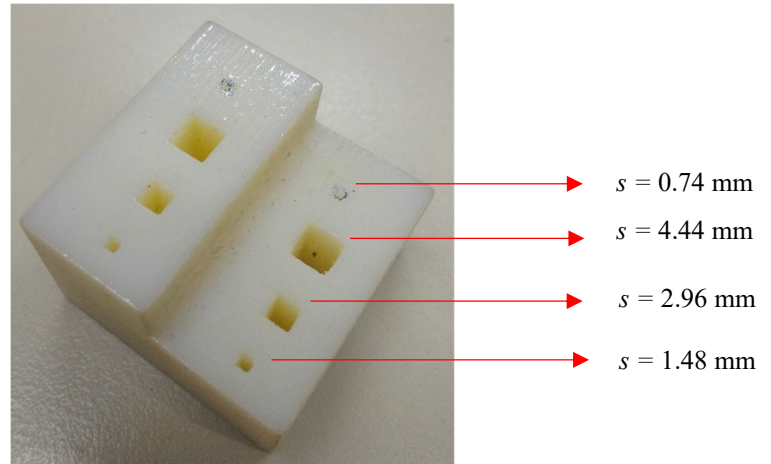
Figure 5.7 Acoustic metamaterial devices with two different thicknesses, each having square holes of different lateral dimensions.

Following the discussion of Chapter 4, the two sample thicknesses are predicted to have fundamental resonant frequencies of about $f_{h_1} = 11.6$ kHz and $f_{h_2} = 8.7$ kHz respectively, with harmonics at every integer multiple of these values. Please note that the sound velocity in air has been assumed to be 343 ms^{-1}, and this reference value will be used for any other theoretical calculation given in this Chapter. This device has been investigated by exploiting the laser vibrometer setup (Section 5.3.1). The input signal was a linear chirp across the frequency range of 1-100 kHz with time duration of 100 ms. The comparison between the frequency spectrum of the input signal from the ribbon tweeter and that measured by the vibrometer at hole number 3 and thickness h_2 is shown in Figure 5.8:
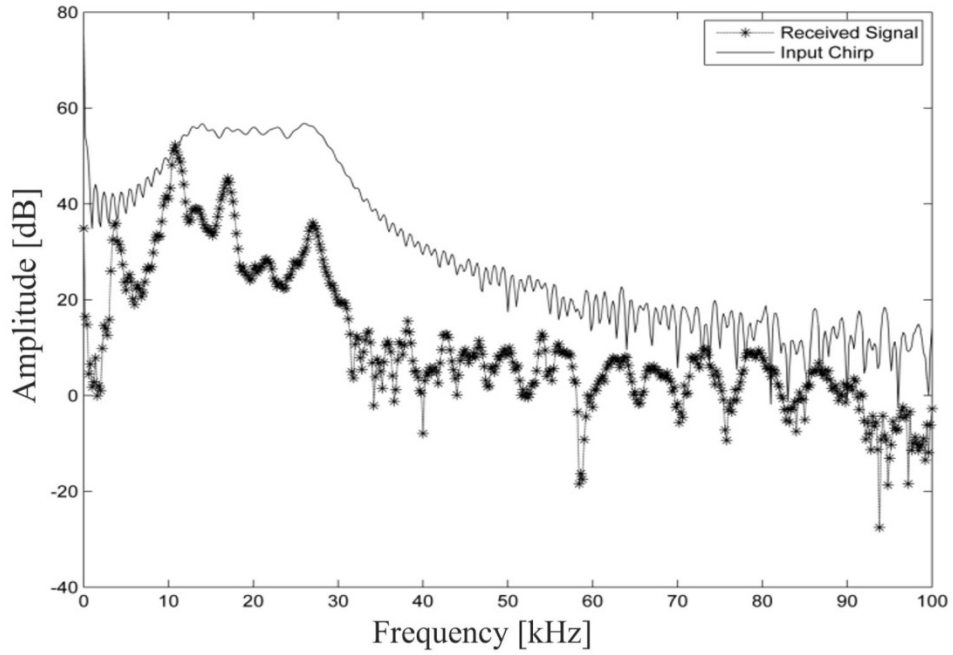
Figure 5.8: Input chirp and received signal spectrum on hole number 3 and thickness h2, in dB.

It can be seen that first resonant peakappears at the expected frequency, *i.e.* at about 11 kHz.

Please note that, although the excitation frequency range was 1-100 kHz, the combination

of source and amplifier used limits the maximum achievable frequency value to about 50-

60 kHz.

Figure 5.9 shows the results achieved by exciting the sample with the same excitation

signal, for all the combinations of side dimension and thicknesses into the frequency range

1-60 kHz. As predicted by the simulations, an increase in sample thicknesses caused a shift

of the expected Fabry-Pèrot resonances towards lower frequencies. Moreover, it can be seen

that the use of a smaller hole side dimension led to an increased number of resonant peaks,

as predicted by FEM simulations.
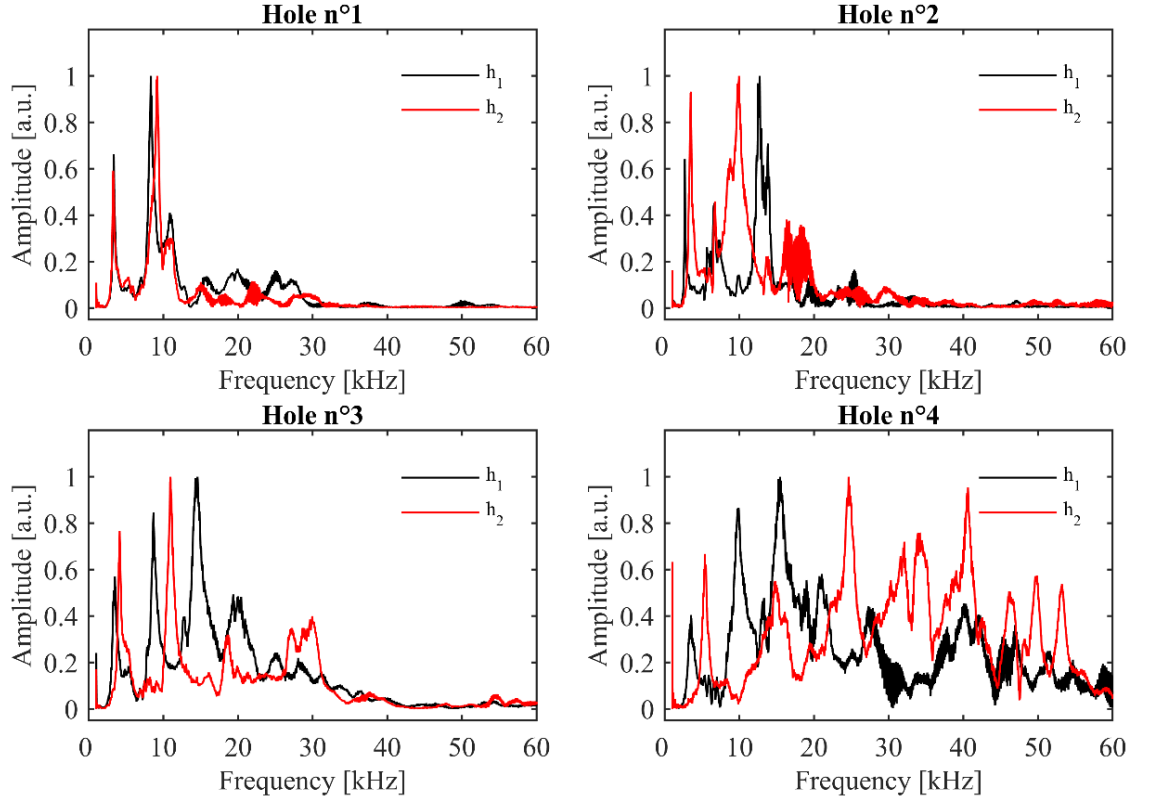
Figure 5.9: Laser vibrometer outputs for different metamaterial thicknesses (h_1 = 19.8 mm and h_2 = 14.8 mm) and hole lateral dimensions (n°1 = 4.44 mm, n°2 = 2.96 mm, n°3 = 1.48 mm and n°4 = 0.74 mm).

5.4.2. An acoustic metamaterial containing 9 holes (3 x 3)

An acoustic metamaterial having 9 holes (3 x 3) has been realized by 3D printing. The dimensions of this device are exactly the same of the one that was investigated numerically in Chapter 4, *i.e.* a thickness h = 14. 8 mm, holes dimension s = 1.48 mm and a hole centre-to-centre distance of Λ = 2.22 mm. Again, for this thickness the resonances are expected for every integer multiple of f_1 =11.587 kHz. Figure 5.10 is a photograph of this device containing 9 holes. This device was investigated by exploiting the MEMS experimental setup (as for Section 5.3.2), where 2D scans of the acoustic field at several different distances from the metamaterial outer surface have been acquired and imaged. The chirp signal had a frequency range of 3-25 kHz and a time duration of 0.5 seconds.
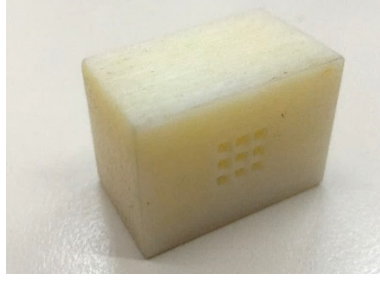
Figure 5.10: 9 by 9 holes acoustic metamaterial device.

Figures 5.11 and 5.12 show a series of 2D acoustic fields acquired at several different distances z from the outer acoustic metamaterial surface. These 2D slices have been plotted for two different frequencies - Figure 5.11 refers to a frequency f = 10.5 kHz, whilst Figure 5.12 refers to a frequency of f = 18.0 kHz. The CZT algorithm has been used to enhance the precision of the frequency analysis [4]. The red squares on both the figures represent ideally the position of the holes:
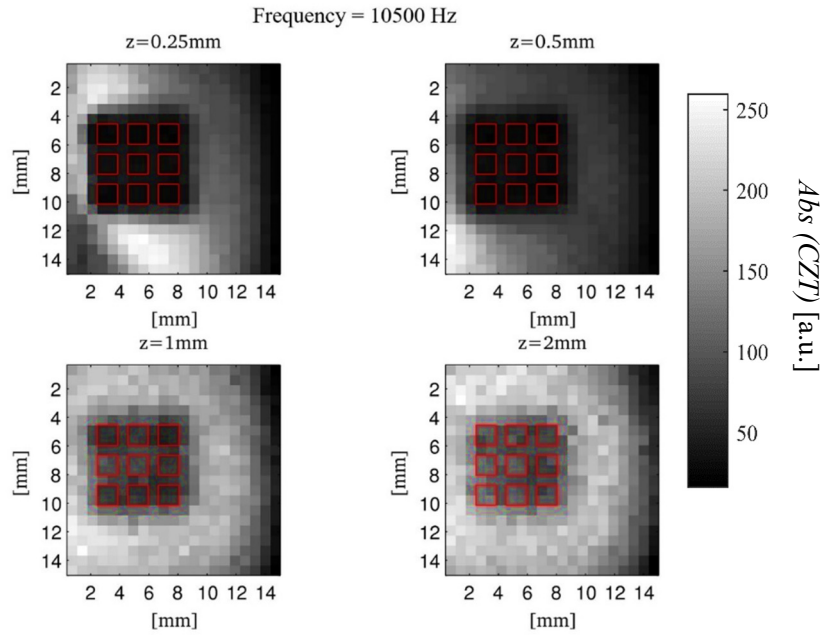
Figure 5.11: 2D scans of the acoustic pressure field at the outer surface of a 3 by 3 holes acoustic metamaterial device, for several different distances z from the outer surface. The frequency used was 10.5 kHz.
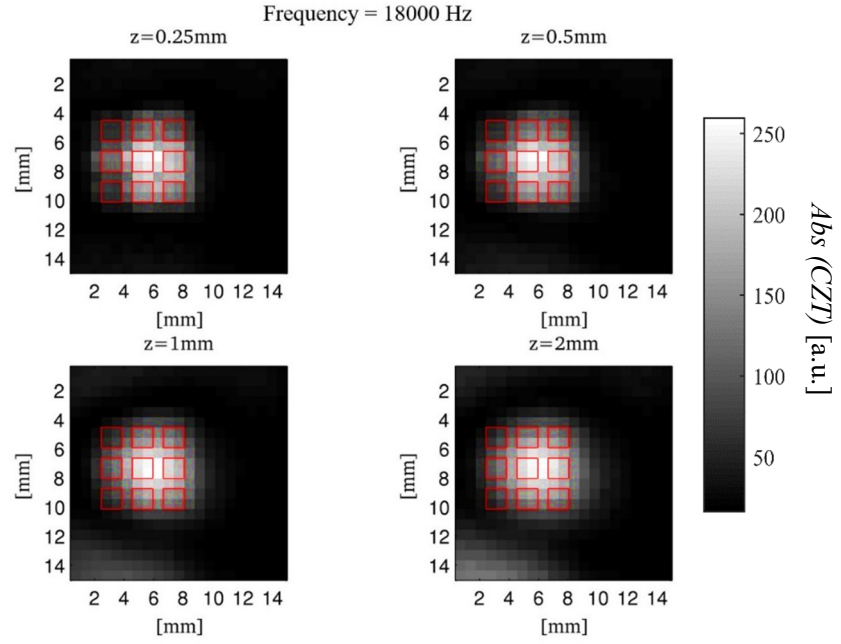
Figure 5.12: 2D scans of the acoustic pressure field at the outer surface of a 3 by 3 holes acoustic metamaterial device, for several different distances z from the outer surface at 18 kHz.

It can be noted that for the off-resonance condition (Fig. 5.11 at 10.5 kHz) the acoustic field showed a minimum in the retrieved acoustic amplitude (black colour) if compared with the acoustic field that it is transmitted through the bulk of polymer (white). This condition is preserved for all the investigated distances *z* from the outer metamaterial surface. On the other hand, an on-resonance condition can be observed for a frequency of 18.0 kHz as shown in Figure 5.12. Please note that the numerical difference from the theoretical value of resonance ($2f_1 = 23.174$ kHz) could be caused by differences in air sound velocity within the air channels from that in bulk air, and the precision of the CZT algorithm. Furthermore, as for the simulated 3 by 3 holes acoustic metamaterial device, the resonant frequency values can vary from the theoretical ones due to the exchange of acoustic energy between the channels. Despite this, these preliminary results indicated that holey-structured metamaterial devices, realized by means of 3D printing, gave results similar to those predicted by FE simulations. This in turn demonstrated that the experimental setups used were capable of measuring the exotic effects expected from these devices [5].

5.5 An acoustic metamaterial device with 10 x 10 holes

The FE simulations of Section 4.3.2 shown that a holey structured acoustic metamaterial device realized by using polymeric material can potentially be used for imaging a subwavelength object. In particular, simulations showed that an acoustic metamaterial of thickness h = 14.8 mm, with 10 x 10 squared-sided holes of lateral dimension s = 1.48 mm and centre-to-centre distance of Λ = 2.22 mm, was capable of imaging a subwavelength dimension object having a width of 3 mm. This metamaterial has been successfully 3D printed (see Figure 5.13(a)), and the object to image distance was chosen to be as close as possible to what have been investigated numerically. A subwavelength "L" shaped aperture was fabricated within a 1 mm thick aluminium slab, as shown in Figure 5.13 (b):

(a)   (b)
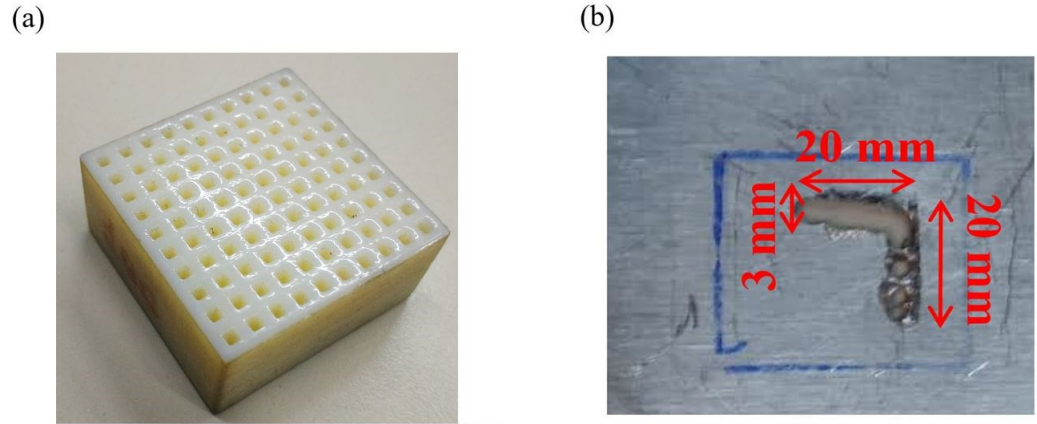
Figure 5.13: (a) 3D printed 10 by 10 hole acoustic metamaterial device with the L-shaped aperture;(b) L-shaped aperture dimensions.

As in the FE simulations (Section 4.3.2), the subwavelength aperture was placed just above the metamaterial surface, so as to have a 2-mm air gap between them. The emitted acoustic field was then measured using the MEMS microphone, using the setup shown in Figure 5.14. A measurement was acquired every 0.1 mm across 2D imaging planes parallel

to the outer metamaterial surface. This process was then repeated for different distances z from the outer metamaterial surface.
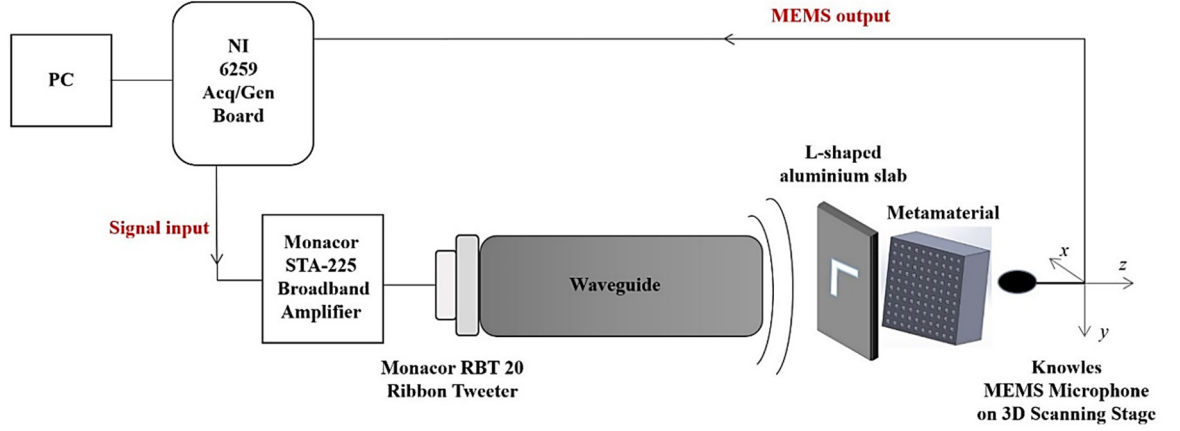
Figure 5.14: sketch of MEMS setup for imaging a subwavelength object.

The experimental results are shown in Figures 5.15 (a) and (b) for $z = 0.5$ mm and 1 mm respectively from the outer metamaterial surface, over the frequency range of 9.8 – 10.3 kHz. A clear reconstruction of the L-shaped aperture can be observed in both cases. In particular, for $z = 0.5$ mm the pattern of the holes can be clearly seen as well as the image of the "L". This result agrees with what was observed in the numerical simulations in Chapter 4. It is also evident from these plots that, at these two fixed distances from the metamaterial surface, images of the sub-wavelength aperture have been recovered over a finite frequency range of 9.8 – 10.3 kHz. This represents a range of 0.5 kHz around a centre frequency of 10.5 kHz, or ~5%. This indicates that the resonances are sufficiently broad that precise frequency control is not needed for such metamaterials, and this would improve their ease of use over ones which have a very narrow spectral resonance.
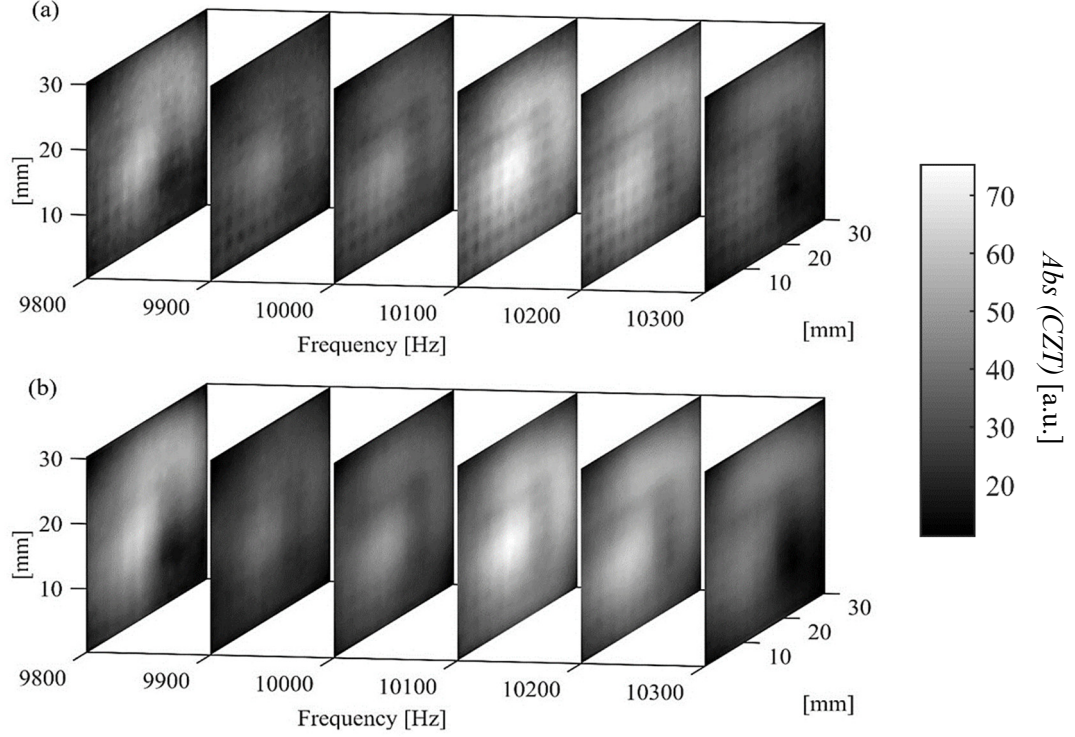
Figure 5.15: (a) Experimental MEMS results at (a) z = 0.5 mm and (b) z = 1 mm from the metamaterial surface.

A 2-mm thick aluminium slab containing a "T" shaped aperture was also tested. The arms of the "T" were 20 mm long, whilst its width d was 3 mm (Figure 5.16 (a)). Figure 5.16 (b) shows the acoustic field retrieved as a function of frequency, at a fixed distance $z = 0.5$ mm from the outer metamaterial surface. This "T" shaped aperture with subwavelength dimensions appears to be imaged clearly using the 10 by 10 holey-structured acoustic metamaterial device, over the range of frequencies quoted [6]. Again it is seen that the image of the aperture has been retrieved over a range of frequencies, underlining the fact that these metamaterials can be operated over a finite bandwidth.
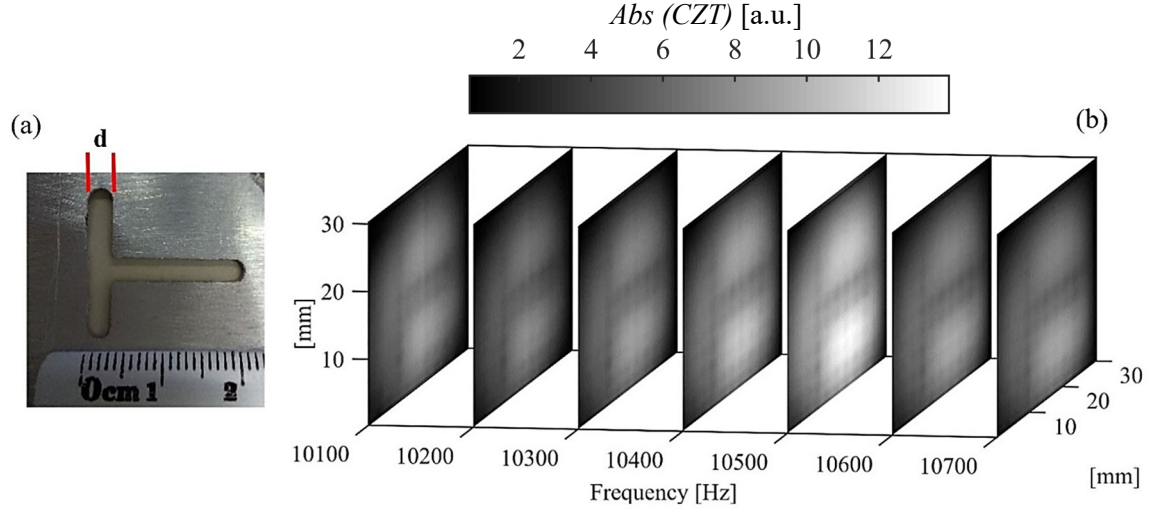
Figure 5.16: (a)"T" shaped aperture dimensions. (b)"T" Experimental results at 0.5 mm from the metamaterial surface.

5.6   Experimental results using a spiral metamaterial

The earlier FE simulations indicated that an acoustic metamaterial device having different path lengths using a spiral path through the object can result in focusing of the acoustic pressure field (a so-called "spiral" geometry for the sake of simplicity). The design simulated earlier using FE (Section 4.4) has been manufactured using 3D printing and is shown in Figure 5.17(a). A sketch of the channel path (Figure 5.17(b)) indicates the internal structure, and Figure 5.17(c) shows how the total length of each of the spiral channels within the device decreases with distance from the centre.
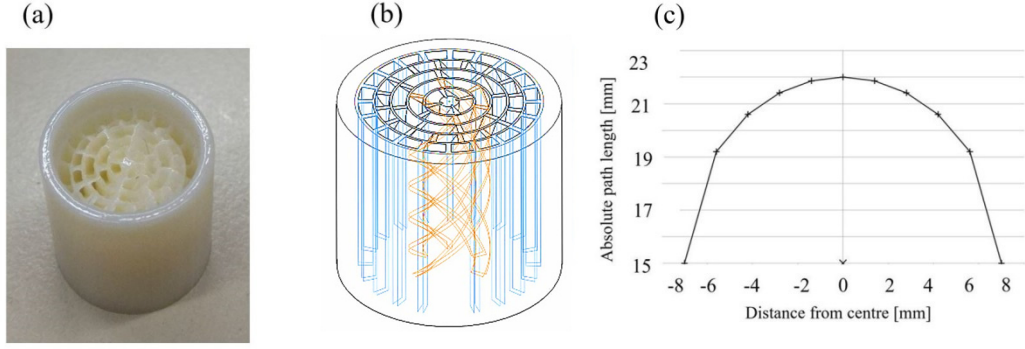
Figure 5.17: (a) 3D printed "spiral" device; (b) sketch of the "spiral" representing channels geometries; (c) change in the absolute path length of each channel with distance from the centre.

The thickness h of the spiral device was 15 mm, which also corresponds to the absolute path length of the channel at the outer circumference, which are straight channels. The MEMS setup was here used again to acquire results across a regular grid of acquisition points, at step intervals of 0.1 mm. As predicted by the earlier FEM simulations, interesting phenomena can be observed by looking at the 2D acoustic pressure field at the outer surface of the spiral. Figure 5.18 shows the acquired pressure field at a distance $z = 0.5$ mm from the outer metamaterial surface for a fixed frequency value $f = 10.25$ kHz. It seems that a focussing effect occurs, with a concentration of energy at towards the centre of the scan area (noting that the device itself was 15 mm in diameter).
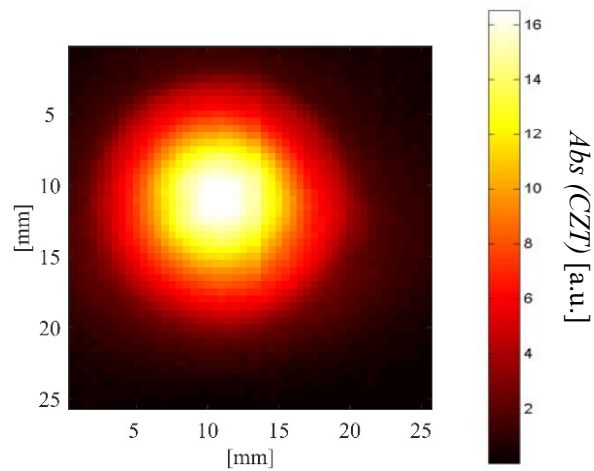
Figure 5.18: 2D pressure field retrieved at the outer side of the spiral at f = 10.25 kHz.

Figure 5.19 shows the how spatial behaviour of the acoustic beam changes as the distance of the MEMS measurement plane from the metamaterial output surface was increased from 0.5 mm to 1.5 mm, at f = 10.25 kHz. It can be seen that the energy is increasingly defocussed as the distance is increased.
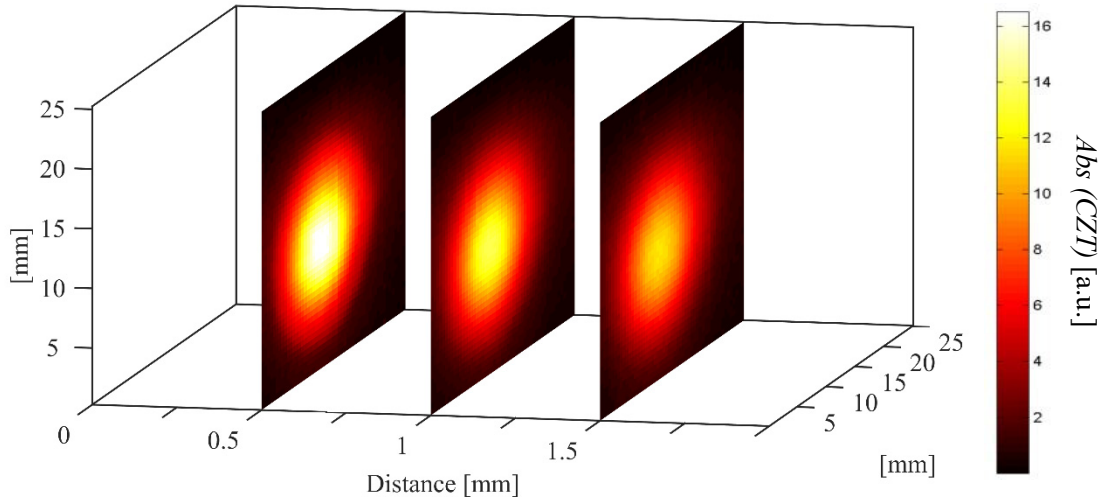
Figure 5.19: Acoustic pressure field behaviour at several distances from the spiral outer surface.

Following the previous numerical studies of Chapter 4, an estimation of the focal spot size can be obtained by looking at the Full Width Half Maximum (FWHM) of the normalized pressure amplitude plotted, for a line crossing the centre of the spiral, as in Figure 5.20. The red lines represents the amplitude value to which the FWHM value is measured.
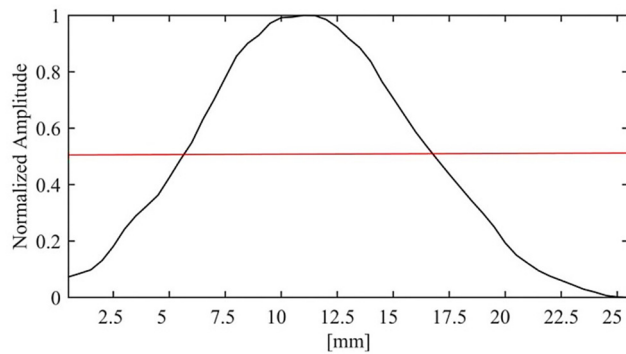
Figure 5.20: 1D pressure field along the centre of the spiral acquire data.

The obtained *FWMH* is equal to 10.5 mm. The wavelength λ in air at the chosen frequency of 10.25 kHz is 33.46 mm in air. Therefore, the ratio between them is:

$$\frac{\lambda}{FWMH} \approx 3.18 \qquad\qquad (5.1)$$

and this is approximately maintained for all the inspected distances. It is worth pointing out again that this value differs from the one obtained by FEM simulations due to different values of air speed of sound considered, MEMS sensitivity and chirp Z-Transform algorithm used. Nevertheless, the device shows promise in being able to focus the impinging planar pressure field.

5.7   Toward the realization of a broad-band acoustic device

As stressed in previous chapters, coded waveforms such as chirps or bipolar sequences can be used to enhance the range of acoustic frequencies that are transmitted through materials, and have been used in many material studies where signals are embedded in noise [7]. Usually, acoustic metamaterials operate over a narrow frequency range, or at discrete set of frequencies, thus it is really difficult to use them into practical NDT applications. Moreover, they work into low (relatively) frequencies. Again, those restrictions are due to the dimensions and geometries of their artificial engineered structures. Therefore, it is of interest to build an acoustic metamaterial device capable of restoring the evanescent field over a broadband frequency range, for possible use in real applications. In particular, this device should successfully work in the ultrasonic region, so that it could be exploited, for example, in ultrasonic NDT and medical imaging applications. In order to achieve this in the ultrasonic frequency range, two key-points have to be satisfied:

(i)   The structures within the acoustic metamaterial have to be realized at a much smaller scale than at present;

(ii)   Acoustic metamaterial devices will need to have a broad bandwidth capability;

One way of producing such a metamaterial design is to consider the work of Zigoneanu *et al.* [8], where the authors demonstrated that a pyramidal geometry can be used to broaden the cloaking effect of an acoustic metamaterial, using the idea that different material thicknesses lead to different resonant frequencies. This latter aspect was verified using FE in Chapter 4 and demonstrated experimentally in Section 5.4.1. A similar approach has been used here trying to extend number of frequencies within an input signal that satisfies Equation (5.2). This equation is satisfied when $\lambda = \frac{2h}{m}$, or when $f = m\frac{c}{2h}$ with m positive and integer and c the sound velocity in air. As a consequence, an acoustic metamaterial having finite stepped increments in its thickness h should theoretically reach resonance conditions at multiple frequency values, restoring the evanescent acoustic field over a wider bandwidth of signal.

$$T_c^{00}\big(\lambda_R, \vec{k}_\parallel\big) = (-1)^m \tag{5.2}$$

The 3D-printed acoustic metamaterial device, plus a sketch of the device (including dimensions), are shown in Figures 5.21(a) and (b) respectively. This device had a square base with ten finite increments in its thickness of 2.96 mm each, here called "steps" for simplicity. For each step there were ten squared-sided holes of 1.48 mm width in each row. The result is again a 10 x 10 holes acoustic metamaterial, but now of varying thickness. The fundamental frequencies at which the Fabry-Pèrot resonances are expected for the corresponding incremental step change in thickness are shown in Figure 5.21(c). Again, integer multiples of these fundamental frequencies would also satisfy the resonance conditions of equation (5.2).

Step Number	Expected Resonance Frequency (Hz)
1	57939
2	28970
3	19313
4	14485
5	11588
6	9656
7	8277
8	7242
9	6437
10	5793
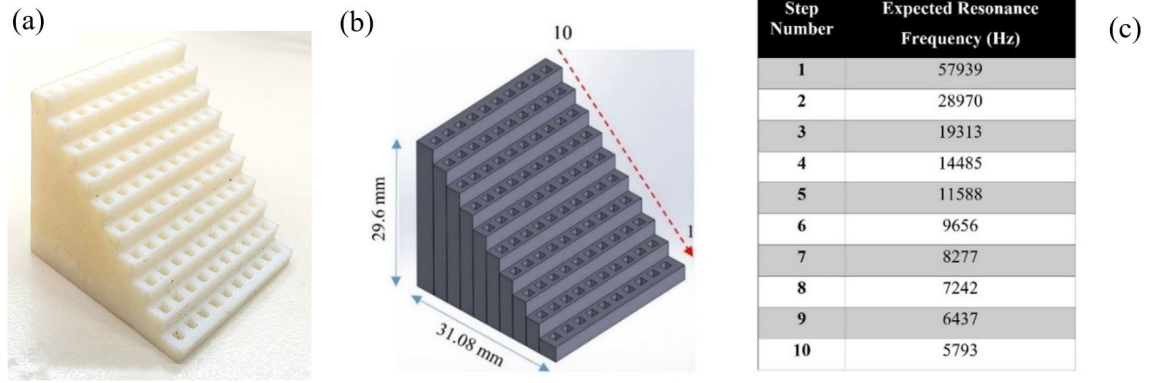
Figure 5.21: (a) 3D printed "Stepped" metamaterial device and (b) a sketch showing dimensions. (c) The expected FPR frequencies in air for each step change in thickness.

The experimental results are shown in Figure 5.22, where again 2D planar scans were performed of the acoustic field at the outer surface of the stepped acoustic metamaterial obtained using the MEMS setup. Each figure subplot title indicates the frequency at which each step reaches its resonance condition. The input signal used was again a linear chirp having the same spectral characteristics of the one in Figure 5.5(a) and time duration of 0.5 seconds. Please note that figures start from the results obtained for Step 10 to Step 2, so as to have the frequencies of resonance increasing as shown. Since Step 1 would have a foundamental resonance condition at 57.9 kHz, its resonance was outside the frequency range achievable by using the present experimental setup, and so is not considered.
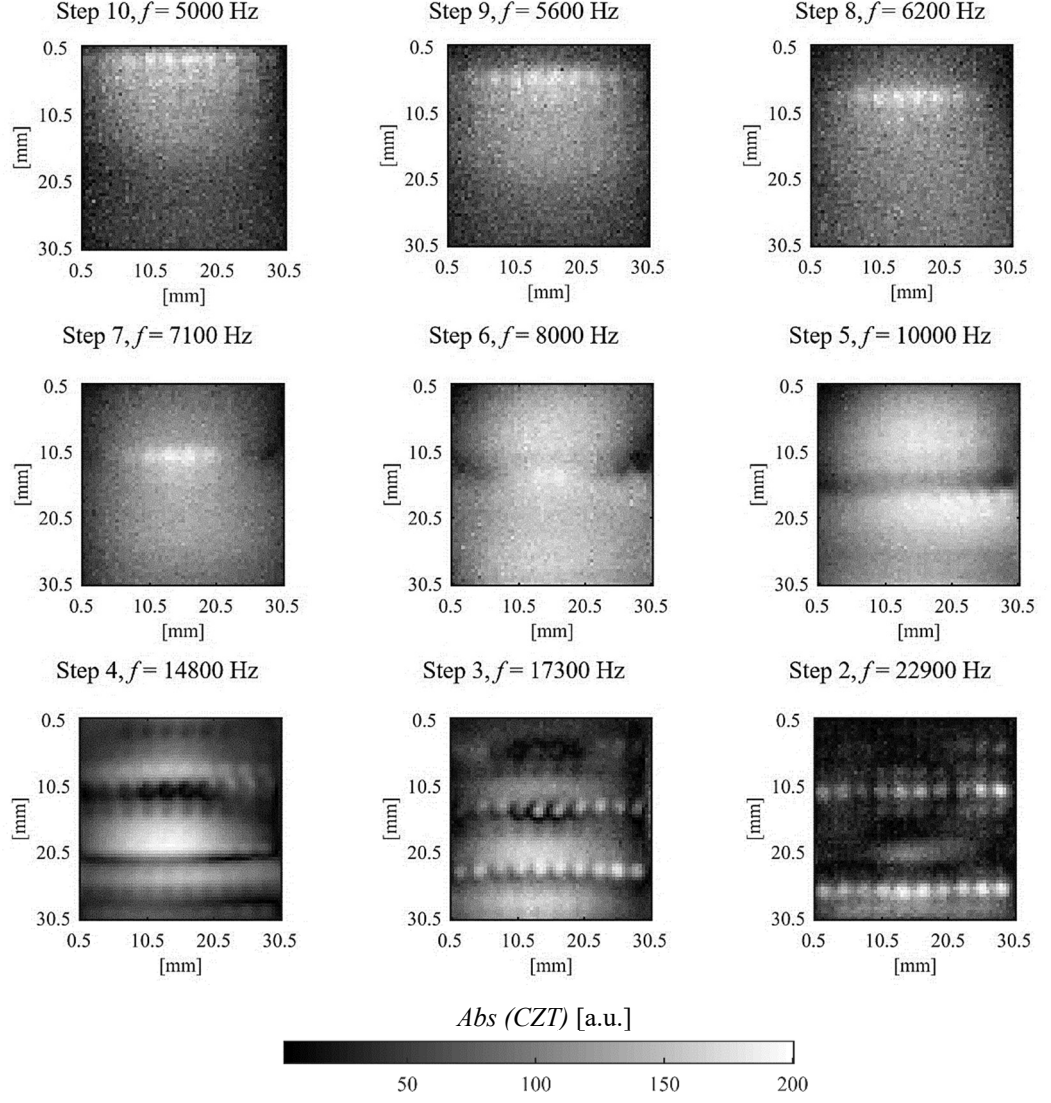
Figure 5.22: Acoustic pressure 2D-plots at a fixed distance from the "stepped" acoustic metamaterial device for several different frequencies. Each subplot title reports the frequency and the corresponding step where the resonance condition is achieved.

As expected, the intensity of the transmitted pressure field increased at specific frequencies and sample thickness. This is clearly visible by the presence of brighter lines dots across the images. It can also be noted that the observed resonance frequency differed slightly from the one predicted theoretically. Again, this is thought to be related to the peak-shaped sensitivity of the MEMS microphone, the resolution of the Z-Transform algorithm used for data analysis, of sound velocity in air and exchange of acoustic energy among the air channels.

Since the each step provides a set of frequencies at which FPR can be reached, different steps can reach resonance condition for the same impinging frequencies. The set of resonance frequencies $f_n^{(s)}$ of the sth step can be expressed as:

$$f_n^{(s)} = n\frac{cN_s}{2(s \times h)} \tag{5.3}$$

where n is the integer number associated to the nth resonance mode of the sth step and $\frac{s \times h}{N_s}$ is the step length. As a consequence, different steps s, s' can show common resonance frequencies for different resonance modes n, n' whenever the following condition is satisfied:

$$\frac{n}{s} = \frac{n'}{s'} \rightarrow \frac{n}{n'} = \frac{s}{s'} \tag{5.4}$$

Subplots within Figure 5.23 shows three example of channels resonating together [6]:
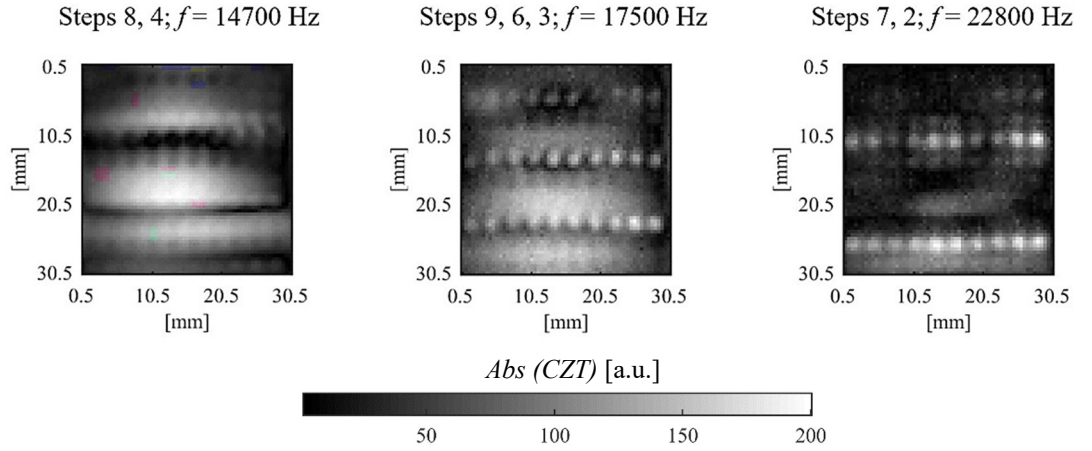
Figure 5.23: 2D-planes of the pressure field intensity at a fixed distance from the "stepped" acoustic metamaterial device for several different frequencies. Each subplot highlights the frequency and the corresponding steps where the common resonance condition is achieved.

It can be concluded from the above that a metamaterial operating over a reasonable bandwidth can be created, using changes in material thickness.

5.8   A 3D printed phononic crystal

As reported in Chapter 3, phononic crystals (PCs) show promise for subwavelength imaging. Their extraordinary properties can be observed when bandgaps in the transmitted pressure field occur [9]–[11]. As in the case of the holey structures described above, additive manufacturing (3D printing) has opened the way to realizing such complicated structures. This fabrication method has thus been exploited here to realize two different kinds of phononic crystal design, both of which are shown in Figure 5.24. These designs have been realized by using a polymeric resin substrate ($c = 2{,}100$ ms^{-1}, $\rho = 1{,}235$ kgm^{-3}) with chrome-steel spheres embedded within them (with properties $c = 4{,}288$ ms^{-1}, $\rho = 7{,}833$ kgm^{-3}). The dimensions were 26 mm by 20 mm, with a 3 mm of thickness. Figure 5.24(a) shows a 2D array of 1 mm diameter spheres embedded into the polymer substrate with repetition step of 3 mm. Figure 5.24(b) shows a second PC sample in which the embedded spheres are placed in contact in columns. The distance between each line of spheres was 3 mm. A reference sample of the substrate material only having the same dimensions as the PCs was also manufactured to compare PC operation with a standard material (Figure 5.24(c)).

(a)   (b)   (c)
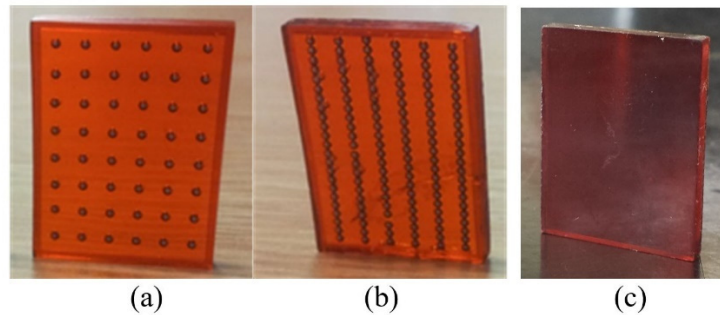
Figure 5.24: PC crystal designs. (a) realized PC having 2D dimensional arrays of spheres embedded and (b) PC with embedded channels of contacting steel spheres; (c) A reference substrate sample.

Applying the theory described in Chapter 3 to the sample in Figure 5.24(a), the Bragg scattering condition is reached at a frequency of 350 kHz at normal incidence (and at integer multiples of it). Hence, attenuation of the transmitted acoustic pressure intensity would be

expected for frequencies around this value. For the sample in Figure 5.24 (b), the application of Bragg scattering theory is not simple. This is because it is not possible to assume that each line/row of spheres would act as a unique source of the scattered field, leading to a difficult modelling of the involved phenomena. However, for the case where the acoustic pressure field impinges normally with respect to the orientation of the parallel lines, an increase in the reflected intensity should still also occur at f = 350 kHz and integer multiples of this fundamental frequency value.

In order to verify these hypotheses, experimental measurements of transmission through the samples shown in Figure 5.24 are reported. In particular, the regularly-spaced embedded sphere sample (Figure 5.24(a)) and the reference sample (Figure 5.24(c)) have been tested in a single configuration. Conversely, the sample containing lines of embedded spheres (Figure 5.24(b)) has been tested with the incident ultrasonic acoustic field being both perpendicular and parallel with respect to the line of spheres.

The experimental acquisitions have been performed in water, by exciting the samples using a piezocomposite water-coupled transducer acting as a transmitter (Tx). The receiver (Rx) was a 0.5 mm diameter Precision Acoustic hydrophone, held within a 2D-motorized step motor scanning stage. The signal generation was managed by an Agilent 33120 arbitrary waveform generator, whilst the signal acquisition was performed by means of a Tektronic DPO 3012 oscilloscope. A sketch of the experimental setup used is shown in Figure 5.25:
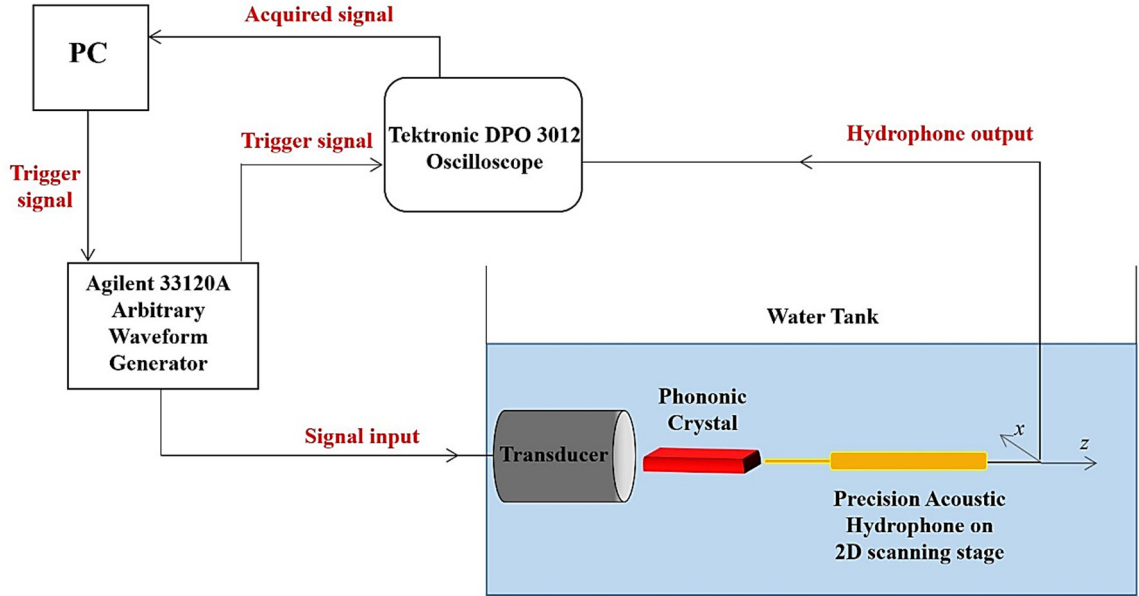
Figure 5.25: Sketch of the phononic crystal measurement setup.

The broad bandwidth piezo-composite source was driven by a Tukey-windowed chirp signal, as shown in Figure 5.26, sweeping the frequency range from 100kHz-1 MHz, allowing the inspection of the PCs over a wide range of frequencies.
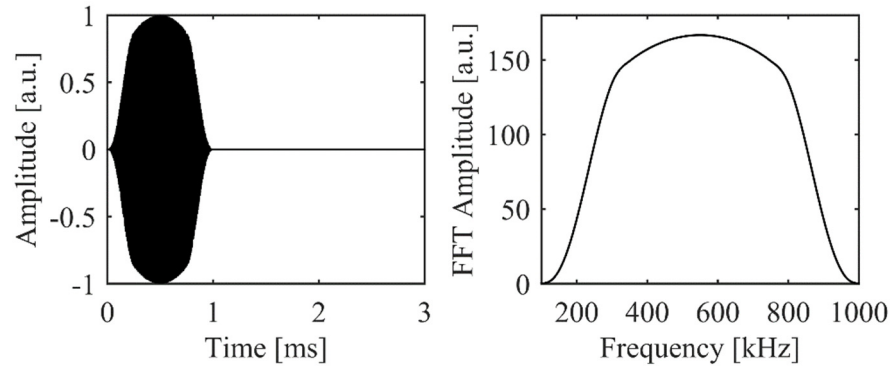
Figure 5.26: Input chirp signal time handling (a) and its frequency spectrum (b).

In order to recover the transmitted ultrasonic signal pressure, the hydrophone was placed at a distance of 0.5 mm from the outer surface of the PC investigated sample. A 1D scan of the pressure field intensity was acquired for each investigated PC, using a scanning step of 0.1 mm in the direction perpendicular to the main axis of propagation. The acquired signals have been then cross-correlated with the input signal to obtain the impulse response by pulse compression, thus characterizing the frequency characteristics of each sample.

The results obtained are shown in Figures 5.28 - 5.31. Each figure is organized as follows: (I) top-left subplot depicts the retrieved impulse response following a B-scan representation; (II) top-right subplot shows the B-scan data displayed in the frequency domain. (III) bottom-left subplot reports a typical A-scan time waveform, averaged over all the measurement line, and (IV) bottom-right subplot shows the corresponding spectrum. The results are plotted over a frequency range of 0 - 500 kHz. Note that the sample in Figure 5.24(b) was placed either vertically on the transducer face so that the lines of spheres are aligned along the transducer axis (Figure 5.27(a)) or horizontally (with its longer dimension in contact with the source (Figure 5.27(b)):
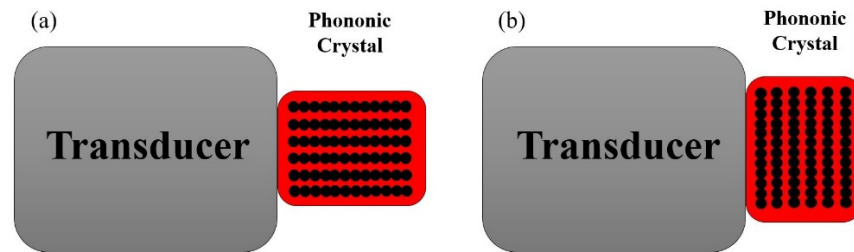
Figure 5.27: (a) Phonic crystal with embedded columns of spheres vertical and (b) horizontal configuration.

a) Reference sample

The results obtained from the reference sample are presented in Figure 5.28:
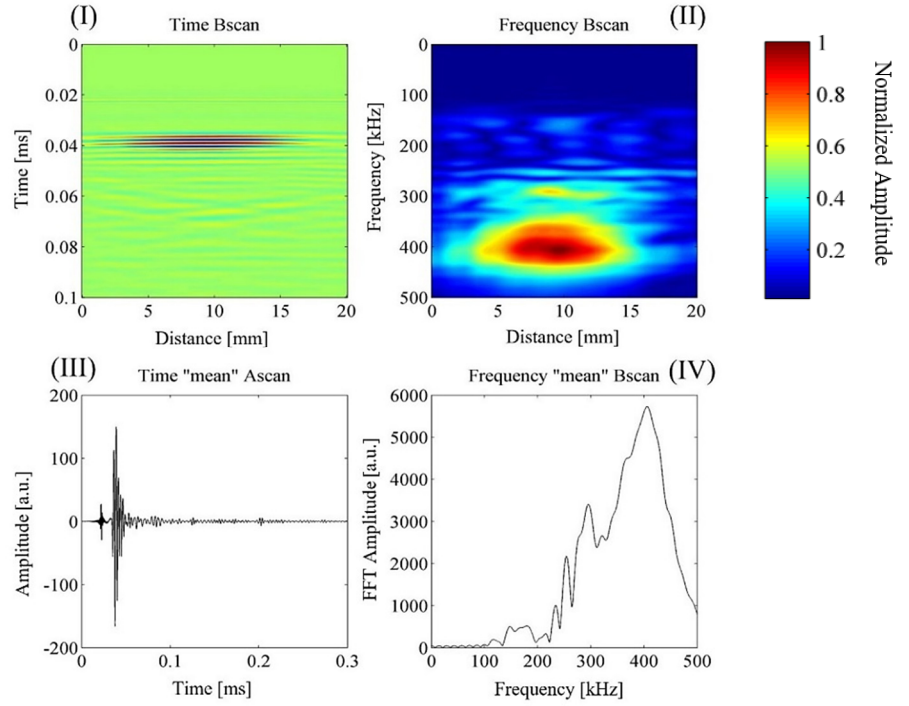
Figure 5.28: Results obtained from the reference sample.

b) Sample with columns of spheres positioned vertically

The results achieved on the sample shown in Figure 5.24 (b) are shown in Figure 5.29, with the sample placed vertically on the transducer face so that the lines of spheres are aligned along the transducer axis (see Figure 5.27(a)):

c) Sample with columns of spheres positioned horizontally

Here the sample shown in Figure 5.24(b) has been placed horizontally (as shown in Figure 5.27(b)), hence with its longer dimension in contact with the source. The results are shown in Figure 5.30.
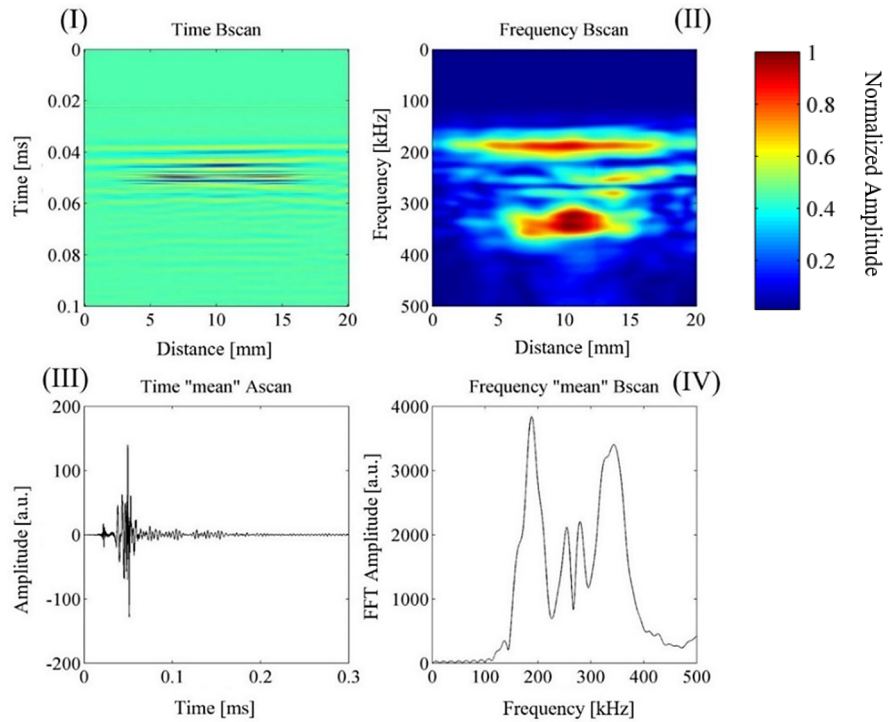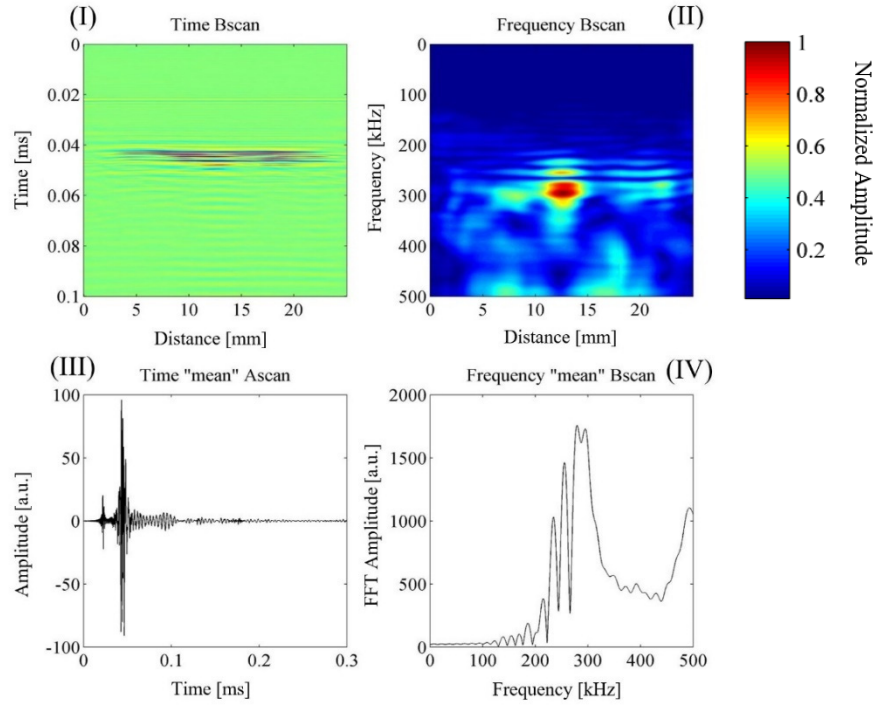
Figure 5.30: Results obtained for the sample containing columns of spheres, when placed horizontally against the source.

d) Sample with 2D array of spheres positioned vertically

Figure 5.31 shows the results obtained by placing the sample in the vertical orientation.
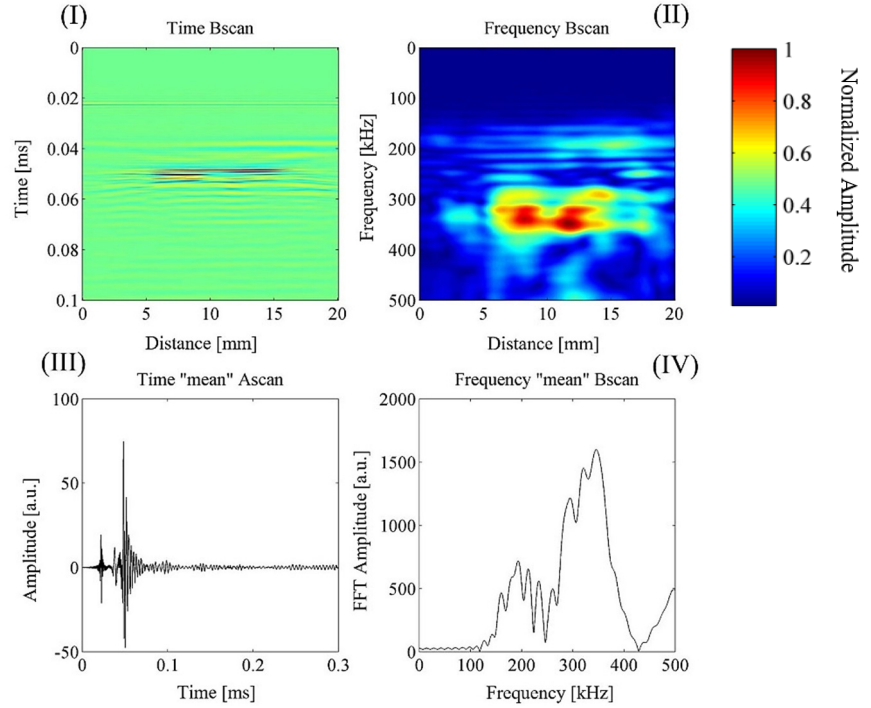
Figure 5.31: Results obtained on the sample containing a 2D array of spheres, by placing its shorter dimension in contact with the Tx.

For the reference sample, the FFT shows an amplitude peak at a frequency of around 400 kHz. This maximum is also quite large in terms of spatial distribution, thus covering a wide portion of the scan range. Conversely, for the samples with embedded spheres, B-scan representations of the frequency domain show a dip in energy at 350 kHz. This decrease in the retrieved acoustic amplitude varies both in magnitude and severity. In addition, the appearance of other interesting phenomena such as interferences seem to occur. These can be noted by the appearance of horizontal dark lines in the B-scan spectral data, as well as the local minima seen in the averaged A-scan spectra. This is evidence of the expected band-gap behaviour, which is one of the features of phononic crystals [12]

Finally, it is of interest to look at the spatial distribution of the spectra. For the 2D-array sample, and for the sample with columns aligned vertically, spatial distributions similar to that of the reference sample can be noted. On the other hand, the sample with the columns aligned horizontally (Figure 5.27), the transmitted energy handling shows a high and sharp

maximum around the mid-point of sample. Although this effect has not been modelled, it seems that a focusing effect has occured, as would be expected from a phononic crystal of the dimensions studied. This phenomenon deserves further analysis [13].

5.9   Conclusions

Following the prediction given by the numerical FEM simulations of Chapter 4, it has been demonstrated in this chapter that acoustic metamaterials of various shapes and dimensions can be successfully realized by means of additive manufacturing (3D Printing). In particular, it has been shown that polymer-based acoustic metamaterials gave the expected Fabry-Pèrot resonance pattern in the 1-60 kHz frequency spectrum in air. This has been demonstrated using a laser vibrometer and a thin reflective membrane glued onto the metamaterial surface, so as to observe the resonances into the air channels by looking at the vibrations of the reflective membrane. Starting from this encouraging result, an experimental setup capable of acquiring and imaging the 3D acoustic pressure field emitted from complex metamaterial structures has been constructed, using a small MEMS microphone to avoid spatial averaging of the acquired pressure field. This allowed precise measurements of the effects provide by the use of the acoustic metamaterials without using any deconvolution algorithm.

It has been proven that a 10 by 10 holey structured acoustic metamaterial can be successfully used to image objects with subwavelength dimensions, here in the form of L-shaped and T-shaped apertures in two different thin aluminium slabs. It is worth stressing again that this has been observed over a frequency range that is unexplored to date, *i.e.* into the ultrasonic range. Experiments further corroborated the numerical predictions for a "spiral" acoustic metamaterial, in which a focus of the acoustic field at a fixed frequency has been observed.

A novel broader bandwidth acoustic metamaterial device was also examined (a "stepped" acoustic metamaterial device), and a range of resonant frequencies observed as increased transmission intensities over the retrieved 2D planes of the acoustic pressure fields. This acoustic metamaterial was capable of transmitting signals at a set of discrete frequencies, ranging from 5 kHz to 22.9 kHz. This demonstrates the first steps towards the realization of a real broad bandwidth device, which could incorporate these and other design features available in 3D printing to develop metamaterials with properties that could be used in real acoustic imaging applications.

Further results on the realization and characterization of an exotic design of a 3D-printed phononic crystals have also been reported.

References

[1]   M. Molerón, M. Serra-Garcia, and C. Daraio, "Acoustic Fresnel lenses with extraordinary transmission," *Appl. Phys. Lett.*, vol. 105, no. 11, 2014.

[2]   J. Zhu, J. Christensen, J. Jung, and L. Martin-Moreno, "A holey-structured metamaterial for acoustic deep-subwavelength imaging," *Nat. Phys.*, vol. 7, no. 1, pp. 52–55, 2011.

[3]   H. Su, X. Zhou, X. Xu, and G. Hu, "Experimental study on acoustic subwavelength imaging of holey-structured metamaterials by resonant tunneling.," *J. Acoust. Soc. Am.*, vol. 135, no. 4, p. 1686, Apr. 2014.

[4]   L. Rabiner and R. Schafer, "The Chirp z-Transform Algorithm and Its Application," *Bell Syst. Tech.*, 1969.

[5]   S. Laureti, L. A. J. Davis, M. Ricci, and D. A. Hutchins, "The study of broadband acoustic metamaterials in air," in *Ultrasonics Symposium (IUS), 2014 IEEE International*, 2014, pp. 1344–1347.

[6] S. Laureti, D. Hutchins, L. Davis, S. Leigh, and M. Ricci, "High-resolution acoustic imaging at low frequencies using 3D-printed metamaterials," *AIP-Advances*, vol. 6, no. 12, 2016.

[7] P. Pallav, T. H. Gan, and D. A. Hutchins, "Elliptical-Tukey Chirp Signal for Ultrasonic Imaging," *IEEE Trans. Ultrason. Ferroeletrics, Freq. Control*, vol. 54, no. 8, pp. 1530–1540.

[8] L. Zigoneanu, B. Popa, and S. a Cummer, "Three-dimensional broadband omnidirectional acoustic ground cloak," *Nat. Mater.*, vol. 13, no. March, pp. 1–4, 2014.

[9] S. Yang, J. H. Page, Z. Liu, M. L. Cowan, C. T. Chan, and P. Sheng, "Focusing of sound in a 3D phononic crystal," *Phys. Rev. Lett.*, vol. 93, no. 2, pp. 24301–1, 2004.

[10] S. Yang, J. H. Page, M. L. Cowan, C. T. Chan, and P. Sheng, "Phononic Crystals," *La Phys. au Canada*, pp. 187–189, 2001.

[11] A. Sukhovich, L. Jing, and J. H. Page, "Negative refraction and focusing of ultrasound in two-dimensional phononic crystals," *Phys. Rev. B - Condens. Matter Mater. Phys.*, vol. 77, no. 1, 2008.

[12] J. H. Page, A. L. Goertzen, S. Yang, Z. Liu, C. T. Chan, and P. Sheng, "Acoustic Band Gap Materials," in *Photonic Crystals and Light Localization in the 21st Century*, 2001, pp. 59–68.

[13] S. Laureti, O. Akanji, L. Davis, and S. Leigh, "Design and characterization of 3D-printed phononic crystals for sub-MHz ultrasound manipulation," *(IUS), 2015 IEEE Int.*, 2015.

CHAPTER 6: NDT Applications of pulse compression

6.1   Introduction

As was shown in Chapter 5, broadband coded signals can be used in combination with either holey structured acoustic metamaterials or phononic crystals. This helped to both observe the peculiar effects arising by the use of 3D printed acoustic metamaterials and to precisely characterize the frequency response of phononic crystal structures by means pulse compression. However, many other applications of pulse compression exist in NDT. This and the following Chapter looks at the application of pulse compression techniques for the NDT of challenging industrial materials and products.

It was shown in Chapter 1 that sound propagation exhibits attenuation, the level of which depends on the propagation medium. The level of attenuation is also related to the ultrasound frequency used for the inspection. It follows that, if highly attenuating materials are to be investigated, an optimal solution should rely on the use of low frequency excitation. However, this approach results in lowering the spatial resolution, as described in Chapter 1. Nevertheless, coded signals can help to counterbalance the sound attenuation by spreading a quantity of energy that is proportional to their time duration, and the spatial resolution can be improved by advanced post-processing algorithms and imaging procedures, as will be shown.

In this Chapter, the inspection of refractory bricks, widely used for structural purposes in the steel industries, and thick polyurethane samples used as riser stiffeners in the off-shore oil and gas industries. This research was performed as part of a larger team of researchers, and has led to publications that are either accepted for publication [1],or have been submitted and are still under review [2]. In each case the work was collaborative with industry, and the contribution of the present author has been identified in each case. In

addition, a portable device for Pulse Compression applications is described, together with a practical example of its inspection capabilities for the detection of reinforcement bars in concrete.

6.2   Experimental Setup

The experimental setup used for both applications was based on a National Instrument PXI chassis that contained a PXI-5412 100 Msamples·s⁻¹ 14-bit arbitrary waveform generator, and a PXI-5105 8 channel 60 Msamples·s⁻¹ 12-bit digitiser. The PXI system is shown in Figure 6.1:

Figure 6.1: A photograph of the PXI system.

Depending on the investigated sample, two different pairs of transducers were utilized. Both sets of transducers were piezocomposite devices manufactured by EofE Ultrasonics Co. Ltd, having different nominal central frequencies f_{ct} and diameters D_t. In particular, Figure 6.2(a) shows a pair of piezo-composite transducers having f_{ct} = 300 kHz and D_t = 25.4 mm, whilst Figure 6.2 (b) depicts a pair of piezo-composite transducers with D_t =50 mm and f_{ct}=170 kHz:
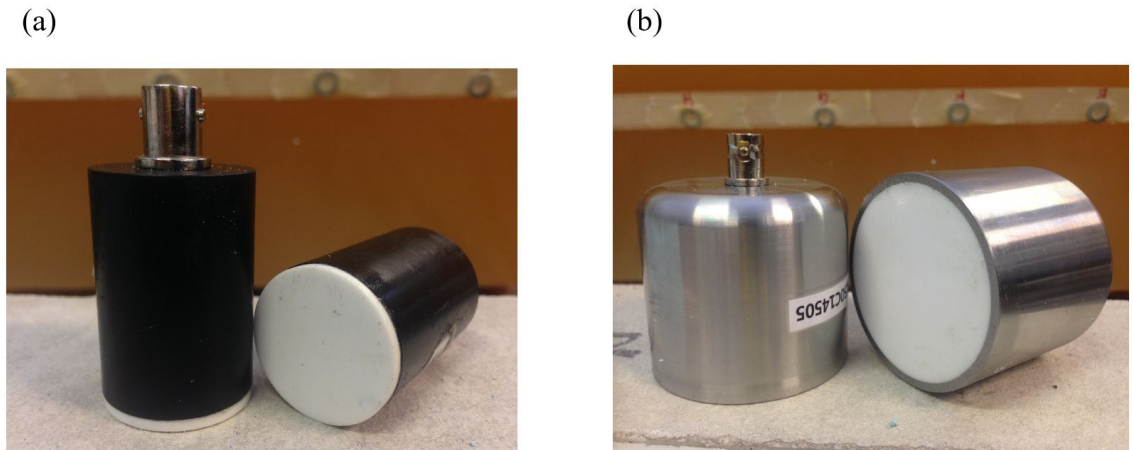
Figure 6.2: (a) a pair of piezo-composite transducer having (a) fct = 300 kHz and Dt = 25.4 mm and (b) Dt =50 mm and fct=170 kHz.

An amplifier has been used to enhance the received signal before it was digitised. This amplifier was a Cooknell Electronics CA6 charge amplifier and SU2 power supply. The transducers were placed typically in pitch-catch configuration. For all the reported results, the data acquisition was performed using a program developed in Labview environment, with post processing achieved using a series of *ad hoc* Matlab scripts. Software for both of the above was written by the author. The choice of a pitch-catch configuration was made because a pulse-echo measurement was not very practical with such a pulse compression system - the long duration of the excitation waveforms overloaded the receiver electronics for a sufficiently-long time that the measurement was often not possible, even with thick samples. The following sections show the application of coded signals and pulse compression to two different important industrial problems. The first is the inspection of refractory bricks, widely used for structural purposes in the steel and metal forming industry; the second is thick polyurethane samples, widely used as part of flexible riser stiffeners in the off-shore oil and gas industry.

6.3   Pulse compression inspection of refractory bricks

6.3.1. Background

The cracking of refractory bricks is a known problem. This is because they are often used as structural elements within steel-making furnaces, and are used to hold the various layers containing the furnace together. When used in a high temperature furnace for structural purposes, cracks can arise due to thermal stresses that arise due to a temperature difference between the inner furnace and the outside environment. Figure 6.3 shows an example of a refractory wall section, and points out the expected stress concentration zones.
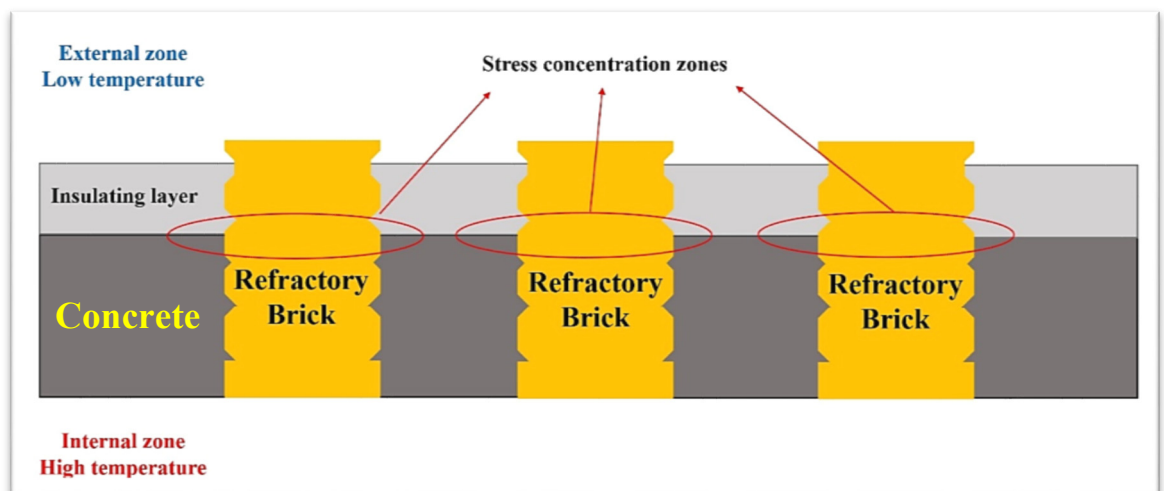
Figure 6.3: refractory wall section sketch. Red circles indicate the zone where a crack or a damage is expected to occur.

The most likely damage is horizontal cracking at the location shown in Figure 6.3, as this is where there is the greatest temperature gradient. The task is to be able to locate this cracking, usually in the form of a complete separation of two parts of the brick, but sometimes a partial crack. This has to be achieved from the outer surface of the sample as a single-sided measurement. For this reason, it is important to be able to check whether or not a brick is damaged. The work presented below is the subject of a journal paper still under preparation for submission [2]. The author's contribution has been the development of the

analysis tools, the writing of all acquisition and data analysis software, and the design of the experimental arrangement and data collection modality.

6.3.2 Experimental results

A photograph of actual undamaged refractory bricks samples is shown in Figure 6.4. They were supplied by a major international metal fabrication company, and this set of samples was composed of six different bricks, each having the same length of 33.5 cm. Note that the supplier of these samples stated that the prime objectives were to determine whether or not a crack was present. Secondary information would be its approximate location in depth from the top surface and, if possible, whether it was a full or partial crack.
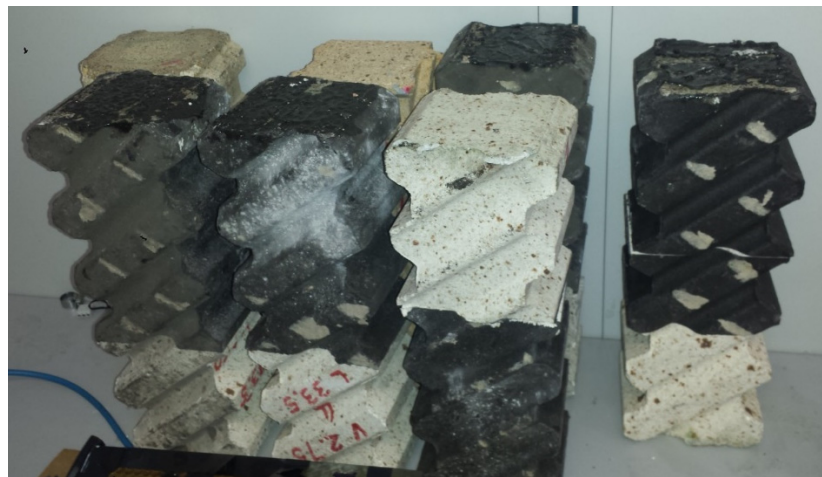
Figure 6.4: Refractory brick samples.

Figures 6.3 and 6.4 illustrate the difficulties that are likely when such samples are to be inspected as part of a structural monitoring programme. First of all, as stated above, the inspection is single sided from the external low temperature zone. In this framework, ultrasonic testing carried out in a pitch-catch configuration seemed to be an optimal solution to face this limitation. However, the refractory bricks are usually made of a mix of a range of aggregates (sometimes alumina), sand and a cement binder. Large aggregates over 10 mm in size are often present in significant amounts of more than 20% in weight. This leads to a

high level of scattering and reflection of the sound energy, meaning that ultrasonic signals are returned continuously to the receiver from scattering at various depths into the sample. The scattering also causes a high absorption of the impinging acoustic energy, leading to noisy measurements. In addition, the irregular shape of the outer surface of the bricks (used for keying in the other structures of the furnace into the bricks) results in a complicated reflection of sound energy from the side walls. This leads to an even more challenging ultrasonic inspection.

To try to cope with the above issues, the inspection was carried out by means of a pair of piezocomposite transducers (see Figure 6.2(b)) excited by a chirp signal swept over a relatively low-frequency range of 50-200 kHz. This is because low-frequencies should lower the attenuation and scattering of the acoustic energy, resulting in higher SNR values. This in turn helps the signal to both penetrate deeper into the inspected brick and to help in recognizing a crack into a sample. The recorded signal was then cross-correlated with the input signal, performing the Pulse Compression (PuC) procedure described in earlier chapters. The PuC output measurement was then used as input into a signal processing step, which is described in more detail below. The aim of this signal processing is to predict whether a crack is present or not within the sample, and also to estimate its depth of penetration horizontally across the sample.

Although the transducer configuration used is a single-sided, pitch-catch set-up, a series of measurements have been carried in through-transmission in order to estimate the sound velocity into each sample. For each sample, three different measurement have been acquired and a value of sound velocity has been estimated for each of them. This information is needed for the post-processing steps described below. The results are reported in Table 6.1.

Samples	Sound Velocity [m/s]			Averaged Velocity [m/s]
Sample 1	3200	3200	3200	3200
Sample 2	2900	2900	3000	2933
Sample 3	3570	3590	3540	3567
Sample 4	3200	3300	3200	3233
Sample 5	3100	3050	3000	3050
Sample 6	3250	3250	3300	3267

Table 6.1: Estimated sound velocity for each sample of the inspected set of bricks.

The three values obtained were then averaged and a single velocity value for each brick calculated. In addition, an overall sound velocity value can be estimated for the whole brick set at 3,208 $\pm$317 ms^{-1}, as in Figure 6.5 (the red line is the averaged overall sound velocity value).
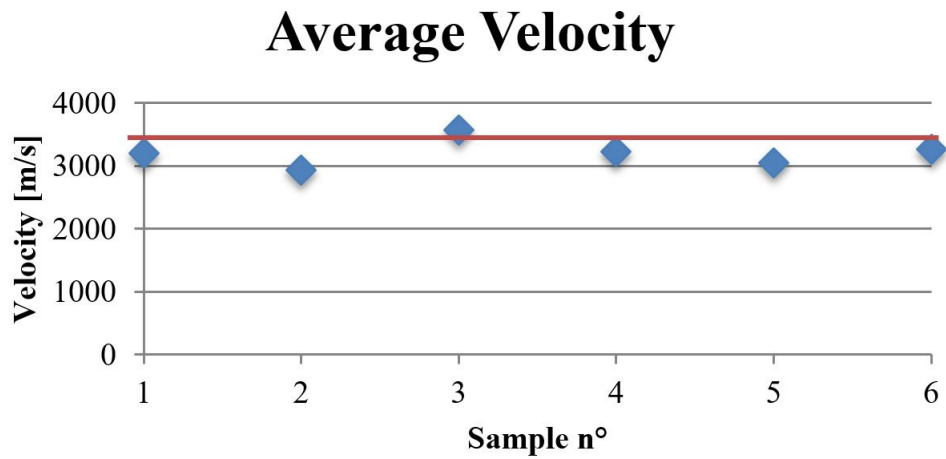
Figure 6.5: Average overall sound velocity for the all set of bricks.

The transducers used for the experimental activity are depicted in Figure 6.2(b), with D_t = 50 mm and f_{ct} =170 kHz. A photograph of the transducer placed in a pitch-catch configuration onto one surface of the sample is shown in Figure 6.6:

Figure 6.6: a picture of the transducers placed in pitch-catch configuration onto the brick sample surface.

The chirp signal frequency spectrum used to inspect the samples in pitch-catch configuration is shown in Figure 6.7:
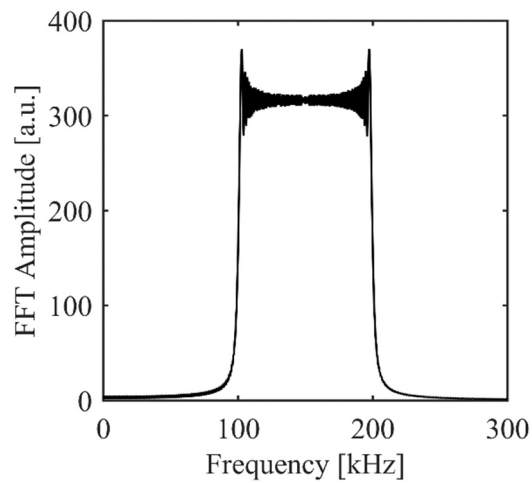
Figure 6.7: input signal-time frequency characteristics.

A typical received signal time-frequency behaviours is depicted in Figure 6.8, where the complicated nature of the received signal can be seen:
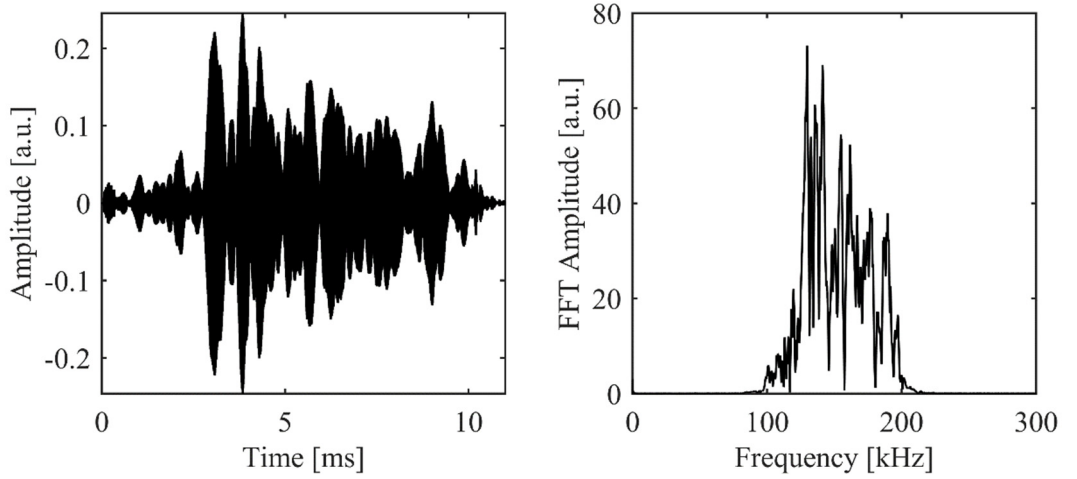
Figure 6.8: an example of the received signal time and frequency behaviour.

An example of the resultant PuC waveform obtained is shown in Figure 6.9. The arrowed sections indicate where multiple echoes from the back-wall are expected, using the known average longitudinal velocity in the sample from the prior through-transmission test:
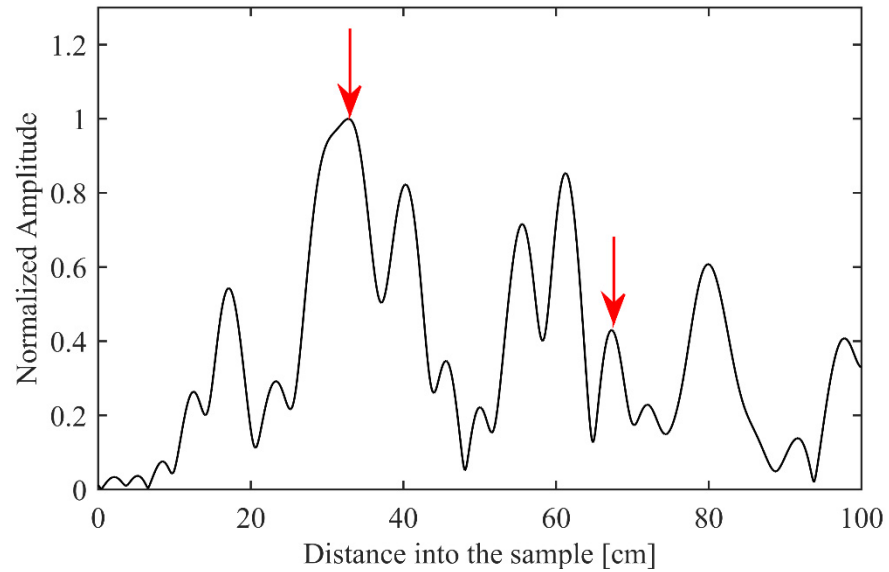
Figure 6.9: Pulse compression output. The red arrows indicate where the multiple echoes from the back-wall are expected.

It is evident that the presence of large aggregates creates a widespread scattering effect that results in several undesired high level peaks in the received signal, which arrive before the first back-wall echo. The presence of these peaks can complicate the identification of reflections from cracks and, in the worst of the cases, can even hide the background echo

of the samples under test. In addition, it was found that the results suffered from high variability. This is because:

1. The received waveforms shape and SNR depend on their position on the top surface of the brick sample, due to the different internal structure (distribution of the aggregates) seen by the transducer in each location.

2. The distribution of aggregates also varies considerably between different samples. This contributes to the problem of variability between readings.

3. The average longitudinal sound velocity varies from one brick to another. This results in a difficult selection of the time-window into which an algorithm for the crack detection must eventually be applied.

4. The dimension of the pair of probes (50 mm each) is comparable to the lateral dimension (115 mm) of the inspected bricks. This results in reflection of the sound energy from the brick side-walls and thus variability in the recorded signal.

A clear example of the received signal variability is shown in Figure 6.10, where three different cross-correlated signals acquired on the same brick but different transducer locations on the top surface are plotted, each one plotted with a different colour. The green arrow shows where the back-wall echo is expected. It can be seen that variability of the acquired signal is high, and also that the back-wall echo can be often hidden by the presence of scatterers and inclusions.
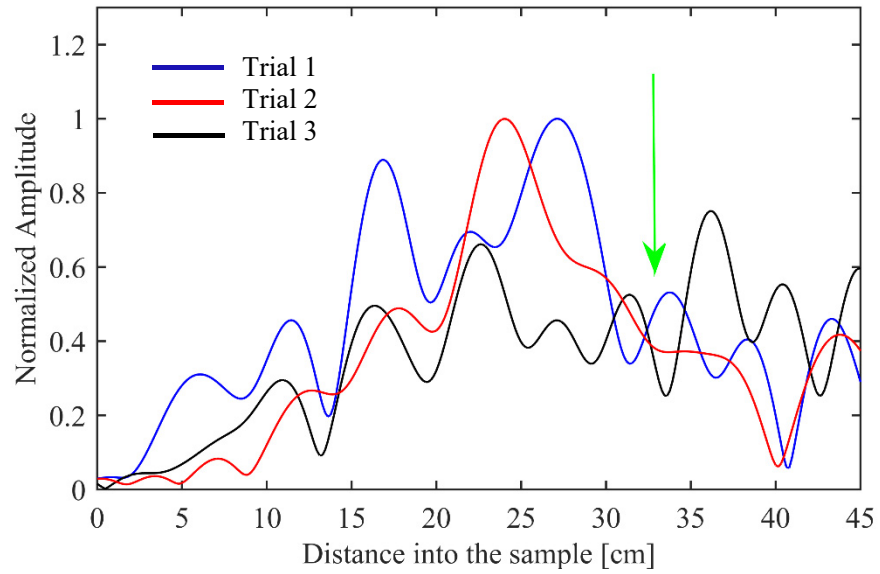
Figure 6.10: Variability of the cross-correlated signals for the same brick. The arrow represents the position at which the back-wall echo is expected.

6.3.3. Additional post processing steps

To tackle this problem, a strategy was developed by the author which analyzed the spatial and temporal distribution of the reflected energy. This was designed to help understand whether a crack was present or not within the sample. In particular, the total integrated energy was obtained from signals scattered back to the top surface by summing the contributions from different distances into the sample, over a chosen depth range. This value could then be plotted as a function of the distance traveled by the ultrasound signal into the sample itself. A threshold level for the cumulative (normalized) amount of the reflected energy was chosen – in this case at 90% of the maximum level. The depth value within the sample at which this threshold was reached was calculated and stored within a database for each sample. The process described was then repeated ten times per sample, with the transducers moved to different locations on the top surface in each case, so as to counterbalance the variability of the signals by means of mathematical averaging. The data is then represented as a histogram of the number of measurements that reached this 90%

level at a particular depth into the sample. A difference in the histogram values, and an average depth derived from them, could then be used to identify the presence of a crack in the sample.

Results are shown below in Figure 6.11 for an unbroken refractory brick (here Brick 1). The sound velocity taken into account for the processing is 3,208 ms^{-1}, which again corresponds to the average value for set 1. Ten waveforms were collected at different transducer locations and a PuC output obtained after cross-correlation with the input signal. Figure 6.11(a) shows the total energy received as a function of the distance traveled into the sample, using the aforementioned value of acoustic velocity. The curves obtained by simply normalizing each cumulative curve in Figure 6.11(a) by their respective maximum value are shown in Figure 6.11(b).
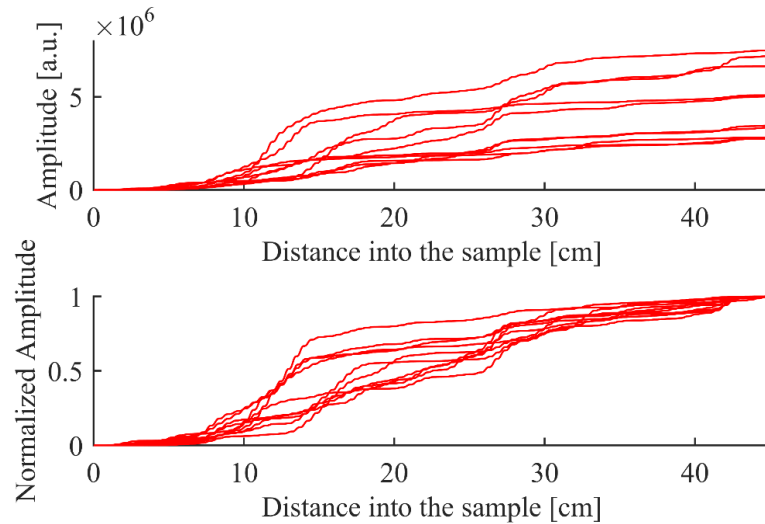
Figure 6.11: (a) Cumulative amplitudes of the reflected signal energy for 10 measurements; (b) normalized data of (a).

The distance for each transducer pair location at which the curves in Figure 6.11(b) reached the threshold level, called for simplicity "effective length", is then plotted as a histogram – a vertical value of 1 is assigned to that location. This is shown In Figure 6.12 for each brick sample, and the averaged value obtain is highlighted within each the plot.
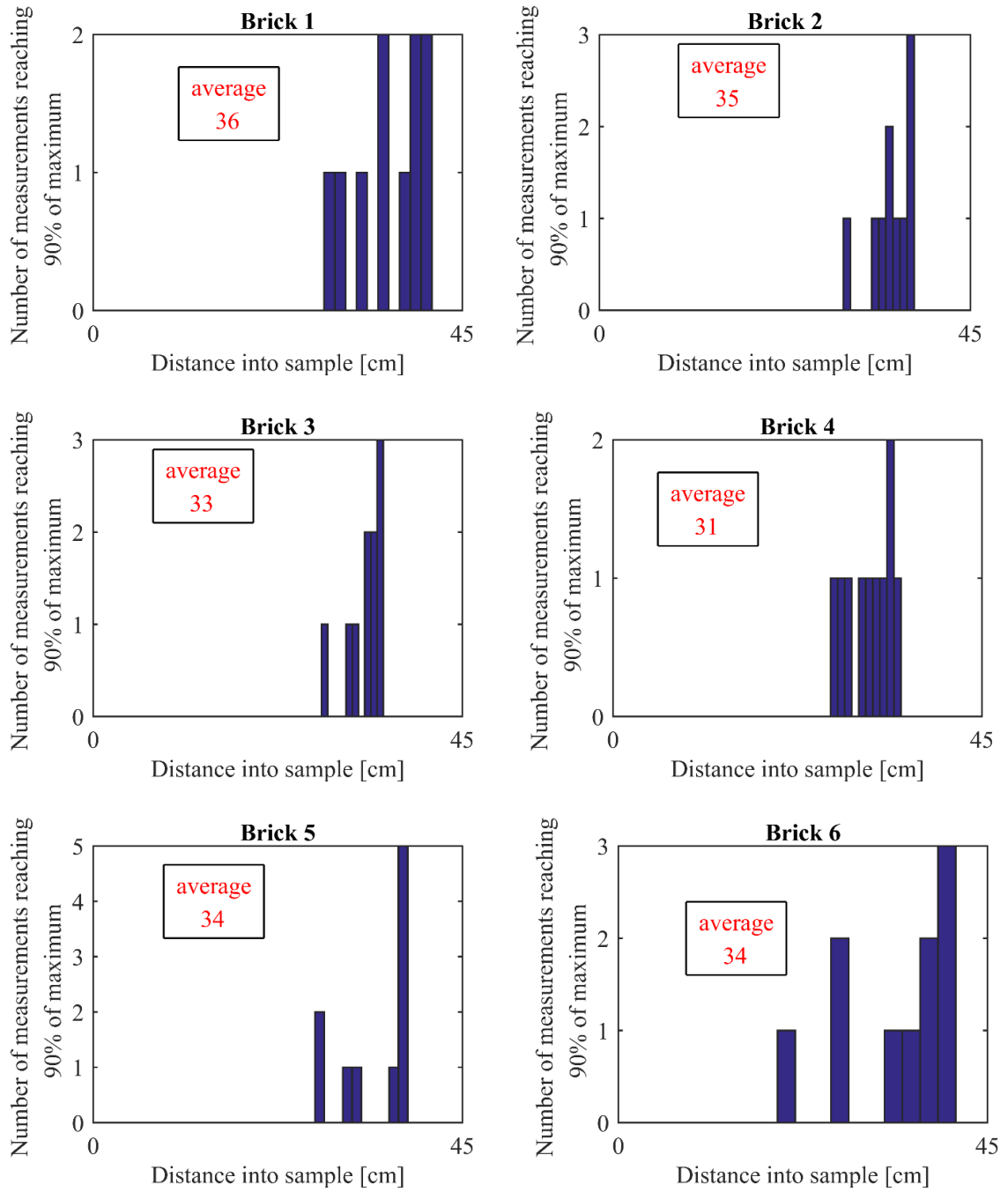
Figure 6.12: Effective length values in cm retrieved for each brick sample in set 1. The average values were derived from the data in each histogram (within the box in each figure).

It can be seen that the method estimated the real length of an unbroken brick well. In fact, the effective length retrieved values that differ from the real length of a brick (33.5 cm) by a maximum of 14%. If the sample is damaged, it would be expected that a change in the estimated effective length values would occur. This is because any crack located at any other position within the brick would act itself as a major reflector, thus shortening the effective

length value. To simulate the presence of a crack, sample 1 was cut into two pieces of 13.5 cm and 20 cm each respectively. The two pieces were then placed again in contact, so as to re-obtain the original brick. Figure 6.13 (a) shows the effective length result for brick 1 when the shortest piece is placed on the top of the longer one, whilst Figure 6.13(b) shows the same results when the inspected broken sample is flipped upside down, hence when the longer part is in contact with the transducers surface:
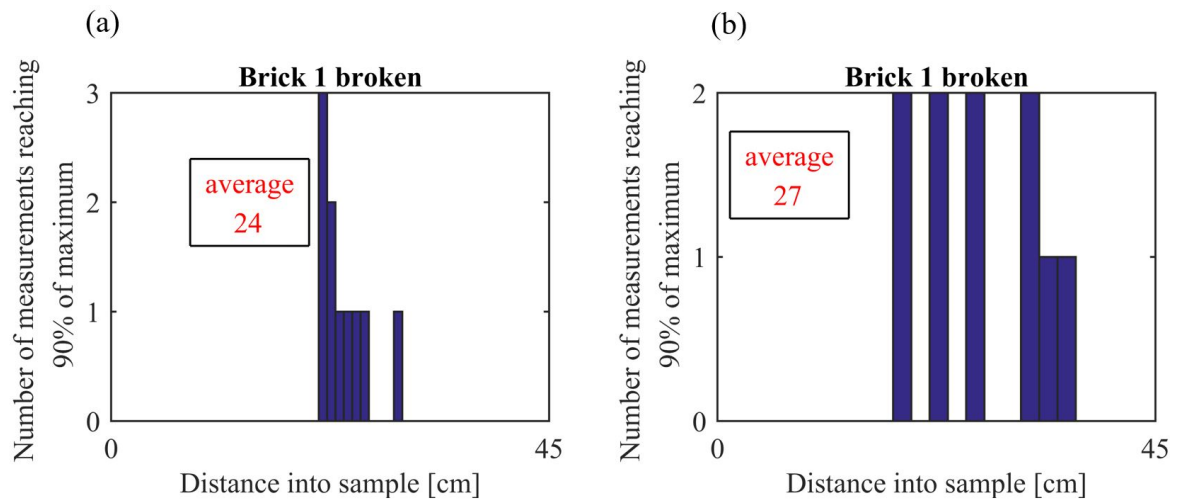
Figure 6.13: Results on brick 1 broken when (a) its shorter part or (b) its longer part is in contact with the transducers.

It can be seen that the effective length values retrieved are shorter than those measured for an unbroken brick (see Figure 6.12). To further corroborate the validity of the chosen approach, sample 3 was cut as for the procedure followed for sample 1. The results are reported in Figure 6.14. Again Figure 6.14(a) shows the effective length result for brick 3 when the shortest piece is placed on the top of the longer one, whilst Figure 6.14(b) shows the same results when the inspected broken sample is flipped upside down, hence when the longer part is in contact with the transducers. Again, the results confirm the validity of the approach used.
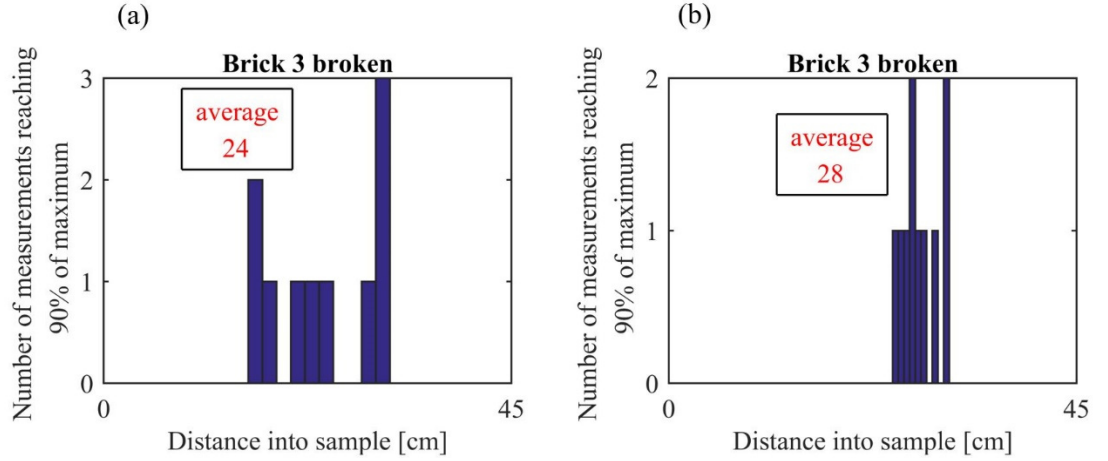
Figure 6.14: Results for broken brick 3 when (a) its shorter part and (b) its longer part is in contact with the transducers.

Another set of brick samples, called for simplicity "set 2", was then inspected for further confirm the results obtained. Those bricks sample are shown in Figure 6.15:
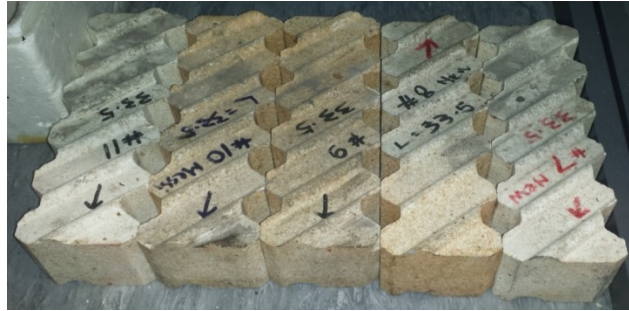
Figure 6.15: A picture of brick samples (set 2).

Those bricks had all the same length as set 1, *i.e.* 33.5 cm, but the average value of the sound velocity was now estimated to be 4,647 ± 215 ms⁻¹. The sound velocity values for each sample of the new set is shown in Figure 6.16, together with the average value (red line). Taking into account the average speed of sound value (4,647 ± 215 ms⁻¹), the estimated length for each sample has been again calculated (Figure 6.17). Again, the retrieved values agree well with the real length of the samples.
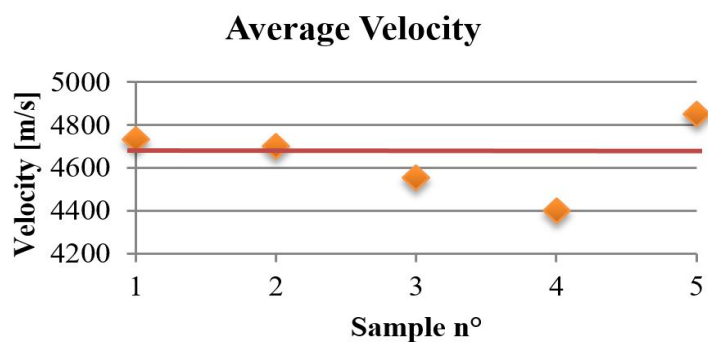
Figure 6.16: Sound velocity for set 2.
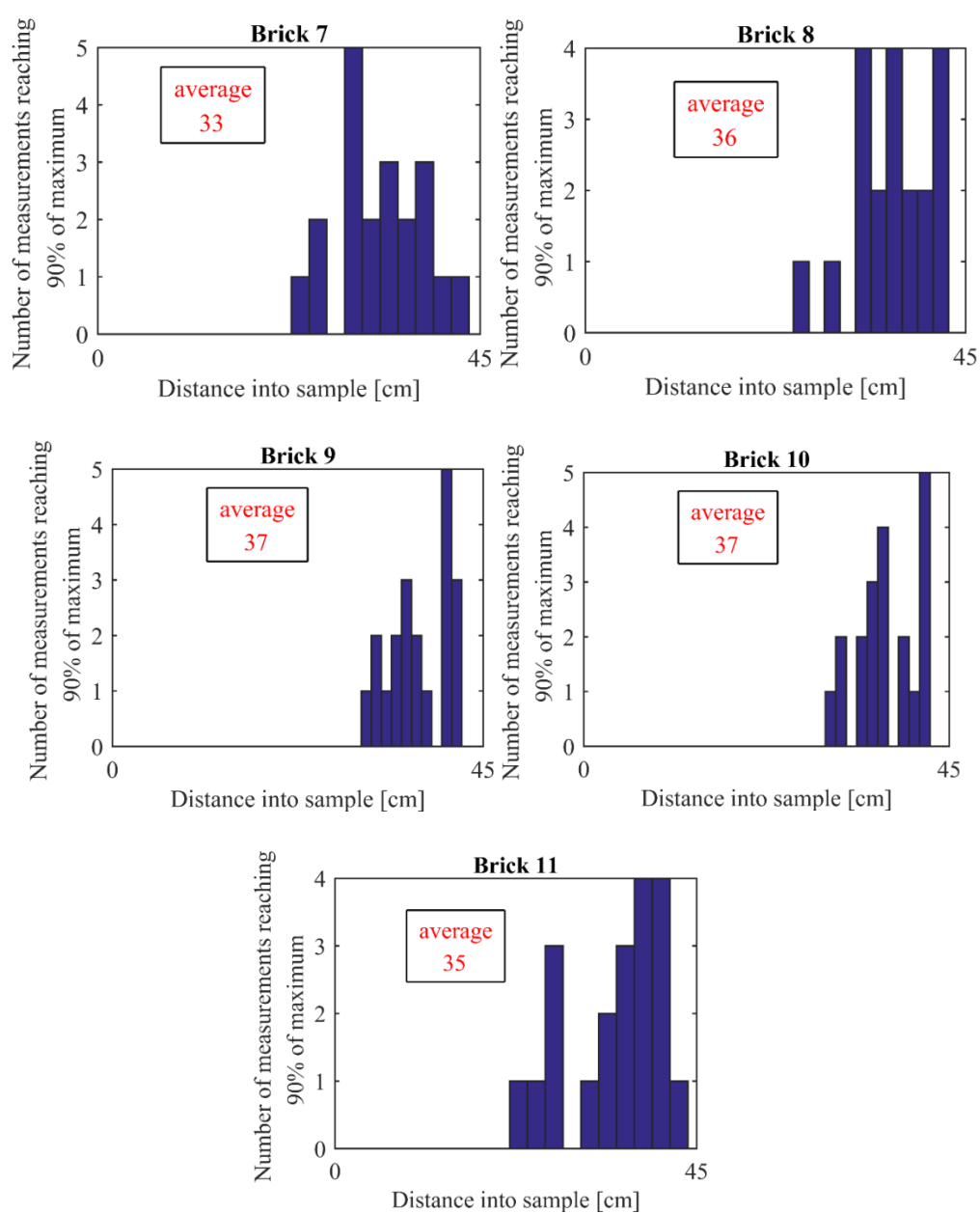
Figure 6.17: Effective length values retrieved for each analysed brick samples, set 2.

As before, brick 10 was now cut into two pieces having different length. The results in Figure 6.18(a) show the effective length retrieved on the broken sample when the shorter piece was placed on top the longer one, and Figure 6.18(b) shows the effective length of the inverted configuration:
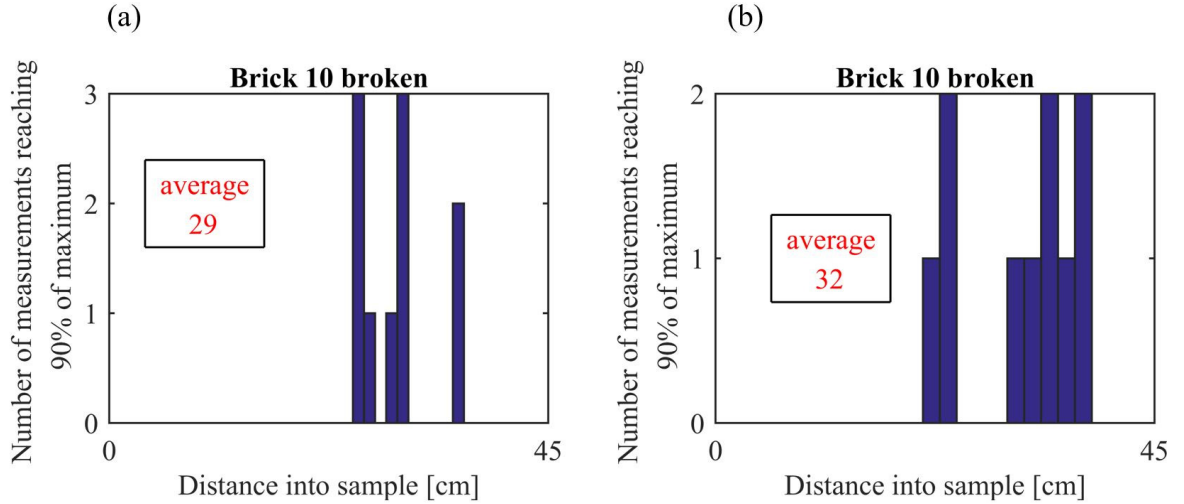
Figure 6.18: Results for brick 10 when broken so that (a) its shorter part or (b) is longer part is in contact with the transducers.

Although the obtained value for the broken sample in Figure 6.18(b) (32 cm) slightly differs from the one retrieved for the sound sample (see Figure 6.17 – brick 10), this value is still likely to be acceptable for the technique to give discrimination between a whole brick and its broken replica.

The described approach relies on the *a priori* knowledge of the velocity of sound of each set brick. In a real application of the technique, it is reasonable to have a database of the sound velocity of the samples used to build a furnace. However, when the inspection takes place it is impossible to know to which set of brick belongs the inspected sample. To simulate this uncertainty, the technique has been again applied on sample 1, sample 3 and sample 10 and their broken replica, by now using a sound velocity value obtained from averaging the sound velocities of set 1 and set 3. This new value was 3,862 ms^{-1}. Those results are reported in Figure 6.19:
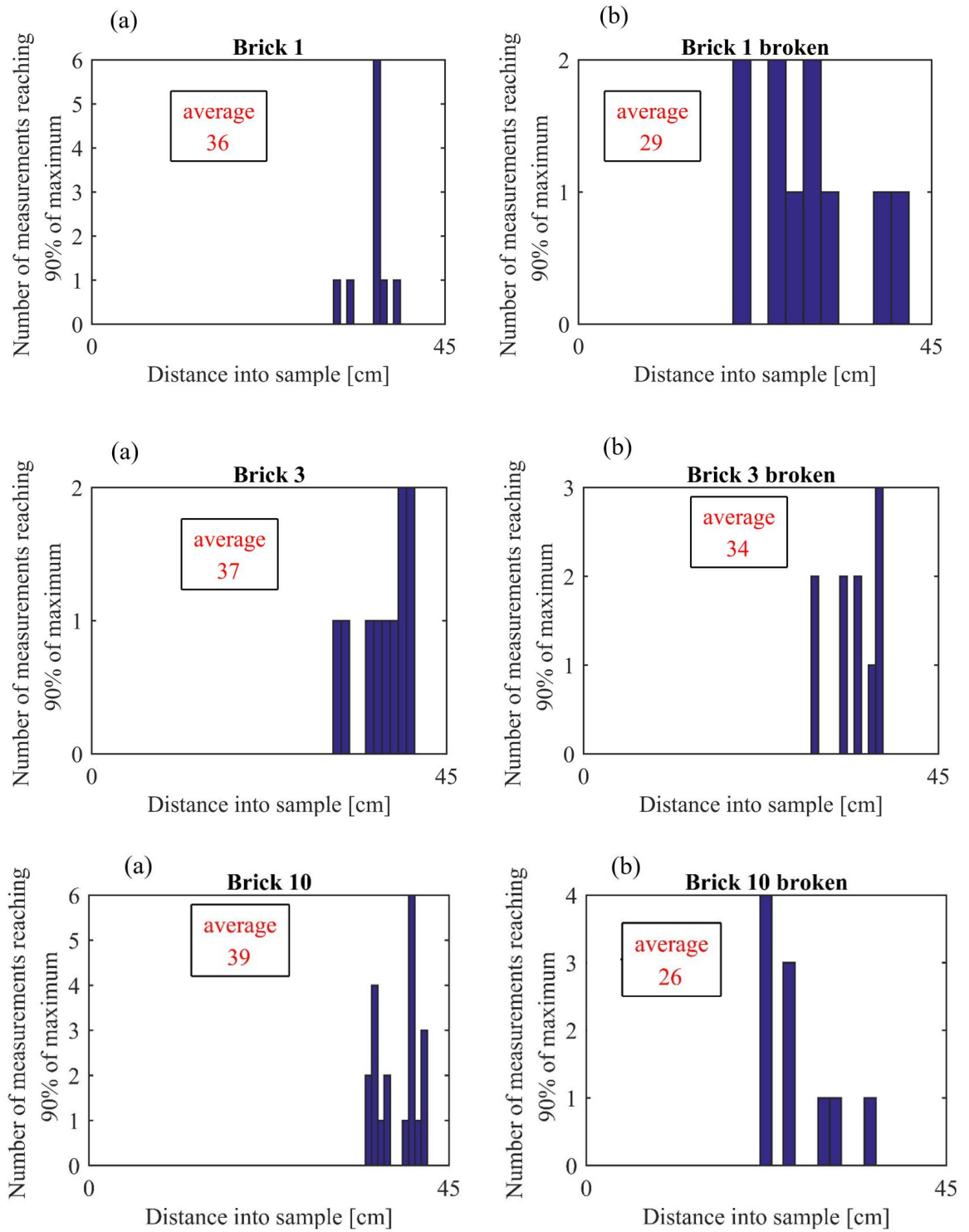
Figure 6.19: Effective length for both (a) unbroken and (b) shortened bricks 1,3 and 10, obtained by using a sound velocity value that was the average of set 1 and set 2.

It can be seen that this method leads to results that are not totally correct, as the effective length value of the samples, whether broken or not, can be much higher than the real sample length. To overcome this uncertainty, an alternative strategy has been looked at

in order to differentiate sound samples from broken ones. Figure 6.20 shows the behavior of the cumulative reflected acoustic energy (normalized) as a function of the distance into the sample. This is shown for sample 3 in both its sound state and its broken state. The blue line indicates the 0.9 threshold level chosen to calculate the effective length parameter.
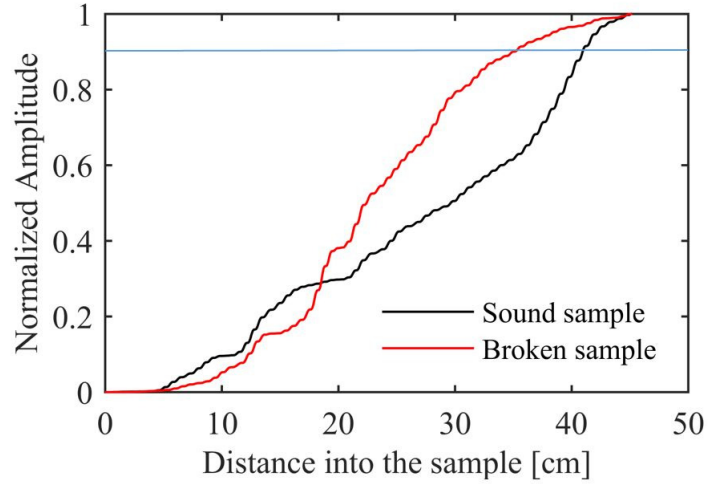
Figure 6.20: Normalized cumulative reflected energy for sample 3 when at full length (black) and broken (red). The blue line indicates the 0.9 threshold level chosen to calculate the effective length parameter.

By looking at Figure 6.20, it can be seen that the amount of energy returning to the top surface in pitch-catch mode increases more quickly to the 90% threshold level for the broken sample (black line) than for the full-length one (red line). Thus, the idea is that the slope of this line, obtained by differentiating this curve, can be used as a parameter to distinguish a full-length sample from a broken one. The steps that have been followed to obtain then new set of comparative results are:

1)   The normalized cumulative of the reflected energy of each of the measurements are first recorded as before for repeated measurements on the same sample. These are then post-processed (Figure 6.21(left)) so as to obtain the average curve (Figure 6.21(right)) to represent the data for that particular sample (in this case sample 1). Please note that the x-

axis is in the form of data points (acquisition samples) and not distance, so that the processing is simplified.
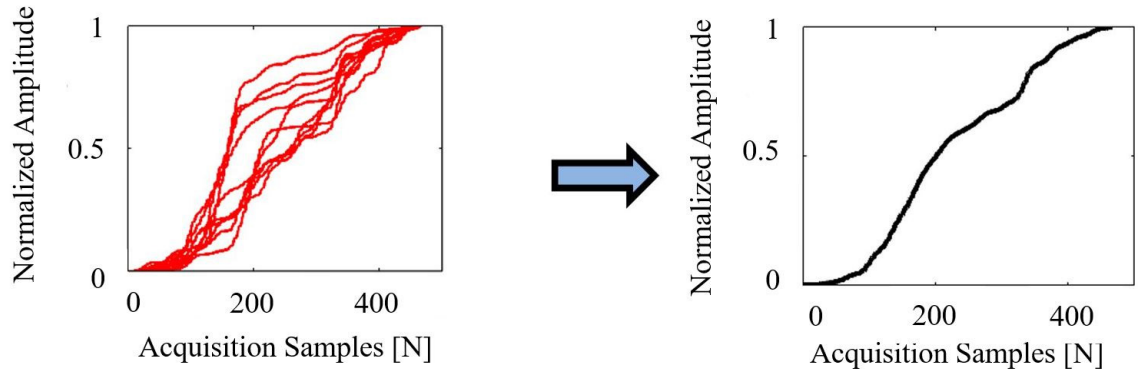
Figure 6.21: Normalized cumulative of the reflected energy for sample 1. This is shown for multiple measurements (left) and their average value (right).

2) This curve is now differentiated to give the behaviour of the mean curve derivative (Figure 6.22 (right)):
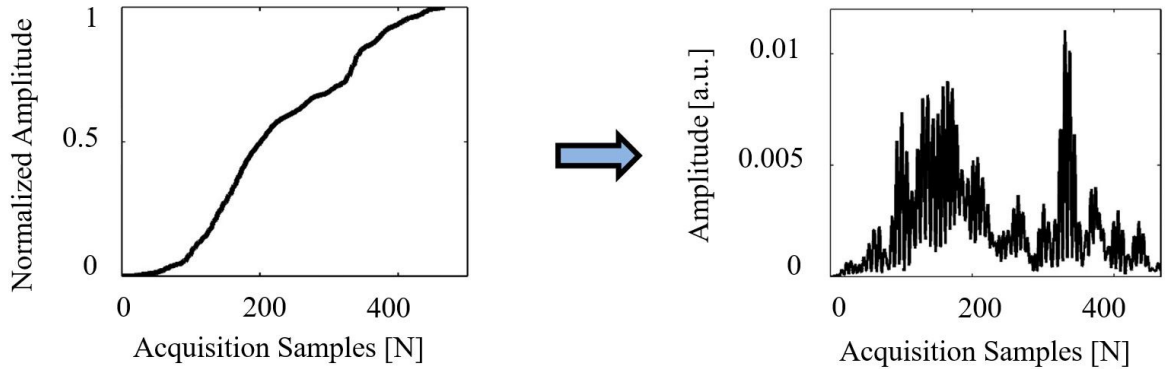
Figure 6.22: Obtaining the derivative of the cumulative energy curve (right).

The results of performing this analysis for samples 1, 3, 10, and comparing the results for full-length samples against their broken counterpart are shown in Figure 6.23. It is clear for these figures that the analysis shows a clear difference between the samples that are at their original length, and those that are broken:
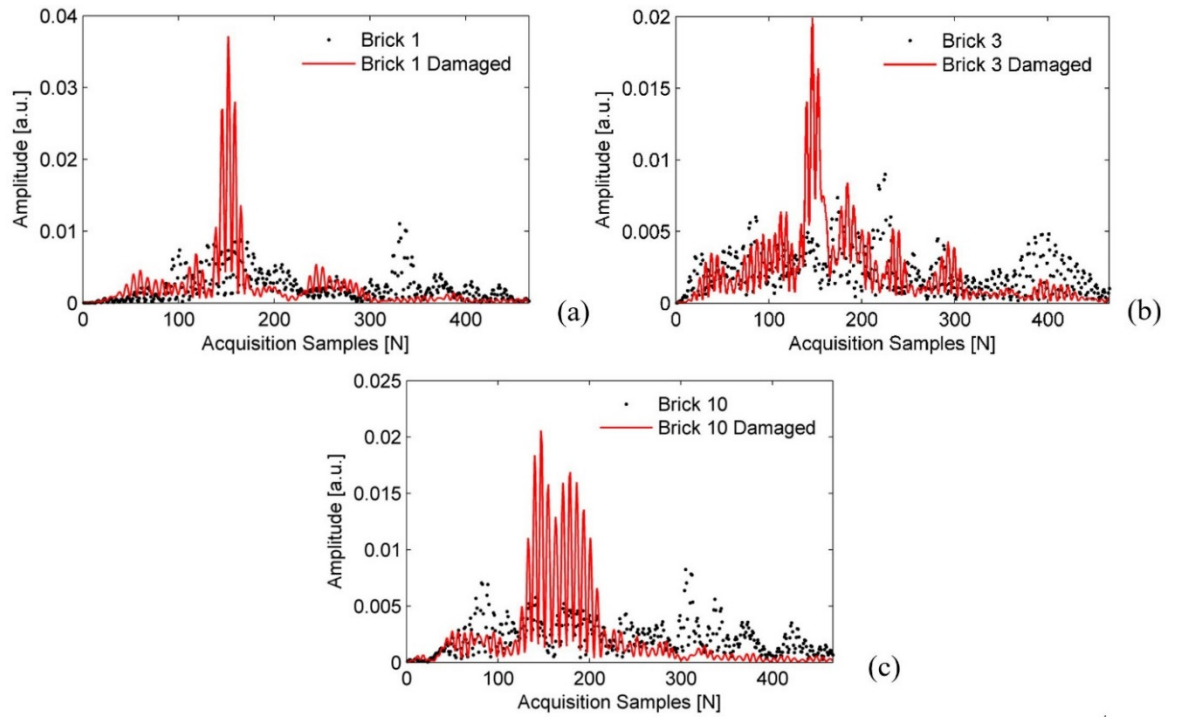
Figure 6.23: Derivative of the normalized reflected energy for: (a) Brick 1(black dotted) and brick 1 broken(red); (b) Brick 3 (black dotted) and brick 3 broken(red); (c) Brick 10 (black dotted) and brick 10 broken (red).

It can be seen in Figure 6.23 that the damaged bricks (the red curves in all three cases) show large peaks that are not present to the same extent in the unbroken samples, and further that they occur earlier in the data sequence (*i.e.* at smaller depths from the sample surface). This analysis could thus be used as a possible screening method. However, a more robust solution is to combine data. This uses both the maximum amplitude of the derivative data, and the estimated effective length of the sample (obtained from thresholding the cumulative returned energy data assuming an average propagation velocity value of 3,862 ms^{-1}). The results of this are shown in Figure 6.24 for all samples, both full-length and broken.
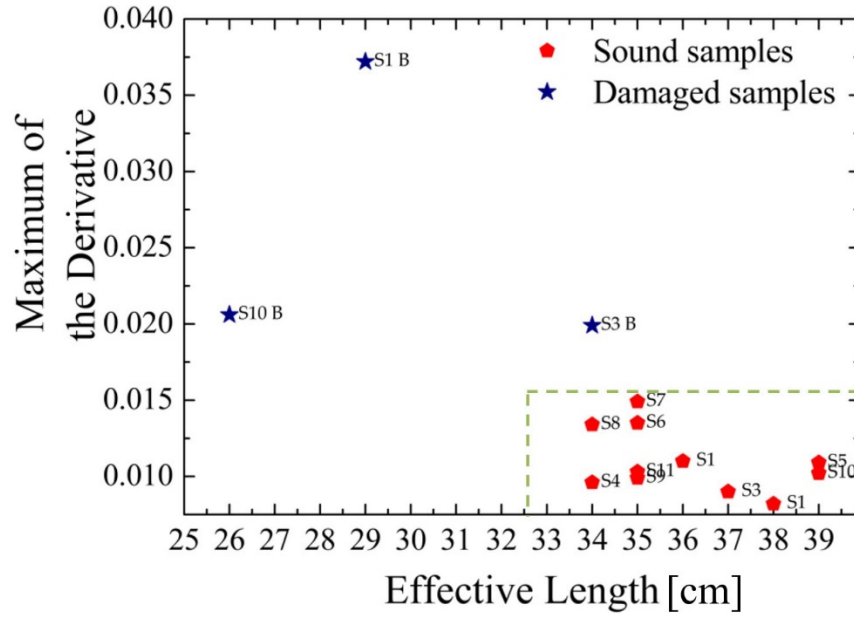
Figure 6.24: Maximum value of the derivative as a function of the effective length for all samples, the latter assuming the average velocity for all bricks in both sets of samples

It can be seen that the broken samples tend to cluster in different regions of the graph than those that are unbroken and at full length. The additional processing methods show that it is possible to see the presence of a crack even though the sound velocity is assumed to be at an average value. This is because the derivative of the normalized cumulative energy curve of a broken sample shows a sharper and higher amplitude peak when compared to a sound sample. In the Effective Length/ Maximum of the Derivative space it is possible to clearly distinguish the broken sample from the sound ones.

6.3.4. Detection of partial cracking

The next problem was trying to establish whether a brick that had a partial fracture, so that it did not extend fully across the sample, could be distinguished from a sound one and in addition whether the algorithm showed sensitivity to increasingly deeper partial cracks. For this purpose, Brick 8 was cut in steps of 1 cm across its width (~ 8 cm), to simulate a crack that grows gradually across the sample at a certain distance from the top

surface. This has been done first for a distance of 10.5 cm from the top surface (Cut I), and then at two other locations (Cut II and Cut III) as shown in Figure 6.25:
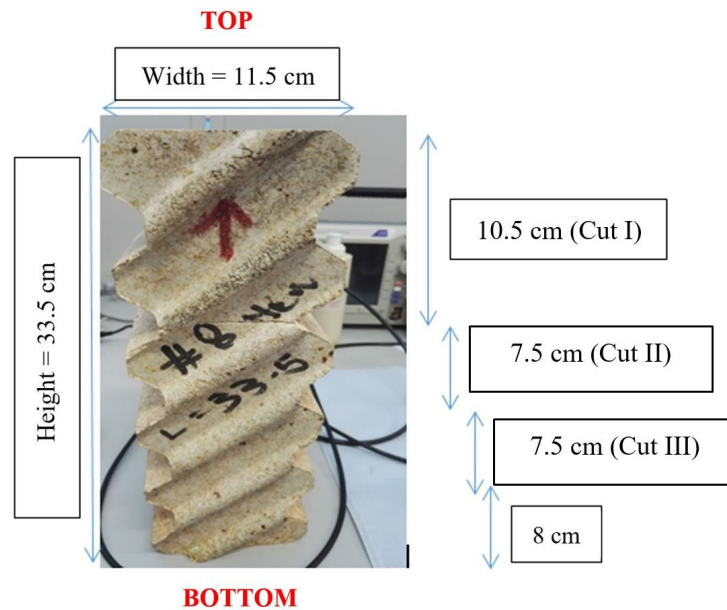
Figure 6.25: Brick 8 samples and steppes cuts relative distances.

The results obtained for "Cut I" after making the simulated horizontal crack deeper in 1 cm steps are shown in Figure 6.26, where the depth of the horizontal cut into the brick and the estimated effective length values are showns. Please note that again the velocity of sound used for the processing is averaged value of both set 1 and set 2 was 3,862 ms^{-1}. It can be seen again that the location of the crack was not determined exactly, as an average value of sound velocity had to be assumed; if this was measured separately, then this could be corrected. However, it can be seen that even the 1 cm deep cut was detected well by the method, and that thereafter the depth of the cut had little effect on the average value of the estimated distance from the top surface.
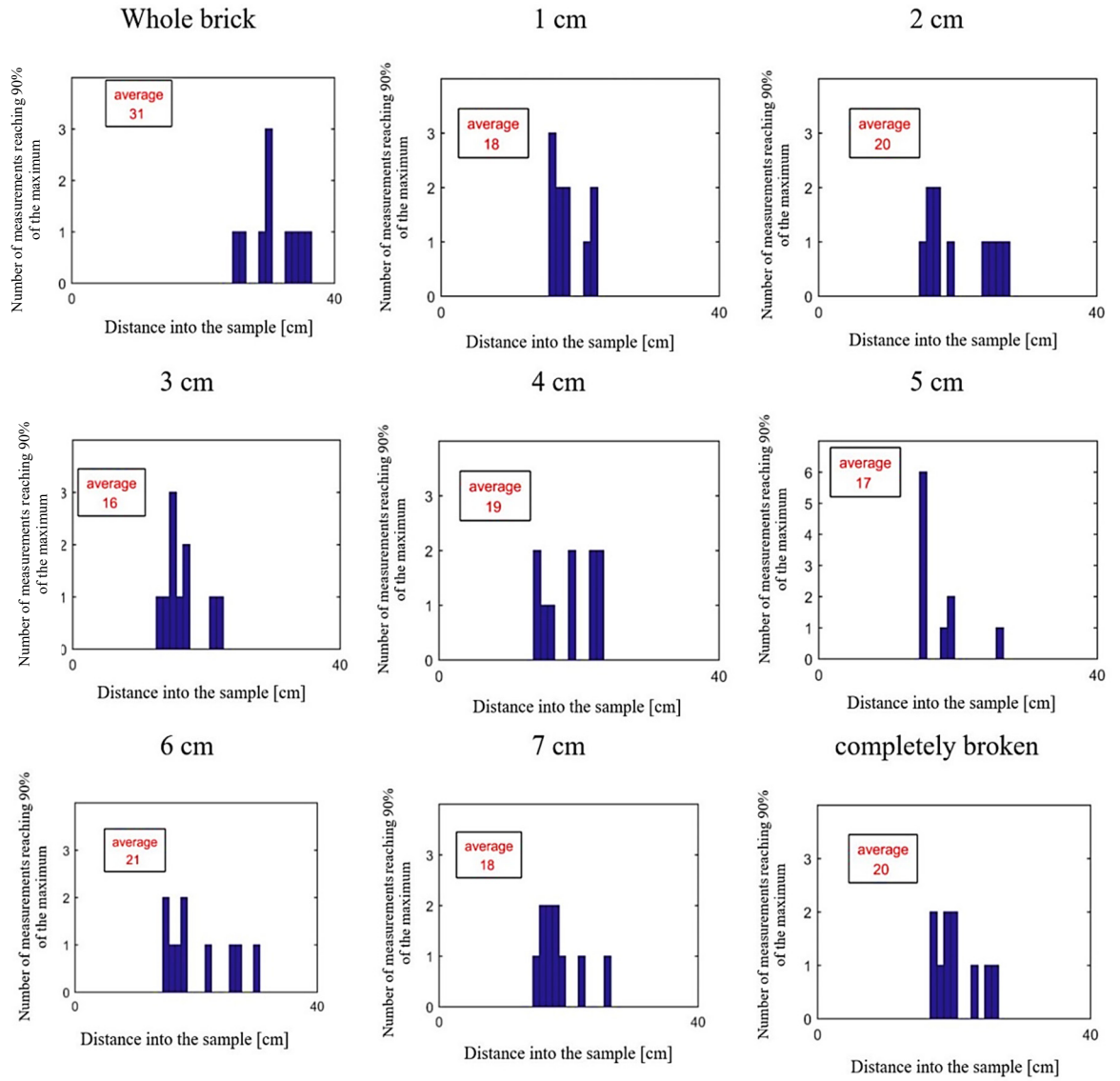
Figure 6.26 : Results for increasing the depth of cut into the sample, at a distance of 10.8 cm from the top surface (Cut I).

An alternative analysis strategy was thus considered: one that relies on the difference of the normalized cumulative reflected energy between a sound sample and broken one. The first step is to take the derivatives of the energy curves, as was shown earlier in Figure 6.23. Then, for each depth of cut, simulating an increasingly deep crack across the sample, the maximum value of the average derivative curve is calculated. This is then combined with the estimated "Effective length" (*i.e.* the estimated distance of the main reflector from the top surface as before) of the sample leads to form a 2D feature plot. This is shown in Figure 6.27 for Cut I:

Figure 6.27: 2D feature plot for Cut I data.

The data point for an unbroken (sound) sample is at a totally different location (at bottom right) than for those for cuts of different depths; these tend to cluster in a different region of the graph than those that are unbroken and at full length (33.5 cm). This additional processing method shows that it is possible to see the presence of a crack even though the sound velocity is assumed to be at an average value. This is because the derivative of the normalized cumulative energy curve of a broken sample shows a sharper and higher amplitude peak when compared to a sound sample. In the "Effective Length/ Maximum of the Derivative" space it is possible to clearly distinguish the broken sample from the sound ones. There also seems to be a trend in the data, with a more extensive crack leading to the data point going more towards the top of the plot, as the maximum derivative value increases. There is also a tendency to move slightly to the left at the same time, i.e. tending towards the true value of the "Effective Length", i.e. the distance from the top surface.

The above analysis was repeated for simulated cracks that were a distance of 18 cm and 25.5 cm from the top surface (Cut II and Cut III respectively). The results are shown in the feature plots of Figure 6.28 and 6.29 respectively. Similar trends are seen. The more extensive the crack across the sample, the more the data point tends towards the top left-hand corner of

the 2D feature plot. It can thus be concluded that, with these additional post-processing steps, the method has shown to be a good one for determining not only whether a horizontal crack is present, but also its approximate location and its depth of penetration across the sample.
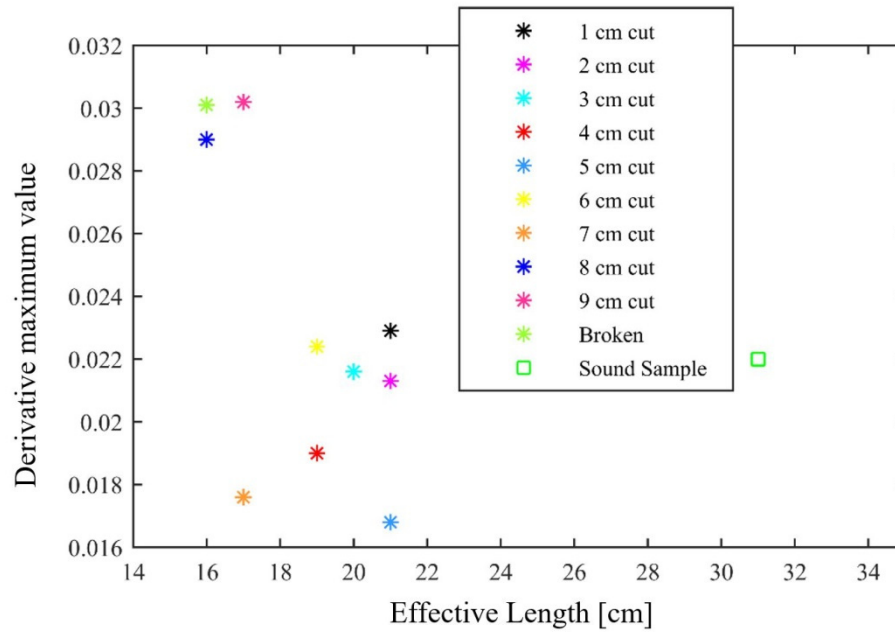
Figure 6.28: 2D feature plot for Cut II data at 18 cm from the top surface.
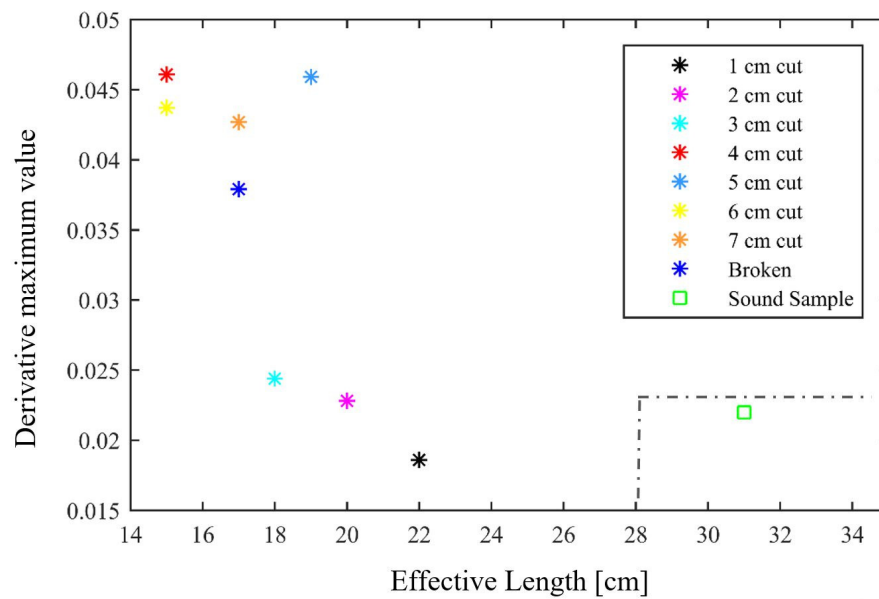
Figure 6.29: 2D feature plot for Cut III data at 25.5 cm from the top surface.

6.4   NDT of a Polyurethane Riser Stiffener

6.4.1. Introduction

Polyurethane polymers are used in many industrial products [3], [4], an example being flexible risers used in the offshore oil and gas industries, used to carry oil and gas to surface platforms from the sea bed [5], [6]. Following oil spills in highly-fragile ecosystems in recent years, it is important that structures containing polyurethane material can be inspected [7]–[10]. In particular, the inspection described in this section shows again the importance of choosing carefully both the coded signal and the imaging processing algorithms to obtain detailed information about the internal structure of the polyurethane sample. It is known that polyurethane exhibits high attenuation at frequencies >1 MHz [11]. It thus seemed to be a good application for pulse compression at lower frequencies.

The work in this Section has been the subject of a recent journal paper [1]. Some of the data used to produce the results contained in this Section was recorded by another researcher as joint work, which was sponsored by BP who donated the samples to this research. The present author developed the PuC software used to capture data, analysed the effects of the pitch-catch geometry used, and created of Synthetic Aperture Focusing Technique (SAFT [12]) analysis software used to analyse the data and plot the results. It is shown here to illustrate the use of PuC in another important industry.

Figure 6.30(a) shows the polyurethane sample, part of a larger conical shape used as a riser stiffener to relieve the strain on the flexible riser at junctions between sections (with some transducers shown attached to each surface (ringed)). The sample shown was 1.2 m long, and 0.16 m thick at its thicker end. Fig. 6.30(b) shows the chosen pair of transducers

for use in pitch-catch mode, these being the same transducers described earlier in Figure 6.2(a), which were spring-loaded onto the sample surface.
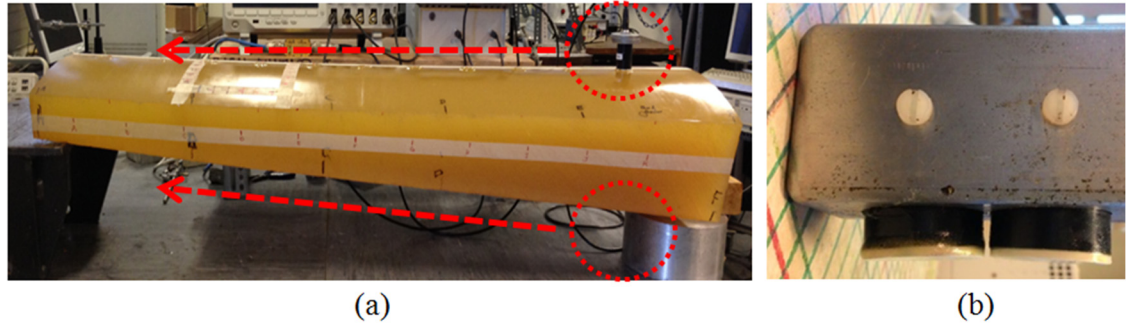
Figure 6.30: (a) The section of riser stiffener under test. (b) The piezocomposite transducer pair.

The sample contained natural air bubble defects which were formed during manufacture. Figure 6.31 shows two air bubbles of ~ 5-7 mm diameter at an unknown depth within the sample. Furthermore, in order to have a reference defect, a 10 mm diameter hole was drilled manually to a depth of 80 mm the top surface of the sample. The data was recorded across a regular 46 mm by 70 mm grid in steps of 2 mm, with the 25.4 mm diameter probes moved in unison in their holder (Figure 6.30(b)) to record a pulse compression waveform at each location.

Figure 6.31: Photograph of the bubbles in the polyurethane sample.

6.4.2. Simulations of probe geometry

A simulation was performed to establish the combined directional characteristics and sensitivity of the pair of transducers shown in Figure 6.25(b). If d and λ are the transducer

diameter and the ultrasonic wavelength in the material, the near-field distance limit Z_{nf} can then be calculated from Equation (6.1) [13]:

$$Z_{nf} = \frac{d^2}{4 * \lambda} \tag{6.1}$$

The longitudinal velocity in the polyurethane sample was calculated to be 1,700 ms^{-1}. This value was estimated by a series of measurement carried out by placing the probes in through transmission configuration. The centre frequency of the excitation waveform was 300 kHz, using piezocomposite transducers having d = 27 mm. Thus, we obtain Z_{nf} = 32 mm. This value is valid only if a single transducer is considered. However, further investigation was needed if two transducers in pitch-catch configuration were to be used for the signal generation/acquisition, as in this work, where both transducers operate at normal incidence, but with overlapping beam profiles within the sample. Thus, a series of numerical simulations was performed, using the geometry shown in Figure 6.32(a).

The approach used for simulating the sensitivity field is similar to that used for Distance Gain Size (DGS) diagrams [14]. DGS diagrams are in fact designed to show the variation of echo amplitude with range and target size. Therefore, the expected defect signal amplitude is here calculated with respect to the back-wall echo (considered as a perfect reflector). The numerically obtained DGS curve at a frequency of 300 kHz for either a single transducer in pulse-echo mode (continuous lines) or a pair of transducers in pitch-catch mode are shown in Figure 6.32(b). The black line (either in foreground or in background) shows the expected signal amplitude from a perfect reflector. It is thus possible to note that in the nearfield, in particular at smaller axial distances, the pulse-echo configuration (background blurred lines) is predicted to be more advantageous than a pitch-catch configuration (foreground). This is mainly due to geometrical reasons - the transmitted and received beams overlap more effectively. However, the sensitivity of both the configurations converge to similar values in the far-field. Therefore, the SNR gain of PuC then improves signal

detectability. This fact is of utmost importance, if the signal echoes have to be retrieved from highly attenuating materials at large distance from the transducers.
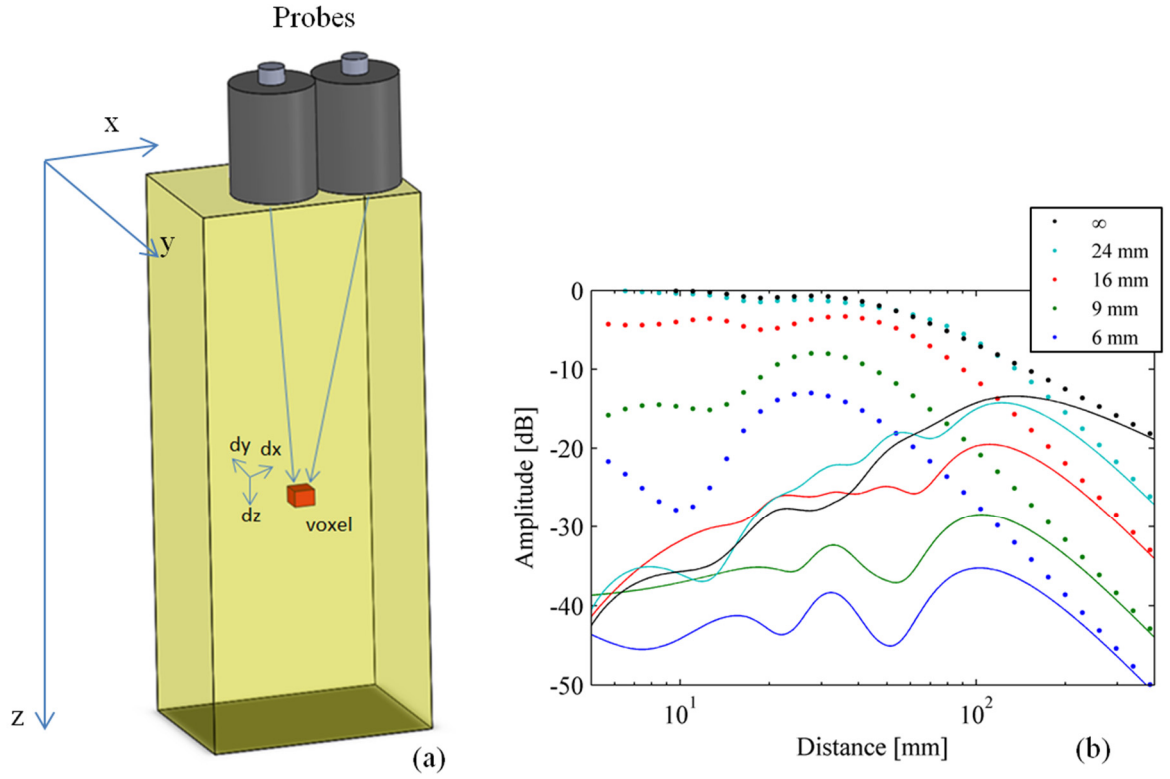
Figure 6.32: (a) Geometry used for simulating the transducer response in pitch-catch mode for transducers of 25.4 mm diameter. (b) Simulated DGS at 300 kHz for different defects sizes in a polyurethane sample. Solid lines: a pitch-catch transducer pair; dashed lines: a single transducer in pulse-echo. The coloured lines show the expected received amplitude levels for spherical defects of diameter 24, 16, 9 and 6 mm. Also shown is the response for a defect of infinite width (black line).

In order to understand better the 3D sensitivity field behaviour of the pitch-catch configuration, an additional series of simulations have been performed. The Rayleigh-Sommerfield integral model has been used for these simulations, together with the piston-transducer approximation [15]. In this way, the sensitivity of the transducers to a certain location in 3D space can be estimated. As an example, numerical simulation results are shown in Figure 6.33 at a depth of 5 mm within the simulated geometry of the polyurethane sample, where the sensitivity level of the two probes has been plotted at 300 kHz. As

expected, the combined sensitivity level of the two probes is higher in the region between the transducers.
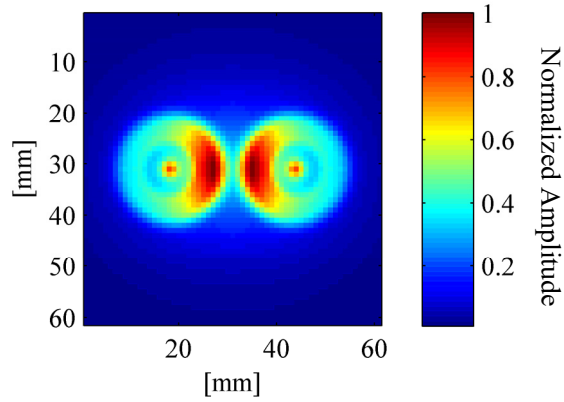
Figure 6.33: Simulated sensitivity for the pair of piezocomposite transducers at 300 kHz, at a depth of 5 mm into the sample.

It would thus be expected that changing the alignment of the pair of the transducers on the surface with respect to the direction of the scan should results in a change on the recorded signals. To gain insight into this, Figure 6.34 shows the 3D transmit/receive sensitivity variation for a pitch-catch transducer configuration for different distances into the sample. Note that the red arrow corresponds to the scanning direction chosen to highlight the effect of the sensitivity along a chosen scanning direction. It can be observed that the combined sensitivity is far from being homogenous for small depths, as the beams from the two transducers have not overlapped fully. This has to be taken into account when small defects have to be detected and imaged at small depth from the scanning surface, as the probability of detection would be a function of the transducer pair orientation. However, it can be seen that the sensitivity field becomes flat at deeper depths within the far field. This far field condition is also reached at distances much greater than that expected for a single transducer (32 mm, as for Equation (6.1)). In the sample under test, the artificial hole is within the near-field, so far-field sensitivity condition cannot be assumed.
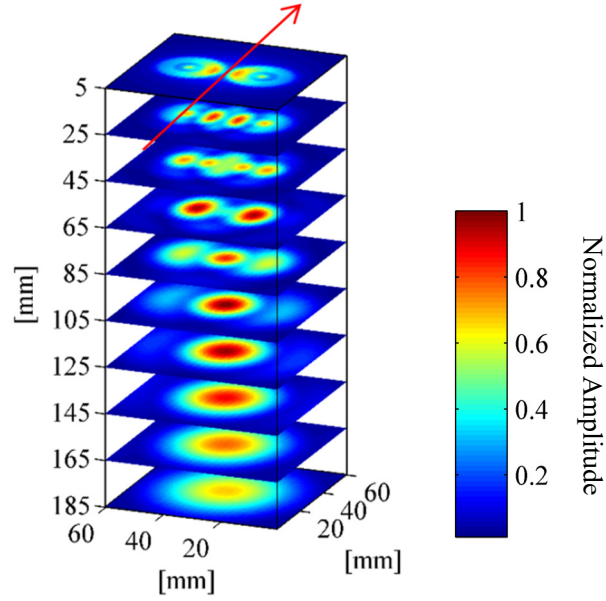
Figure 6.34: Simulated 3D sensitivity field for two piezocomposite transducers in pitch-catch mode. The red arrow indicates the scan direction chosen.

6.4.3. Experimental results

The high attenuation in the material meant that the input signal waveform has to be chosen carefully, so as to maximize the output amplitude from a given transducer. In this experimental activity, a linear chirp and an Inverse Repeated Sequences Golay (IRS-Golay) binary sequence were compared. The properties and performace of those signals were deeply described in Chapter 2. Again, a Golay-code would be expected to be an optimal excitation for a wide bandwidth transduction systems, whereas the chirp could be tuned to suit a narrower, more resonant transduction. In the present case, the transducers have a quite large bandwidth, so both schemes could work. Furthermore, the IRS Golay scheme allows a centre frequency to be selected. For this reason, it was selected here for the comparison.

Figures 6.35 and Figure 6.36 show the chirp and IRS-Golay input signals, using the same voltage level of 2V pk-pk. The linear chirp was Elliptical-Tukey windowed, so as to assure low side-lobes level [16]. It can be also noted from Figure 6.36 that the bandwidth of the IRS-Golay was greater (almost extended to DC), without having a completely

symmetrical frequency spectrum. As expected, the spectrum amplitude of the IRS-Golay code was higher with respect to the chirp one, as explained in Chapter 2. Note that for the sake of clarity, shorter signals were depicted in Figures 6.35 and 6.36, with respect to that used for the experimental data campaign (see Figures 6.37 and 6.38). In particular, the experimental results were collected by using a Chirp signal of about 1.5 ms of duration. This was to increase the SNR gain and the compression quality, as explained below.
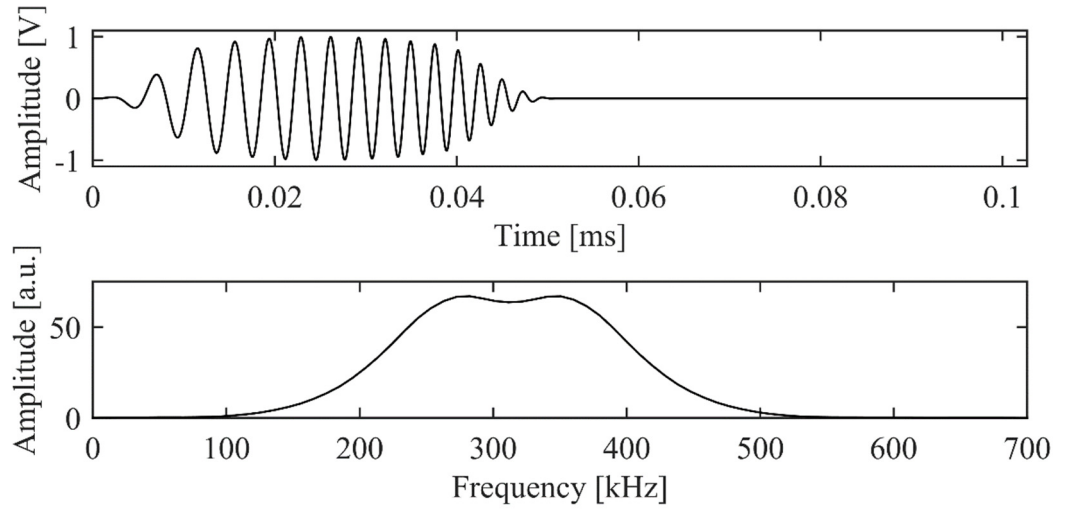
Figure 6.35: input chirp signal and its spectrum.
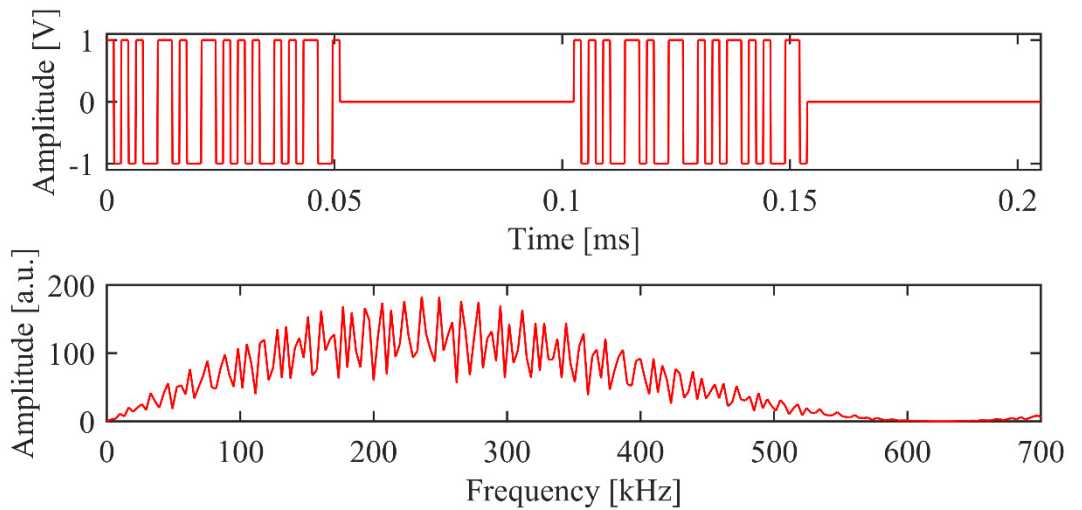
Figure 6.36: Input IRS-Golay signal and its spectrum.

Figure 6.37 the autocorrelation output of chirp and IRS-Golay signals:
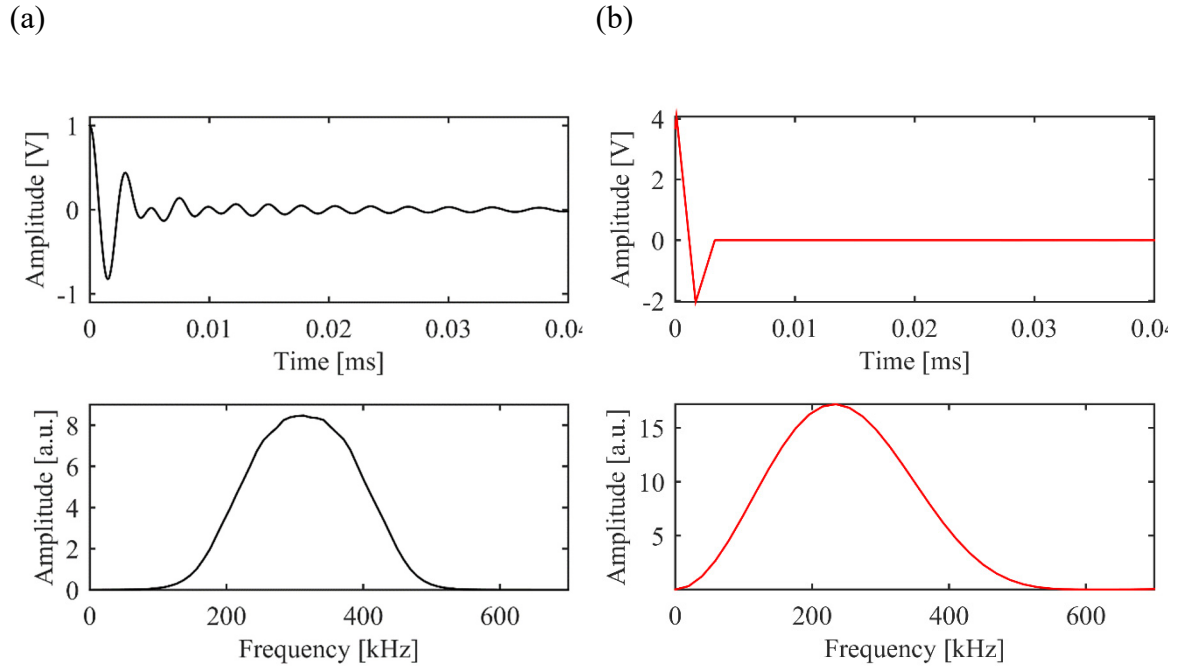
Figure 6.37: Autocorrelation function of (a) Chirp and (b) bipolar Golay code signals, showing the time waveform at the top and the corresponding frequency spectrum below.

Figure 6.38 shows an example of an acquired signal obtained in a pitch-catch configuration. The signal show an echo before the back-wall reflection, which is due from the sound reflection on one of the air-bubble defects of Figure 6.31, located approximatively at a depth 50 mm below the scanning surface. The two figures show the differences in the response when either the chirp or the Golay code was used to drive the transducer. For chirp excitation, it is clear that a very good signal was obtained with the piezocomposite pair, showing that PuC had worked very well with these transducers in this highly-attenuating material. In particular, the extension of bandwidth up to frequencies of 350 kHz was an excellent result. For the Golay code excitation, this bandwidth was extended even further.
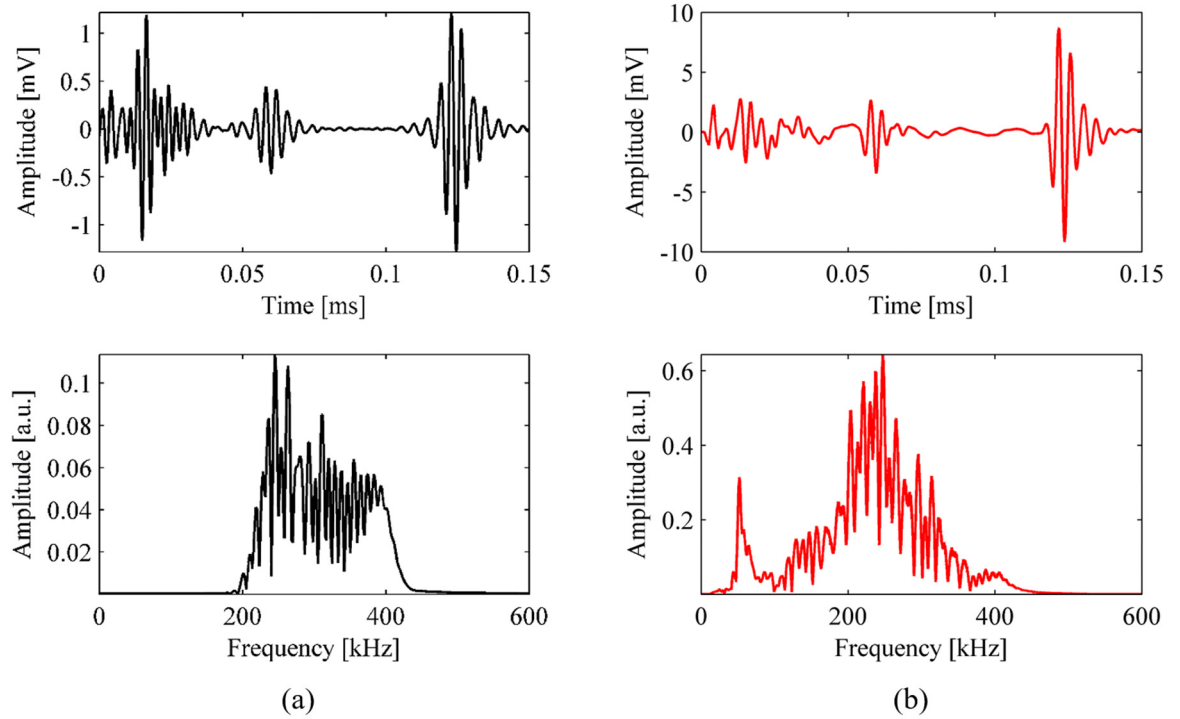
Figure 6.38: recorded signal scattered from a sub-surface air bubble defect using pulse compression for (a) a chirp and (b) IRS-Golay code.

An Elliptical-Tukey windowed chirp signal having a 312 kHz centre frequency was found to be the best solution for maximizing the output from the transducers, by tailoring the excitation frequencies to suit the bandwidth of the transduction system. In addition, safety rules need to be taken into account for on-site inspection of off-shore oil and gas structures, especially when they have to be performed in hostile environments. For this reason, the signal voltage used to drive the transmitter transducer was chosen to be only 1 V. A Cooknell charger amplifier was used to enhance the received signal level, which has described in Section 6.2.

An example of a received signal, both before and after pulse-compression, is shown in Figure 6.39. This clearly demonstrates that a small bubble defect clearly appears at a peak in the PuC output before the back-wall echo.

171
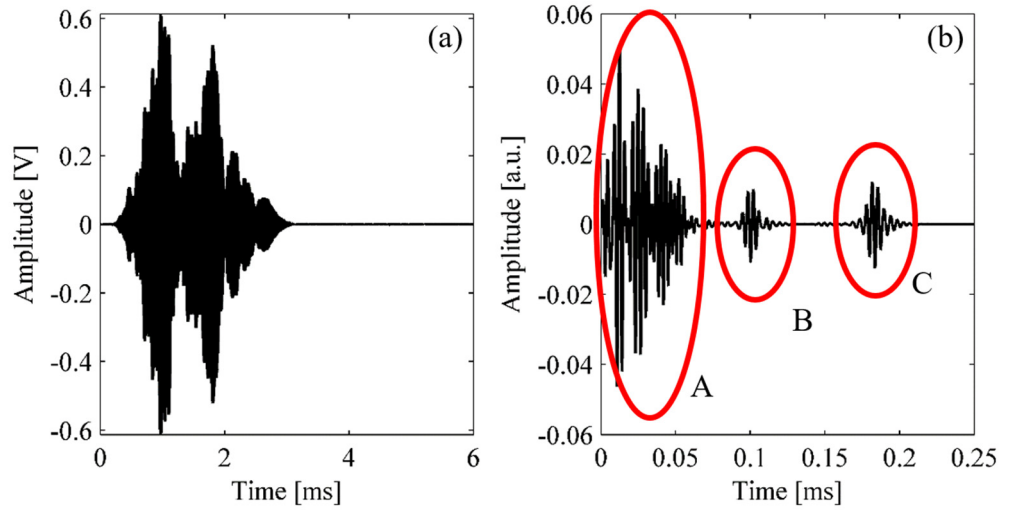
Figure 6.39: An example of a PuC output for a 6 mm diameter defect at a depth of 70 mm. (a) the received time signal before cross-correlation, and (b) the pulse compression output. In (b), region A is due to electrical cross-coupling, B is the defect echo, and C is the reflection from the back wall.

6.4.4. SAFT imaging

Two types of defects were imaged – the bubble defects of Figure 6.31, and the flat-bottomed hole. The raw data was acquired at each scanning point ((x,y)) and stored in a 3D matrix. Two types of imaging were reported. The first was a standard C-scan approach, where the data is displayed as horizontal sections of the material, or extrapolated into a B-scan (effectively a vertical section). The second approach was Synthetic Aperture Focusing Technique (SAFT) imaging. SAFT mimics a narrow synthetic beam by coherent time summation of the acquired A-scans signals [17]. It has been shown that SAFT can lead to up to 20dB Signal-to-Noise Ratio (SNR) gain in several ultrasonic testing applications [12]. Defects which are undetectable with standard ultrasonic imaging can be highlighted when SAFT is used for the coherent reconstruction of ultrasonic images. Moreover, SAFT increases spatial resolution of the reconstructed images allowing a better evaluation of the size of a defect [18]. In addition, the final image resolution can be varied.

A control volume (mesh) consisting of a controlled and finite number of voxels (3D pixels) was built up, as was shown earlier in Figure 6.32. As for the Finite Element Simulations described in Chapter 4, the dimensions of the voxels affected deeply the quality of the results, and thus they have to be chosen carefully. In general, SAFT assumes homogenous far-field sensitivity conditions and coherently sums the received signals by applying a mathematical weight to them, derived from the far-field sensitivity amplitude weighting. However, in this case both the drilled hole and the air bubbles are within the near-field. Therefore, the 3D simulated field shown in Figure 6.34 was used as a weight to the response from each scanning location. This helped to reduce noise levels in the images [19].

A series of different visualizations of C-scan data are shown in Figure 6.40 for the drilled defect. In the 3D view the presence of a defect is evident (top part of the drilled hole) at a depth of 8 cm from the scanning surface. However, it can also be seen that the first part of the image is affected by an unwanted cross-coupling noise signal between the two transducers. Even though this noise can be lowered by using different post-processing techniques [12], it cannot be totally cancelled. As expected, the back-wall echo appears clearly at a depth of 15 cm within the sample. The B-scan slices (XZ view) make the presence of the hole evident. The blurred defect shape is due from the spread ultrasonic beam outgoing from the transducer, which at this relatively low frequencies and with relatively big transducer dimension is quite broad. The C-scan (XY view- bottom right subplot) highlights the defect location relatively to the scanning area at a depth of 90 mm into the sample.
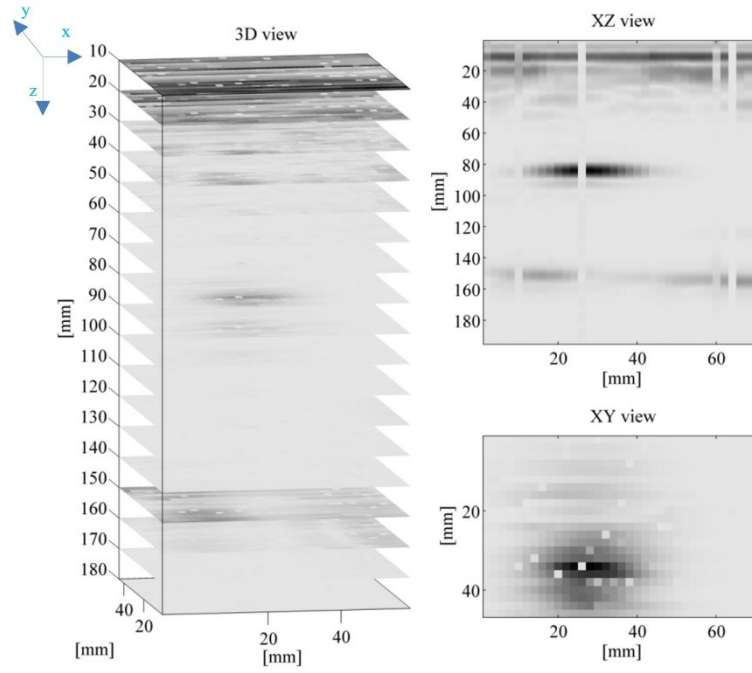
Figure 6.40: C-Scan results for the flat-bottomed hole.

SAFT results are shown in Figure 6.41. In order to obtain this image, a voxel volume of 2 x 2 x 1 mm was used for the dx, dy and dz dimensions respectively. This was found to be the optimum voxel volume. It can be noted that the defect image contrast is enhanced and de-blurred with respect to a normal C-Scan (Figure 6.40). Furthermore, the cross-coupling noise is lowered both in amplitude and duration. In addition, a presence of defect signatures at a depth of 4 cm have appeared.

In real industrial applications, being able to realize an experimental setup capable to provide significant results without being slow is of high importance. For SAFT, this can be obtained by lowering the number of (x,y) experimental measurements taken into account for the image reconstruction. Figure 6.41 shows the results obtained by sub-sampling the measurement grid by a factor of two. It can be seen that good image quality is still preserved.
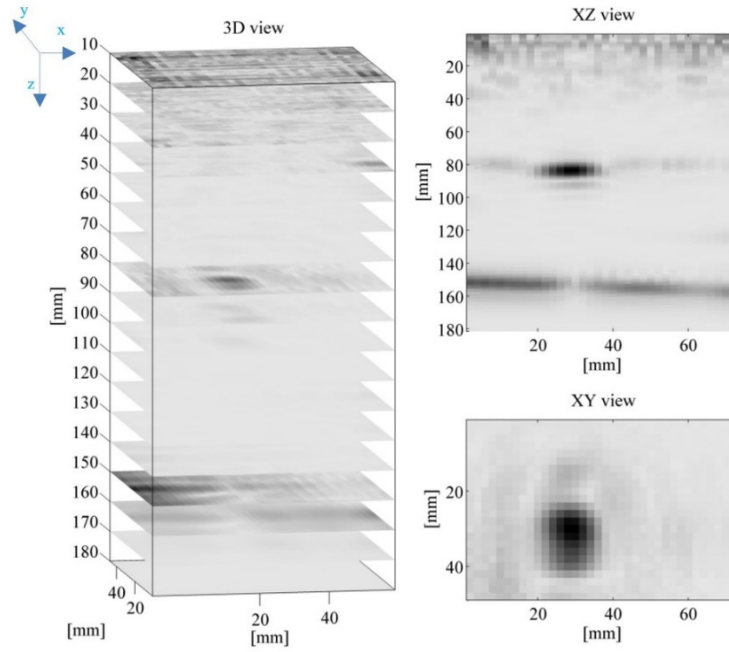
Figure 6.41: SAFT result using a sub-sampled data set (sub-sampling factor equal to 2).

The image obtained from C-scan data on the air-bubbles defect is shown in Figure 6.42(a). A typical recorded signal over the bubble after PuC is shown Figure 6.42(b). The C-scan shows that defected areas can be estimated to be between 6-8 cm and 7-9 cm respectively. Again, the presence of a darker area close to the surface due mainly to cross-coupling between the probes is evident.
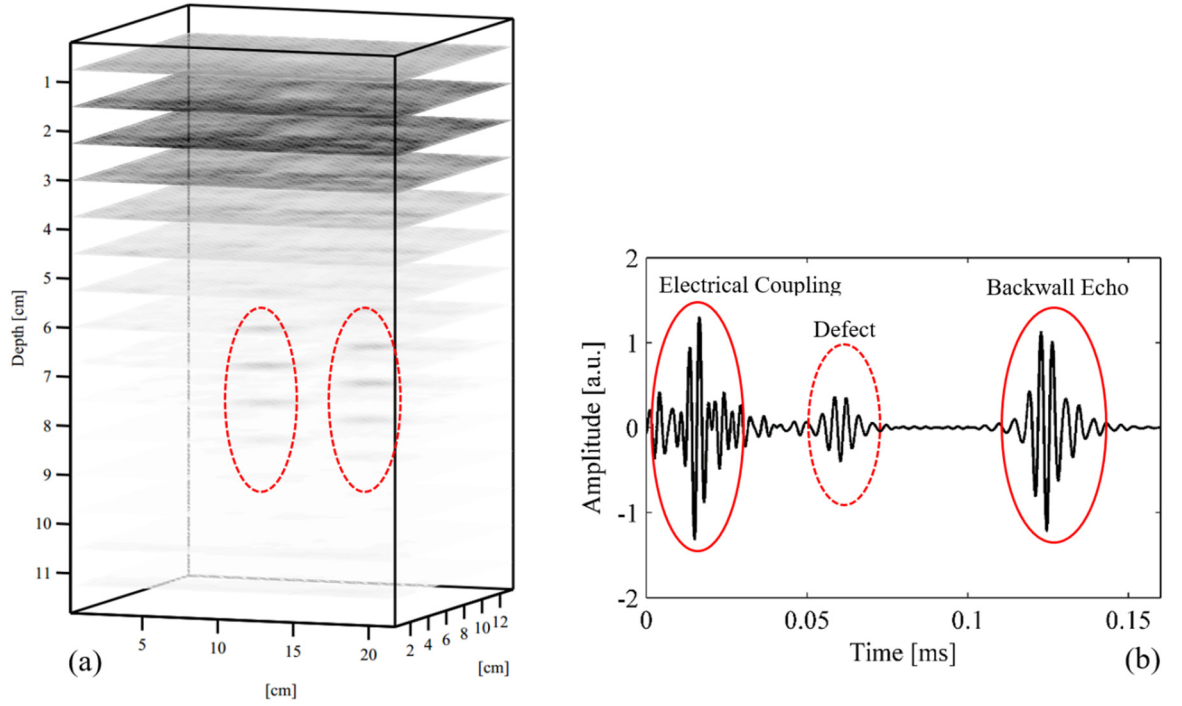
Figure 6.42: (a) 3-Dimensional C-Scans imaging of the polyurethane sample. The two red ellipses that at depths of 6-9 cm indicate the location of the defects. (b) An example of the PuC output in the in the presence of a defect.

In order to try to improve the image quality, some post processing techniques have been tested as an alternative to standard PuC, where the data recorded by the transducers is cross-correlated with the time replica of the input signal, i.e. matched filter, (labelled "Standard" in Figure 6.43(a)). In fact, the matched filter can also be obtained by the time replica of the signal recorded from either the direct contact of the two transducers (labelled "Probe") or from a through-transmission measurement on a sound area of the sample ("Material"). This results in a more modelling of the transducer and material properties for the compression of the signal, i.e. pulse compression. It can be noted that in the "Probe" and "Material" cases, the duration of the cross-correlation time peak is reduced, leading to a better estimation of defect depth. Note that the amplitude is arbitrary and the red signal is the larger of the two. As another alternative strategy to lower both the electrical noise to

enhance depth resolution, a Total Variation (TV) deconvolution [20] has been applied to the

"Standard" case, see Figure 6.43 (b).
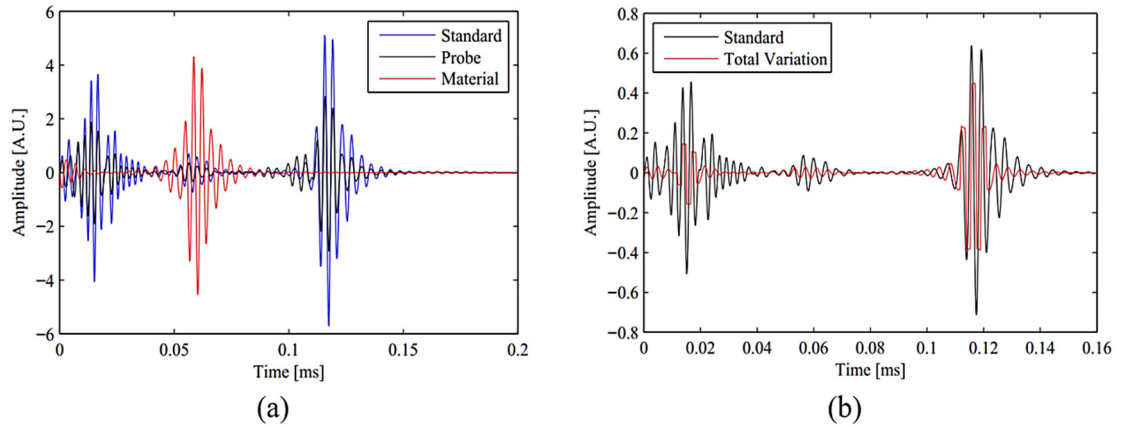
Figure 6.43: (a) Comparison of standard PuC technique (blue), PuC obtained by using the signal modified by the transducers spectrum as a matched filter(black), and by the sample + material properties (red); (b) Comparison between the standard matched filter technique (black) and the Total Variation (TV) deconvolution (red).

The TV algorithm can enhance the imaging and inspection capability. This is demonstrated

in Figure 6.44 by the 3D images obtained using these two different techniques, where the

images intensities were normalized to the maximum intensity of the defect area, *i.e.* the

bubble on the right-hand side.
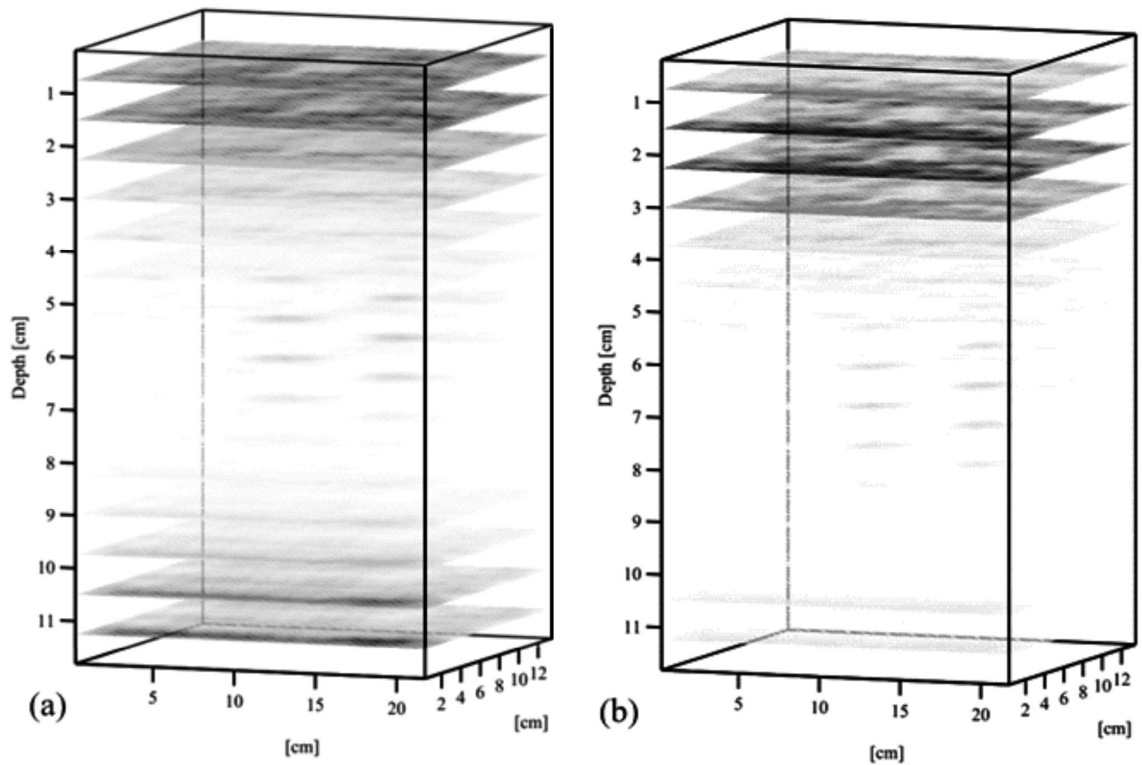
Figure 6.44: Three-Dimensional imaging obtained with the "Transducer" recorded signal as (a) a matched filter and (b) with the Total Variation (TV) method.

The SAFT approach results for the air bubbles are shown in Figure 6.45. In Figure 6.45(a), the data is shown including the back-wall echo in a linear amplitude scale. It can be noted that the bubbles are not clearly visible. By showing the same image in a dB scale (Figure 6.45(b)), the defects are now evident. Those are even more evident if the back-wall echo is removed from the data (Figure 6.45(c)).
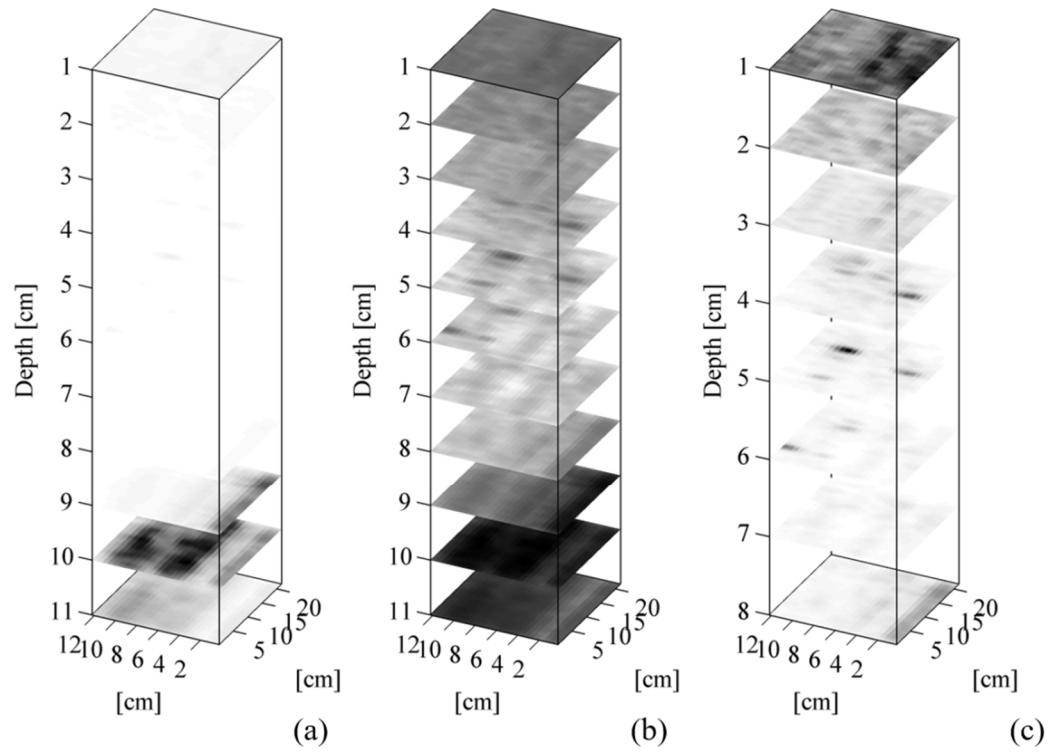
Figure 6.45: SAFT images of the hole defects shown in Figure 6.31. (a) 3D image in linear scale with the backwall echo data included; (b) as (a) but plotted with a dB scale; (c) as (a), but with the backwall echo excluded.

The results achieved by standard C-scan image after PuC have been here compared to those from the SAFT algorithm. Figures 6.46 and 6.47 show the C-scan obtained for both techniques on a single air-bubble defect. The C-scan images in the said figures are reported together with two 1D sections of the C-scan along x and y directions. To better appreciate the difference in the spatial resolution normalized dB scale was used with the same axis limits.
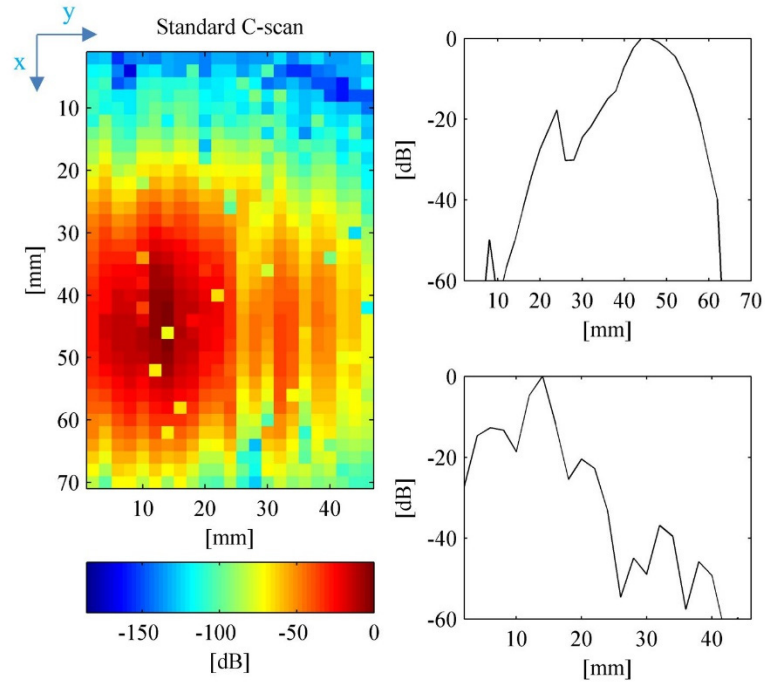
Figure 6.46: standard PuC data for an air bubble defect. (left) C-scan at z=80mm, (top right) cross-section of the C-scan along the x axis, (bottom right) cross-section of the C-scan along the y axis.
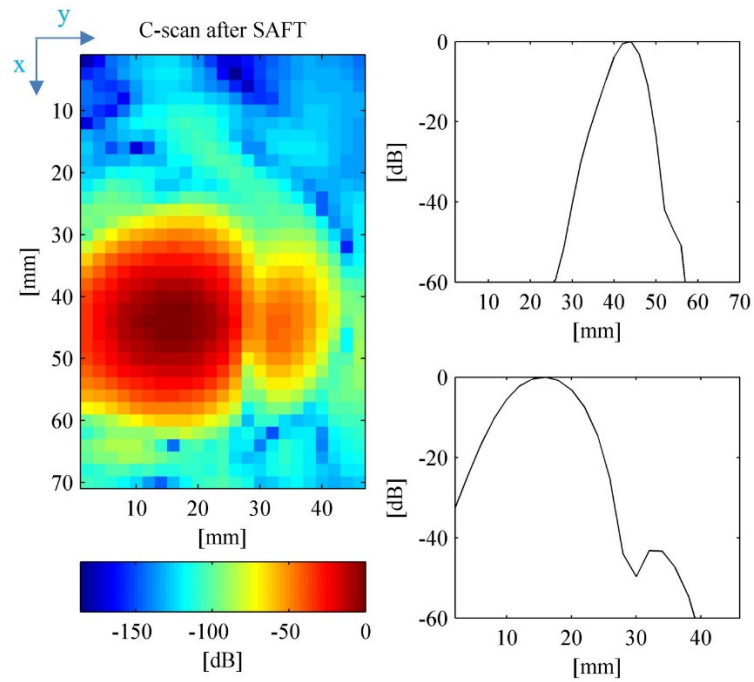
Figure 6.47: SAFT data on an air bubble defect. (left) C-scan at z=80mm, (top right) cross-section of the C-scan along the x axis, (bottom right) cross-section of the C-scan along the y axis.

It is evident that the SAFT approach results in a better spatial resolution and a higher SNR if compared to a standard C-scan data. This is even more evident by comparing Figures 6.46 and 6.47, which contain a cross-section through the drilled hole defect. In fact, the C-scan relies on the availability of the acquired data for each-scanning point (see Figure 6.46). Conversely, the SAFT algorithm is robust against missing signals.

Figure 6.48(a) shows the image obtained of the two air bubbles using the SAFT algorithm. The image refers to a depth of 45 mm within the sample. Figure 6.48(b) shows a zoomed image of the larger defect (circled). The dimensions of each bubble were estimated to be 7-8 mm and 6 mm and respectively in diameter, and these estimates agree well with the sizes estimated from the photograph shown earlier in Figure 6.31 [1].
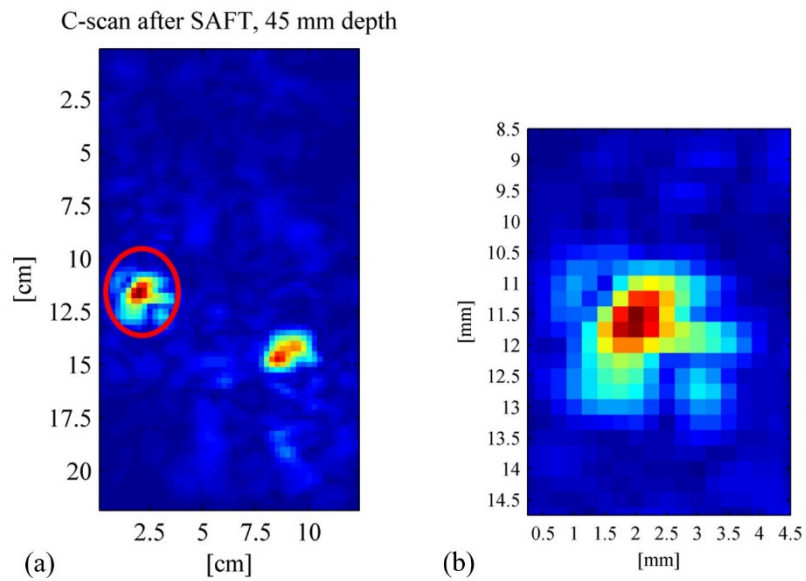
Figure 6.48: (a) SAFT image of the two bubble defects, depth= 45 mm within the sample, and (b) zoomed view of the larger defect (circled).

6.5   Pulse compression portable device

6.5.1. Introduction

Although PuC is a flexible algorithm in terms of the applications in which it can be exploited, it can be noted from Chapter 5 and Section 6.2 that the setups used to for PuC can be bulky. The realization of a compact, cheap and highly portable device having an embedded software managing the PuC algorithm, could be thus of interest for NDT operators having to deal with the inspection of large structures and/or space-limited environments. For this reason, in this section a prototype portable device for PuC applications it is shown. The inspection capabilities of this device will be demonstrated by the detection of embedded reinforcement bars ("rebars") in concrete samples.

6.5.2. Pulse compression portable device description and features

The prototype portable device is based on a TiePie HS5 USB oscilloscope/arbitrary waveform generator (http://www.tiepie.com). A photograph of the device is shown in Figure 6.49:

Figure 6.49: A picture of TiePie HS5 device.

This device has one channel serving as an output for the arbitrary waveform generator (AWG) and two channels available as oscilloscopes for acquiring signals, i.e. Ch1 and Ch2. Signal generation/acquisition can be carried out by exploiting the internal clock trigger or by using one of the available oscilloscope channels for external triggering purposes. In addition, if a multi-input/multi-output system is needed, this platform offers the possibility to connect multiple identical devices in cascade. It can be powered directly from

an attached laptop running the generation/acquisition software. The device presented here has a maximum acquisition/generation sampling rate of 500 Msamples·s^{-1} at a 14 bit resolution, whilst this value drops down to 6.25 Msamples·s^{-1} if 16 bits are used for both input and output. The available bandwidths (- 3dB) at 75% of full scale input are 250 MHz and 100 MHz for Ch1 and Ch2 respectively. The AWG provides a maximum output voltage of 24 Volt peak-to-peak.

The portable system also exploits a low-noise amplifier from ANALOG DEVICE AD8331-EVALZ, in its evaluation board versions. In particular, for this device the voltage noise is 0.74 nV·Hz$^{-1/2}$, whilst the current noise is of 2.5 Pa·Hz$^{-1/2}$. It has a bandwidth of 120 MHz (at 3dB) and runs off a 5V voltage supply. A photograph of the amplifier board is shown in Figure 6.50:

Figure 6.50: A picture of the low-noise amplifier AD8331-EVALZ.

A picture of both the devices as they have been exploited for the experimental acquisition campaign reported in the next section is shown in Figure 6.51:

Figure 6.51: A picture of the portable device prototype.

This offers a much more portable and cost effective solution for wider use than the use of the PXI System described earlier.

In parallel, a virtual instrument for the PuC procedure was developed to manage the signal acquisition/generation of the portable device. As the TiePie offers the possibility of using C libraries within LabView to manage their devices, the virtual instrumentation software has been programmed in this environment. This in turn, lead to convenient programming of the graphic interface, where meaningful signal acquisition/generation parameters could be easily changed. A screenshot of the developed software can be seen in Figure 6.52:
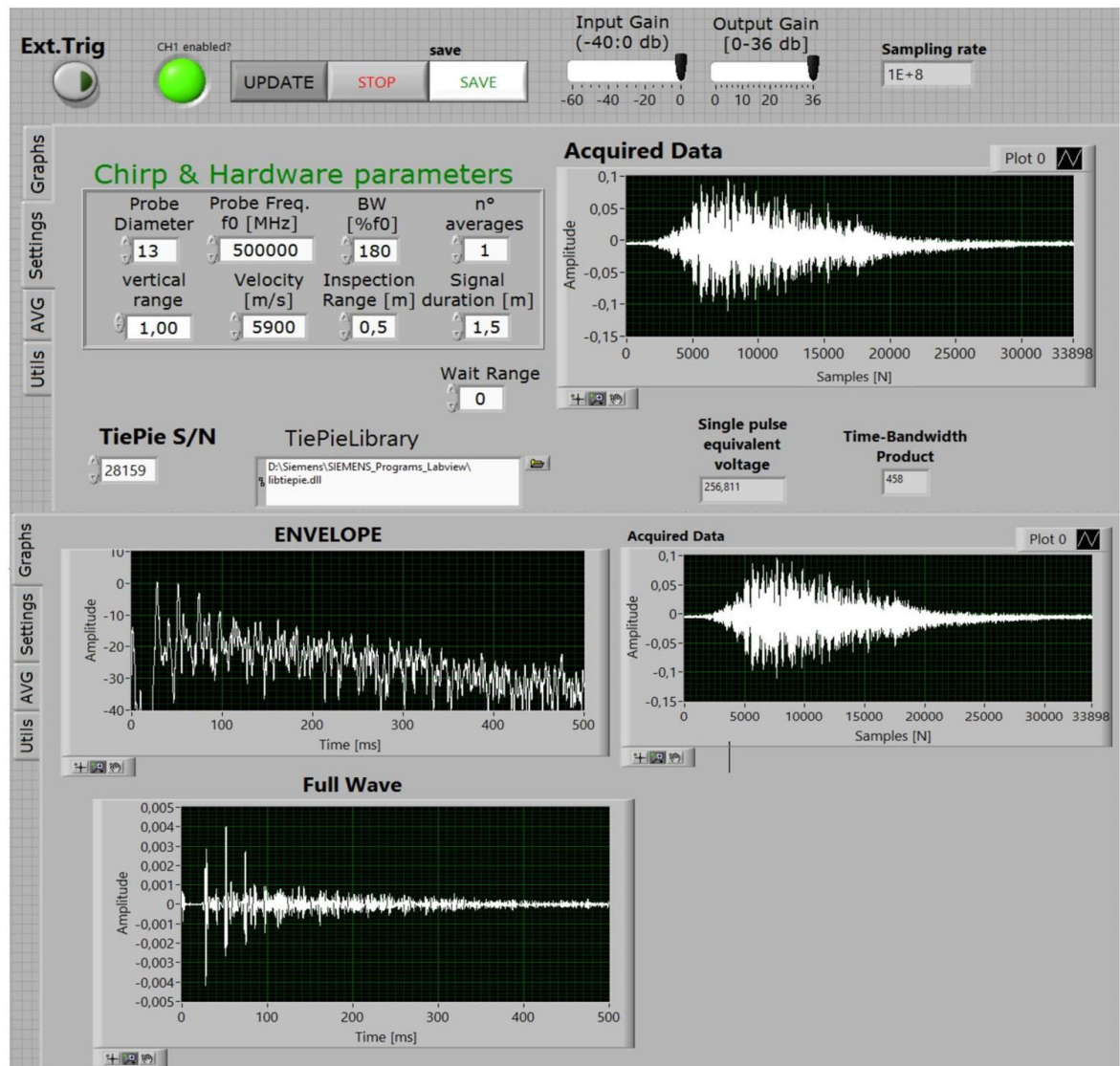
Figure 6.52: Pulse compression virtual instrument main panel screenshot.

Note that the portable devices could be made even more compact if a powerful tablet and executable LabView script was exploited. In particular, an attempt has been done to realize a compact device and this can be seen in Figure 6.53, where both the TiePie and the low noise amplifier have been embedded within a plastic case. The virtual instrument can be managed by means of a touch screen tablet.

Figure 6.53: A picture of the embedded portable device, manageable by means of a touch screen tablet.

As this last version was in its early stage during my PhD research, the instrument utilized in order to achieve the experimental results described in the next section was arranged as in Figure 6.51.

6.5.3. Experimental results: concrete with embedded bar

The ultrasonic NDT of concrete is challenging [21]. This is because of the presence of aggregates, sand and inclusions of various dimensions and densities which cause scattering, especially when the inspection has to be carried out in pitch-catch configuration [22]. However, due to the very common use of concrete in any kind of buildings and facilities, it is of utmost importance being able to test its quality. Here, the problem of testing the integrity of concrete containing a rebar has been faced. It is known that concrete has to be reinforced with steel bars in order to resist to high lateralstresses. In this way, for example, buildings are able to resist to seismic events [23], [24]. Corrosion and damage can occur to these bars, especially when the concrete structure into which they are embedded is exposed to thermal stresses and, in general, faces hostile environments such as water ingress. A

picture of the damage that can occur in a concrete structure with embedded rebars is shown in Figure 6.54:

Figure 6.54: A picture of the corrosion/damage of rebar embedded in a concrete structure, taken from [25].

Commonly, the device used to test the integrity of rebars is based on pulse induction electromagnetic techniques, known as a "concrete cover meter". However, these devices have many limitations, such as a limited depth of penetration (100 - 125 mm [26]) and the unavailability of the raw acquired signals for further signal processing. In addition, to successfully exploit those devices the embedded bars have to be separated by a minimum distance, resulting in a wrong detection of the bar integrity otherwise.

As an attempt to overcome those limitations, ultrasonic testing was thought to be an exploitable method to successfully test and image the rebar condition into thick concrete samples. Thus, the portable device was used on cast concrete samples with embedded bars, together with a pair of piezo-composite transducers, to get information about the sample inner structure.

6.5.4. Cast sample

The first aim to reach was to cast a thick concrete sample with an embedded rebar having known characteristics. In particular, it was chosen to cast a mixture of concrete based

on Portland cement containing aggregate of specific dimension. Aggregates were in the form of small stones (i.e.gravel), widely used to cast the most common type of concrete for buildings . In particular, the aggregates used to cast the sample had average dimension (i.e. diameter) of 10 mm. Table 6.2 shows the detailed composition of this mixture:

	Ratio of the components to cement weight		
Cement	Water	Aggregate	Sand
Portland	0.5	2	2

Table 6.2: Concrete samples detailed composition.

The dimensions of the samples were of 30 by 30 centimeters, with a thickness of 8.5 cm. The sample has been cast to have an steel bar embedded within at a known depth. The bar used had a diameter d_{bar} of 20 millimeters. A rendered sketch of the samples is depicted in Figure 6.55(a), whilst is quoted counterpart is in Figure 6.55(b):
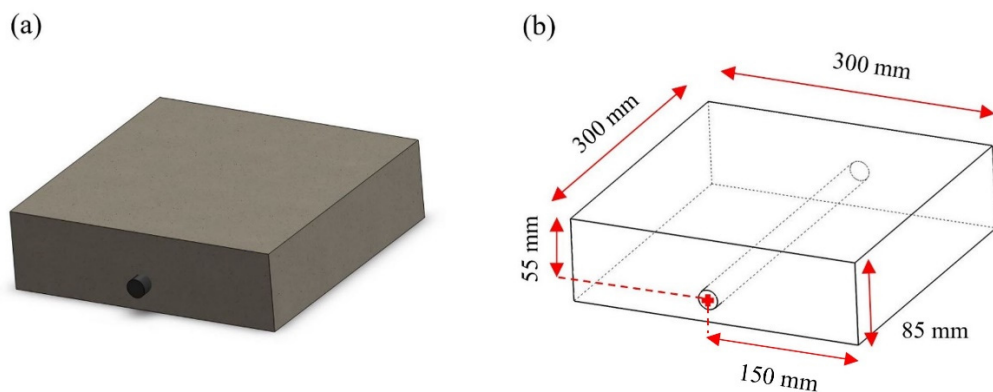
Figure 6.55:(a) A render of the concrete samples with the embedded bar and (b) its quoted counterpart.

6.5.5. Experimental Setup

As said, the experimental setup used used the portable device as in Figure 6.51. A LabView software programmed by the author of this thesis managed the signal acquisition/generation parameters. The data collected was then post-processed with a script programmed again by the author. The probe used were a pair of piezo-composite probes

having diameter D_t = 25.4 mm and nominal central frequency f_{ct} = 300 kHz, i.e. the same used for the polyurethane inspection in Chapter 6.4 (see Figure 6.2(a)).

A sketch of the experimental setup is shown in Figure 6.56:
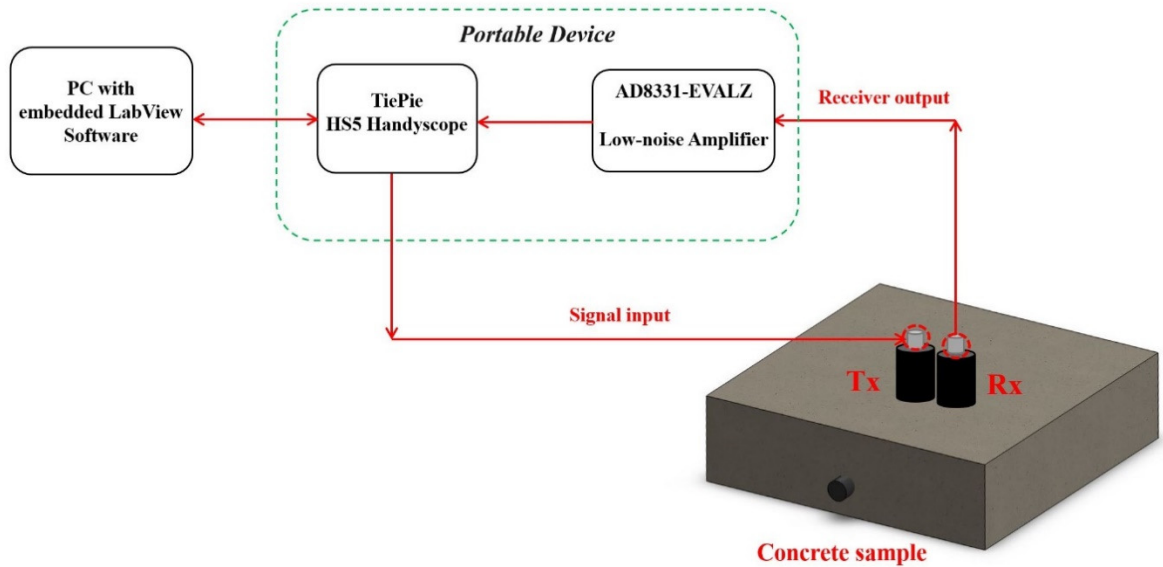
Figure 6.56: Sketch of the experimental setup.

The experimental activity was performed by arranging the transmitter (Tx) and the receiver (Rx) in pitch-catch configuration. For the sake of clarity, Figure 6.57 shows a picture of the investigated sample, with the transducer held together by a metal case and oriented as for all the experimental acquisition campaign:
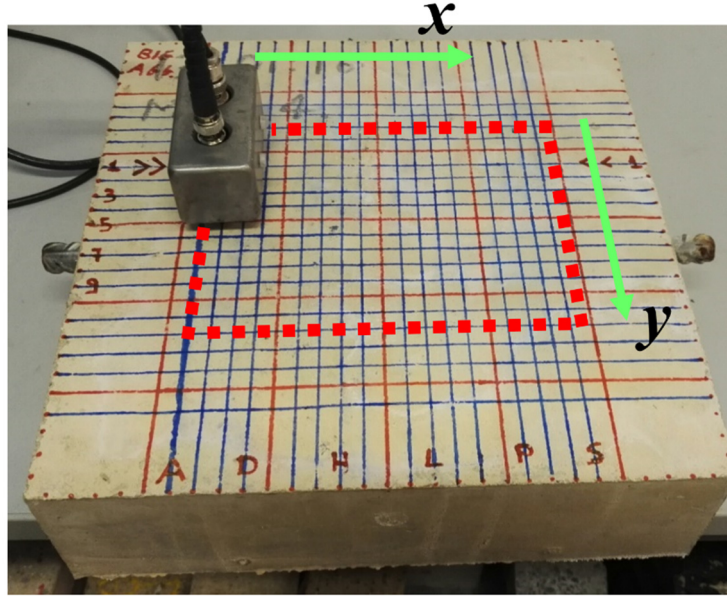
Figure 6.57: Concrete with rebar experimental setup sketch. The red-dotted rectangle shows the limits of the scanning area.

The scanning area, i.e. red-dotted rectangle in Figure 6.57, was chosen to be sufficiently far from the edges of the sample, so as to avoid lateral reflections of the ultrasonic beam. The acquisitions followed a grid of points orientated along the *x-y* axis. In particular, one acquisition was made every 1 centimeter along the *x*-axis, whilst the measurement step was halved along the *y* axis, i.e. 0.5 centimeter, so as to increase the scanning resolution along the smaller rebar axis. The overall scanned area was 19 by 9.5 centimeters. The scanned side of the sample was the one having the higher distance from the rebar geometrical center, i.e. 55 millimeters between them (see Figure 6.55).

6.5.6. Experimental Results

The signal used to drive the transmitter was a 24 volt peak-to-peak windowed linear-chirp, sweeping the frequency range 0-500 kHz, having a time duration of 0.65 ms. The signal was then zero-padded at its end so as to apply successfully PuC in acyclic mode, (see Chapter 2). The input signal characteristic time-frequency are shown in Figure 6.58:
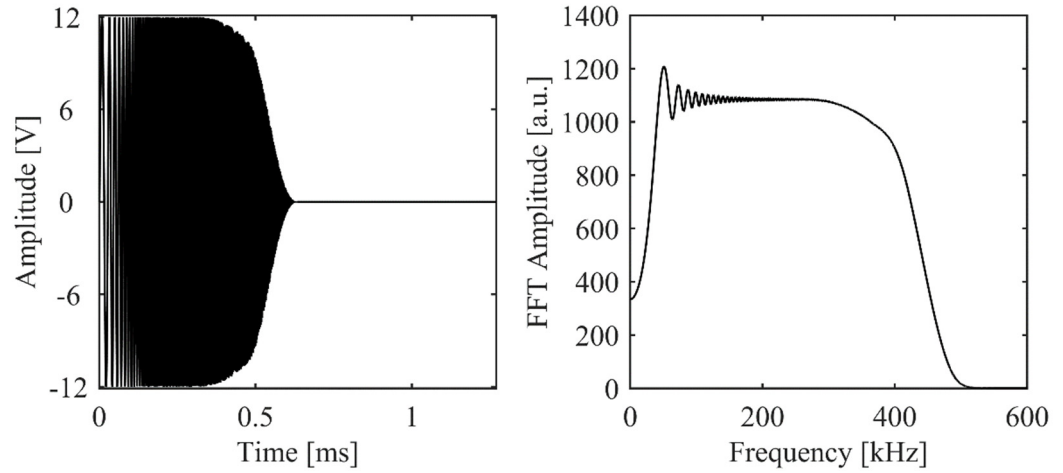
Figure 6.58: Input signal and its frequency spectrum.

The chirp was Elliptical-Tukey windowed only at high frequency, i.e. frequencies higher than 250 kHz (central frequency), so as to reduce the sidelobes noise without lowering the signal amplitude at low frequency. This is because low frequencies are less attenuated than higher ones, thus they assure more penetration into the sample under test. The acquisition/generation rate was 5 Msamples·s^{-1} at 14 bits of vertical resolution.

An example of a received signal after cross-correlation from an acquisition point far from the rebar location, i.e. sound location, is reported in Figure 6.59. The signal amplitude is plotted in mV, so as to give to the reader an idea of the sample attenuation magnitude.
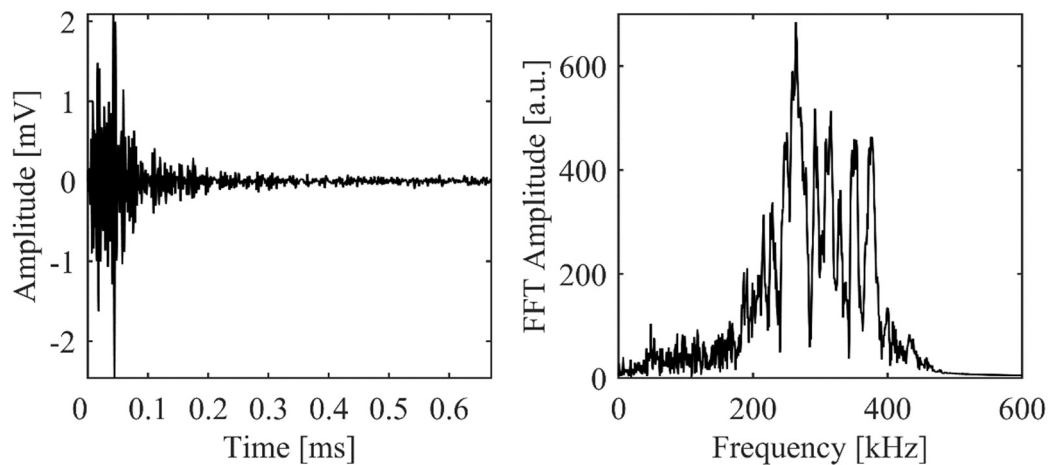
Figure 6.59: a received signal after cross-correlation from an acquisition point far from the rebar location.

Figure 6.60(a) shows the received signal after cross-correlation from a sound location compared to one signal acquired in a scanning position upon the bar. Figure 6.60(b) reports the same graph plotted for the distance travelled by the sound into the sample. This was obtained by using an estimated value of the sound velocity of 3,862 ms^{-1}.
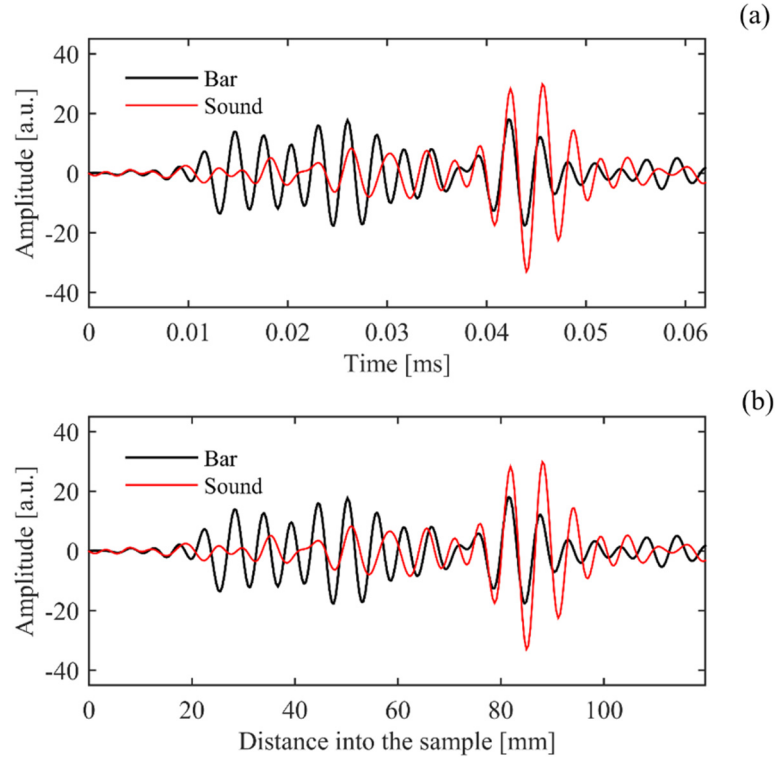
Figure 6.60: (a) received signal after cross-correlation from a sound location compared to the one acquired in a scanning position on the top of the bar; (b) same as (a), but plotted with respect to the distance traveled by the sound into the sample.

It can be seen that the back-wall echo is clearly visible at a distance into the sample of about 85 mm (red line plot). In addition, a peak in the cross-correlated signal at a distance into the sample of 45 mm appear clearly. Since the geometrical center of the bar was located at 55 mm from the scanned surface and the bar radius was 10 mm, the retrieved peak value of 45 mm suits with real depth of the bar external surface.

Although the results in Figure 6.60 shown promises on the reconstruction of an image of the bar buried into the sample, it can be seen in Figure 6.61 that the C-Scan obtained by

imaging the maximum of the cross-correlated signal envelope amplitude for the time range 0.02-0.03 ms, i.e. bar expected echo, it is unclear:
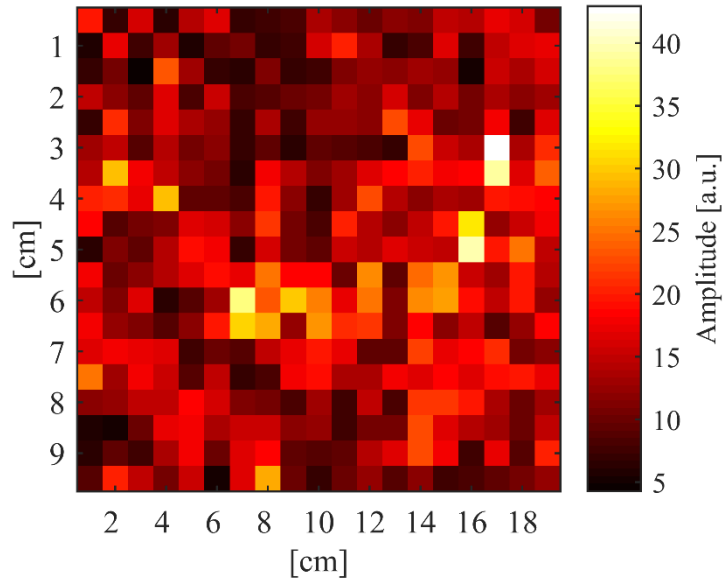
Figure 6.61: C-Scan of the concrete with rebar obtained by plotting the signal envelope amplitude into the time range where the echo is expected.

It has been thought that the same approach used for the inspection of refractory bricks, i.e. Effective Length parameter obtained by thresholding the cumulative of the reflected energy (see Section 6.3.3), could in theory help to obtain a clearer image of the rebar. In fact, fixed a range of interest, i.e. distance travelled by the sound into the sample, the normalized cumulative of the reflected energy can be plotted for both a sound and a rebar acquisition position, as shown in Figure 6.62. A difference on the steepness of the two plotted curves appears clearly. By choosing a proper threshold value for the estimation of the Effective Length parameters, it could be possible to clear distinguish the rebar buried into the sample.
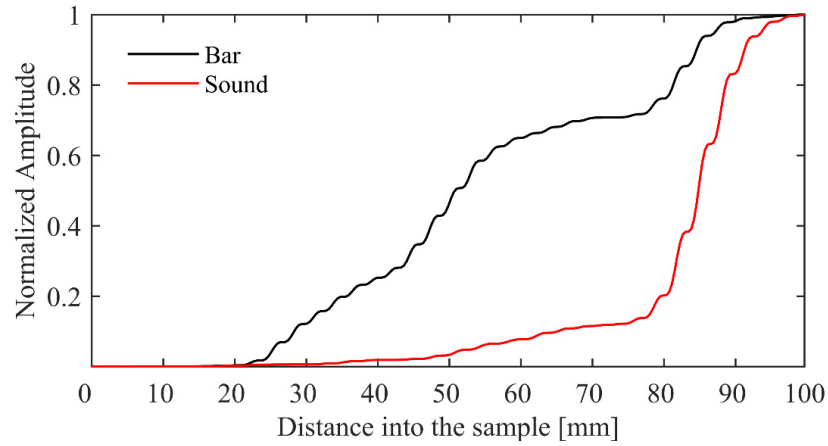
Figure 6.62: Normalized cumulative of the reflected energy for a sound (full thickness) and rebar.

The threshold value has been fixed to be equal to the 50% of the normalized cumulative amplitude. By calculating the Effective Length for each measurement on the acquisition grid, i.e. the distance into the sample at which the chosen threshold value is reached, a C-Scan can be obtained, as shown in Figure 6.63: The rebar is seen as the darker zone, and arises from energy scattered from the rebar which reaches the threshold level (at an Effective Length of ~50 mm) before signals from a sound sample. The larger width of the rebar image compared to the real rebar diameter is due to the wide diameter of the piezocomposite transducers.
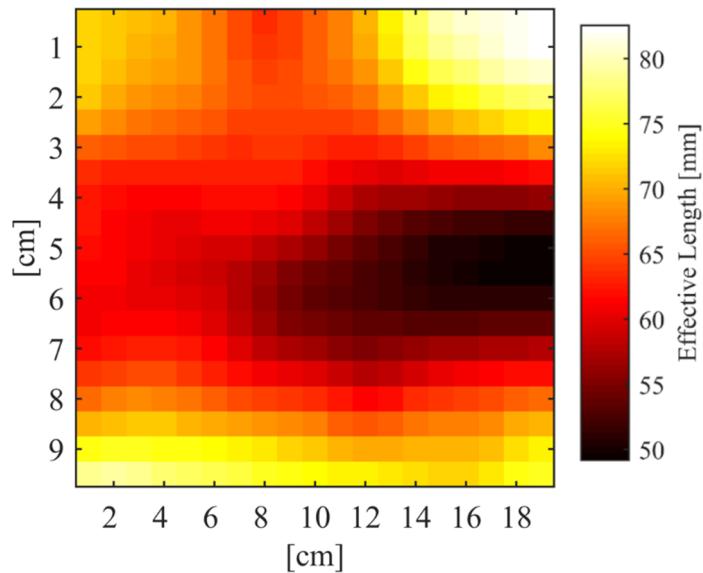
Figure 6.63: C-Scan obtained by imaging the retrieved Effective Length parameter calculated for each acquired signal of the scanning grid position.

6.6 Conclusions

This chapter focused on applications of the pulse compression technique and coded signals in challenging NDT applications. In particular, it has been shown that pulse compression cannot be applied straightforwardly when highly scattering and attenuating material needs to be investigated. The choice of the combination of transducers, coded waveform, post-processing algorithm and imaging techniques is of utmost importance, and has to be taken by carefully considering the mechanical properties of the sample under examination.

The first application concerned the investigation of refractory bricks samples. The aim was to discriminate broken sample from sound ones when a pitch-catch configuration of the transducers is used. It has been demonstrated that a robust discrimination method has been developed, using the ultrasonic energy scattered back from the investigated sample.

The second application demonstrated that PuC-based SAFT imaging can be successfully exploited into the near field to restore the imaging resolution when low frequency ultrasound excitation is used in very lossy materials (in this case polyurethane). Both artificial and manufacturing defects have been successfully imaged by means of a chirp signal onto a thick polyurethane sample.

Finally, the possibility to realize a portable device for PuC applications has been reported. The device inspection capabilities, together with advanced post processing techniques, have been illustrated by the detection of a rebar in a cast concrete sample.

References

[1]   M. Mohamed, I., Hutchins, D., Davis, L., Laureti, S., Ricci, "Ultrasonic NDE of thick polyurethane flexible riser stiffener material," *Nondestruct. Test. Eval.*, pp. 1–20, 2016.

[2]   S. Laureti, M. Ricci, M. N. I. B. Mohamed, L. A. J. Davis, and D. A. Hutchins, "A pulse compression ultrasonic approach to concrete integrity inspection," *Cem. Concr. Res.*, p. (in preparation for submission), 2016.

[3]   R. Deng, P. Davies, and A. K. Bajaj, "Flexible polyurethane foam modelling and identification of viscoelastic parameters for automotive seating applications," in *Journal of Sound and Vibration*, 2003, vol. 262, no. 3, pp. 391–417.

[4]   S. Grad, L. Kupcsik, K. Gorna, S. Gogolewski, and M. Alini, "The use of biodegradable polyurethane scaffolds for cartilage tissue engineering: Potential and limitations," *Biomaterials*, vol. 24, no. 28, pp. 5163–5171, 2003.

[5]   W. Boet and J. Out, "Analysis of a flexible-riser top connection with bend restrictor," *Offshore Technol. Conf.*, 1990.

[6]   F. Demanze and D. Hanonge, "Fatigue life analysis of polyurethane bending stiffeners," *ASME 2005*, 2005.

[7]   M. G. Marinho, J. M. dos Santos, and R. de O. Carneval, "Integrity Assessment and Repair Techniques of Flexible Risers," *Vol. 4 Terry Jones Pipeline Technol. Ocean Sp. Util. CFD VIV Symp.*, vol. 2006, pp. 253–260, 2006.

[8]   A. Felix-Henry and P. Lembeye, "Flexible pipes in-service monitoring," *ASME 2004*, 2004.

[9]   R. Jacques, T. Clarke, S. Morikawa, and T. Strohaecker, "Monitoring the structural integrity of a flexible riser during a full-scale fatigue test with combination of non-destructive testing methods," *NDT&E Int.*, vol. 43, pp. 501–506, 2010.

[10]   E. Veith, C. Bucherie, J. L. Lechien, J. L. Jarrousse, and B. Rattoni, "Inspection of offshore flexible risers with electromagnetic and radiographic techniques," *Insight Non-Destructive Test. Cond. Monit.*, vol. 43, no. 6, pp. 404–408, 2001.

[11]   F. Bastianini, A. Di Tommaso, and G. Pascale, "Ultrasonic non-destructive

assessment of bonding defects in composite structural strengthenings," *Compos. Struct.*, vol. 53, no. 4, pp. 463–467, 2001.

[12] M. H. Skjelvareid, Y. Birkelund, and Y. Larsen, "Synthetic aperture focusing of outwardly directed cylindrical ultrasound scans," *IEEE Trans. Ultrason. Ferroelectr. Freq. Control*, vol. 59, no. 11, pp. 2460–2469, 2012.

[13] A. Jensen and B. Svendsen, "Calculation of Pressure Fields from Arbitrarily," *Ultrason. Ferroelectr. Freq. Control. IEEE Trans.*, vol. 39, no. 2, pp. 262–267, 1992.

[14] J. Krautkrämer, "Determination of the size of defects by the ultrasonic impulse echo method," *Br. J. Appl. Phys.*, vol. 10, no. 6, pp. 240–245, 1959.

[15] E. Wolf and E. W. Marchand, "Comparison of the Kirchhoff and the Rayleigh-- Sommerfeld Theories of Diffraction at an Aperture," *J. Opt. Soc. Am.*, vol. 54, no. 5, pp. 587–594, 1964.

[16] P. Pallav, T. H. Gan, and D. A. Hutchins, "Elliptical-Tukey Chirp Signal for Ultrasonic Imaging," *IEEE Trans. Ultrason. Ferroeletrics, Freq. Control*, vol. 54, no. 8, pp. 1530–1540.

[17] J. A. Jensen, S. I. Nikolov, K. L. Gammelmark, and M. H. Pedersen, "Synthetic aperture ultrasound imaging," *Ultrasonics*, vol. 44 Suppl 1, pp. e5-15, 2006.

[18] M. Spies and H. Rieder, "Synthetic aperture focusing of ultrasonic inspection data to enhance the probability of detection of defects in strongly attenuating materials," *NDT E Int.*, vol. 43, no. 5, pp. 425–431, 2010.

[19] W. Masri, M. Mina, S. S. Udpa, L. Udpa, T. Xue, and W. Lord, "Synthetic aperture focusing techniques applied in the near field of a focused transducer," *1995 IEEE Ultrason. Symp. Proceedings. An Int. Symp.*, vol. 1, pp. 783–786, 1995.

[20] L. I. Rudin, S. Osher, and E. Fatemi, "Nonlinear total variation based noise removal algorithms," *Phys. D Nonlinear Phenom.*, vol. 60, no. 1–4, pp. 259–268, 1992.

[21] B. C. Kim and J. Y. Kim, "Characterization of ultrasonic properties of concrete," *Mech. Res. Commun.*, vol. 36, no. 2, pp. 207–214, 2009.

[22] M. Schickert, M. Krause, and W. Müller, "Ultrasonic Imaging of Concrete Elements Using Reconstruction by Synthetic Aperture Focusing Technique," *J. Mater. Civ. Eng.*, vol. 15, no. 3, pp. 235–246, 2003.

[23] M. J. N. Priestley, R. Verma, and Y. Xiao, "Seismic shear strength of reinforced concrete columns," *ASCE J. Struct. Eng.*, vol. 120, no. 8, pp. 2310–2329, 1994.

[24] Takeda, Sozen, and Nielsen, "Reinforced Concrete Response to Simulated Earthquakes," *Journal of the Structural Division*, vol. 96, no. 12. pp. 2557–2573, 1970.

[25] "http://www.climatemonitor.it/." .

[26] "Non-Destructive Testing (NDT) of Concrete in Structures," *Tech. Note, Vicroads*, no. December, pp. 1–4, 2010.

CHAPTER 7: Pulse compression and thermography

7.1 Introduction

It has been shown in previous Chapters that the pulse compression (PuC) algorithm is a flexible procedure that can be applied to a wide range of problems within the ultrasonic non-destructive testing (NDT) field. In this thesis, this has included acoustic metamaterials, highly-attenuating thick polyurethane structures, refractory bricks and the detection of rebars in concrete. However, PuC and coded signals have also been used in eddy-current testing [1] and thermography [2], [3]. In this Chapter, it is shown that the combined use of PuC and coded-signal excitation can enhance the SNR of the thermal images obtained from carbon fibre reinforced composites containing artificially defects, noting that carbon fibre is widely used in the aerospace industry.

7.2 Application of pulse compression to thermography

7.2.1. Introduction

Thermography is a very powerful NDT method, widely used in many civil and industrial sectors. As an example this technique is used to detect damage to buildings [4], [5] or to inspect composites used in the aerospace industry [6], [7]. The basic idea behind the thermography inspection is that the electromagnetic radiation emitted by each object in the near/far infrared range of the electromagnetic spectrum (roughly a wavelength range $\lambda =$ 1–25 μm) can be detected using thermal cameras (thermograms). It is known from the basic physics that each object at temperatures above the absolute zero emits radiation [8]. In addition, each material has different emissivity properties [9]. This means that a particular material emits electromagnetic radiations into the infrared with a specific spectrum shape,

depending on its specific atomic/molecular structure. Therefore, different materials within the same inspected object may be distinguished in a thermogram.

This latter aspect is very useful for the NDT of composites materials, which are usually made of a polymeric matrix combined with carbon fibres, so as to obtain a final material having enhanced mechanical properties with respect to its fundamentals constituent. However, each layer of material (known as a ply) that make up the finished composite are highly anisotropic, both mechanically and thermally, depending on the direction in which the fibres are aligned. A very common way to overcome this issue is to glue two or more plies together, so as to obtain a composite material with fibres oriented in multiple directions. Nevertheless, under high stress conditions, delaminations can occur between adjacent composite plies, and this type of failure can tremendously affect aircraft safety. Therefore, it is of utmost importance to be able to check the integrity of composites material and to identify manufacturing defects and delamination occurring within them. Thermography is well-suited to this task, as delamination and defects embedded between adjacent composite plies can be identified by area having different temperature in a thermogram.

In general, two different kinds of thermography techniques exist:

(i)   Passive Thermography, in which the features of interest are at a temperature higher than the background. As an example, this technique is used to monitor the temperature of people [10], [11] or for security purposes [12], [13].

(ii)   Active Thermography (AT), in which an electromagnetic source is used to obtain a thermal contrast between the inspected feature and the background [14], [15]. AT is extensively applied to the inspection of composite structures [27], [28],

This Chapter focuses on an innovative AT scheme. As for the ultrasonic NDT, the time-handling of the excitation signal, here provided commonly by flash-head lamps, halogen lamps, LED or any other kind of electromagnetic source, defines the type of thermographic inspection. The most common signals used to modulate the heat source generation are a (i) single pulse and a (ii) single frequency, leading respectively to Pulsed Thermography (PT) [16]–[19], and Lock-In Thermography (LIT) [20]–[22].

As described in Chapter 1, single pulse excitation could ideally provide more information than single frequency methods because a continuous frequency bandwidth is excited. On the other hand, if the signal energy is concentrated within selected excitation frequencies, the use of LIT assures higher values of Signal-to-Noise Ratio (SNR) at the cost of less information. Lately, several techniques have been developed trying to fuse the advantages of both the said approaches, such as Pulsed-Phase Thermography (PPT) [23] and Multi-Frequency Lock-in Thermography (MF-LIT) [24].

The use of coded waveforms and PuC can enhance both the SNR and the defect detection capability, as seen in earlier Chapters for ultrasonic NDT. Pulse-Compression Thermography (PuCT) is a recent technique developed by Mandelis *et al.* [25], [26] and Mulaveesala *et al*. [27]–[29]. The heating stimulus is here in the form of a coded signal. By using a coded excitation, both time and frequency domain processing can be implemented at the same time. The former can be retrieved after the application of the PuC that outputs an estimate of the impulse response; the latter can be directly performed on the acquired data. The main aim of PuCT is to retrieve the time and spatial resolution given by the use of PT with the SNR given by exploiting LIT. Recently, several PuC schemes have been developed, differing mainly in the type of coded waveforms used (binary sequences or frequency modulated "chirp" signal) or the type of heating source [25], [30]–[33]. The

performance of those PuCT setups have been compared with the respective PT and LIT [34] counterparts.

However, some issues still remain. In fact, generally the implementations of PuCT focus on the obtained SNR gain and do not analyze the quality of the retrieved impulse responses after the cross-correlation algorithm. The aim of this work is thus to give a measurement protocol that optimizes both the SNR gain and the quality of the impulse response reconstruction. The next subsections are focused on the theoretical and practical limitations that limit the full exploitation of PuC in thermography.

7.2.2. Heat exchange: a brief overview

Heat transmission is a very complex phenomenon. Therefore, an easy mathematical description can be given only by taking into consideration ideal cases or ideal approximations. In addition, the mathematical modelling depends strictly on the kind of thermal source used for the experimental activity and the related physical principle of heating [34].

For this experimental activity, LED lamps have been used to deliver energy toward the surface of the sample under test. In this case, a 1-D propagation of the heat can be used as an approximation of the transmission phenomenon, in which the thermal front propagates by diffusion from the sample surface towards the inner volume of the sample, and assuming also a negligible contribution of lateral diffusion [35]. In the presence of a subsurface defect, e.g delaminations, voids, etc., the heat diffusion rate changes locally. This, in turn, causes local variations of the surface temperature. As a consequence, the presence of a defect can be seen by analyzing the radiation emitted from the sample surface. In addition, the defect depth can be predicted theoretically by a time-analysis of the emitted radiation. This is

because the heat diffusion into the sample does not occur instantaneously. Therefore, defects at different depths produce changes in the emitted radiation at different times.

This can be mathematically explained by looking at some specials solutions of a simplified 1D model of the heat equation [35]:

$$\frac{\partial^2 \Theta(z,t)}{\partial z^2} - \frac{c_s \rho}{k_T} \frac{\partial \Theta(z,t)}{\partial \Theta} = -\frac{q(z,t)}{k_T} \tag{7.1}$$

with z the direction perpendicular to the inspection surface plane. $\Theta(z,t)$ (K) and $q(z,t)$ (W·m^{-3}) are the sample temperature and heat source magnitude respectively at both a fixed position z and time t, c_s is the specific heat (J·kg^{-1}·K), ρ is the density (kg·m^{-3}) and k_T the thermal conductivity (W·m^{-1}·k^{-1}). Consider the ideal case of an external sinusoidal heat source with frequency f impinging only on the sample inspection surface, so as to have $q(z)$ = 0 for $z \neq 0$. Assuming that the sample is a semi-infinite body, equation (7.1) can be rearranged as a wave equation in the frequency domain as:

$$\frac{\partial^2 \Theta(z,f)}{\partial z^2} - \sigma^2 \Theta(z,f) = 0 \tag{7.2}$$

where i is the imaginary unit, $\sigma = \sqrt{\frac{i 2\pi f}{\alpha}} = (1+i)\sqrt{\frac{\pi f}{\alpha}} = \frac{(1+i)}{\mu_T}$ is the complex wave number (rad·m^{-1}), $\alpha = \frac{k k_T}{c_s \rho}$ is the thermal diffusivity (m^2·s^{-1}) and $\mu_T = \sqrt{\frac{\alpha}{\pi f}}$ the thermal diffusion length (m). If a boundary condition of heat flux continuity on the sample surface is taken into account, the solution of equation (7.2) is:

$$\Theta(z,t) = \Theta_0 e^{-\frac{z}{\mu}} \cos(\frac{z}{\mu_T} - 2\pi f t + \frac{\pi}{4}) \tag{7.3}$$

which is an evanescent wave that does not propagate into the sample. This means that the heat flux decreases exponentially with the depth following a characteristic scale μ_T. As a rule of thumb, the excitation frequency $f_{opt}(z_d)$ that assures the highest sensitivity to a defect located at a depth z_d is approximately $f_{opt}(z_d) = \frac{\alpha}{\pi z_d^2}$, for which $\mu_T = z_d$.

If the most general case of heating source is taken into account, equation (7.3) shows that the thermal front is affected by dispersion. This is because different frequencies have different values of phase velocity:

$$v_{phase}(f) = 2\pi f \mu_T = 2\sqrt{\pi f \alpha} \tag{7.4}$$

As pulsed thermography is the most common thermography NDE technique, it is of utmost importance to see what are the implications of equations (7.1-7.4) in the case when the heating stimulus is modelled as a Dirac Delta function ($\delta(t)$) short time excitation. Assuming again that the sample under test is a semi-finite body, the solution of equation (7.2) turns out to be [35]:

$$\Theta(z,t) = \Theta(z,0) + \frac{Q}{c_s \rho \sqrt{\pi \alpha t}} e^{-\frac{z_d^2}{4\alpha t}} \tag{7.5}$$

If a more realistic model of the sample under test is taken into account, i.e. a finite slab of material, the excitation heat pulse is spread out in time. This is because the dispersion effect does not make the pulse excitation travelling with constant velocity and fixed shape through the sample. The direct consequence is that the impulse response $h(j_x, j_y, z, t)$ of the generic acquired image pixel (j_x, j_y) is not only a simple attenuated and delayed replica of the pulse excitation, but is a decay function in which the presence of defects is identified as "smooth" and "slow" variations of the decay itself. As a consequence, it is not possible to simply assign a Time-of-Flight value to dispersive phenomena and thus the identification of defect depths is challenging. To cope with this, an average velocity of diffusion is considered. In this way, the defect depth can be estimated by considering the time delay at which the signal of the defect shows a maximum in its value.

Commonly, it is found in the literature that the optimum frequency for the detection of a defect at a depth z_d for which $\mu_T = z_d$ is $f_{opt}(z_d) = \frac{\alpha}{\pi z_d^2}$. In addition, if the phase velocity

at the optimal frequency is $v_{phase}(f_{opt}) = 2\frac{\alpha}{z_d}$, then the time at which the maximum of the

defect signature signal is expected to be [36]:

$$t_{max}(z_d) \sim \frac{z_d}{v_{phase}(z_d)} = \frac{z_d{}^2}{2\alpha} \qquad (7.6)$$

The depth of the defects can be thus obtained by calculating t_{max} as for equation (7.6).

It is clear that the aim is the optimal reconstruction of the impulse response. The cross-correlation output resulting from coded signals and PuC is always an estimation of the real impulse response. However, the delivered power to the system is extended over a longer time period with respect to the standard pulse, thus increasing the maximum achievable SNR. Although the PuC procedure was explained in Chapter 2, it is important to stress the mathematical algorithm at that is the basis of this fact. If *s(t)* is an arbitrary coded signal excitation having time duration T, and if its matched filter $\Psi(t)$ is such that their convolution approximates the Dirac's Delta function $\delta(t)$, $s(t) \otimes \Psi(t) = \tilde{\delta}(t) \sim \delta(t)$, the impulse response $h(t)$ can be estimated ($h_{es}(t)$, having estimate duration T_h) by convolving the Linear Time Invariant (LTI) system output $y(t)$ with the matched filter, as explained in Figure 7.1.

Again, Section 2.4.1. pointed out the importance to use advanced algorithms such as windowing and Wiener filter as a matched filter to both decrease the side-lobe levels and the width of the main PuC output peak. In addition, it has been chosen that the reconstruction of the impulse response depends strictly on the correct application of either Cyclic or Acyclic PuC, respectively (CPC) or (APC) algorithm (see again Chapter 2). Thus, the following sections will report how to successfully implement the PuC algorithm for thermography inspection.
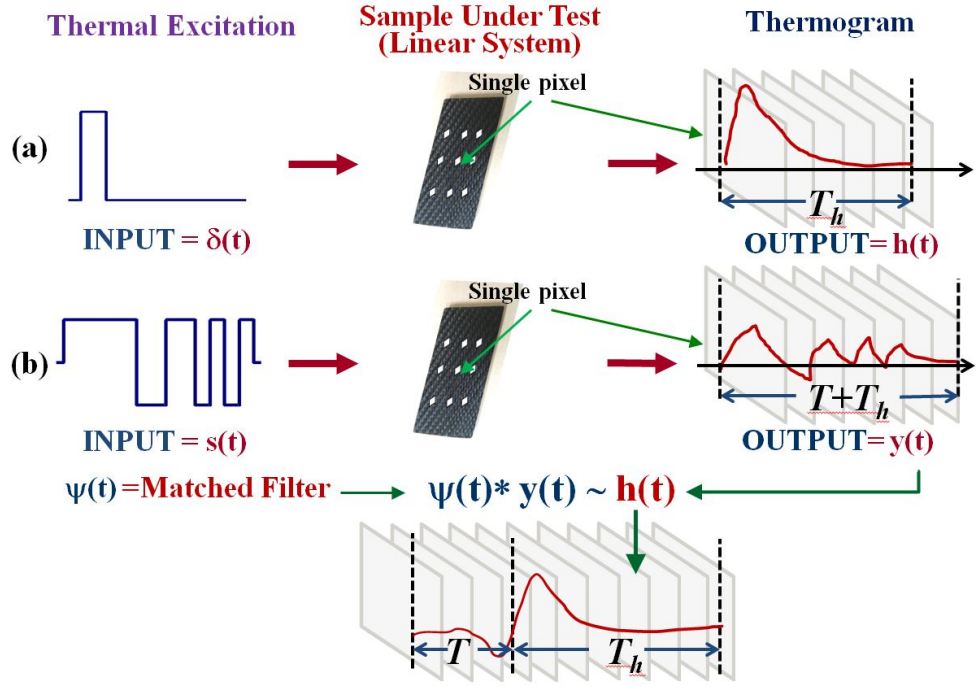
Figure 7.1: Comparison between (a) Pulsed Thermography (PT) and (b) Pulse-Compression Thermography (PuCT).

7.2.3. Issues on the application of PuC in thermography

In order to apply PuC successfully to active thermography, there are two main practical issues that have to be faced:

(A)   Coded waveforms, which are normally bipolar, have to be transformed into unipolar sequences in order to modulate a heating source.

(B)   Long time-duration excitations are needed in order to concentrate the excitation energy. This in turn would assure a high sensitivity to hidden defects.

When a coded bipolar waveform is successfully transformed to a monopolar coded excitation, so as to cope with (A), the "true" excitation signal $s_{TR}(t) = s(t) + s_{SQ}(t)$ is a superposition of a coded excitation $s(t)$ and a square pulse $s_{SQ}(t) = C\{\vartheta(t) - \vartheta(t - T)\}$, in which $\vartheta(t)$ is the Heaviside step function and T is the duration of the excitation. As a consequence, the "true" output signal will be $y_{TR}(t) = h(t) * s(t) + h(t) * s_{SQ}(t) + e(t) = y(t) + y_{SQ}(t)$, as shown in Figure 7.2:
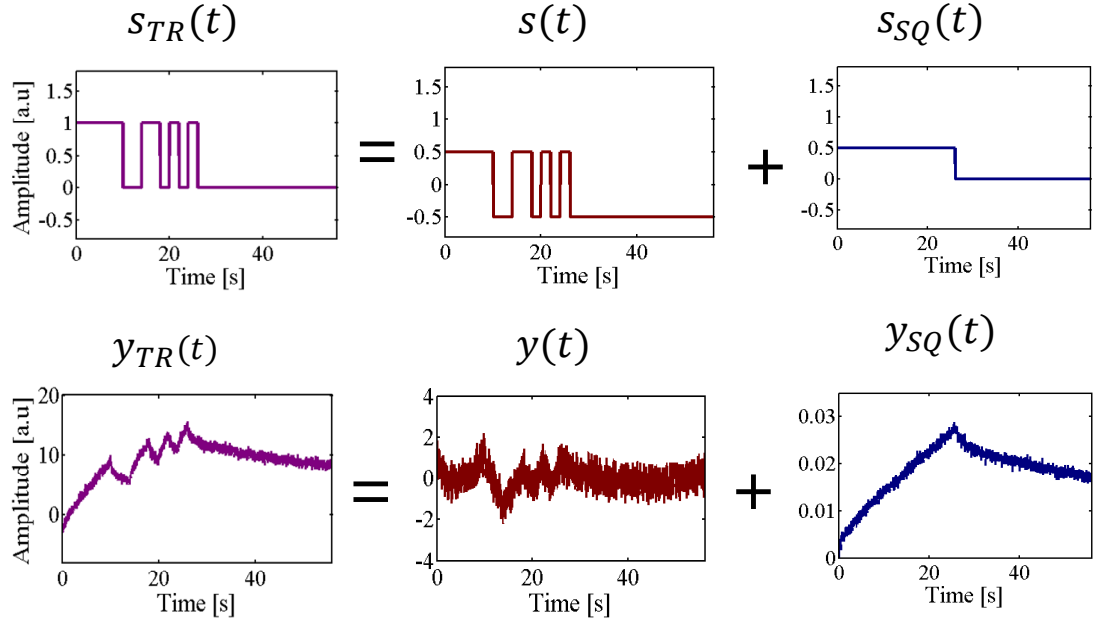
Figure 7.2: "true" input $s_{TR}(t)$ and "true" output $y_{TR}(t)$ signals of a PuCT experimental scheme. The input signal (top) is a superposition of the coded excitation $s(t)$ and a square pulse $s_{SQ}(t)$. The output signal (bottom) is a superposition of a coded response $y(t)$ and a step heating response $y_{SQ}(t)$.

Therefore, to successfully implement PuC algorithm, the contribution $y_{SQ}(t)$ of the square pulse on the acquired signal has to be removed. This can be done by exploiting two different fitting procedures, which can be modelled so as to remove the unwanted bias term $y_{bias}(t)$. Furthermore, the presence of the bias forces the choice to be the APC scheme. This is because the CPC scheme needs a stable response to be gained in a short time, but the presence of a DC bias does not allow this condition to be reached. Following the earlier discussion in Chapter 2, APC applied to thermography must consist of:

(i)   Exciting the sample with a coded modulation of the heat excitation having time duration T;

(ii)   Acquiring thermograms for a time duration $(T+T_h)$, with T_h the predicted duration of the impulse response of interest (i.e. the impulse response time duration of the equivalent PT analysis);

(iii)   Obtaining the estimation of the impulse response of duration T_h by performing a pixel-by-pixel convolution between the matched filter and the acquired signals (see Figure 7.1).

It can be found in the literature that usually the collection of the thermograms is made only for the time duration T of the coded signal itself; hence, PuC was performed by only analyzing the first T seconds. As described in Chapter 2, this strategy is correct only in the case of a periodic excitation, and only when the steady-state is reached. By stopping the acquisition of the output signal at T seconds, the retrieved estimation impulse response $h_{es}(t)$ in ACP is afflicted by an additional mathematical error. The magnitude of this error is very low when T_h is significantly shorter than T. However, this condition is not reached in PuCT. Theoretically, this noise should not hamper the defect detection, but it dramatically affects the impulse responses time analysis for defect depth estimation. The error created in this way is estimated numerically in Section 7.4, where the truncated procedure has been compared with its correctly-applied counterpart.

Regarding point (B), taking into account values of thermal diffusivity which are common for composite and thermoplastic materials ($\alpha \sim 10^{-6}\text{-}10^{-7}$ m^2*s^{-1}), it turns out that even embedded defects located at a depth of 1 millimetre require an excitation frequency that ranges from tens to hundreds of millihertz. The optimal coded excitation design is thus not easy and the maximum SNR value achievable by using PuC is limited. In general, the sidelobe amplitude $\tilde{\delta}'s$ is inversely proportional to the Time-Bandwidth product TB of the waveform, which coincides for binary codes with the number of bits L (see again Chapter 2). As a consequence, if the coded signal excitation bandwidth B is limited to a fraction of Hertz, the excitation should be a few minutes long for assuring high TB products ($TB>100$). However, this duration cannot be implemented for on-line and/or in-situ real thermography inspections.

As the SNR gain provided by PuC is proportional to the parameter *TB,* a trade-off between SNR*,* sidelobe levels and measurement time must be found. The optimal choice when low *TB* values have to be faced is given by the use of binary Barker Codes [37]–[40]. These codes exhibit the lowest sidelobes level when used in a single-shot scheme. Furthermore, with respect to Golay codes for example, Barker codes do not require two measurements to successfully apply PuC (as compared to GolayA + GolayB for example). This fact makes them easier to be exploited for thermography over long measurement times. However, Barker codes exist only up to a bit length *L=13*, limiting in turn both the maximum achievable SNR gain and the sidelobe suppression to ~22 dB. To face this issue, the standard matched filter has been here replaced with an optimally-designed Wiener Filter (see Section 2.4.1), and the experiments reported in Section 7.3 make use of this strategy. Figure 7.3 shows the simulated impulse response estimation $\tilde{\delta}(t)$ obtained using either a standard matched filter (black) and a Wiener Filter (red), with a *L=13* Barker code. It can be seen that the main lobe amplitude and shape are not affected by the use of Wiener filter, whilst sidelobes are suppressed by up to 30 dB.
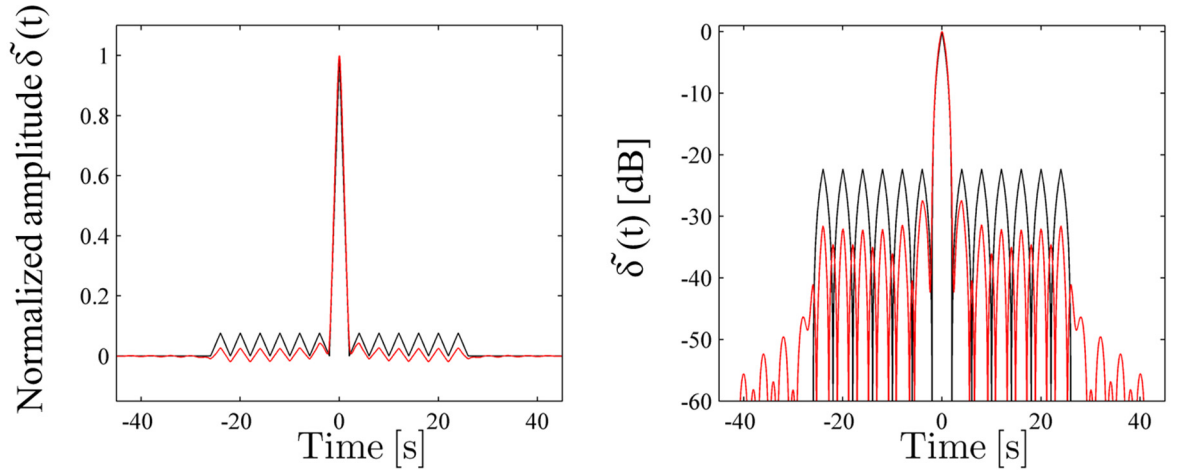

Figure 7.3: Simulated impulse response obtained by using the Standard matched filter approach (black) and Wiener filter (red).

7.2.4. Square pulse response removal (DC removal)

As stated above, there is the need to remove the square pulse excitation contribution, i.e. the DC bias, to apply PuCT successfully. To reach this aim, the idea is to fit the signal of each image pixel with a known function. Commonly, a simply linear fit model is used [30], [34]. This fitting model is applied to the output signal only by taking in consideration a time interval T for which the input signal is switched on.

However, this fitting model leads to errors in the impulse response estimation for two main reasons: (i) the model is linear, thus non-linear phenomena are not taken into account; (ii) the output signals must be collected for a time T_h after the end of the coded excitation of duration T in order to estimate the first T_h seconds of the impulse. As a consequence, the fitting function must be defined for $t>T$. Hence, even the decay curve must be separated into two contributions, one from the coded excitation $s(t)$, the other from the square pulse $s_{SQ}(t)$.

In order to implement this separation successfully, two different excitation strategies have been tested, exploiting their ad hoc designed fitting function. The mathematical model of both the excitations and their proper fitting functions are given in Equations 7.7 and 7.8, whereas Figure 7.4 shows schematically the excitation strategies that are used.

Excitation Signal 1 – "Single Barker"

$$s_{TR}(t) = \begin{cases} \dfrac{A}{2}(s(t) + 1) \ for \ 0 \leq t \leq T \\ 0 \ for \ T < t \leq T + T_h \end{cases}$$

(7.7)

Fitting Function 1

$$y_{SQ}(t) = \begin{cases} a_1 t + a_2 t^{0.9} + a_3 t^{0.8} \ for \ 0 \leq t \leq T \\ y_{SQ}(T) - a_1 t - a_2 t^{0.9} - a_3 t^{0.8} \ for \ T < t \leq T + T_h \end{cases}$$

210

Excitation Signal 2 – "Barker&Step"

$$s_{TR}(t) = \begin{cases} \dfrac{A}{2}(s(t)+1) \ for \ 0 \le t < T \\ A/2 \ for \ T < t < T + T_h \end{cases}$$

(7.8)

Fitting Function 2

$$y_{SQ}(t) = a_1 t + a_2 t^{0.9} + a_3 t^{0.8} \ \forall t$$
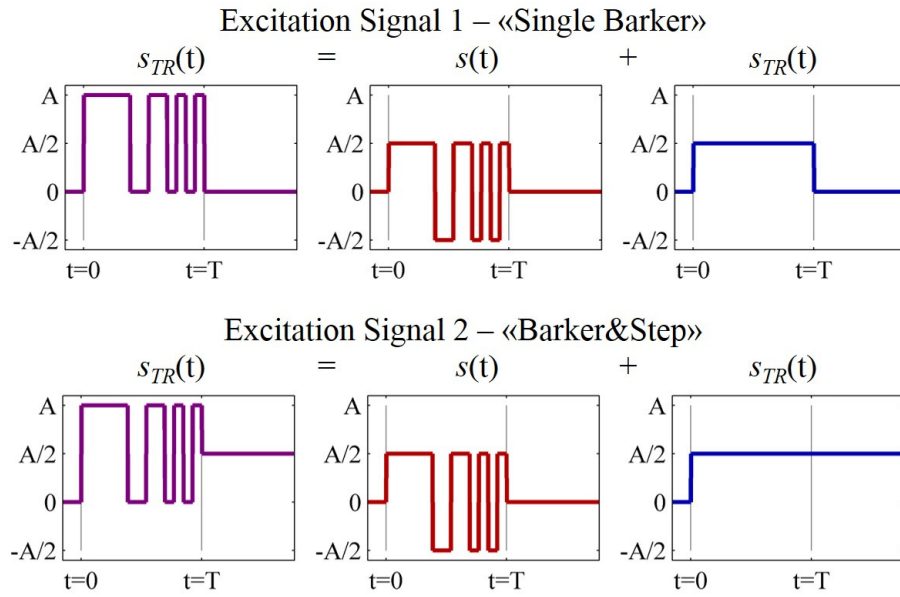
Figure 7.4: Decomposition of the true excitation signal $s_{TR}(t)$ into a proper coded excitation $s(t)$ plus a square pulse $s_{SQ}(t)$ for the two procedures proposed: "Single Barker" and "Barker&Step"

The coefficient magnitudes used in the fitting functions come from a previous experimental optimization on Step-Heating data acquired on the same sample. Figure 7.5 shows the results achieved by using both "Excitation 1" and "Fitting Function 1" for various duration of the step heating excitation T_{SQ}:
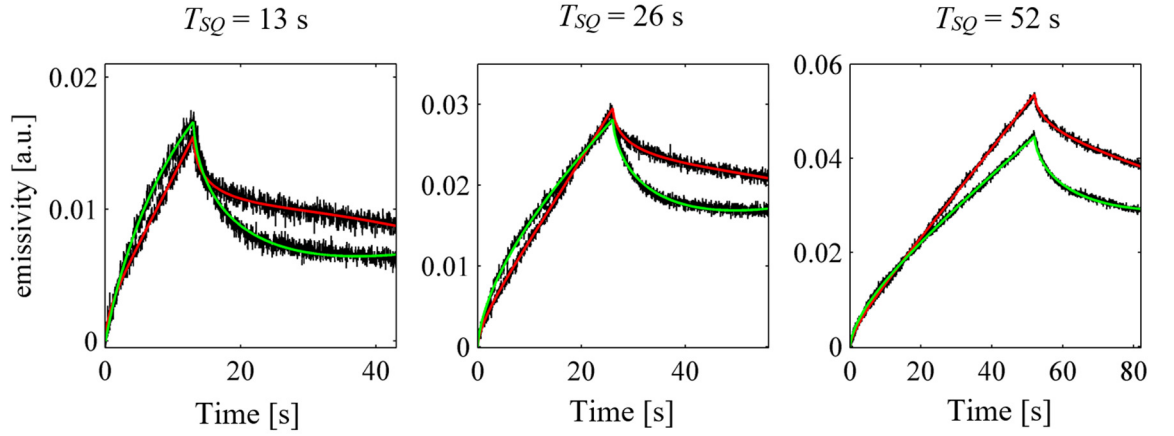
Figure 7.5: Examples of the application of the fitting function 1 (as for equation(7.7)) to various step-heating data.

It can be seen that the fitting approach used follows both the rise and decay of the acquired signal successfully. Figure 7.6(a) shows the application of the fitting functions (Equations (7.7) and (7.8)) to PuCT data acquired by exploiting the relative excitation signals "Single Barker" and "Barker&Step". Figure 7.6(b) shows the final output obtained after fitting, in which the contribution of the coded excitation and that of the square excitation are differentiated.
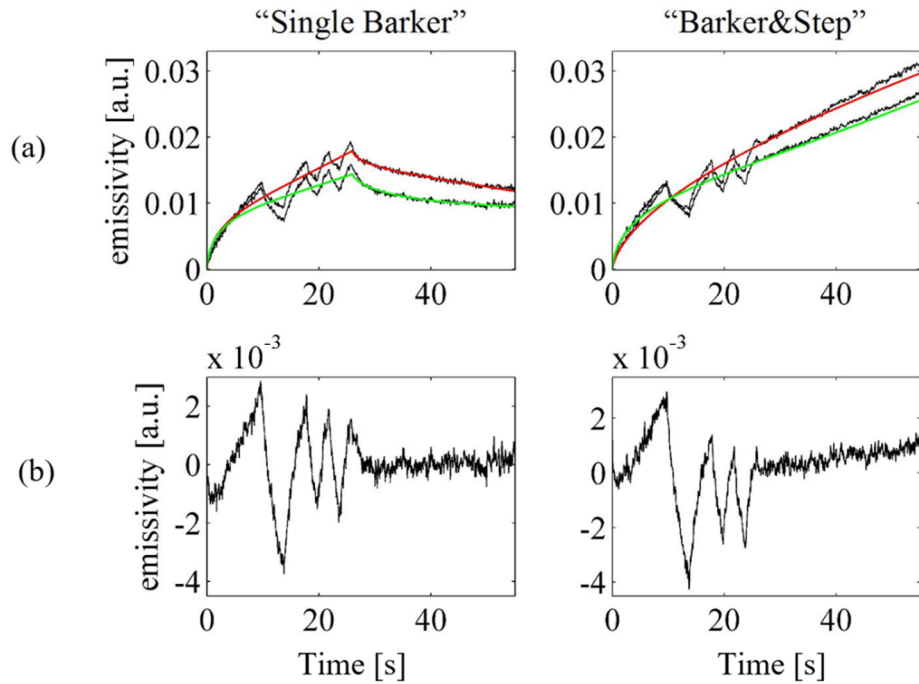
Figure 7.6:(a) Application of the fitting procedures to single-pixel output curves obtained by exploiting "Single Barker" and the "Barker&Step" excitations; (b) resulting coded output signals $y(t)$ after removal of the respective square pulse outputs $y_{SQ}(t)$.

The differences between the quality of the results achieved by using the two different signals excitation/fitting strategies are reported in Section 7.4, both in terms of SNR and of impulse response reconstruction quality. The experimental setup used to compare the proposed strategies with respect to the state-of-art PuCT is reported in the next section, together with the characteristics of the sample used for benchmarking. Please note again that for the proposed innovative techniques, an optimally-designed Wiener matched filter has been used.

7.3   Experimental Setup

The signal generation/acquisition was managed by means of a National Instrument PCI-6711 Arbitrary Waveform Generation (AWG) board and by a NI-1433 Camera Link Frame Grubber. They were linked to a PC and managed with an ad hoc develop Labview virtual instrument. The Barker code excitation modulated the power emission of TDK Lambda GEN 750W power supply. This in turn, was connected to four 50 W LED chips placed at about 30 cm from the sample under inspection. In addition, the AWG board sent a clock signal for a Xenics Onca-MWIR-InSb IR camera, which acquired the needed thermograms. A sketch of the experimental setup is depicted in Figure 7.7. Please note that the brand and the model of each instruments have not been reported on the sketch, so as to avoid giving a confused picture of the setup:
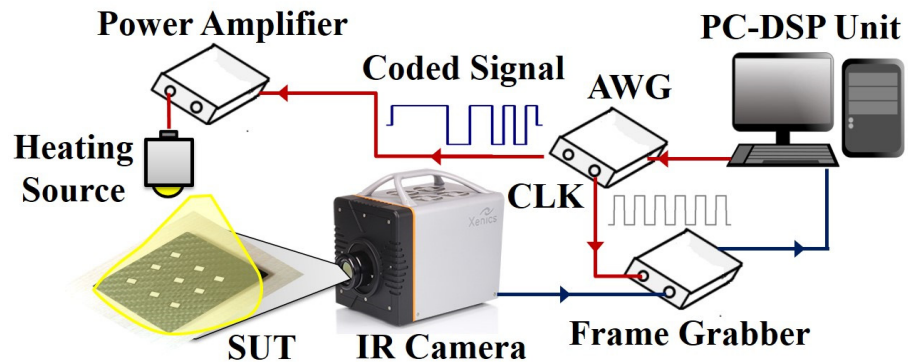
Figure 7.7: Sketch of the experimental setup.

The benchmark sample was a carbon fiber composite laminate, made of twelve plies of carbon fiber fabric with an areal density of 200 g/m^2. The fibers orientations were 0° and 90° and the matrix was an Epoxy Resin RIM 935.The laminate was made by vacuum assisted resin infusion and cured at room temperature and postured at 110°C for two hours, so as to obtain a fully cured sample. The dimensions of the sample were 240 by 200 mm, whilst the thickness was about 2.80 millimetres. A series of delaminations were artificially realized by placing several square pieces of Teflon tape between subsequent plies, having lateral dimensions of 20 by 20 millimiters and thickness of 75 μm.

Nine defects were chosen to be inserted at increasing depths: the outer was placed under the 2nd ply at a depth $z_d \sim 0.46$ mm, the inner under the 10th ply at a depth $z_d \sim 2.3$ mm. A sketch of the sample is reported in Figure 7.8, where the artificially realized embedded defects positions are highlighted in red:
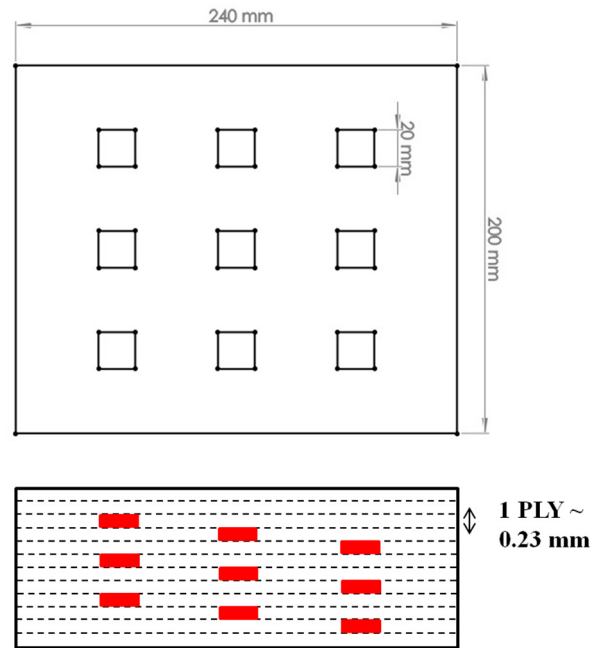
Figure 7.8: A sketch of the carbon fibre composite sample.

The thermal diffusivity of the benchmark sample α_{th} was retrieved by exploiting an empirical function calculated for a carbon fiber reinforced polymer sample for a time t equal to 0.5 seconds:

$$\alpha_{th} = (2.829 * 10^{-9}) * V_f + 1.247 * 10^{-7} \qquad (7.9)$$

where the quantity V_f is the fiber volume fraction . For the benchmark sample V_f is estimated

to be equal to 0.5 [41]. It resulted to be equal to $\alpha_{th} = 0.125$ mm^2*s^{-1}.

7.4   Experimental results

In this section the results obtained by applying the procedures "Single Barker" and

"Barker&Step" introduced in the previous section are reported. These proposed techniques

are compared under the same conditions with the "State-of-the-art" procedure (the one with

the truncated acquisition and the linear fitting for DC removal). The comparison is given so

as to identify which strategy assures the higher SNR and best estimation of the impulse

response. In order to reach this aim, the position of each defect within the sample has to be

identified on the acquired thermogram. In this way, their respective impulse responses can

be compared. Figure 7.9 shows a thermogram of the inspected sample obtained after PuC:
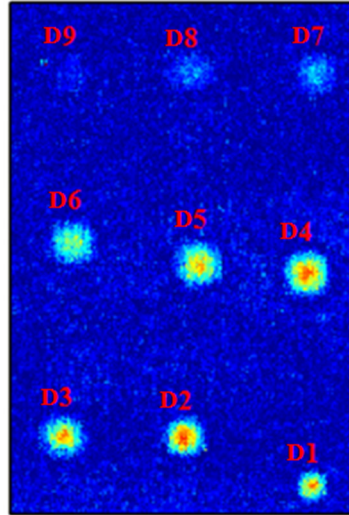
Figure 7.9: Example of a thermogram of the inspected sample. The defects were labeled from D1 to D9 as for the increasing depth from the inspection surface.

It can be seen that all the defects are clearly distinguished. For the sake of clarity, the defects

were ordered as for their relative depth within the sample: D1 was the defect nearest the

illumination surface, whilst D9 was the deeper one. An area of 3 by 3 pixels around each

defect geometrical centre location was taken into account to obtain an averaged impulse response for each procedure, which are again "State-of-the-art", "Single Barker" and "Barker&Step".

The results are shown in Figure 7.10, where the impulse responses obtained for D1-D8 have been plotted. D9 was chosen to be not investigated as the SNR value associated to its location was very low.
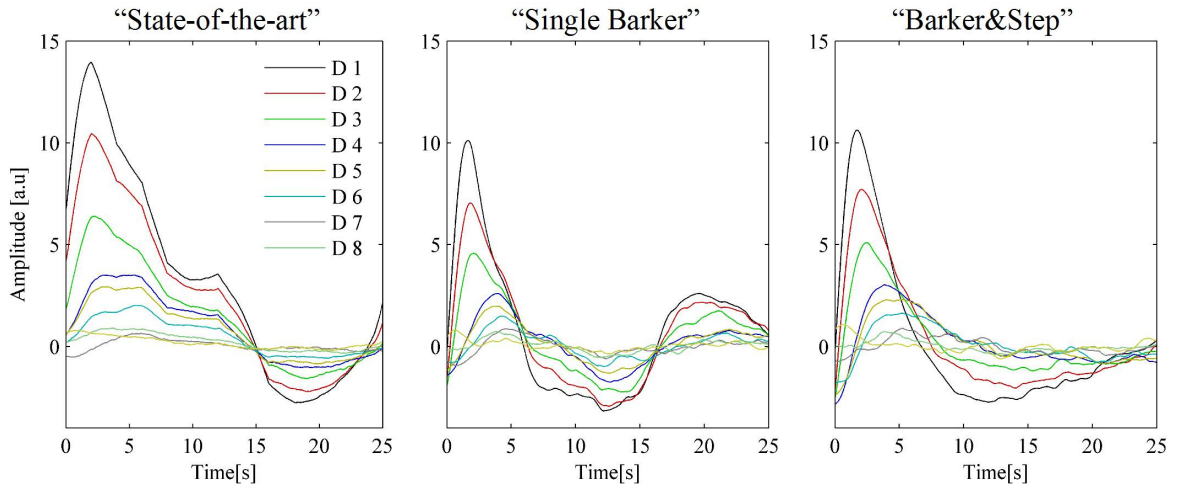
Figure 7.10: Defects impulse responses obtained by exploiting the three labelled different investigated techniques.

It can be clearly seen that the combined use of (1) the polynomial fitting, (2) the full pulse-compression procedure and (3) the Wiener filter approach makes the estimation of the impulse response with either the "Single Barker" or "Barker&Step" approach more regular than their "State-of-the-art" counterparts. In fact, the impulse responses handling obtained by exploiting the "State-of-the-art" approach show sharp variations and resulted in having a quite similar time-behaviour among the investigated different defects depths. On the other hand, the impulse responses retrieved by using "Barker&Step" strategy show a dependence of the signal handling with the defect depth. This in turn is corroborated by theory explained in Section 7.2.2, where it was pointed out that the heat transmission into such a sample suffers from diffusion in time and dispersion. Finally, several abrupt oscillations are still evident on "Single Barker" results. Hence, it is possible to conclude that the polynomial

fitting approach applied in combination with "Barker Step" excitation procedure appears to be the best solution among the investigated techniques. In fact, the said method shows the best separation and cancellation of the square pulse response $y_{SQ}(t)$ from the coded excitation response $y(t)$, thus lowering the mathematical noise on the estimated impulse response.

In order to have a quantitative comparison of the investigated techniques features, the results obtained have been compared in terms of SNR, which has been defined as follow:

$$SNR_{D_k} = \frac{h_{D_k}(t) - \bar{h}(t)}{\sigma_h(t)} \tag{7.10}$$

where $h_{D_k}(t)$ represents the impulse response of the k-th defect averaged over the 3 by 3 pixel area, $\bar{h}(t)$ is the impulse response averaged over all the investigated thermogram of the sample area and $\sigma_h(t)$ is its standard deviation. Figure 7.11 shows the obtained SNR curves for the D1-D8 defects:
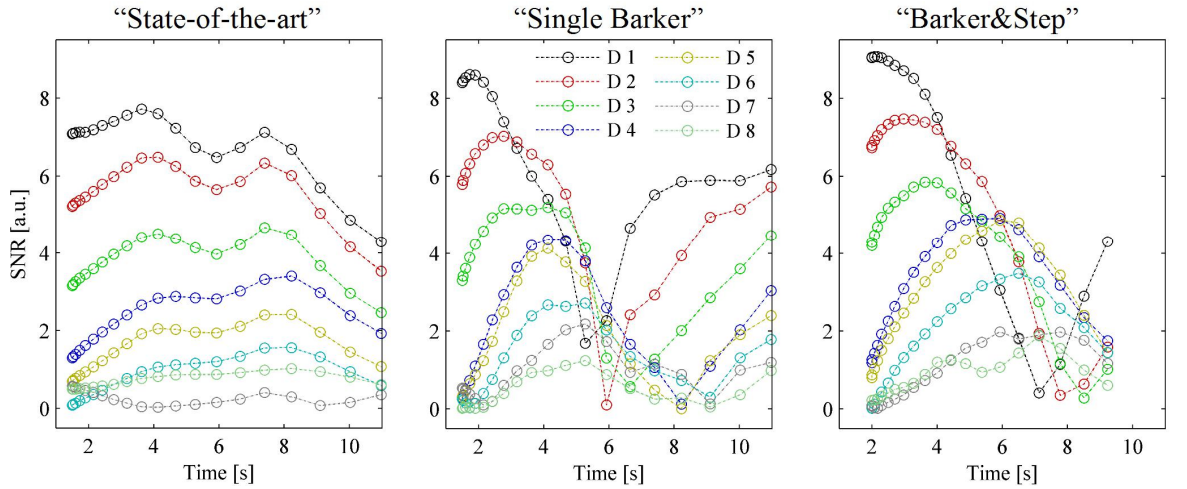
Figure 7.11: Defects SNR time-curves obtained by exploiting the three different labelled investigated techniques.

Again, the "Barker&Step" approach shows the best results among the three techniques analysed. In particular, the "State-of-the-art" SNRs are the lowest, especially for deeper defects. Furthermore, the SNR peak value obtained with this latter technique had not clear link with defect depth z_d, which is theoretically predicted to follow a relation close to the one reported for $t_{max}(z_d)$ in equation (7.6).

On the other hand, the use of the "Barker&Step" technique resulted in an enhanced defect discrimination capability in terms of both SNR and time of the maximum SNR. This is clearly shown in Figure 7.12(a) where the values of $t_{max}(z_d)$ calculated from the SNR curves of Figure 7.11 are shown for the "Barker&Step" and the "State-of-the-art" technique. Note that in the "State-of-the-art" approach, $t_{max}(z_d)$ does not seems to be linked to the defect depth, the "Barker&Step" procedure resulted in having an evident correlation between $t_{max}(z_d)$ and z_d.
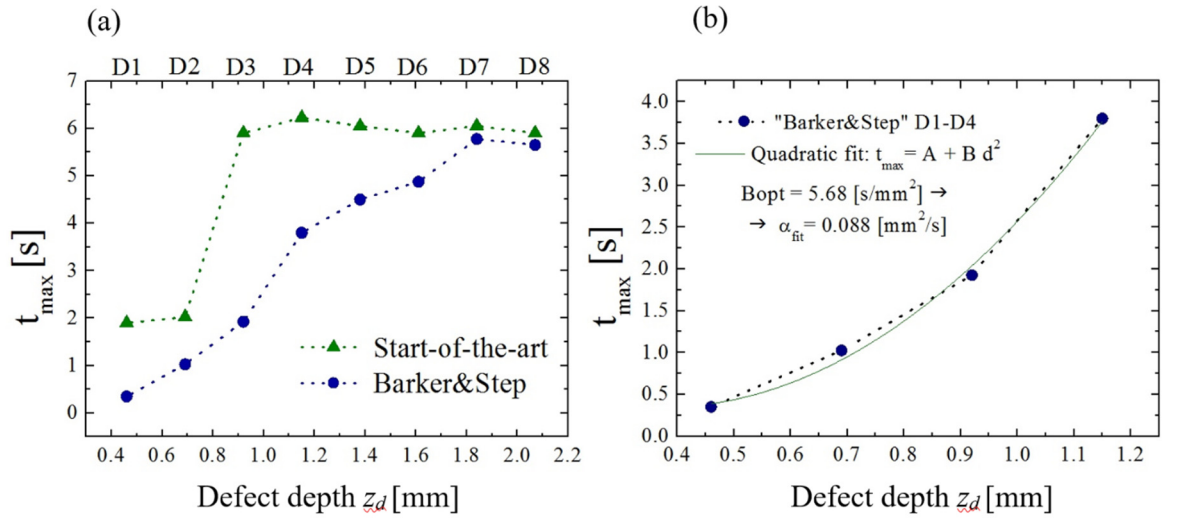
Figure 7.12: (a) Values of $t_{max}(d)$ estimated from the SNR curves for the "State-of-the-art" and the "Barker&Step". (b) $t_{max}(z_d)$ calculated for the outer defects (D1-D4) and its data fit.

By looking at Figure 7.12(b), it can be noted that $t_{max}(z_d)$ calculated for the outer defects (D1-D4), fits well with the quadratic handling of equation (7.6). In addition, from the feaures plotted in Figure7.12(b), the "effective" thermal diffusivity can be calculated. This value was found to be $\alpha_{fit} = 0.088$ mm²s⁻¹, which is very close to the expected value of $\alpha_{th} = 0.125$ mm²s⁻¹.

7.5   Conclusions

In this chapter, PuC technique has been applied to active thermographic NDE. The results obtained with three different measurement procedures have been compared. Some

strategies capable of improving the performance of the pulse compression active thermography with respect to the state-of-the-art techniques have been investigated.

In particular, the optimization of the both the fitting and excitation functions, together with the use of an optimal Wiener filter for sidelobe suppression, allows the thermal impulse response of the sample under inspection to be reconstructed with an improved SNR and enhanced fidelity. This resulted in an enhanced defect characterization performance with respect to state-of-the-art procedure [42].

References

[1]   G. Betta, L. Ferrigno, M. Laracca, P. Burrascano, M. Ricci, and G. Silipigni, "An experimental comparison of multi-frequency and chirp excitations for eddy current testing on thin defects," *Meas. J. Int. Meas. Confed.*, vol. 63, pp. 207–220, 2015.

[2]   S. Tuli and R. Mulaveesala, "Defect detection by pulse compression in frequency modulated thermal wave imaging," *Quant. Infrared Thermogr. J.*, vol. 2, no. 1, pp. 41–54, 2005.

[3]   R. Mulaveesala, J. S. Vaddi, and P. Singh, "Pulse compression approach to infrared nondestructive characterization," *Rev. Sci. Instrum.*, vol. 79, no. 9, 2008.

[4]   C. A. Balaras and A. A. Argiriou, "Infrared thermography for building diagnostics," *Energy Build.*, vol. 34, no. 2, pp. 171–183, 2002.

[5]   E. Barreira and V. P. Freitas, "Evaluation of building materials using infrared thermography," *Constr. Build. Mater.*, vol. 21, pp. 218–224, 2007.

[6]   C. Meola, G. M. Carlomagno, A. Squillace, and A. Vitiello, "Non-destructive evaluation of aerospace materials with lock-in thermography," *Eng. Fail. Anal.*, vol. 13, no. 3 SPEC. ISS., pp. 380–388, 2006.

[7]   N. P. Avdelidis, B. C. Hawtin, and D. P. Almond, "Transient thermography in the

assessment of defects of aircraft composites," *NDT E Int.*, vol. 36, no. 6, pp. 433–439, 2003.

[8]   M. Planck, "Ueber das Gesetz der Energieverteilung im Normalspectrum," *Ann. Phys.*, vol. 309, no. 3, pp. 553–563, 1901.

[9]   M. Planck, "The theory of heat radiation (Translation)," *Masius, P. Blackiston's Son Co, Philadelphia*, 1914.

[10]   G. Bm and M. Anbar, "Thermology and facial telethermography : Part II . Current and future clinical applications in dentistry . Thermology and facial telethermography . Part I : History and technical review . Infrared thermography . Its role in dental research with particular," *Dentomaxillofacial Radiol.*, pp. 1–42, 2007.

[11]   M. Anbar, B. M. Gratt, and D. Hong, "Thermology and facial telethermography. Part I: History and technical review," *Dentomaxillofacial Radiology*, vol. 27, no. 2. pp. 61–67, 1998.

[12]   W. K. Wong, P. N. Tan, C. K. Loo, and W. S. Lim, "An effective surveillance system using thermal camera," in *2009 International Conference on Signal Acquisition and Processing, ICSAP 2009*, 2009, pp. 13–17.

[13]   F. Prokoski, R. Riedel, and J. Coffin, "Identification of individuals by means of facial thermography," *Secur. Technol. 1992.*, 1992.

[14]   C. Ibarra-Castanedo *et al.*, "Comparative Study of Active Thermography Techniques for the Nondestructive Evaluation of Honeycomb Structures," *Res. Nondestruct. Eval.*, vol. 20, no. 1, pp. 1–31, 2009.

[15]   M. Y. Y. Hung, Y. S. Chen, S. P. Ng, S. M. Shepard, Y. Hou, and J. R. Lhota, "Review and comparison of shearography and pulsed thermography for adhesive bond evaluation," *Opt. Eng.*, vol. 46, no. 5, p. 51007, 2007.

[16]   S. M. Shepard, "<title>Advances in pulsed thermography</title>," 2001,

pp. 511–515.

[17] X. Maldague, F. Galmiche, and A. Ziadi, "Advances in pulsed phase thermography," *Infrared Phys. Technol.*, vol. 43, no. 3, pp. 175–181, 2002.

[18] N. P. Avdelidis, D. P. Almond, A. Dobbinson, and B. C. Hawtin, *Pulsed thermography : philosophy , qualitative quantitative analysis on aircraft materials & applications*. 2006.

[19] D. L. Balageas, "Defense and illustration of time-resolved pulsed thermography for NDE," *QIRT J.*, vol. 6733, no. June, pp. 1–1, 2012.

[20] D. Wu and G. Busse, "Lock-in thermography for nondestructive evaluation of materials," *Rev. Générale Therm.*, vol. 37, no. 8, pp. 693–703, 1998.

[21] T. Sakagami and S. Kubo, "Applications of pulse heating thermography and lock-in thermography to quantitative nondestructive evaluations," *Infrared Phys. Technol.*, vol. 43, no. 3, pp. 211–218, 2002.

[22] S. Pickering and D. Almond, "Matched excitation energy comparison of the pulse and lock-in thermography NDE techniques," *NDT E Int.*, vol. 41, no. 7, pp. 501–509, 2008.

[23] X. Maldague and S. Marinetti, "Pulse phase infrared thermography," *J. Appl. Phys.*, vol. 79, no. 5, p. 2694, 1996.

[24] G. Pitarresi, "Lock-In Signal Post-Processing Techniques in Infra-Red Thermography for Materials Structural Evaluation," *Exp. Mech.*, vol. 55, no. 4, pp. 667–680, 2015.

[25] N. Tabatabaei and A. Mandelis, "Thermal-wave radar: A novel subsurface imaging modality with extended depth-resolution dynamic range," *Rev. Sci. Instrum.*, vol. 80, no. 3, pp. 1–11, 2009.

[26] N. Tabatabaei and A. Mandelis, "Thermal coherence tomography using match filter binary phase coded diffusion waves," *Phys. Rev. Lett.*, vol. 107, no. 16, pp. 1–5, 2011.

[27] R. Mulaveesala and S. Tuli, "Theory of frequency modulated thermal wave imaging for nondestructive subsurface defect detection," *Appl. Phys. Lett.*, vol. 89, no. 19, 2006.

[28] V. S. Ghali, N. Jonnalagadda, and R. Mulaveesala, "Three-dimensional pulse compression for infrared nondestructive testing," *IEEE Sens. J.*, vol. 9, no. 7, pp. 832–833, 2009.

[29] V. S. Ghali, S. S. B. Panda, and R. Mulaveesala, "Barker coded thermal wave imaging for defect detection in carbon fibre-reinforced plastics," *Insight - Non-Destructive Test. Cond. Monit.*, vol. 53, no. 11, pp. 621–624, 2011.

[30] R. Mulaveesala and S. Venkata Ghali, "Coded excitation for infrared non-destructive testing of carbon fiber reinforced plastics," *Rev. Sci. Instrum.*, vol. 82, no. 5, 2011.

[31] J. Gong, J. Liu, L. Qin, and Y. Wang, "Investigation of carbon fiber reinforced polymer (CFRP) sheet with subsurface defects inspection using thermal-wave radar imaging (TWRI) based on the multi-transform technique," *NDT E Int.*, vol. 62, pp. 130–136, 2014.

[32] J. A. Siddiqui, V. Arora, R. Mulaveesala, and A. Muniyappa, "Infrared Thermal Wave Imaging for Nondestructive Testing of Fibre Reinforced Polymers," *Exp. Mech.*, vol. 55, no. 7, pp. 1239–1245, 2015.

[33] R. Yang and Y. He, "Pulsed Inductive Thermal Wave Radar (PI-TWR) Using Cross Correlation Matched Filtering in Eddy Current Thermography," *Infrared Phys. Technol.*, vol. 71, pp. 469–474, 2015.

[34] N. E. I. 44 (2011) 655–667. doi:10. 1016/j. ndteint. 2011. 06. 008. Chatterjee, Krishnendu[1] K. Chatterjee, S. Tuli, S.G. Pickering, D.P. Almond, A comparison of the pulsed, lock-in and frequency modulated thermography nondestructive evaluation techniques, S. Tuli, S. G. Pickering, and D. P. Almond, "A comparison of the pulsed,

lock-in and frequency modulated thermography nondestructive evaluation techniques," *NDT E Int.*, vol. 44, no. 7, pp. 655–667, 2011.

[35] H. Carslaw and J. Jaeger, "Conduction of heat in solids," *Oxford Clarendon Press. 1959, 2nd*, 1959.

[36] F. Lopez, V. De Paulo Nicolau, C. Ibarra-Castanedo, and X. Maldague, "Thermal-numerical model and computational simulation of pulsed thermography inspection of carbon fiber-reinforced composites," *Int. J. Therm. Sci.*, vol. 86, pp. 325–340, 2014.

[37] R. H. Barker, "Group synchronizing of binary digital systems," *Commun. theory*, pp. 273–287, 1953.

[38] R. Turyn and J. Storer, "On binary sequences," *Proc. Am. Math. Soc.*, vol. 19, no. xi, pp. 394–399, 1960.

[39] T. Misaridis and J. A. Jensen, "Use of modulated excitation signals in medical ultrasound. Part III: High frame rate imaging," *IEEE Trans. Ultrason. Ferroelectr. Freq. Control*, vol. 52, no. 2, pp. 208–218, 2005.

[40] R. Y. Chiao and X. Hao, "Coded Excitation for Diagnostic Ultrasound : A System Developer ' s Perspective Preprint for 2003 IEEE Ultrasonics Symposium Preprint for 2003 IEEE Ultrasonics Symposium," *IEEE Trans. Ultrason. Ferroelectr. Freq. Control*, vol. 52, no. 2, pp. 160–170, 2003.

[41] G. Wróbel and Z. Rdzawski, "Determination of thermal diffusivity of carbon/epoxy composites with different fiber content using transient thermography," *J. Achiev. Mater. Manuf. Eng.*, vol. 37, no. 2, pp. 518–525, 2009.

[42] G. Silipigni, P. Burrascano, D.A. Hutchins, S. Laureti, R. Petrucci, L. Senni, L. Torre, M. Ricci, "Optimization of the pulse compression technique applied to the infrared thermography nondestructive evaluation," *NDT&E, (SUBMITTED).*

CHAPTER 8: Conclusions and further work

8.1   Conclusions

It has been demonstrated in this thesis that acoustic metamaterial can be designed to work successfully at frequencies into the middle audible - low ultrasonic range. This has been investigated by means of both Finite Element Modelling (FEM) and by a series of experimental acquisitions. In particular, it has been demonstrated that acoustic metamaterial realized by means of additive manufacturing with a polymeric material substrate can be used successfully for imaging a subwavelength object within a frequency range that was not previously explored. In addition, it has been demonstrated the exotic acoustic lens design can lead to superlensing effects in the middle audible frequency range. The experimental setup used to demonstrate these capabilities exploited coded signals, in the form of chirp signals, to characterize in the frequency domain the features provided by the use of such metamaterials. As a consequence, a first step towards the realization of an acoustic metamaterial device capable to show exotic effect over a broader frequency range has been made here in the form of a "pyramid" geometry acoustic metamaterial.

Parallel research on the use of coded signals with pulse compression techniques has been carried out. The main characteristics of several widely-used coded waveforms and advanced algorithms have been reported. Their features have been investigated numerically so as to give to the reader a benchmark for choosing an optimal coded waveform and pulse compression algorithm for a given application. In addition, the improvement in inspection capabilities given by the use of these advanced signal processing techniques has been tested using real industrial non-destructive testing applications. For example, advanced algorithms have been designed for the inspection of highly attenuating materials using pulse compression. This included thick polymeric riser stiffeners, widely used in the oil and gas

off-shore industry, and refractory bricks samples, serving as structural features in large furnaces. In addition, the possibility to realize a portable device capable of having the same fidelity of the commonly-available standard pulse compression instruments has been also explored. Its capabilities have been tested for the inspection of concrete containing rebars. Finally, an innovative strategy for using coded signals and pulse compression in active thermography inspection has investigated. This resulted in an enhanced defect discrimination in challenging materials with respect to the standard pulse compression thermography procedure.

The above has made a real contribution to the knowledge on this subject, and has shown that pulse compression is a powerful tool, provided that it is used in the correct way, and with the appropriate additional analysis tools. The choice of pulse compression waveform and post data acquisition analysis has been shown to be an important feature.

8.2   Further work

Further work should focus on the creation of an acoustic metamaterial device which can be used for broadband sub-wavelength imaging purposes. This will allow the complete exploitation of the pulse compression algorithms and advanced post-processing techniques. In particular, many applications require the use of a metamaterial at higher frequencies, and which can be used in water immersion. This would be of high importance for medical ultrasonic imaging, for example.

The advanced inspection capabilities and flexibility provided by the use of the portable device will be used for the inspection of more complex materials and geometries. Ad hoc software could be developed and embedded within the portable device itself, so as to produce a real portable inspection instrument. This would make it ideal for the inspection of more complex civil engineering structures containing rebars. More studies should confirm

the maximum depth of penetration for this application, perhaps at different centre frequencies, and of interest will be whether it is possible to image multiple rebar layers rebar.

The application of the pulse compression algorithm in thermography should be further investigated. This will be done by optimally design linear and non-linear chirp in order to further reduce errors in the impulse response estimation.

APPENDIX

Fountek NeoCD 2.0 ribbon tweeter

**Fountek Electronics Co.,Ltd**

NeoCD2.0 ribbon tweeter is a high-performance component which is probably the best choice to building/upgrade your loudspeaker.

Features
- Advanced composite material ribbon diaphragm, which provide higher power handling and guarantees a high degree of signal fidelity and broad frequency response.
- Super strong Neodymium magnet fro high efficiency
- Build-in impedance conversion transformer
- Effective from 1,200Hz upwards due to the large diaphragm area and low self-resonance.
- Low distortion factor, good power-handling capabilities, high linear impedance and amplitude frequency response and the broad frequency response range.

Specifications	
Ribbon material	Advanced composite material
Ribbon mass	34mg
Ribbon dimension	8mmX120mmX0.02mm
Ribbon area	960square micrometer
Gap flux	0.6 Telsa
Gap height	3mm
Impedance	7 Ohm
DCR	0.02 Ohm
Frequency response	1,200~40,000Hz
Sensitivity	98dB/2.83V@1M
Resonance frequency	300Hz
Power handling	20W Nominal, 50W Max
Recommended crossover	2,000Hz / 2nd-Order
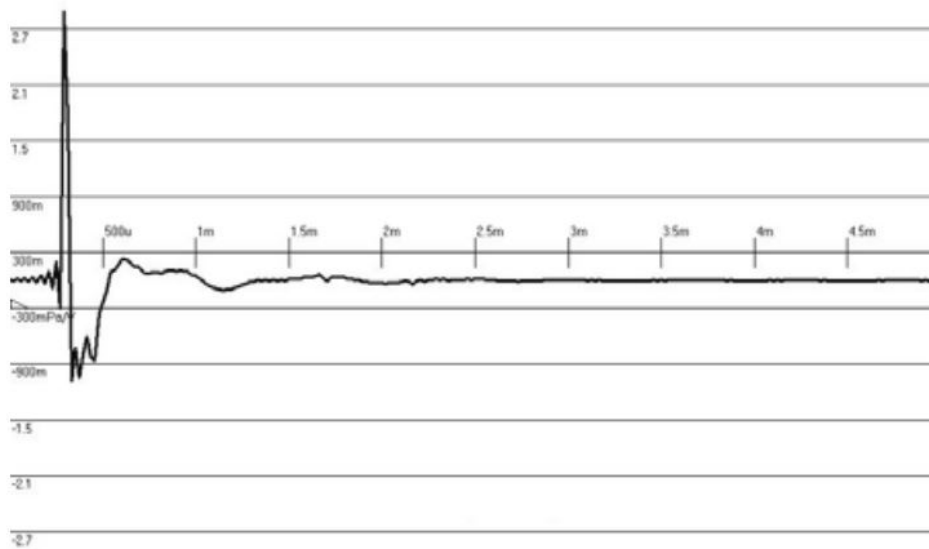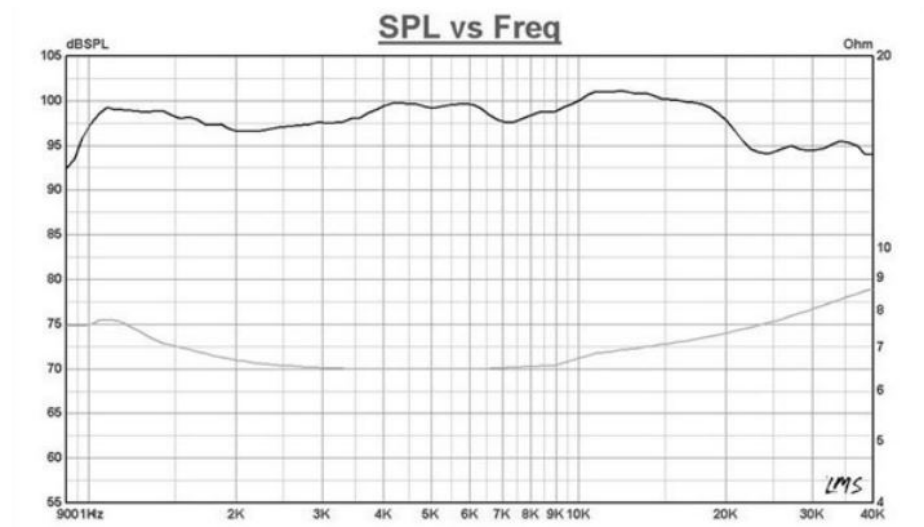
Monacor RBT-20 Ribbon Tweeter

RBT-20

Order No.: 10.5710

EUR 269,00
RRP *

PRODUCTINFOS

The new high-end tweeters RBT-10, RBT-20 and RBT-35SR

are part of the so-called real ribbon tweeters. The audio signal flows through the entire cone which is of extra low weight and consists of an aluminium film. A built-in high-quality transformer converts the low impedance of this cone into 5-8 Ω which is non-critical for the amplifier. Ribbon tweeters impress by an extra fine and brilliant reproduction of the high frequency range. Due to continuous further development, it is already possible to use these ribbon tweeters with crossover frequencies from 2,500 Hz on, depending on the type. This makes them a top choice whenever hi-fi speakers or studio monitors of the highest quality are required. Ribbon tweeters require a crossover network for operation!

Pair of high-end ribbon tweeters, matched, 25 W, 8 Ω

- Real ribbon tweeter with neodymium magnet system and transformer
- Fine and brilliant reproduction of the high frequency range
- Smooth, unembossed aluminium sandwich cone: 12 x 60 x 0.01 mm
- For use from 2,300 Hz on via 18 dB filter
- Robust aluminium front panel with waveguide and protective grille

Klang+Ton 2/2015

"Ribbon tweeter of neat workmanship for 2-way or 3-way systems. It features an excellent omnidirectional radiation."

TECHNICAL SPECIFICATIONS

RBT-20

Impedance (Z)	8 Ω
Operating voltage	-
Frequency range	1200 - 40000 Hz
Resonant frequency (fs)	-
Rec. crossov. frequ. (fmax.) (12 dB/oct.)	>2800 Hz
Power rating	25 W
Peak music power output	50 W
Sensitivity	94 dB/W/m
Max. rated SPL	-
Max. voltage	-
Radiation angle, horizontal	-
Radiation angle, vertical	-
Suspension compl. (Cms)	-
Moving mass (Mms)	-
Mech. Q factor (Qms)	-
Electr. Q factor (Qes)	-
Total Q factor (Qts)	-
Equivalent volume (Vas)	-
DC resistance (Re)	-
Force factor (BxL)	-
Voice coil induct. (Le)	-
Voice coil diameter	-
Voice coil former	-
Linear excursion (X_{max})	-
Eff. cone area (Sd)	-
Magnet weight	-
Magnet diameter	-
Mounting cutout	-
Mounting depth	85 mm
Mounting hole diameter	-

RBT-20

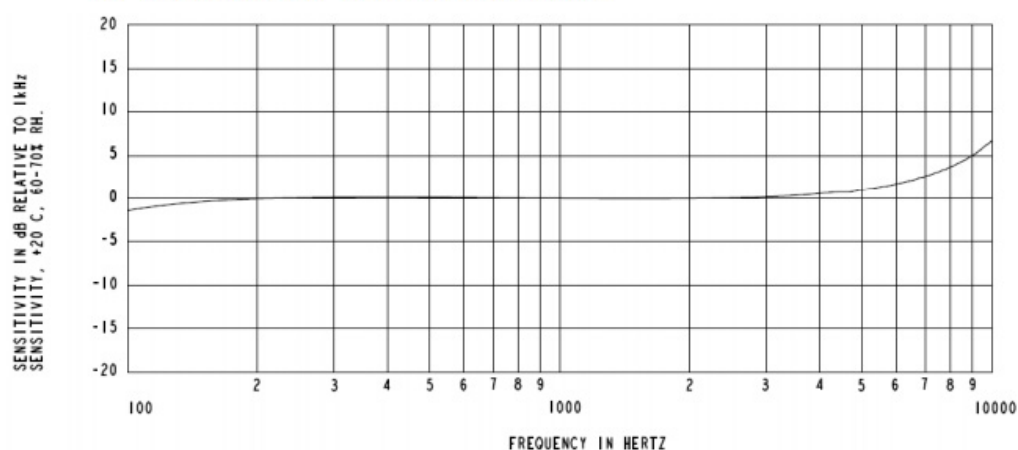|	
Hole spacing X-axis	-
Hole spacing Y-axis	-
Dimensions	Ø 127 mm x 85 mm
Outside diameter	Ø127 mm
Width	Ø127 mm
Height	-
Depth	85 mm
Protective class	-
Admiss. ambient temp.	0 - 40 °C
Weight	1,654 kg
Sales unit	1
Type of speaker	-

231

4. ACOUSTIC & ELECTRICAL SPECIFICATIONS

	Symbol	Condition	Limits			Unit
			Min.	Nom.	Max.	
Directivity		Omni-directional				
Sensitivity	S	@ 1kHz (0dB=1V/Pa)	-45	-42	-39	dB
Output impedance	Z_{OUT}	@ 1kHz (0dB=1V/Pa)	---	---	300	Ω
Current Consumption	I_{DSS}	across 1.5 to 3.6 volts	---	---	250	μA
Signal to Noise Ratio	S/N	@ 1kHz (0dB=1V/Pa)	---	59	---	dB
Supply Voltage	Vs		1.5	---	3.6	V
Sensitivity Loss across Voltage		Change in sensitivity over 3.6v to 1.5v	No Change Across Voltage Range			dB
THD		At 100dB SPL, THD < 1% At 115dB SPL, THD = < 10%				dB

5. FREQUENCY RESPONSE CURVE